Graded Injector, Wide Bandgap Light Emitters and XPS Studies of the InAs/GaSb Heterointerface

Thesis by

Michael Wei-Ching Wang

In Partial Fulfillment of the Requirements

for the Degree of

Doctor of Philosophy

California Institute of Technology

Pasadena, California

1995

(Submitted August 23, 1994)

to

QT

Acknowledgements

This thesis would not have been possible without the support and friendship of a number of people. Without Tom McGill, my advisor, I would not have survived the first few years at Caltech. His support and faith in my abilities kept me going at times when I was sure that I would not succeed. The education that he has provided to me goes well beyond what I have learned in the lab or the classroom. For that I am in his debt.

Besides being the most crucial person to the operation of the group, Marcia Hudson has always been able to make me smile. Her charm and friendliness made frequent visits to her office commonplace (the snacks were nice too). Thanks also to the adminstrative assistance of Sandy Brooks and Phil Cheetham.

A number of former students have provided considerable guidance to me in my earlier years in the group. Mike Jackson eased the transition into the group with his helpful advice. David Chow got me started on my first project. Ed Croke was just fun to be around. Ed Yu taught me more than can be listed here. Much of the work presented in this thesis was based on what he has taught me. Besides guiding me on the II-VI project, Mark Phillips, and his wife Becky, took me on bike rides in the hills that were . . . truly breathtaking.

More recently, I have enjoyed working closely with Doug Collins and Johanes Swenberg. During our "two week project" together, Doug has taught me all I know about III-V MBE growth and RHEED. His patience in explaining things two or three times to me, and his expertise in UHV systems have been greatly appreciated.

Working together with Jo on the II-VI project has been a great experience. Despite the long hours, the deadlines, and the infamous four hour Saturday meetings, I have thoroughly enjoyed the time we've spent together on the II-VI project. His good taste in restaurants also came in handy.

Another of Tom's achievements is the quality of senior researchers that he brings to the group. I have been lucky enough to interact with a few of them. Dr. Jim McCaldin has provided invaluable guidance during the course of the II-VI project. I have benifitted greatly from Dr. Ron Grant's expertise on XPS. Ogden Marsh has provided support and advice in a number of ways. Drs. Tom Keuch and Randy Feenstra have shown me how much more there is to learn; my respect for their abilities continues to grow.

I have greatly enjoyed my interactions with the other members of the group. I have gone to David Ting for advice on a number of issues over the years, and I respect his opinion greatly. His patience with my swimming excuses is also appreciated. Yixin Liu has provided me with many interesting stories and reflections on Chinese culture. He also taught me how painful badminton can be. Besides being an ever helpful computer guru, Harold Levy's unique brand of humor and outlook on life have kept me entertained throughout the years. Ron Marquardt's good nature and friendship have been invaluable over the years. In contrast to his apparent conservative reputation within the group, Ron's partying and womanizing tendencies outside of the group have amazed me over the years. Rob Miles, more than anyone else, kept things lively in the group. His comments and queries in the coffee room will be sorely missed. I have benefited greatly from my interactions with Per-Olov Pettersson (Peo); his energy and enthusiasm are to be admired. Chris Springfield has given much of his time helping me with numerous computer and video related problems. I have also made much use of his ever-ready movie review capabilities.

I have also enjoyed my interactions with some of the more recent members of the group; Alicia Alonzo, Xiao-Chang Cheng, Erik Daniel, and Eric Piquette. I

look forward to future interactions with them.

My interactions outside of the group have helped to keep me sane these years at Caltech. I have enjoyed all of the relaxing times I've had with John, Gemma, and Ron. Thanks.

To Barb, my fiancee, I owe my present happiness. Her love, support and understanding have changed my life.

Finally, without the unquestioning love and support of my parents, brother and sister (in-law) I would not be here today.

List of Publications

Work related to this thesis has been, or will be, published under the following titles:

Effect of Interface Composition and Growth Order on the Mixed Anion InAs/GaSb Valence Band Offset,
M.W. Wang, D.A. Collins, R.W. Grant, R.M. Feenstra, and T.C. McGill, to be submitted to *Appl. Phys. Lett.*

X-ray Photoelectron Spectroscopy Measurement of Valence Band Offsets in Mg-based Semiconductor Compounds,
M.W. Wang, J.F. Swenberg, M.C. Phillips, E.T. Yu, J.O. McCaldin, R.W. Grant, and T.C. McGill, *Appl. Phys. Lett.* **64**, 3455-3457 (1994).

Measurement of the MgSe/CdZnSe Valence Band Offset by X-ray Photoelectron Spectroscopy,
M.W. Wang, J.F. Swenberg, R. J. Miles, M.C. Phillips, E.T. Yu, J.O. McCaldin, R.W. Grant, and T.C. McGill, *J. Cryst. Growth* **138**, 508-512 (1994).

XPS Investigation of the Mixed Anion GaSb/InAs Heterointerface,
M.W. Wang, D.A. Collins, T.C. McGill, and R.W. Grant, *J. Vac. Sci. Technol.* **11**, 1418-1422 (1993).

n-CdSe/p-ZnTe Based Wide Bandgap Light Emitters: Numerical Simulation and Design,
M.W. Wang, M.C. Phillips, J.F. Swenberg, E.T. Yu, J.O. McCaldin and T.C. McGill, *J. Appl. Phys.* **73**, 4660-4668 (1993).

Study of the Abruptness of the InAs-GaSb Interface,
D.A. Collins, M.W. Wang, R.W. Grant, R.M. Feenstra, and T.C. McGill, to be submitted to *Appl. Phys. Lett.*

Scanning Tunneling Microscopy of InAs/GaSb Superlattices: Subbands, Interface Roughness, and Interface Asymmetry,
R.M. Feenstra, D.A. Collins, D.Z.-Y. Ting, M.W. Wang and T.C. McGill, *J. Vac. Sci. Technol.* (1994).

Interface Roughness and Asymmetry in InAs/GaSb Superlattices Studied by Scanning Tunneling Microscopy,
R.M. Feenstra, D.A. Collins, D.Z.-Y. Ting, M.W. Wang and T.C. McGill, *Phys. Rev. Lett.* **72**, 2749 (1994).

Status of $Ga_{1-x}In_xSb$/InAs Superlattices for Infrared Detection,
R.H. Miles, D.H. Chow, J. N. Schulman, D.A. Collins, M.W. Wang, R.W. Grant, and T.C. McGill, submitted to *J. Elect. Materials.*

RHEED Observation of Exchange Reaction Dynamics of InAs Surfaces,
D.A. Collins, M.W. Wang, R.W. Grant, and T.C. McGill, *J. Appl. Phys.* **75**, 259-262 (1994).

Advances in the Development of Graded Injector Visible Light Emitters,
J.F. Swenberg, M.C. Phillips, M.W. Wang, R. J. Miles, J.O. McCaldin, and T.C. McGill, *J. Cryst. Growth* **138**, 692-696 (1994).

Investigation of Crystal Quality and Surface Morphology of ZnTe:N Epilayers Grown on ZnTe and GaSb Substrates,
R. J. Miles, J.F. Swenberg, M.W. Wang, and T.C. McGill, *J. Cryst. Growth* **138**, 523-528 (1994).

A New Approach to Wide Bandgap Visible Light Emitters,
M.C. Phillips, J.F. Swenberg, M.W. Wang, J.O. McCaldin, and T.C. McGill, *Physica B* **185**, 485-489 (1993).

Interfacial Reactions and Band Offsets in the AlSb/GaSb/ZnTe Material System,
E.T. Yu, M.C. Phillips, D.H. Chow, D.A. Collins, M.W. Wang, J.O. McCaldin, and T.C. McGill, *Phys. Rev. B* **46**, 13379-13388 (1992).

Proposal and Verification of a New Visible Light Emitter Based on Wide Bandgap II-VI Semiconductors,
M.C. Phillips, M.W. Wang, J.F. Swenberg, J.O. McCaldin, and T.C. McGill, *Appl. Phys. Lett.* **61**, 1962-1964 (1992).

Forming of Al-doped ZnTe Epilayers Grown by Molecular Beam Epitaxy,
M.C. Phillips, J.F. Swenberg, Y.X. Liu, M.W. Wang, J.O. McCaldin, and T.C. McGill, *J. Cryst. Growth* **117**, 1050-1054 (1992).

Proposal for the Formation of a Minority Carrier Injecting Contact on Wide Bandgap Semiconductors,
Y.X. Liu, M.W. Wang, J.O. McCaldin, and T.C. McGill, *J. Cryst. Growth* **117**, 913-917 (1992).

Schottky Barrier Induced Injecting Contact on Wide Band Gap Semiconductors,
Y.X. Liu, M.W. Wang, J.O. McCaldin, and T.C. McGill, *J. Vac. Sci. Technol. B* **10**, 2072-2076 (1992).

Abstract

This thesis consists of two parts: research performed towards the development of a II-VI graded electron injector wide bandgap light emitter and characterization of the InAs/GaSb heterointerface, for application to InAs/$In_xGa_{1-x}Sb$ infrared superlattice detectors. Background and motivation for both projects are presented.

Investigations of the II-VI graded electron injector light emitter consist of simulations to test the feasibility of a number of LED designs, band alignment measurements, materials characterization and device performance studies. The simulations, based on the Drift-Diffusion model with modifications to account for heterojunctions, demonstrate that the graded electron injector LED design is feasible. Improvements to the basic design can be implemented by incorporating confining layers and active layers with wider bandgaps using ternaries and quaternaries. The XPS measurements of the MgSe/$Cd_{0.54}Zn_{0.46}Se$ and MgTe/$Cd_{0.88}Zn_{0.12}Te$ valence band offsets show a deviation from the common anion rule with the valence band edge of the Mg-based semiconductor lower in both cases. The significance of these results is discussed. XRD, TEM and SIMS characterization of the graded injector devices reveal potential problems in material quality. Device performance characterization show good current-voltage and electroluminescence properties, but poor external quantum efficiency and device lifetimes.

Characterization of the InAs/GaSb heterointerface consists of surface exchange reaction studies, band alignment measurements and interface abruptness studies. The XPS/RHEED investigation of surface exchange reactions shows monolayer

exchange and Sb island formation for the Sb soaks of InAs surfaces, and As exchange with Sb past the terminating monolayer of Sb into the underlying GaSb for the As soaks of GaSb surfaces. The XPS band alignment studies show that the InAs/GaSb valence band offset is independent of interface composition, but changes with growth direction. Possible mechanisms for this behavior are discussed. Finally, the XPS, RHEED, cross-sectional STM and SIMS studies of the abruptness of the InAs/GaSb interface show that the GaSb-on-InAs growth direction is more abrupt than the InAs-on-GaSb growth direction. Mechanisms for this asymmetry in the interface abruptness are presented.

Contents

Acknowledgements iii

List of Publications vi

Abstract x

List of Figures xvi

List of Tables xix

Glossary of Acronyms xx

1 Introduction 1

1.1 Introduction to Thesis 1

1.1.1 General Motivation 1

1.1.2 Summary of Results 3

1.2 Wide Bandgap II-VI Light Emitters 5

1.2.1 Motivation 5

1.2.2 Commercially Available LED Products 8

1.2.3 Wide Bandgap LED Design Issues 12

1.2.4 History and Current Status of Research Efforts 16

1.2.5 Introduction to Graded Electron Injector 25

1.3 The Mixed Anion InAs/GaSb Heterointerface 28

1.3.1 Motivation 28

1.3.2 InAs/$In_xGa_{1-x}Sb$ IR SL Detectors 30
1.3.3 Challenges and Issues for Mixed Anion Interfaces 32
1.3.4 Characterization Techniques 35
1.4 Outline of Thesis 39
References 41

I Graded Electron Injector, II-VI Wide Bandgap Light Emitters 48

2 Light Emitter Simulation and Design 49
2.1 Introduction and Outline 49
2.2 Design Methodology 50
2.3 Model 56
2.4 Simulation Results 63
2.4.1 CdSe/ZnTe 63
2.4.2 Graded Injector 67
2.4.3 Graded Injector with Confining Layer 72
2.4.4 Tunable Bandgap LED 76
2.5 Recent Developments 81
2.5.1 Current LED Structure 81
2.5.2 Possible Quaternary LED Designs 82
2.6 Summary 85
References 87

3 XPS Measurements of Band Offsets for Mg-based Semiconductor Compounds 90
3.1 Introduction and Outline 90
3.2 Experiment 92
3.2.1 Sample Growth 92

3.2.2 XPS Measurements 93
3.3 XPS Data Analysis 94
3.4 Results and Discussion 103
3.4.1 $MgSe/Cd_{0.54}Zn_{0.46}Se$ Valence Band Offset 103
3.4.2 $MgTe/Cd_{0.88}Zn_{0.12}Te$ Valence Band Offset 104
3.5 Summary 105
References 107

4 Status of the Graded Electron Injector Project 110
4.1 Introduction and Outline 110
4.2 Material Characterization 111
4.2.1 XRD 111
4.2.2 TEM 113
4.2.3 SIMS 115
4.3 Device Performance 117
4.3.1 Current-Voltage Characteristics 117
4.3.2 Electroluminescence 119
4.3.3 External Quantum Efficiency 120
4.3.4 Device Degradation Studies 123
4.4 Summary 123
References 126

II XPS Studies of the Mixed Anion InAs/GaSb Heterointerface 127

5 Surface Exchange Reaction Studies 128
5.1 Introduction and Outline 128
5.2 Experiment 130
5.2.1 Sample Growth 130

5.2.2 XPS and RHEED Measurements 130
5.3 Data Analysis 131
5.4 Results 135
5.4.1 Sb Soaks of InAs Surfaces 135
5.4.2 As Soaks of GaSb Surfaces 139
5.5 Discussion 141
5.5.1 Sb Soaks of InAs Surfaces 141
5.5.2 As Soaks of GaSb Surfaces 144
5.6 Summary 146
References 149

6 InAs/GaSb Heterojunction Studies **151**
6.1 Introduction and Outline 151
6.2 InAs/GaSb Band Alignment Studies 152
6.2.1 Motivation 152
6.2.2 Experiment 153
6.2.3 Results and Discussion 156
6.3 Abruptness of the InAs/GaSb Heterointerface 161
6.3.1 Motivation 161
6.3.2 Experiment 162
6.3.3 Observation of Interfacial Asymmetry 165
6.3.4 Underlying Causes of Interfacial Asymmetry 172
6.4 Summary 178
References 181

List of Figures

1.1 External quantum efficiency of existing commercial technologies and spectral eye response 9
1.2 Luminous efficiency of existing commercial LED technologies 10
1.3 p-n homojunction LED operation 13
1.4 Use of McCaldin diagrams in LED design 15
1.5 External quantum efficiency of commercial and developing LED technologies 24
1.6 Schematic of graded injector device 27
1.7 Band edges for InAs/GaSb/AlSb and InAs/GaInSb 29
1.8 Band edges and carrier probability densities for InAs/GaSb and InAs/GaInSb superlattices 33
1.9 Interface composition and growth order in InAs/GaSb heterojunctions 34
1.10 Schematic of X-ray photoelectron spectroscopy 37
1.11 Schematic of reflection high energy electron diffraction setup 38

2.1 McCaldin diagram for common semiconductors 51
2.2 McCaldin diagram for common II-VI semiconductors 53
2.3 Flatband diagram of graded injector device 55
2.4 Bandgap versus lattice constant 57
2.5 CdSe/ZnTe: energy band diagrams 64
2.6 CdSe/ZnTe: charge distributions 65

2.7 CdSe/ZnTe: current densities . . . 66
2.8 Graded device: energy band diagrams . . . 69
2.9 Graded device: charge distribution . . . 70
2.10 Graded device: current densities . . . 71
2.11 Graded device with confining layer: energy band diagrams . . . 73
2.12 Graded device with confining layer: charge distributions . . . 74
2.13 Graded device with confining layer: current densities . . . 75
2.14 Flatband diagram of tunable bandgap LED . . . 77
2.15 Tunable bandgap LED: energy band diagrams . . . 78
2.16 Tunable bandgap LED: charge distributions . . . 79
2.17 Tunable bandgap LED: current densities . . . 80
2.18 Bandgap versus lattice parameter for $Zn_{1-x}Mg_xSe_yTe_{1-y}$ and $Cd_{1-x}Mg_xSe_yTe_{1-y}$ quaternaries . . . 83
2.19 Schematic diagram of fully lattice matched graded injector structure 85

3.1 XPS spectra for $MgSe/Cd_{0.54}Zn_{0.46}Se$ band offset measurement . . . 95
3.2 XPS spectra for $MgTe/Cd_{0.88}Zn_{0.12}Te$ band offset measurement . . . 96
3.3 Fitting of Zn $3p$ 3/2 and Mg $2s$ core level peaks . . . 97
3.4 Fitting of $Cd_{0.54}Zn_{0.46}Se$ and MgSe VBDOS . . . 100
3.5 $Cd_{0.88}Zn_{0.12}Te$ and MgTe VBM separation as function of fitting interval . . . 101
3.6 $Cd_{0.54}Zn_{0.46}Se$ and MgSe VBM separation as function of fitting interval 102
3.7 Measured $MgSe/Cd_{0.54}Zn_{0.46}Se$ and $MgTe/Cd_{0.88}Zn_{0.12}Te$ valence band offsets . . . 103

4.1 XRD data for graded electron injector device . . . 112
4.2 TEM image of graded electron injector device . . . 114
4.3 SIMS impurity profiles . . . 116
4.4 Current-voltage characteristics . . . 118
4.5 Electroluminescence data . . . 120

4.6 Light extraction and contacting issues 121
4.7 Device lifetime studies 124

5.1 XPS spectra: Sb_2 soak of InAs surface, and InAs-on-GaSb heterojunction 132
5.2 Sb 4*d* core level with two chemically shifted peaks 134
5.3 Effect of cracker power on exchange reaction rates 136
5.4 Sb-As exchange as a function of soak time and cracker power 137
5.5 RHEED/XPS studies of Sb soaks of InAs surfaces 138
5.6 As_2 soak of GaSb surface as a function of soak time 140
5.7 Comparison of chemically shifted Sb 3*d* and Sb 4*d* core levels 142
5.8 Other XPS peak intensity ratios for As soaks of GaSb surfaces . . . 145
5.9 Schematic diagram of surface exchange reactions 146

6.1 XPS measurements for InAs/GaSb valence band offset 155
6.2 Fits for As 3*d*, Sb 4*d*, Ga 3*d* and In 4*d* core level peaks 157
6.3 Schematic diagram of cross-sectional STM setup 163
6.4 Schematic diagram of SIMS setup 164
6.5 RHEED reconstruction and intensity oscillation studies of interface asymmetry 168
6.6 Cross-sectional STM images of the InAs/GaSb SLs 171
6.7 XPS/ion sputtering studies. 173
6.8 XPS observation of Sb riding on InAs growth front. 175
6.9 SIMS analysis of InAs-on-GaSb interface abruptness 177
6.10 Schematic diagram of asymmetry in the InAs/GaSb interface 179

List of Tables

1.1 Recent progress of ZnSe-based and GaN-based LEDs 23

6.1 Core level energy separations as a function of interface composition 158

6.2 Core level energy separations as a function of growth order 159

6.3 XPS peak intensity ratios 166

Glossary of Acronyms

CD	compact disc
CW	continuous wave
FWHM	full width at half maximum
HBT	heterojunction bipolar transistor
HH	heavy hole
IR	infrared
ITO	indium tin oxide
LD	laser diode
LED	light-emitting diode
LEEBI	low energy electron beam irradiation
LH	light hole
MBE	molecular-beam epitaxy
MOCVD	(=OMVPE=MOVPE) metalorganic chemical vapor deposition
MOMBE	metalorganic molecular-beam epitaxy
MOVPE	(=MOCVD=OMVPE) metalorganic vapor-phase epitaxy
OMVPE	(=MOCVD=MOVPE) organometallic vapor-phase epitaxy
PL	photoluminescence
QW	quantum well
QWIP	quantum well infrared photodetector
RHEED	reflection high energy electron diffraction

SCH	separate confinement heterostructure
SIMS	secondary ion mass spectrometry
SL	superlattice
SRH	Shockley-Read-Hall
STM	scanning tunneling microscopy
TEM	transmission electron microscopy
UHV	ultra-high vacuum
XPS	X-ray photoemission spectroscopy
XRD	X-ray diffractometry

Chapter 1

Introduction

1.1 Introduction to Thesis

This thesis consists of two parts. Part I describes research performed towards the development of a new II-VI wide bandgap light emitter design. Part II presents characterization of the InAs/GaSb heterointerface, for application to InAs/$In_xGa_{1-x}Sb$ infrared superlattice (IR SL) detectors.

1.1.1 General Motivation

Recent advances in semiconductor growth capabilities have stimulated interest in the development of a wide variety of innovative semiconductor heterostructure devices. In some cases, these device applications rely on the recently developed ability to grow semiconductor layers with extremely small length scales and near monolayer control of growth thicknesses. At these length scales, structures can be fabricated which make use of quantum mechanical phenomena such as quantization of states, resonant tunneling through closely spaced, thin barriers, and wavefunction penetration into barriers. Devices which exploit these phenomena include laser diodes, a variety of inter- and intra-band tunneling structures, and various structures which implement superlattices. Other devices currently under

development rely more heavily on the ability to grow semiconductor materials which previously could not be grown at all, or could not be grown with the desired characteristics. II-VI and nitride semiconductor compounds fall into this category.

In this thesis, various aspects of two semiconductor heterojunction device applications are studied: specifically, the design, fabrication and characterization of novel II-VI wide bandgap light emitters and investigation of the mixed anion InAs/GaSb interface used in IR SL detectors. The II-VI wide bandgap light emitter makes use of the recently developed capability to grow certain II-VI compounds with the necessary material quality and dopant levels, while development of the $InAs/In_xGa_{1-x}Sb$ IR SL detectors relies on the ability to grow very thin (< 100 Å) alternating semiconductor layers with the desired interfacial properties.

The II-VI wide bandgap light emitter design studied in this thesis makes use of an innovative graded electron injector design [1] to overcome fundamental difficulties inherent to II-VI light emitter fabrication. The originality of this light emitting diode (LED) design made it necessary to investigate various design parameters in order to obtain and then optimize proper LED device performance. Additionally, the device incorporates semiconductor materials that are relatively uncharacterized, hence characterization of a number of material parameters was required to ensure optimal performance of the LED.

The InAs/GaSb interface is of interest not only because of its application to $InAs/In_xGa_{1-x}Sb$ IR SL detectors and other device technologies, but also because studies yield insight into the physics of mixed anion interface formation. Since both the anions (As and Sb) and the cations (In and Ga) change across the $InAs/In_xGa_{1-x}Sb$ interface, control of the interfaces in this system is difficult. Add to this the differing bond lengths, bond strengths, and surface free energies in this system, and control of the interfaces becomes even more complicated. Since the interfaces comprise a significant fraction of the layers in the IR SL detector, it is critical to have strict control over both their abruptness and their composition.

1.1.2 Summary of Results

In the first part of this thesis (Chapters 2-4) the simulation, characterization, and fabrication of a graded electron injector II-VI wide bandgap light emitter are discussed. The simulations, based on the Drift-Diffusion model with modifications to account for the effects of heterojunctions, are used to test for LED design feasibility. Results for a variety of devices are presented to demonstrate the design procedure and to explain in detail the operation of the graded electron injector device. The first device is an n-CdSe/p-ZnTe heterojunction LED, which simulations show does not function correctly as an LED due to high levels of interfacial recombination and carrier injection into the narrow bandgap CdSe layer. The second simulated device contains an added graded electron injector layer ($Mg_xCd_{1-x}Se$) between the CdSe and the ZnTe layers. In this case, simulations demonstrate that the device should function correctly as an LED, with electron injection into the wide bandgap ZnTe layer and minimal interfacial recombination. The next two device designs are modified from the standard graded injector device to increase electron confinement, and to shorten the wavelength of emitted light. Finally, the most recent device structure, and a proposed design which allows for a completely lattice matched graded electron injector structure are presented.

Some of the more important parameters affecting LED device operation are the band alignments between the various semiconductor layers used in the LED; however, these parameters are essentially unknown for the the Mg-based semiconductor compounds used in the graded electron injector device. A measurement of the band alignment for two Mg-based semiconductor heterointerfaces was performed using *in situ* X-ray photoemission spectroscopy (XPS) analysis. Specifically, the two heterojunction interfaces were $MgSe/Cd_{0.54}Zn_{0.46}Se$ and $MgTe/Cd_{0.88}Zn_{0.12}Te$, both of which are lattice-matched and share a common anion. The measured valence band offsets are 0.56 ± 0.07 eV and 0.43 ± 0.11 eV for the $MgSe/Cd_{0.54}Zn_{0.46}Se$ and $MgTe/Cd_{0.88}Zn_{0.12}Te$ heterojunctions respectively, with the valence band of

the Mg-based semiconductor lower in each case. These results are significant not only because band alignments are important for device applications but also because the results deviate from the well known common anion rule. A possible explanation for the cause of this deviation is presented.

In addition to band offset measurements, other materials characterization studies are discussed, as well as the latest device performance results. X-ray diffractometry (XRD), transmission electron microscopy (TEM) and secondary ion mass spectrometry (SIMS) studies of graded electron injector devices are presented. The XRD and TEM studies reveal materials quality problems in the devices, attributed in part to the strain induced in the highly lattice mismatched graded region. The SIMS analysis also brings to light potential problems in the form of increased impurity levels in the neighborhood of the graded region. The latest current-voltage and electroluminescence studies of the graded electron device show excellent electrical characteristics and green luminescence. The best external quantum efficiency exhibited to date by our devices is 0.007%. Device degradation studies show evidence for long lifetimes, but our recent devices show lifetimes on the order of only 100s of hours.

The second part of the thesis presents studies of the mixed anion InAs/GaSb heterointerface. Surface exchange reaction studies are made during both Sb interrupts (or soaks) of InAs surfaces, and As soaks of GaSb surfaces as a function of soak time and soak species. XPS analysis of the Sb on InAs exchange reaction shows that Sb exchanges for the terminating As layer with some Sb island formation. For the As on GaSb exchange reaction, it was observed that As exchanges not with only the terminating Sb layer, but also exchanges into the underlying GaSb layer. The mechanism responsible for the difference between the two different exchange reactions is attributed primarily to the interplay between the different bond strengths and the steady state fluxes involved in each exchange reaction. The impact of the difference in soak reaction behavior on subsequent interface abruptness is discussed.

Finally, XPS measurements of the effect of interface composition and growth order on the InAs/GaSb valence band offset and investigations of asymmetry in the abruptness of the InAs/GaSb interface are presented. The InAs/GaSb valence band offset was found to be independent of changes in interface composition, but not independent of changes in growth order. Possible mechanisms for this effect are discussed. XPS, reflection high energy electron diffraction (RHEED), cross-sectional scanning tunneling microscopy (STM) and SIMS investigations of the InAs/GaSb heterojunction show that interfaces for the InAs-on-GaSb growth direction are more extended than for the GaSb-on-InAs growth direction. These analysis techniques provide near-surface chemical information, real-time structural information, high spatial resolution imaging and spectroscopy and high sensitivity, low depth resolution chemical information respectively.

1.2 Wide Bandgap II-VI Light Emitters

1.2.1 Motivation

The development of short wavelength light emitting diodes (LEDs) and laser diodes (LDs) is of significant commercial and technological interest. To better understand why this is so, it is helpful to have some background on the advantages, disadvantages, applications, and markets of currently available LEDs and LDs.

LEDs have a number of clear performance advantages over conventional incandescent lamps. The features that immediately come to mind are efficiency, reliability, fast switching speeds, and narrow linewidths. Typical efficiencies are roughly 2% for incandescent bulbs compared to 18% for the best high brightness commercial red LEDs [2]. Reliability is another area where LEDs have the advantage with lifetimes as high as $\sim 10^5$ hours compared to the $\sim 10^4$ hours typical for incandescent lamps. Another advantage of LEDs is the fast switching speed attainable, especially when compared to fluorescent lamps. Finally, the narrow linewidth

can also be a very desirable quality in many applications where a specific color of emitted light is desired.

Currently, the visible LED market is roughly 20 billion units per year for a total market value of roughly $1 billion per year [3], with the primary application being indicator lamps. Should high brightness, high efficiency green and blue LEDs become available, they will increase the size of this market considerably, even without accounting for new applications. There are many uses for bright green or blue indicator lamps (e.g., outdoor settings or automobile displays) where ambient lighting requires high brightness LEDs, and where colors other than red and amber are desired. The main markets sought after by developers of high efficiency green and blue LEDs, however, are those where the development of these LEDs is expected to open up potentially very large markets that currently do not even exist. As an example of this, the introduction of the ultra-bright, high efficiency red AlGaAs LEDs found an immediate, very large market in automobile brake lights which could not have been accessed with lower efficiency, lower brightness LEDs.

Two potentially large markets are in the areas of full color displays and traffic signal lights. Full color displays based on LEDs would have the advantages of being flat, bright, efficient and scalable to large sizes. The market for this is very large, given the demand for full color, flat panel displays for portable computers, and the potential demand for large area flat panel displays to replace conventional CRT TVs and computer screens. Red and green LEDs also have a large potential market in traffic signal lights. Because lamps used for traffic signal lights must have reasonably fast switching speeds, standard low efficiency incandescent lamps must be used instead of higher efficiency fluorescent lamps. A simple analysis shows that by replacing existing lamps with high efficiency red and green LEDs, an energy savings of over $100 per year per traffic signal head can be achieved [4]. This does not include reduced maintenance and replacement costs associated with the longer LED lifetimes. The energy savings alone would pay for the cost of the LED lamps years before they would need to be replaced. Multiply the savings per

lamp by the number of lamps in a typical city [5], and one can see why LEDs are a very attractive light source for traffic signal lights.

It is estimated that the current market for flat panel displays is roughly $5 billion, projected to reach $40 billion by the year 2000 [6]. To replace all of the traffic signal lights in the United States would require an estimated 4 billion each of discrete red, green and amber LEDs [7]. Though these numbers are approximate, it is clear that enormous markets for high brightness, high efficiency blue and green LEDs exist if only they can be fabricated.

The market for LDs is much smaller than that for LEDs, with 1992 sales of only roughly $287 million/year at an average cost of just under $6/unit [8]. The motivating force for companies such as Sony, which are leading the development of ZnSe-based LDs, is actually the market for systems utilizing the LDs. For instance, although the market for LDs used in compact disc (CD) players and laser printers is small, the market value for CDs, CD players, and laser printers that incorporate these LDs is enormous. Thus, the motivation for producing LDs is not to produce and sell LDs, but to increase sales of systems such as CD players, which have a much larger market value, by providing unique features unattainable by other vendors. The unique feature provided by shortening the wavelength of lasing to the blue for CD players is that the storage density in optical recording can be increased by factors of four or more due to the reduced bit size attainable with shorter wavelengths. With current video compression techniques, this would allow storage of full length movies on standard sized CDs. For laser printers, shorter wavelength LDs would increase both resolution and throughput. Thus, despite the smaller dollar value of the LD market compared to the LED market, there is still very good reason to develop shorter wavelength LDs.

1.2.2 Commercially Available LED Products

In order to properly understand the motivation for the tremendous efforts invested in wide bandgap light emitter research, it is important to evaluate the performance of existing commercial LED technologies. Commercial LDs in the blue and green wavelength regimes simply do not exist, so the discussion will center on commercial LED technologies. Figures 1.1 and 1.2, published by researchers from Hewlett-Packard [9] and modified to include SiC, show the performance of existing commercial LEDs. The AlGaInP LEDs shown are not currently available, but are expected to be commercialized in the near future. Figure 1.1 shows both the external quantum efficiency of the LEDs and the relative response of a light-adapted human eye, as functions of wavelength. The photometric luminous efficiency, expressed in lumens/watt, accounts for the eye response by combining the relative eye sensitivity with the external quantum efficiency. Figure 1.2 shows a plot of the luminous efficiency versus peak wavelength.

In the red wavelength regime, the highest performance LEDs are $Al_xGa_{1-x}As$-based double heterostructure LEDs. External quantum efficiencies of 7% at 645 nm and 18% at 650 nm for absorbing GaAs substrates and transparent AlGaAs substrates, respectively, have been reported [2]. The luminous efficiency of the transparent substrate $Al_xGa_{1-x}As$ LEDs is only slightly below that of a tungsten incandescent lamp and is far superior to a red filtered incandescent lamp.

If we now study the shorter wavelength yellow LEDs, we start to see a drop in the external quantum efficiency, although this is more than compensated for by the higher eye sensitivity to the shorter wavelengths. Two technologies are shown in this wavelength range: $GaAs_xP_{1-x}$ on GaP substrates and $Al_{1-x}In_{0.5x}Ga_{0.5x}P$ on GaAs substrates. The $GaAs_xP_{1-x}$ LEDs perform relatively poorly as seen in Figures 1.1 and 1.2. This is because $GaAs_xP_{1-x}$ becomes an indirect semiconductor at wavelengths less than 627nm. The only reason these devices perform as well as they do is because they are doped with nitrogen which acts as an isoelectronic

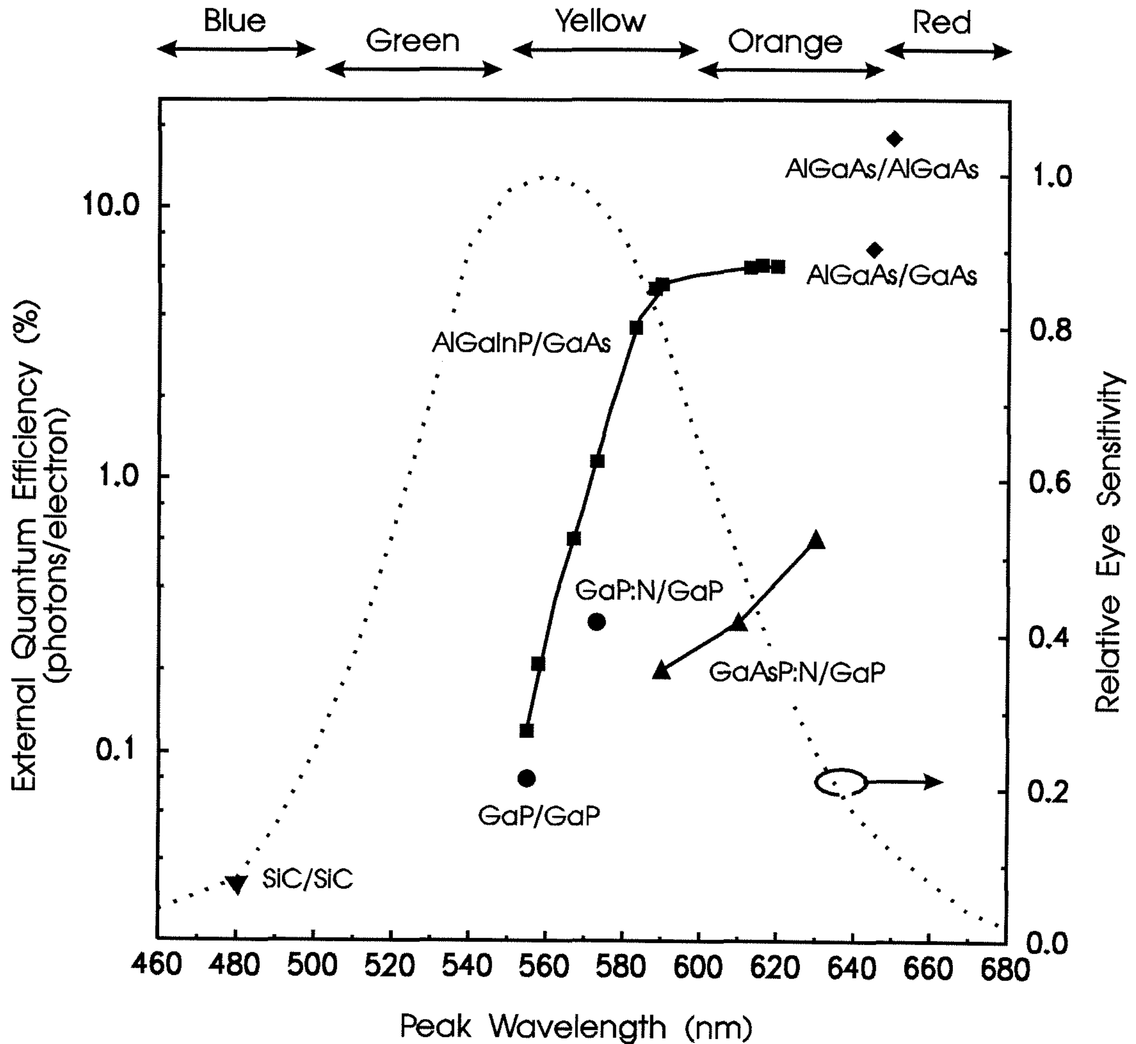

Figure 1.1: External quantum efficiencies of existing commercial LED technologies as a function of peak wavelength at forward biases of 20 mA [9]. Notation for labels is active layer/substrate. Where applicable, nitrogen isoelectronic centers are indicated after the active layer. Dashed line shows the relative eye sensitivity at the different wavelengths.

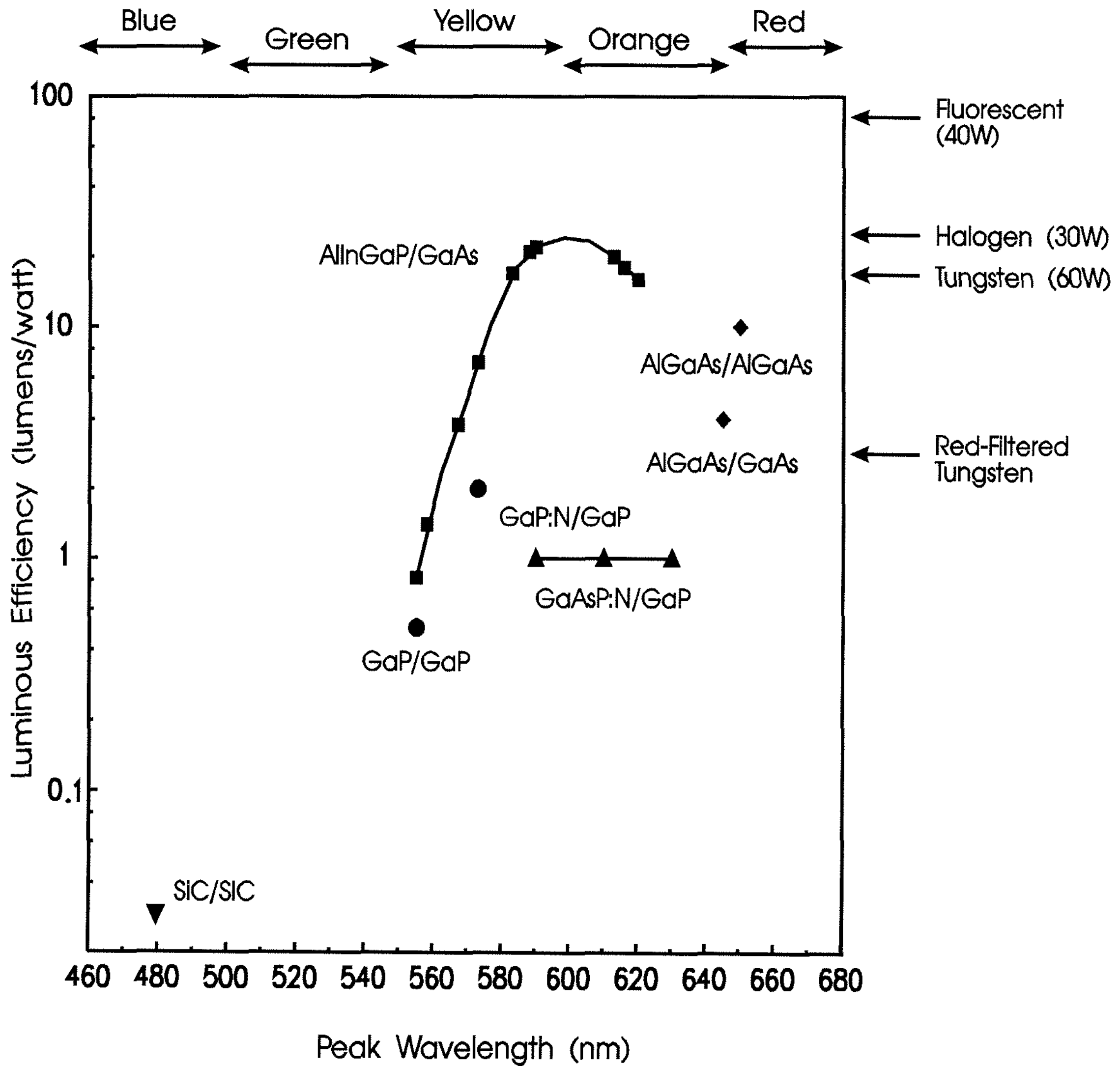

Figure 1.2: Luminous efficiency of existing commercial LED technologies as a function of peak wavelength at forward biases of 20 mA [9]. The luminous efficiency is obtained by applying the spectral response of the human eye to the external quantum efficiency. The luminous efficiency of conventional fluorescent and incandescent lamps are also indicated for comparison purposes.

center, allowing radiative recombination without the involvement of a phonon.

The other technology for yellow LEDs is based on $Al_{1-x}In_{0.5x}Ga_{0.5x}P$, grown by organometallic vapor-phase epitaxy (OMVPE) and lattice matched to GaAs. Progress in this material system has been substantial since the first orange LEDs were demonstrated in 1984 [10]: first transparent $Al_xGa_{1-x}As$ window layers [11] and lattice mismatched GaP window layers [12] were introduced, then the thickness of the GaP window layer was increased to 45 microns [9], and most recently (not shown in Figures 1.1 and 1.2) the removal of the GaAs substrate and subsequent wafer bonding of a transparent GaP substrate was achieved [13]. Although the most recent of these devices has not yet been commercialized, no degradation in device reliability has been observed, hence they are expected to be commercialized soon. The maximum luminous efficiency observed is 41.5 L/W, which is greater than even unfiltered halogen or tungsten incandescent lamps and is only roughly a factor of two lower than the luminous efficiency of fluorescent lamps.

If we now look at the green wavelength regime, we start to understand why so much research has been directed toward developing wide bandgap LEDs. The performance of both the GaP- and $Al_{1-x}In_{0.5x}Ga_{0.5x}P$-based green LEDs is significantly worse than that of the yellow LEDs. GaP, as mentioned before, is an indirect semiconductor, so the green LEDs made from it expectedly have very low quantum efficiencies. The addition of N to act as an isoelectronic center improves the efficiency significantly, but also shifts the wavelength into the yellow-green, leaving its performance below that of $Al_{1-x}In_{0.5x}Ga_{0.5x}P$. The $Al_{1-x}In_{0.5x}Ga_{0.5x}P$ technology, although somewhat improved over GaP, still has much lower luminous efficiency than LEDs in the yellow wavelength regime, despite the improved eye response to green. The dropoff in efficiency for $Al_{1-x}In_{0.5x}Ga_{0.5x}P$ LEDs is not entirely understood yet, but is expected to be related to the approach of the direct-indirect transition at shorter wavelengths [14].

The decrease in performance continues as even shorter-wavelength, blue SiC LEDs are examined (recently announced, high performance $GaN/In_xGa_{1-x}N/GaN$

LEDs are discussed in the following section). The low quantum efficiency of these devices is compounded by the sharp dropoff in the eye response for wavelengths shorter than that of green light. The best SiC LEDs today have luminous efficiencies of roughly 0.03 lumens/watt [15], 1000 times lower than the best $Al_{1-x}In_{0.5x}Ga_{0.5x}P$ LEDs. Again, the low efficiency is due to the indirect nature of SiC. Because of the fundamentally poor radiative recombination efficiency of indirect bandgap semiconductors, it is unlikely that the SiC, GaP, GaP:N or $Al_{1-x}In_{0.5x}Ga_{0.5x}P$ technologies will be able to achieve significant improvements in the efficiencies of green or blue LEDs in the near future. Thus, new materials which have direct bandgaps at the shorter blue and green wavelengths must be investigated. The history and current status of these research efforts are discussed in Section 1.2.4.

1.2.3 Wide Bandgap LED Design Issues

For better understanding of Sections 1.2.4 and 1.2.5, a brief discussion of wide bandgap LED design issues is given below. In its simplest from, an LED consists of only a p-n homojunction as shown in Figure 1.3. Figure 1.3(a) shows the conduction and valence band edges and Fermi levels for the n- and p-type regions before charge redistribution occurs. Upon charge redistribution, at zero bias, the band profiles are as shown in Figure 1.3(b). Applying a forward bias to the device forces electrons into the p-type material, resulting in radiative recombination of electron-hole pairs, as show in Figure 1.3(c). Similarly, holes forced to the left in Figure 1.3(c) recombine radiatively with the electrons in the n-type material.

This simple p-n homojunction design is sufficient for narrow bandgap (long wavelength) LEDs. However, it is much more difficult to implement this design for a wide bandgap LED, since wide bandgap semiconductors are generally very difficult to dope both n- and p-type. Until very recently it was not possible to dope direct wide bandgap semiconductors both n- and p-type to sufficient levels

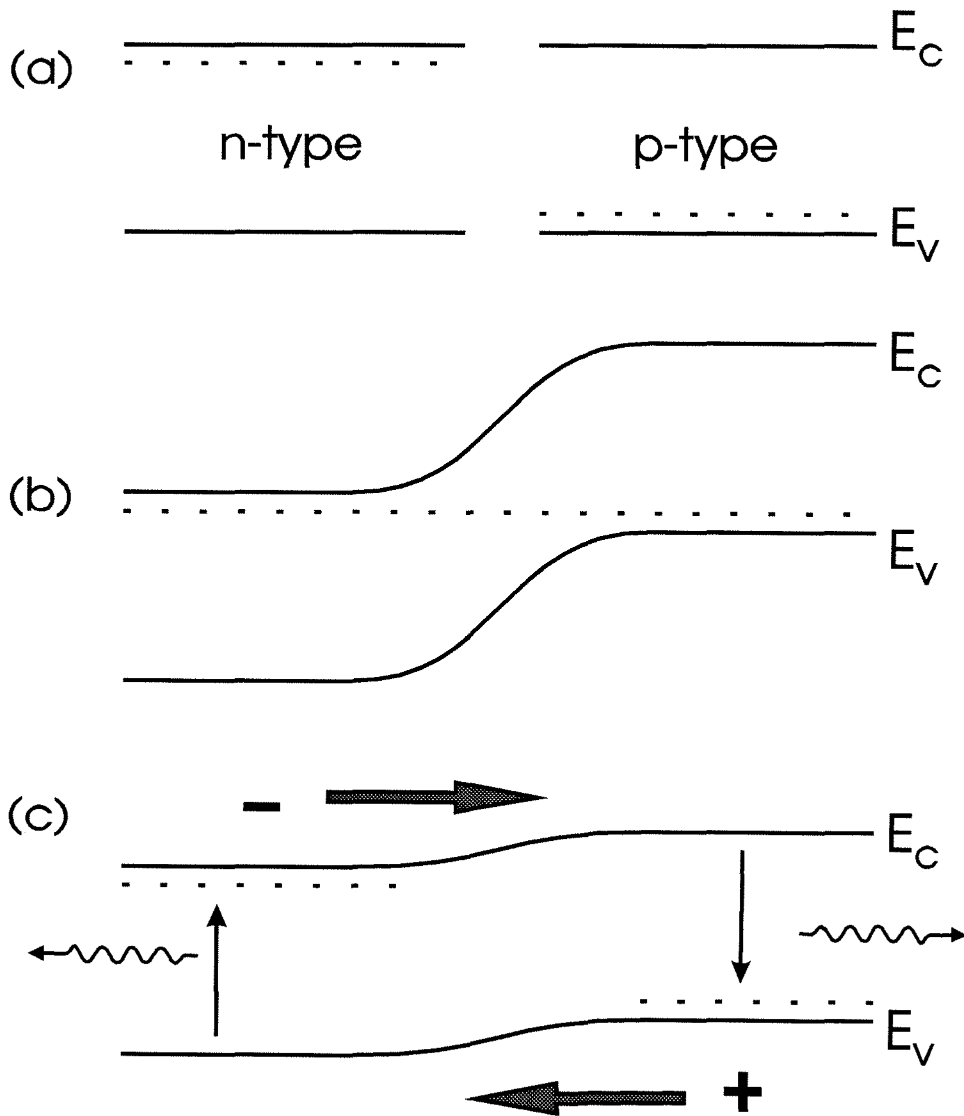

Figure 1.3: Schematic diagram of the operation of a simple p-n homojunction LED. The band profiles and Fermi levels are shown prior to and after charge redistribution in (a) and (b) respectively. At forward bias carrier injection occurs, resulting in radiative recombination, as shown in (c). Dashed lines denote the hole and electron Fermi levels.

to afford low resistance ohmic contacts and low series resistance devices. As a result of the inherent difficulties in amphoteric (both n- and p-type) doping of wide bandgap semiconductors, it has been necessary to go to more sophisticated LED structures. Some of these approaches address contacting problems directly using, for example, highly doped graded regions [16]. Other approaches address the doping problem by using heterojunctions of easily doped semiconductors.

In either case, we must now examine material parameters that were not of concern when dealing only with p-n homojunctions. The three primary parameters that need to be assessed are the lattice parameter, band alignment and dopability, which can be displayed together in a McCaldin diagram [17], shown in Figure 1.4. In McCaldin diagrams each semiconductor is represented by a vertical line with length proportional to its bandgap. The vertical position of each line is determined either by experimental measurements or theoretical predictions of band alignments; the horizontal position is determined by the lattice parameter. Dopability is indicated by filled triangles (n-type dopable) and filled squares (p-type dopable). Empty symbols indicate poor dopability. Using McCaldin diagrams then, it is a straightforward procedure to determine if a combination of semiconductor materials satisfies LED design constraints, at least to first order. These constraints require that: 1) the LED structure be closely lattice matched, 2) the band alignments of the semiconductor be amenable to efficient carrier injection into a semiconductor with the desired bandgap, and 3) both n- and p-type doping be sufficient for ohmic contacting and low series resistance. For example, an n-ZnSe/p-ZnTe heterojunction is unlikely to perform well because of the large lattice mismatch between ZnSe and ZnTe which will result in a high defect density. Similarly, an n-AlSb/p-ZnTe heterojunction has band alignments that favor carrier injection into the indirect, narrower bandgap AlSb layer. More detailed usage of McCaldin diagrams will be given in Chapter 2.

Another design issue that is important for LEDs and critical for LDs is that of availability of quantum wells (QWs) and confining regions. In LEDs, these can

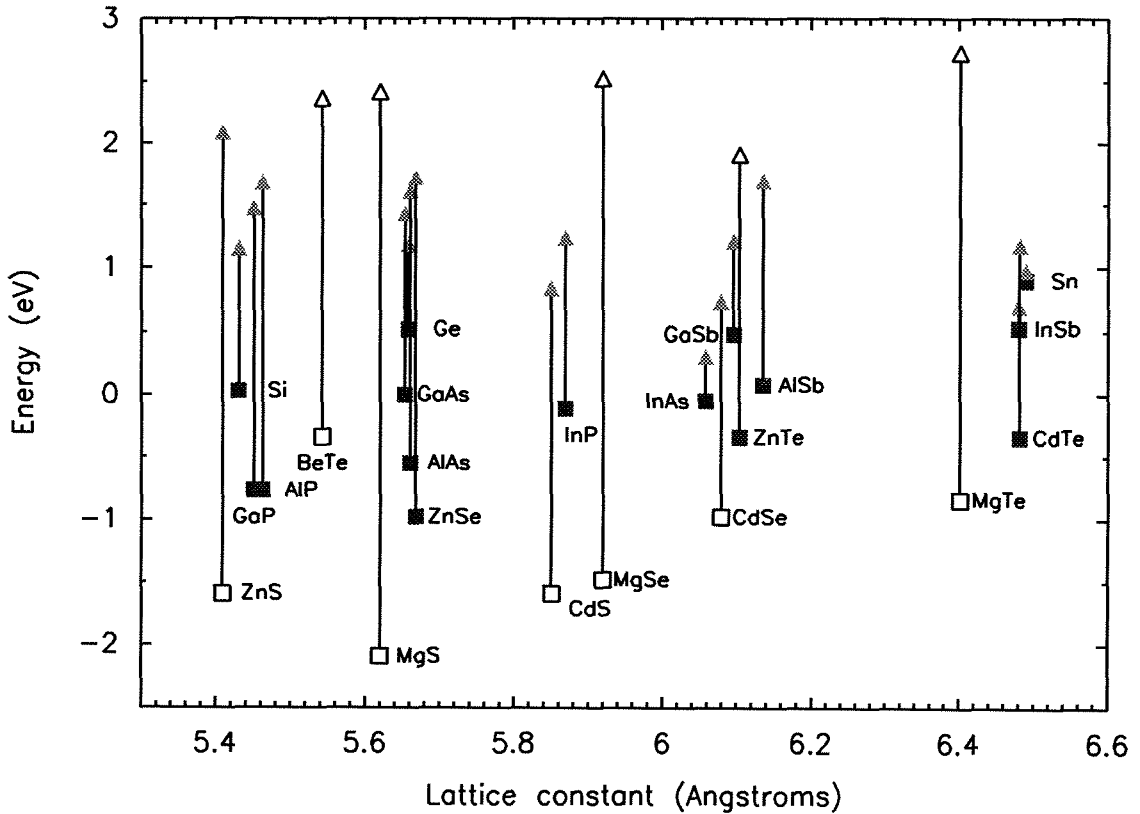

Figure 1.4: Each material in a McCaldin diagram is represented by a vertical line with a square at the bottom, corresponding to the VBE, and a triangle at the top, corresponding to the CBE. The horizontal position of each line is determined by the lattice parameter, and the length of each line scales with the bandgap of the material that it represents. The vertical position of each line is determined by predicted or experimental band alignments. Open triangles and squares represent semiconductors that cannot be doped n or p type respectively using conventional doping techniques.

be used to significantly increase the efficiency of the device, while in LDs they are essential to achieve lasing. Separate confinement heterostructure (SCH) LDs require a QW, confining layers and cladding layers, all with the same, or nearly the same lattice parameter.

Extraction of the emitted light is an issue that will be dealt with in more detail in Chapter 4. The only point to be made here is that the absorption of light by semiconductors with bandgaps smaller than the energy of the emitted light is detrimental to device performance and must be accounted for in the design evaluation. This is important both for the epilayers and for substrates, since as will be seen in the next section, the difference between absorbing and transparent substrates can lead to a significant change in external quantum efficiency.

One other technical issue is the availability of lattice-matched substrates. Growing a device on a highly mismatched substrate will result in heavily dislocated layers which, in general, leads to poor device performance. A notable exception to this is the GaN/$In_xGa_{1-x}N$/GaN developed by Nichia [18]. Details of the exceptional performance of these devices despite relatively poor material quality will be given in Section 1.2.4.

1.2.4 History and Current Status of Research Efforts

In Section 1.2.2, the status of existing commercial LED technologies was described, and the need for research efforts into new materials systems in order to achieve high efficiency blue and green LEDs was justified. Progress for two of these efforts has been very rapid over the past few years, so the history and current status of both efforts will be described. The first is the ZnSe-based system which had early successes with the development of LDs and high efficiency blue and green LEDs. The second effort is based on the GaN/InN/AlN material system, for which recent results report high efficiency, long lifetime blue and green LEDs.

ZnSe

The majority of II-VI wide bandgap light emitter research is focussed on the ZnSe material system. There are a number of features of ZnSe that initially made it a very favorable material to investigate, including its close lattice match to GaAs substrates, a bandgap in the blue and favorable band alignments to n-GaAs for electron injection. The main challenge initially encountered was to achieve p-type doping. Many different dopants were tried, but only two were even moderately successful. The first successful p-type doing of molecular-beam epitaxy (MBE) grown ZnSe was reported by researchers at 3M [19], who used lithium doping to obtain a maximum hole concentration of 3.6×10^{13} cm^{-3}. Eventually, net acceptor levels of roughly 1×10^{17} cm^{-3} [20] were obtained; however, this was still insufficient for good ohmic contacting, and the possibility of Li diffusion cast doubt on the long term suitability of Li as a p-type dopant for ZnSe. In addition, efforts to dope ZnSe with nitrogen were beginning to achieve some impressive results, so as a result interest in Li doping waned. By 1990 N-doped p-ZnSe with hole concentrations greater than 1×10^{17} cm^{-3} was obtained using both metalorganic molecular-beam epitaxy (MOMBE) [21] and MBE [22, 23]. Since then, despite the efforts of many research groups around the world, the hole concentrations achieved in ZnSe using N have saturated at roughly 1×10^{18} cm^{-3} [24], with observation of high levels of compensation. While these hole concentrations are sufficient for the epilayers within LED and LD structures, they are insufficient for good ohmic contacting, as will be discussed below.

Despite the contacting problems, the successful p-type doping of ZnSe led to the first ever blue-green LD, operating under pulsed current injection at 77 K and a threshold voltage of 20V [25]. Understandably, research into ZnSe intensified considerably as a result of this report, and soon groups from around the world were presenting ZnSe-based LD results. Many publications reported marginal improvements in device structure, and/or performance; however, it wasn't until the issues of cladding layers, ohmic contacts and obtaining pseudomorphic structures

were addressed that truly significant improvements in device performance were obtained.

The proposal and characterization of $Zn_{1-x}Mg_xS_ySe_{1-y}$ quaternary layers as a suitable cladding layer for ZnSe LDs was first presented by researchers at Sony [26]. The use of the $Zn_{1-x}Mg_xS_ySe_{1-y}$ cladding layers was advantageous because the bandgap and lattice constant could be independently varied. Also, the wavelength of light emission could be more freely adjusted to shorter wavelengths because of the large bandgap attainable by $Zn_{1-x}Mg_xS_ySe_{1-y}$. These benefits soon resulted in the first blue LD, operating under continuous wave (CW) operation at 77 K [27], the pulsed operation of pseudomorphic blue-green LDs up to temperatures as high as 394K [28], and the lasing of photopumped blue (464.5 nm) double heterostructure lasers up to 500 K [29].

The issue of ohmic contacting continued to be a problem in these improved devices, which still operated at voltages in excess of 10 V. In addition to annealing schemes, a number of other more sophisticated approaches have been proposed to improve the contact to the p-type ZnSe. The first of these was proposed by Schetzina *et al.* at North Carolina State University [30]. Taking advantage of the semimetallic nature and large electronegativity of HgSe, they were able to fabricate LEDs with low turn-on voltages using a metal/HgSe/p-ZnSe contacting scheme. The 4.4 V operating voltage of the LEDs produced was significantly better than the 6-10 V typically required at the time. A further improvement, reported in the same paper, makes use of a metal/HgSe/graded $ZnTe_{1-y}Se_y$/p-ZnSe contacting scheme.

Shortly thereafter, researchers at Brown/Purdue [16] reported a pseudograded bandgap contacting scheme using alternating layers of p-ZnTe/p-ZnSe in which the thickness of the ZnTe layers became progressively narrower and the thickness of the ZnSe layers, progressively wider as the bulk p-ZnSe was approached. This technique was successful in producing contact resistances of 2 to $8 \times 10^{-3}\ \Omega\,cm^2$, which is considered acceptable for contacts to LEDs and LDs. The operating

voltage of the LDs using this contacting scheme was reduced considerably to 15-17 V from approximately 30 V. However, this was still higher than the operating voltages obtained at that time by other groups which were not using a graded contacting scheme.

Researchers at Sony also presented an approach using ZnTe/ZnSe multiquantum wells to achieve low contact resistances [31]. Their approach was similar to that used at Brown/Purdue, except that the thicknesses of the ZnTe QWs were adjusted so that, accounting for bandbending, the lowest energy level of holes in each ZnTe QW was aligned with the top of the ZnSe valence band. By doing this, resonant tunneling through the multiquantum well structure is enhanced over a simple pseudograded ZnTe/ZnSe structure. However, the contact resistances achieved using this method were $5 \times 10^{-2}\ \Omega\,\mathrm{cm}^2$, higher than those obtained using the pseudograded structure. This effect may have been due to the overall lower doping levels used in both the ZnTe and ZnSe layers for the multiquantum well structure.

Finally, a $Be_xZn_{1-x}Te_ySe_{1-y}$ graded bandgap ohmic contacting scheme was proposed by Philips [32] and Xerox [33]. Although no experimental data was presented, this approach is theoretically feasible and has all the benefits of the ZnTe/ZnSe contacting schemes with the additional advantage of maintaining full lattice match to the device layers throughout the contacting layers.

The improvement in LED performance using the HgSe and ZnTe/ZnSe contacting schemes is shown in Table 1.1. This table shows the progression of LED results for both the ZnSe-based material system and the GaN-based material system. In 1992, researchers at Brown/Purdue reported both blue and blue-green LEDs [34, 35]. These LEDs did not implement the pseudograded ZnTe/ZnSe contacting scheme as evidenced by their high operating voltages (7-20 V), and had relatively poor efficiencies. Later, in 1993, green and yellow LEDs implementing the ZnTe/ZnSe pseudograded contact were reported with operating voltages of approximately 6 V [36]. At roughly the same time, blue and green LEDs incorporating the HgSe contact were reported with low operating voltages (roughly 3.7 to

3.8 V) but again having relatively low efficiencies [37].

More recent results by the same group show similar current-voltage characteristics, but much improved external quantum efficiencies of 5.7 to 6.2×10^{-3}, attributed to improved growth procedures which reduced the number of non-radiative centers in the active layers [38]. These efficiencies were much better than current commercial LEDs; however, the device lifetimes were still inadequate, with even the best devices degrading by 60-65% after 250 hours. The latest devices from the same group, also shown in Figure 1.5, use ZnSe instead of GaAs substrates. Efficiencies as high as 3.2% have been obtained, with lifetimes increasing to over 1000 hours despite higher defect densities than in previous structures [39].

The incorporation of both the pseudograded and the multiquantum well ZnSe/ZnTe contacting schemes has also resulted in improved performance of LD structures. Recent results for the pseudograded contact show respectable threshold voltages and current densities of 4.2 V and 600-1100 A/cm^2, respectively for 509 nm LDs. Device lifetimes at room temperature were $>$ 20 seconds [40]. Blue (489.9 nm) and green (523.5 nm) LDs incorporating the multiquantum well ZnSe/ZnTe contacts show thresholds of $<$ 4 V and 400 A/cm^2, and room temperature CW operation for greater than 9 minutes [41].

The main challenge remaining for both LEDs and LDs is the issue of device degradation. One study by the researchers at 3M [42] showed that the LED and LD degradation was caused by the propagation of crystal defects from the vicinity of pre-existing defects, such as stacking faults. This was shown to lead to the formation of dark line defects. Another study [43] showed that N-doping of ZnSe can lead to a higher occurrence of stacking faults. Thus, it may be that the poor device lifetimes in the ZnSe-based structures are related to the N-doping of the Se layers, especially considering that highly p-doped ZnSe is very difficult to achieve and is heavily compensated. Another possibility is that strain and interdiffusion at the GaAs/ZnSe interface results in increased defect densities which adversely affect device lifetimes. LED results presented recently [39] support this, and LD

structures grown on ZnSe substrates are currently being investigated to test this hypothesis [44]. It is also possible that greatly improved lifetimes will be achieved simply by improving growth and fabrication procedures to reduce defect densities.

GaN/AlN/InN

GaN/AlN/InN is both a promising and a challenging material system for LED and LD design. Some attributes of this system include the large range in bandgaps (1.9 eV for InN, 3.4 eV for GaN, and 6.2 eV for AlN, all for wurzite crystals) and the robust nature of the materials. The challenges lie in the lack of a lattice matched substrate, obtaining p-type dopability, as well as in processing difficulties resulting from the resistance of the materials to wet chemical etches. Detailed reviews of the nitride material system and early results can be found in References [45, 46, 47]. We now give a brief review of the recent progress in nitride development.

As late as 1989, there still remained many obstacles to the development of nitride LEDs and LDs: p-type doping was still unattainable, material quality was poor and heterostructure growth was still undeveloped. Also, most structures at the time were grown on sapphire substrates which has a large lattice mismatch to GaN. Metal insulating semiconductor (MIS) structures had been fabricated, but no p-n homojunction LEDs had yet been produced. In 1989, however, Amano *et al.* [48] made a significant advance with the announcement of p-type conduction in Mg-doped, OMVPE grown GaN, using a low-energy electron beam irradiation treatment (LEEBI). As grown, the Mg-doped GaN is highly resistive, but after the LEEBI treatment the resistivity dropped by more than five orders of magnitude. Using this LEEBI treatment Amano *et al.* were able to fabricate the first ever p-n homojunction LED in the nitride system.

At the time, a thin AlN buffer layer was required to obtain reasonable GaN growth [49], due to the large lattice mismatch between GaN and the sapphire substrates being used. Using this technique, x-ray rocking curves with full width half maximas (FWHMs) as low as 2 arc minutes were attainable. In 1991 Nakamura

showed that a low temperature GaN buffer layer could also be used to obtain GaN layers of reasonable quality (FWHMs of approximately 5 arc minutes) [50]. Improvements on this technique led to the development of GaN p-n homojunction blue LEDs with external quantum efficiencies of 0.18% and good current-voltage characteristics [51] (see Table 1.1). The efficiencies of these devices were already much better than the efficiencies of commercial SiC blue LEDs. At roughly the same time, investigation of InGaN growth was yielding films of relatively high quality [52]. These advances, combined with the growth of high quality Si-doped n-InGaN films [53], eventually led to the demonstration of p-GaN/n-InGaN/n-GaN blue [54] and violet [55] LEDs. The active region in these devices was Si-doped InGaN, producing luminescence between 411 and 440 nm with FWHMs of 22-26 nm. While the external quantum efficiencies were 0.15-0.22%, current-voltage characteristics were poor. This was attributed to high resistivity of the p-type GaN layer, even after LEEBI treatment. Work on LED structures using AlN buffer layers had also progressed considerably during this time, with a report in 1993 by Akasaki *et al.* of ultra-violet LEDs with efficiencies of 0.33% under a forward current of 90 mA and bias of 5.0 V [56]. These results were quite respectable but would soon be bettered by the results of Nakamura and co-workers.

Their first development was the improvement of p-type conductivity in GaN using N_2-ambient thermal annealing [57, 58]. It was concluded that acceptor-H neutral complexes was the cause of the high resistivity in Mg-doped GaN, and that both the N_2-ambient thermal anneal and the LEEBI treatments lower the resistivity by removing the hydrogen from the GaN film. The second development was the successful Zn-doping of p-InGaN [18]. These two developments led to the first demonstration of candela-class InGaN/AlGaN blue LEDs [18] with external quantum efficiencies of 2.7%. This is roughly two orders of magnitude better than commercial blue SiC LEDs. Recent versions of this device [59] (see also Figure 1.5) have an external quantum efficiency of 4.4% and luminous intensity of roughly 2.8 candela, operating at an injection current of 30 mA at 3.8 V. Blue-green LEDs in

Ref.	Active Layer	Comment	λ (nm)	Ext. Qu. Eff. (%)	V_{op} (V)	J_{op} (A/cm^2)	Lifetime (hours)
(a) ZnSe-based							
[34]	CdZnSe*	—	506	0.01	7	4	—
[35]	ZnSSe*	—	494	0.1	20	1	—
[36]	CdZnSe:Te*	—	$\sim$486	—	>10	—	—
		—	$\sim$560	0.03	>10	—	—
[36]	CdZnSe:Te	"graded"	$\sim$486	<0.03	6	4	—
			$\sim$560	<0.03	6	4	—
[37]	ZnCdSSe	HgSe	480	0.03	3.7	4	—
	ZnTeSSe		$\sim$504	0.05	3.6	20	—
[38]	ZnCdSSe	HgSe	490	0.57	3.7	4	10^2
	ZnTeSSe		$\sim$506	0.62	3.8	4	10^2
[39]	ZnTeSSe	HgSe ZnSe sub.	510	3.2	4.0	16	10^3
(b) Nitride-based							
[51]	GaN	GaN buf.	$\sim$430	0.18	4	6.7	—
[54]	InGaN:Si		440	0.22	19	6.7	—
[56]	GaN	AlN buf.	372	0.33	5	—	—
[18]	InGaN:Zn	GaN buf. Anneal	$\sim$450	2.7	3.6	$6.7^\dagger$	10^4
[59]	InGaN:Zn	GaN buf.	$\sim$450	4.4	3.8	$10^\dagger$	10^4
		Anneal	$\sim$500	1.4	3.7	$10^\dagger$	10^4

Table 1.1: Recent Progress of (a) ZnSe-based and (b) GaN-based LEDs. Tildes before a specified wavelength indicate a broad emission peak (> 50 nm). Dashes indicate that the quantity was not specific in the reference.

* Indicates p-type GaAs substrates used so no contact was made to p-ZnSe.

† Assumes device size unchanged from Reference [54].

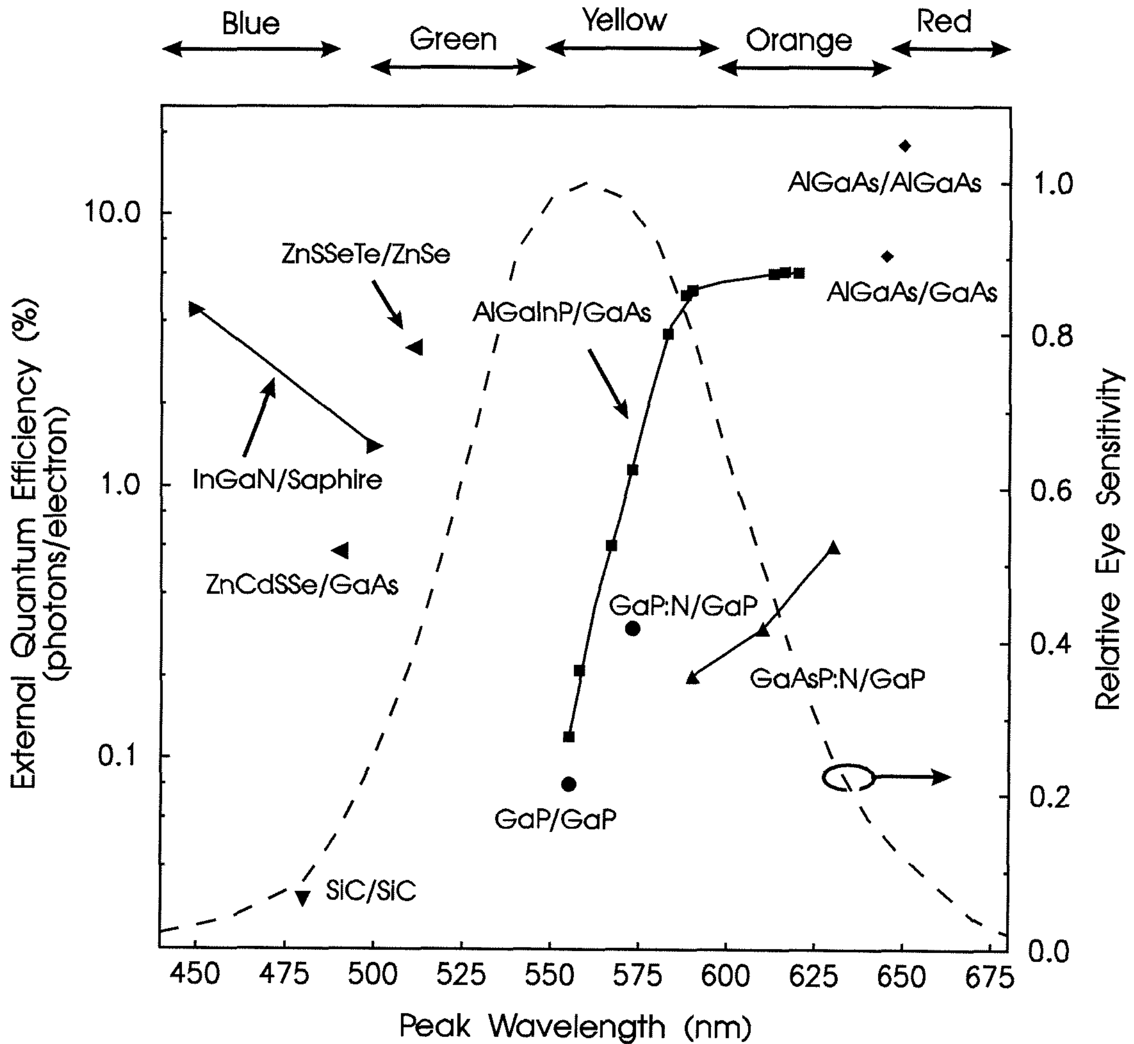

Figure 1.5: External quantum efficiencies of both commercial and developing LED technologies as a function of peak wavelength. Notation for labels is active layer/substrate. Dashed line shows the relative eye sensitivity at the different wavelengths.

this system have also been recently demonstrated with injection currents of 30 mA at 3.7 V and external quantum efficiencies of 1.4%. Device lifetimes for both the blue and the blue-green LEDs are several tens of thousands of hours.

Despite these spectacular results, there are still many issues that need to be addressed in the nitride system. For example, the emission linewidths in the recent nitride devices are very broad (70-80 nm) which is not conducive to achieving lasing. Also, the material quality is still very poor, primarily because of the lack of a lattice matched substrate. Some early work in this area on the growth of thick (200-400 μm) GaN layers appears promising [60]; however, no commercial lattice matched substrates for GaN exist as of yet. Another issue that needs to be addressed is device processing; since GaN cannot be etched by standard wet chemical processes, reactive ion etching procedures must be explored. Finally, there is still much work to be done on the lower temperature growth of nitrides using MBE, which is still in the early stages of development.

1.2.5 Introduction to Graded Electron Injector

A brief description of the graded electron injector is given here as an introduction; a more detailed description of its operation is given in Chapter 2. As was pointed out above, the initial challenge for groups pursuing wide bandgap LEDs was to obtain both p- and n-type dopability. In the case of GaN efforts, an additional difficulty exists due to lack of lattice-matched substrates. In both the ZnSe and nitride systems, amphoteric (both p- and n-type) doping has been achieved at least to first order. However, it is still possible that the poor device lifetimes in the ZnSe-based devices will remain a problem for some time, and that broad luminescence from deep acceptor levels as well as poor material quality in the nitrides will preclude LD structures.

In anticipation of the difficulties associated with forcing amphoteric doping, the approach used in the graded electron injector was to form a heterojunction of

one n-type and one p-type dopable semiconductor, while satisfying the constraints of close lattice match and carrier injection into a semiconductor with the desired bandgap. One promising pair of semiconductors that satisfies both the dopability and lattice match constraints is CdSe and ZnTe. CdSe can be easily doped n-type, while ZnTe can be doped p-type, and the two semiconductor have a lattice mismatch of only 0.4% (Figure 1.4). To obtain carrier injection into the wider bandgap, ZnTe material requires the insertion of a graded $Mg_xCd_{1-x}Se$ layer to facilitate electron injection into the ZnTe layer, while blocking holes from entering the lower bandgap CdSe region. A schematic diagram of the operation of this device is shown in Figure 1.6.

The main challenge in the graded electron injector approach lies in optimizing the graded $Mg_xCd_{1-x}Se$ layer, not in obtaining amphoteric doping as was the case initially in the ZnSe- and nitride-based systems. For ideal operation, the conduction band edge of $Mg_xCd_{1-x}Se$ must line up with the conduction band edge of ZnTe at the Se/Te interface. The ideal composition of $Mg_xCd_{1-x}Se$ to accomplish this depends on both the bandgap of MgSe and the band alignment of $Mg_xCd_{1-x}Se$ to ZnTe. Thus, optimization of the graded injector design requires characterization of the properties of $Mg_xCd_{1-x}Se$ ternaries, and careful design of the graded injector layer itself. Characterization of materials properties is also required, using such techniques as XRD, TEM, and SIMS. Current-voltage, electroluminescence, photoluminescence, efficiency and device lifetime measurements are also needed in order to evaluate LED device performance.

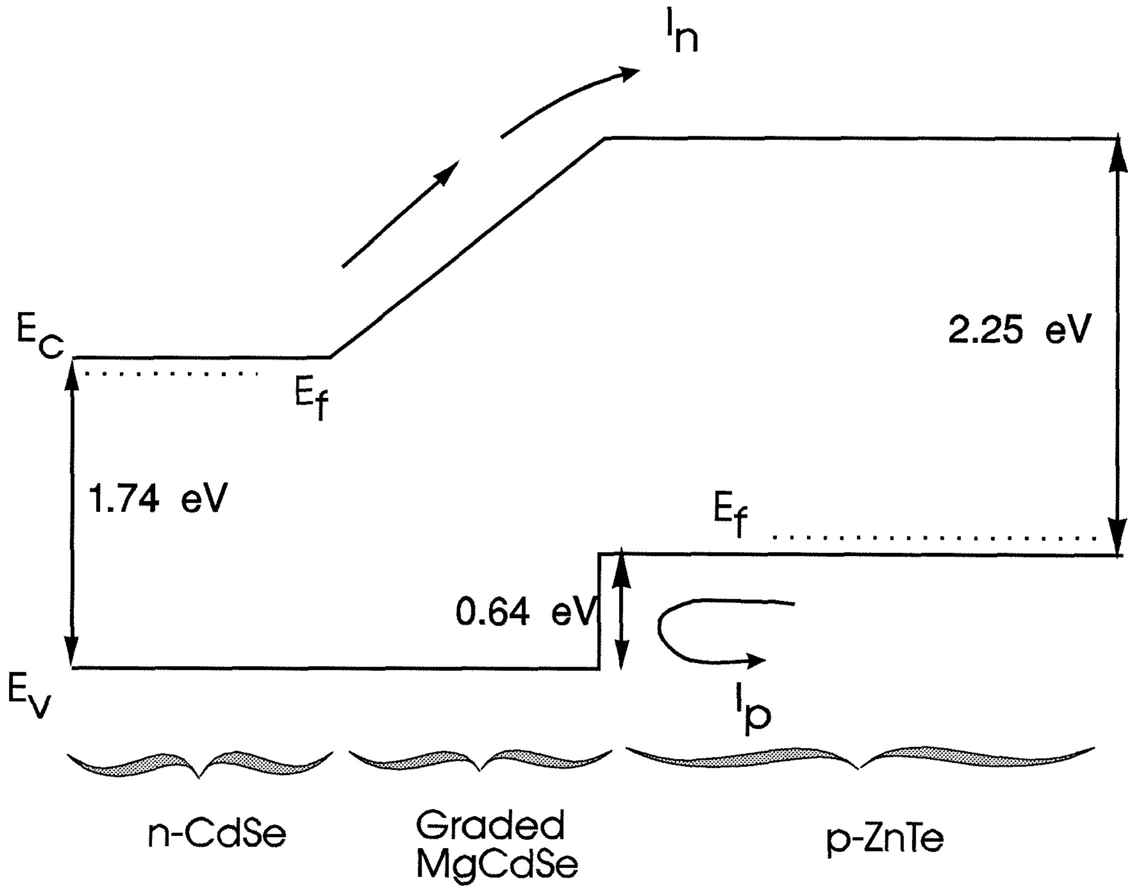

Figure 1.6: Schematic diagram showing the CBE and VBE for the graded injector device at flatband. The graded $Mg_xCd_{1-x}Se$ region facilitates electron injection into the higher bandgap material. The valence band offset between the $Mg_xCd_{1-x}Se$ and the ZnTe epilayer remains abrupt, blocking hole injection into the narrower bandgap CdSe material.

1.3 The Mixed Anion InAs/GaSb Heterointerface

1.3.1 Motivation

The InAs/GaSb/AlSb material system is of interest because it has a number of technologically significant applications, and is also relevant to fundamental studies of mixed anion interfaces. Applications of the this material system include: InAs/AlSb oscillators operating at frequencies greater than 700GHz [61], novel InAs/AlSb/GaSb [62, 63, 64] and InAs/GaSb [65] based tunnel structures, InAs/$Ga_{1-x}In_xSb$ IR SL detectors [66, 67], high power GaInAsSb/AlGaAsSb LDs operating at wavelengths useful for fiber optics communication [68] and InAs/AlSb/GaSb based quantum effect transistors [69]. One reason that the InAs/GaSb/AlSb material system is of such interest is because of the flexibility in band alignments that can be obtained without having to sacrifice lattice-match. This is shown in Figure 1.7(a), where we see that a variety of band alignments can be formed in this system. Other material systems of technical interest could also benefit from general studies of mixed anion interfaces. These include GaInP/GaAs heterojunction bipolar transistors (HBTs) [70, 71] and lattice matched heterojunction InP/GaInAs/InP LDs [72, 73]. Interface characteristics are important in these two material systems as well, and the effect of interface composition and growth order on the valence band offset has been investigated [74]. The application directly motivating our investigation of the InAs/GaSb interface is the IR SL detector, which makes use of the type II band alignment for InAs/$In_xGa_{1-x}Sb$. More details concerning this device are given in the following section.

For many of the applications mentioned above, parameters such as interface abruptness, interface composition and band alignments can have a large effect on the performance of the device. For example, cross-incorporation of the anion species can result in shorter carrier lifetimes and poor material quality, while

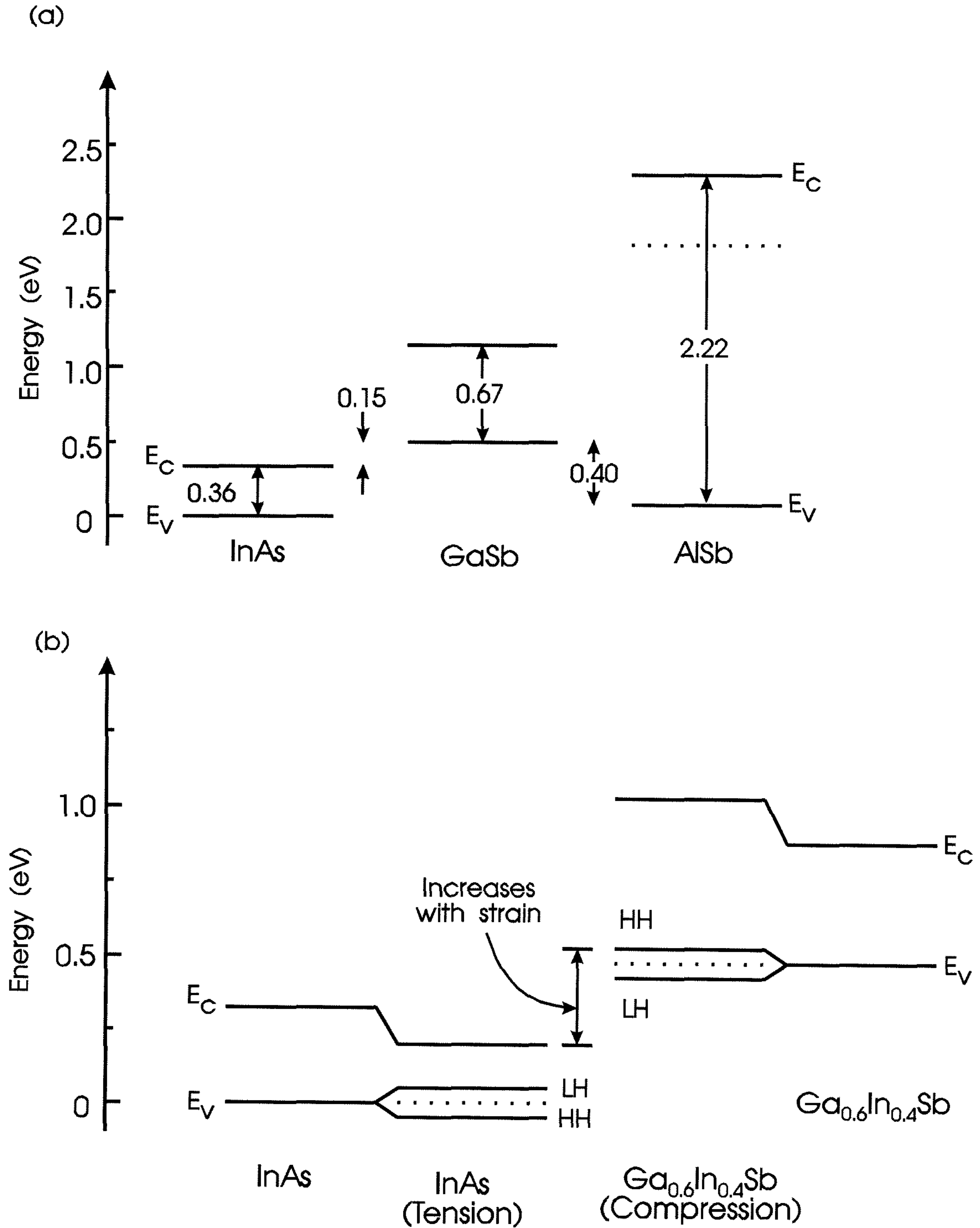

Figure 1.7: (a) Schematic of the conduction and valence band edges for the InAs/GaSb/AlSb material system. For the AlSb conduction band, dashed and solid lines indicates the indirect and direct conduction band minima respectively. (b) The band edges for strained and unstrained InAs and GaInSb.

the interfacial composition affects the strain configurations at the interface which changes the type and level of background doping, as well as the SL bandgap [75]. Furthermore, the interface composition in the InAs/AlSb system can also affect the carrier mobility, carrier concentration, and the InAs/AlSb valence band offset [76, 77]. Thus, for the purposes of device applications, it is critical to be able to grow arsenide/antimonide structures with no anion cross-incorporation and with abrupt, composition-controlled interfaces. However, atomic level control of the interface properties is very difficult because of the range of bond strengths, surface free energies and bond lengths in the InAs/GaSb system. In addition, III-V structures are typically grown with group V overpressures, since their vapor pressures are much larger than those of group III elements which results in lower sticking coefficients. For growth of mixed anion structures, this overflux of the group V component becomes a problem and can lead to cross-incorporation of the anion species as well as difficulty in controlling the interface composition. Details of these issues are presented in section 1.3.3.

1.3.2 InAs/$In_xGa_{1-x}Sb$ IR SL Detectors

Uses for IR detectors include not only military and civilian surveillance applications, but also satellite monitoring of the earth's temperature, IR astronomy, chemically sensitive monitoring of the atmosphere for pollution control purposes and medical imaging applications [78].

The strained layer InAs/$In_xGa_{1-x}Sb$ IR SL detector was first proposed by Smith and Mailhiot in 1987 [66]. The basic operation of this device relies on the type II nature of the InAs/GaSb band offset. Since the conduction band minimum of InAs lies below the valence band maximum of GaSb (see Figure 1.7(a)), a superlattice constructed from these semiconductors can potentially have an effective bandgap that is much smaller than either of the two constituent semiconductors, which is desirable for long wavelength detection applications. This is seen in Figure 1.8(a)

where the InAs and GaSb band edges and the hole and electron probability density functions are shown schematically on the same plot. Note that the probability and energy plots are superimposed in this figure for visualization purposes only, and that the SL bandgap is determined by the *energies* of the electrons and holes whose probability density is shown, not by the minima and maxima in the probability density plots. We see that for sufficiently short SL periods, the wavefunction of an electron in the InAs well will penetrate into the GaSb layers on either side of the well. Similarly, holes in the GaSb will have a finite probability density in the InAs layers. The effective SL bandgap then becomes the difference in energy between the lowest-energy electron state in the InAs and the highest-energy hole state in the GaSb. This is represented by the shaded region in Figure 1.8(a). Note that the effective SL bandgap will increase with shorter SL periods due to quantum confinement effects which increase the minimum electron energy and decrease the maximum hole energy. However, to obtain the narrow bandgaps needed for long wavelength (> 10 μm) detection, the layers become so thick that the wavefunction overlap and the optical matrix elements become too small for detector applications [79].

Smith and Mailhiot's proposal was to replace the GaSb in the SL with $In_xGa_{1-x}Sb$. Since GaInSb and InAs are not lattice matched, the individual layers in the SL will be strained, splitting the valence bands and changing the bandgaps as shown in Figure 1.8(b). We see in this figure that while the tensile strain in InAs causes the light hole (LH) band to shift up and the heavy hole (HH) band to shift down and reduces the bandgap, the compressive strain in $In_xGa_{1-x}Sb$ splits the HH band up and the LH band down and increases the bandgap. The net effect is an increase in the energy separation between the bottom of the InAs conduction band and the top of the $In_xGa_{1-x}Sb$ HH band. This results in a decrease in the effective SL bandgap for a given set of layer thicknesses, as shown in Figure 1.8(b). Thus, the strained layer IR SL detector design proposed by Smith and Mailhiot should, in theory, result in long wavelength detectors with short SL periods and

therefore reasonable optical matrix elements.

1.3.3 Challenges and Issues for Mixed Anion Interfaces

In addition to the reasons given in Section 1.3.1 for studying the InAs/GaSb interface, motivation exists to determine the cause of the short lifetimes in InAs/$In_xGa_{1-x}Sb$ IR SL detectors. In theory, these detectors have several advantages over other long wavelength IR detector technologies, including the current industry standard, $Hg_xCd_{1-x}Te$ detectors. Benefits offered by the InAs/$In_xGa_{1-x}Sb$ system include: (a) smaller leakage currents due to the decoupling of bandgap and effective mass, allowing for detectors with small bandgaps but large effective masses, (b) more precise control of uniformity, since the detection wavelength is determined primarily by layer thicknesses rather than ternary composition, (c) compatibility with more well developed III-V processing technologies and (d) suppression of Auger processes which limits the upper limit on detectivity in detectors [80].

Another competing technology is the GaAs/$Al_xGa_{1-x}As$ quantum well infrared photodetector (QWIP) [81]. However, despite recent advances in this approach [82], calculations have shown that the limiting performance of QWIPs will be significantly below that of $Hg_xCd_{1-x}Te$ devices [83].

Despite the apparent advantages of the InAs/$In_xGa_{1-x}Sb$ IR SL design, detectors competitive with $Hg_xCd_{1-x}Te$ technologies have not yet been fabricated in this system [84]. This poor performance has been attributed to the shorter extrinsic lifetime in InAs/$In_xGa_{1-x}Sb$ IR SL devices, due to the presence of Shockley-Read-Hall (SRH) centers [80]. One possible explanation for this is that the generation of SRH centers is somehow related to difficulties in controlling the mixed anion As/Sb interface, which could result in antisite defects.

Figure 1.9 shows schematically why the control of this mixed anion interface is so difficult. Details of the mechanisms of InAs/GaSb interface formation are

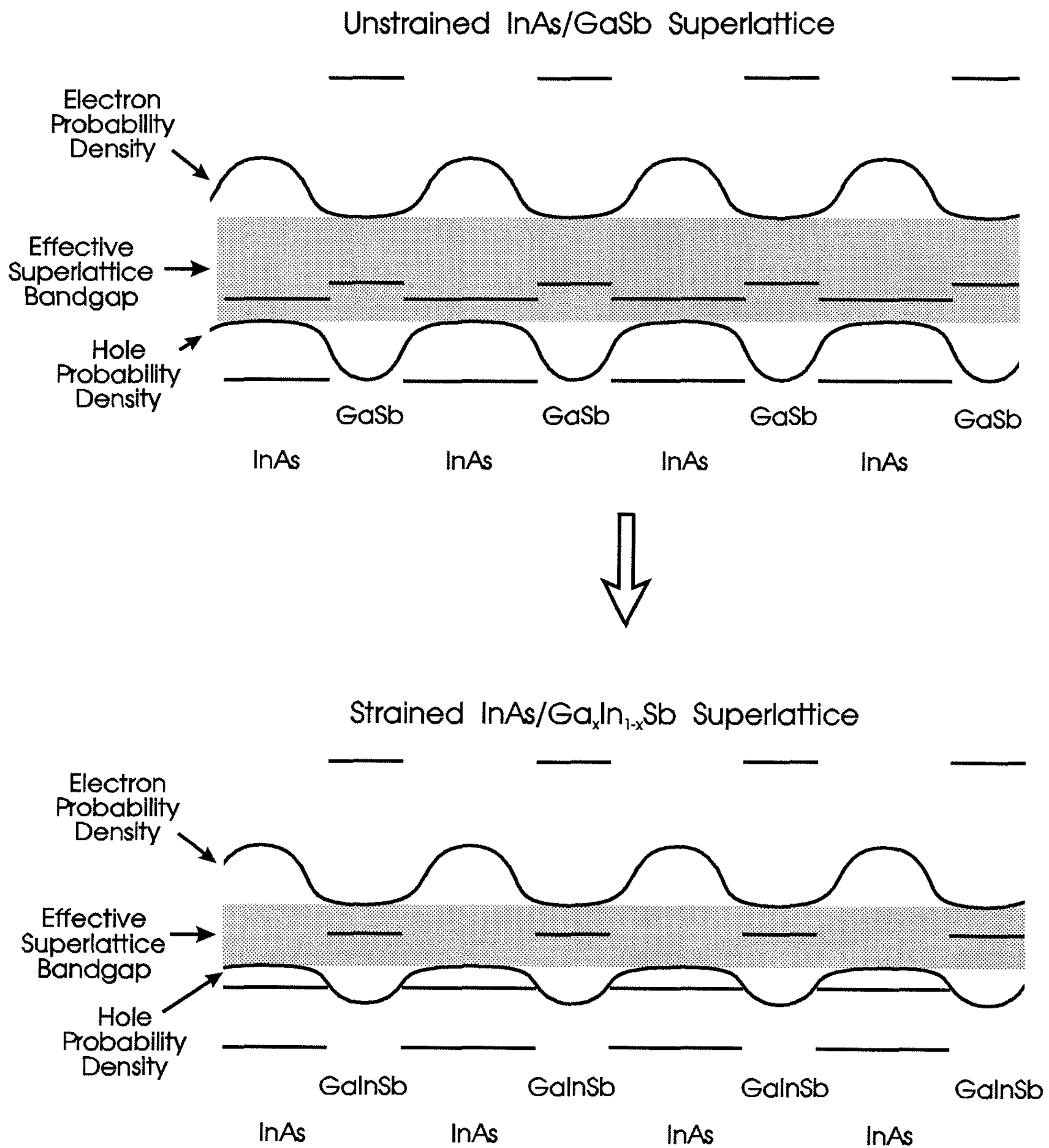

Figure 1.8: Schematic of band edges and carrier probability densities for InAs/GaSb (top) and InAs/GaInSb (bottom) SLs. Notice the decrease in effective superlattice bandgap (shaded region) for the strained SL. The probability and energy plots are superimposed for visualization purposes only.

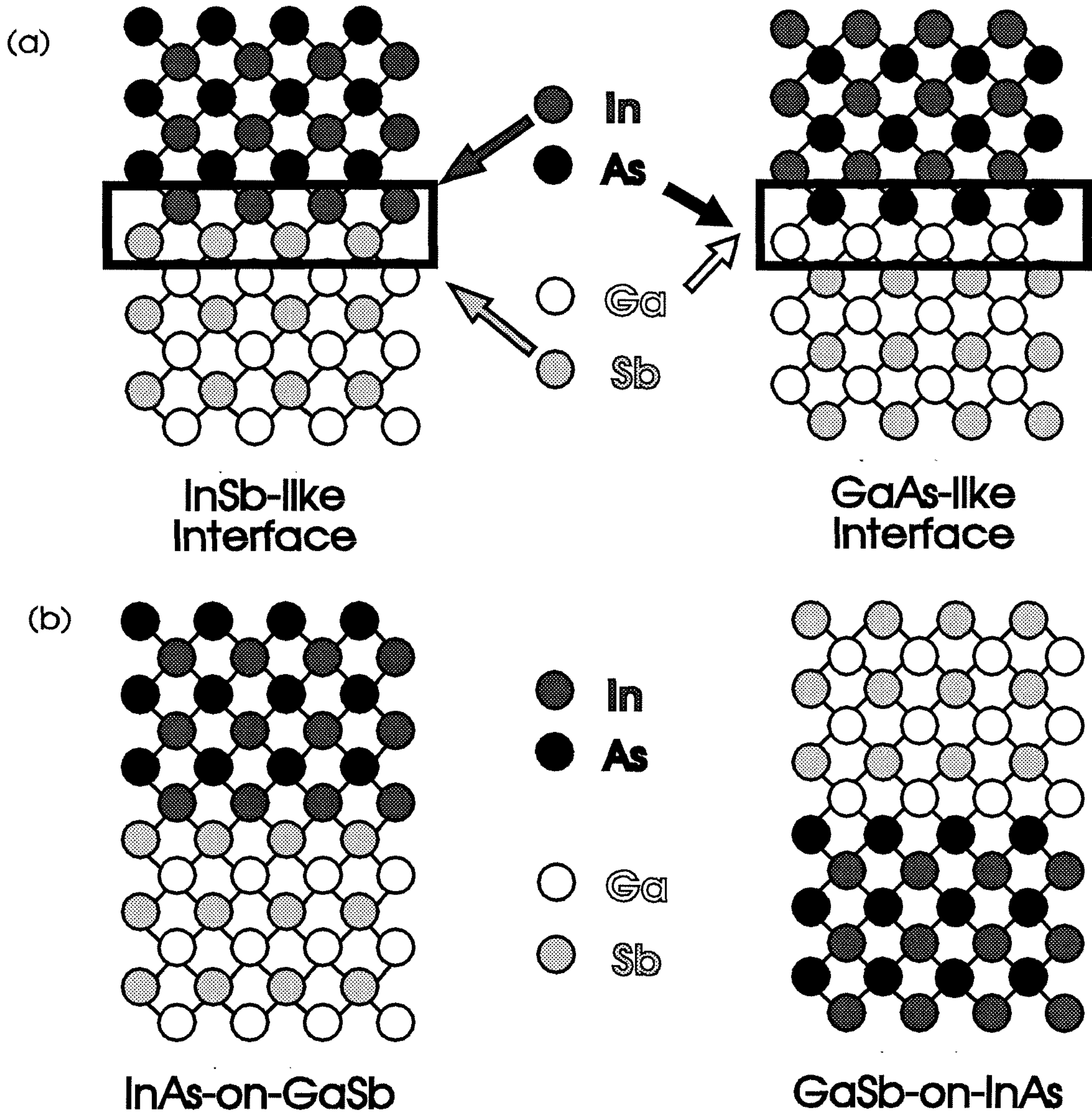

Figure 1.9: (a) Schematic of two possible interface compositions that may be formed in an InAs-on-GaSb heterojunction. Changing the interface composition may change such quantities as carrier mobility, carrier concentration, and band alignment. (b) Schematic of the two possible growth orders. Some of the effects that may affect interface abruptness and cross-incorporation are bond strengths, surface free energies, and bond lengths.

analyzed in Chapters 5 and 6. Figure 1.9(a) shows an obvious complication introduced with mixed anion interfaces. Since there is no common element across the interface, two possible interface compositions may be formed; in the case of InAs/GaSb, both InSb-like and GaAs-like interfaces are possible. Figure 1.9(b) shows the two possible growth orders available: InAs-on-GaSb and GaSb-on-InAs.

Other, somewhat more subtle mechanisms influencing interface formation are differing bond strengths, bond lengths and surface free energies, all of which can affect the dynamics and chemistry of interface formation. For example, in the InAs/GaSb material system, the very strong GaAs bond could drive the exchange of Sb with As in GaSb layers, the strong surfactant nature of Sb could influence interface abruptness and the large lattice mismatch ($\sim$ 6-7%) between GaAs and InSb with respect to GaSb could also have a large effect on interface formation. In light of these factors, growth of the mixed anion InAs/GaSb interfaces is very challenging and requires systematic characterization to achieve proper control of the interface properties. It should be noted that many of the difficulties in controlling the InAs/GaSb interface are common to other mixed anion systems as well.

1.3.4 Characterization Techniques

Due to the very small length scales that are of interest in studies of interface abruptness, it is very difficult to obtain a good measure of interface quality using only one characterization technique. In the studies presented in Chapters 5 and 6 a number of experimental techniques (XPS, RHEED, cross-sectional scanning tunneling microscopy (STM), and SIMS) were utilized in order to characterize the InAs/GaSb interface. Since results in this thesis deal primarily with the XPS and RHEED studies, brief overviews of these two techniques are given here. Cross-sectional STM and SIMS studies are presented only in Chapter 6; therefore, description of the respective techniques are given there. It should be emphasized that the RHEED, STM and SIMS studies were all performed by other researchers.

Figure 1.10 shows a schematic drawing of a typical XPS setup, with a representative XPS binding energy spectrum. In the X-ray source, electron bombardment of a metal target, typically Mg or Al, produces X-rays including K$\alpha_{1,2}$ lines at energies of 1253.6 eV and 1486.6 eV respectively. The Kα line is used because it accounts for roughly one-half of the X-rays produced by the electron bombardment. The shape of this line without a monochrometer is asymmetric with a FWHM of ~ 1.0 eV for Al and ~ 0.8 eV for Mg. If a monochrometer is used, this can be reduced to 0.3-0.4 eV. The X-rays impinge on the sample, ejecting photoelectrons from the core levels within the sample. The photoelectrons detected at the electron spectrometer have a kinetic energy determined by

$$h\nu = E_b + \phi_{sp} + T_{sp}, \tag{1.1}$$

where $h\nu$ is the incident X-ray energy, E_b is the binding energy of the core level from which the photoelectron was ejected, ϕ_{sp} is the work function of the spectrometer and T_{sp} is the photoelectron kinetic energy measured at the spectrometer. Thus, for a given X-ray source and spectrometer work function, measuring the photoelectron kinetic energy determines the binding energy of its respective core level allowing chemical identification as shown in Figure 1.10. Both the binding energy and relative intensities of core level peaks are used in XPS data analysis. It should be noted that for the X-ray energies typically used in XPS, the photoelectron escape depths are tens of angstroms, thus XPS is a near-surface chemical analysis technique.

A schematic diagram of a typical RHEED setup is shown in Figure 1.11. In RHEED, high energy electrons (~ 10 keV) impinge on the sample surface at grazing angles. Since the surface of crystalline samples have characteristic periodicities in certain directions, the electrons will diffract from the sample surface with a characteristic pattern which is captured by a phosphor screen. The RHEED pattern on the phosphor screen can then be analyzed in real time, or captured and digitized for later analysis. Since the electrons have very shallow incident angles

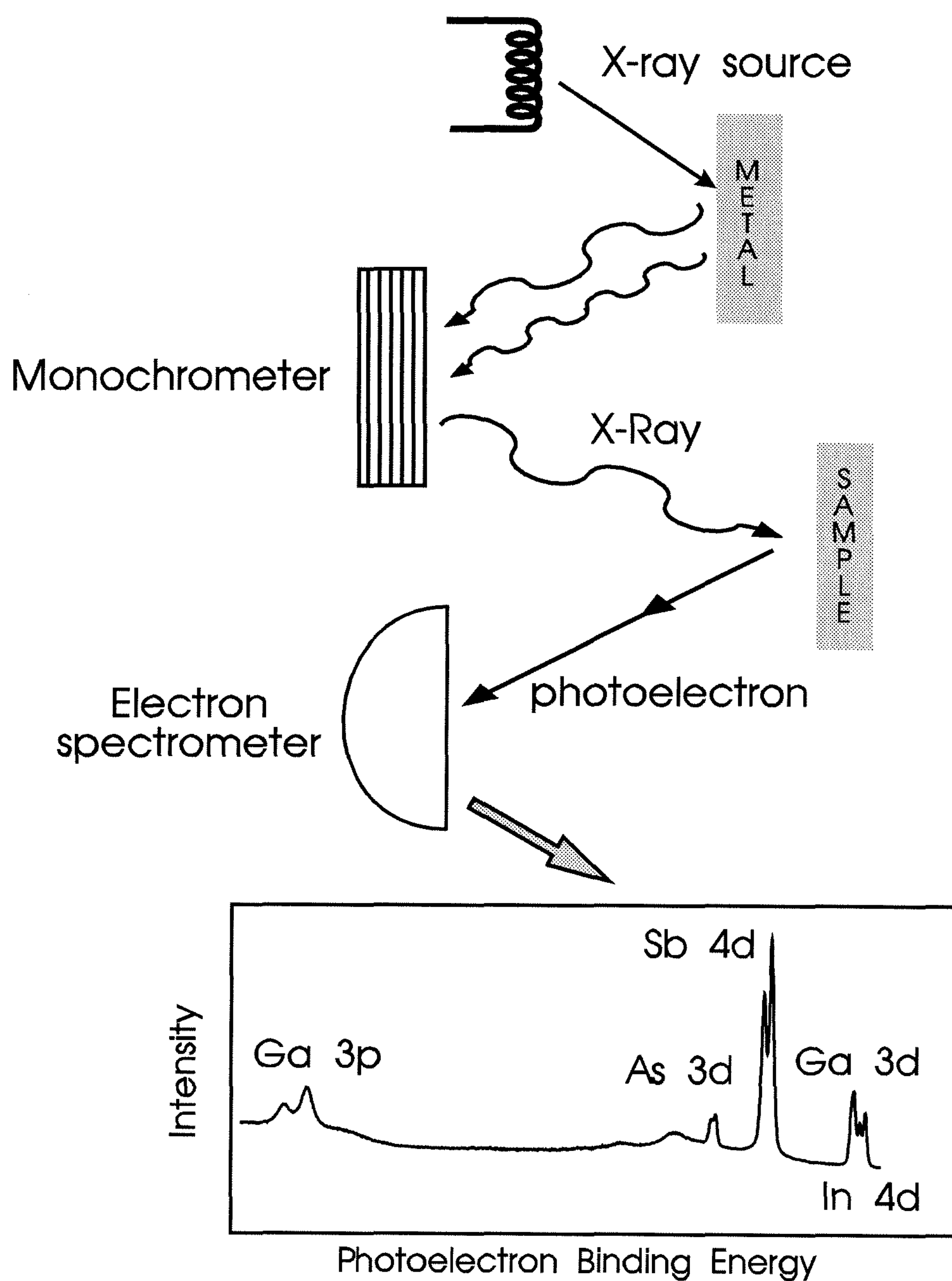

Figure 1.10: Schematic of the X-ray Photoelectron Spectroscopy (XPS) experimental setup, and a representative photoelectron spectrum.

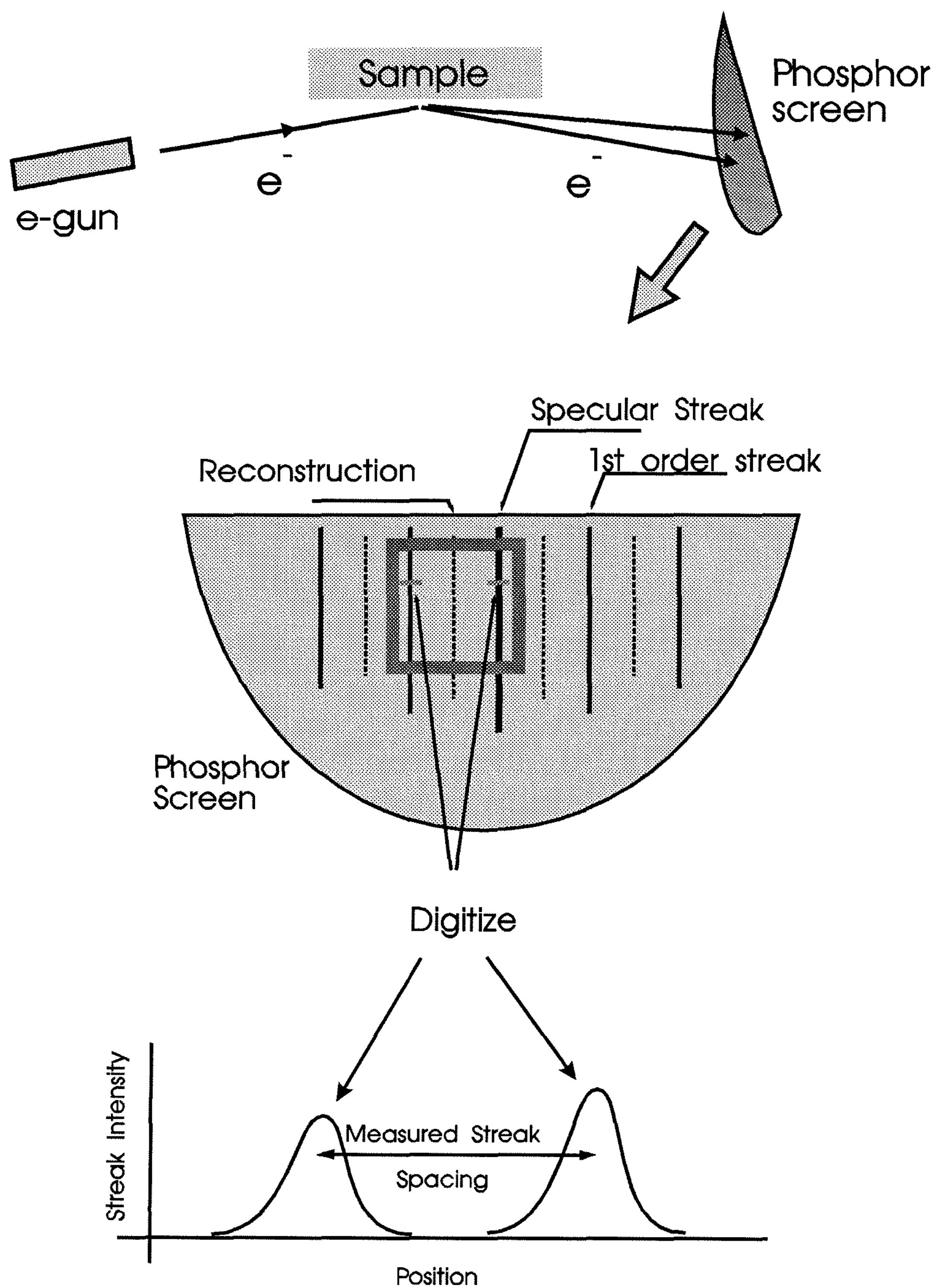

Figure 1.11: Schematic of the Reflection High Energy Electron Diffraction (RHEED) experimental setup. Quantities of interest are the reconstruction pattern, the specular streak intensity and the streak separation.

(1-3 °), they penetrate only ~5 Å into the sample, so RHEED effectively measures only very near surface structure.

Three main pieces of information can be extracted from a RHEED pattern: the surface reconstruction pattern, the specular streak intensity and the streak separation. The surface reconstruction pattern is due to the rearrangement of the surface atoms to terminate dangling bonds. This surface reconstruction can change significantly depending on the exact growth conditions, so it is useful in monitoring the effect of parameters such as substrate temperature and flux ratios. The specular streak intensity varies as each layer proceeds through various stages of nucleation. Partial nucleation results in surface roughness which reduces the specular streak intensity. This feature can be used to monitor growth rates and changes in growth modes. While the steak separation can also be obtained from RHEED patterns, it is more difficult to extract conclusive information from this quantity.

1.4 Outline of Thesis

The thesis is divided into two parts. Part I (Chapters 2-4) describes work that has been performed on the II-VI graded injector LED. Simulation results, materials characterization and device fabrication issues will be discussed. Part II of this thesis (Chapters 5-6) describes the characterization of the InAs/GaSb heterointerface. Most of the work presented is based on XPS analysis; however, results from other characterization techniques will also be discussed.

Chapter 2 describes in detail the design and operation of the graded electron injector LED, as well as other proposed devices. Simulations based on the Drift-Diffusion model are used to determine the feasibility of a variety of device designs, including one that does not perform optimally, two that have been experimentally implemented and others that have not yet been implemented. Details of the model, which was modified from the standard Drift-Diffusion model to account for

heterostructures, are presented.

In Chapter 3 of the thesis XPS measurements of the MgSe/$Cd_{0.54}Zn_{0.46}Se$ and MgTe/$Cd_{0.88}Zn_{0.12}Te$ valence band offsets are presented. Background on the methods used to measure valence band offsets using XPS are given. Also specific details of the sample growth and XPS measurements and data analysis are presented. The implications of the measured band offsets on current II-VI light emitter design are discussed.

In Chapter 4, we present materials characterization studies and the latest device results. XRD, TEM and SIMS studies of the graded electron injector are presented. Potential materials problems brought to light by these characterization techniques are discussed. The most recent current-voltage, electroluminescence and efficiency measurements of LED devices are given. Device degradation and device fabrication issues are also addressed.

In Chapter 5 surface exchange reaction studies of the InAs/GaSb heterointerface are presented. The exchange of As with Sb during Sb interrupts of InAs surfaces, and the exchange of Sb with As during As interrupts of GaSb surfaces are presented. The exchange reactions are studied using XPS and RHEED; details of the technique are given. The implications of our results for IR SL detectors are discussed.

Finally, Chapter 6 presents studies of the InAs/GaSb heterojunction. XPS measurements of the InAs/GaSb valence band offset as a function of interface type and growth order are presented. Implications of the results to both device applications and interface studies of mixed anion systems are discussed. Lastly, investigations of asymmetry in the abruptness of the InAs/GaSb interface using XPS, RHEED, cross-sectional STM and SIMS are presented.

Bibliography

[1] M.C. Phillips, M.W. Wang, J.F. Swenberg, J.O. McCaldin, and T.C. McGill, *Appl. Phys. Lett.* **61**, 1962 (1992).

[2] L.W. Cook, M.D. Camras, S.L. Rudaz, and F.M. Steranka, in *Proceedings of the 14th International Symposium on GaAs and Related Compounds 1987* (Institute of Physics, Bristol, 1988), pp. 777-780.

[3] G.M. Craford, Circuits and Devices **8**, 24 (1992).

[4] A red LED traffic signal lamp uses 25 W compared to 150 W for conventional incandescent lamps. This results in a savings of 1095 kWh/year or $131/year (at $0.12/kWh) for each signal head. (Econolite Control Products, Inc. 1993 Catalog.)

[5] For example, the energy savings for Pasadena, which has over 3000 traffic signal heads, would be roughly $400,000/year.

[6] Business Week, page 82, July 25, 1994.

[7] Projected from number of signal heads in Pasadena and number of LEDs used in Econolite LED lamps.

[8] M. Levitt, Proc. *SPIE - Int. Soc. Opt. Eng.* **1719**, 1 (1992).

[9] K.H. Huang, J.G. Yu, C.P. Kuo, R.M. Fletcher, T.D. Osentowski, L.J. Stinson, M.G. Craford, and A.S.H. Liao, *Appl. Phys. Lett.* **61**, 1045 (1992).

[10] I. Hino, K. Kobayashi, and T. Suzuki, *Jpn. J. Appl. Phys.* **23** L746 (1984).

[11] H. Sugawara, M. Ishikawa, and G. Hatakoshi, *Appl. Phys. Lett.* **58**, 1010 (1991).

[12] R.M. Fletcher, C.P Kuo, T.D. Osentowski, K.H. Huang, M.G. Craford, and V.M. Robbins, *J. Elect. Materials* **20**, 1125 (1991).

[13] F.A. Kish, F.M. Steranka, D.C. DeFevere, D.A. Vanderwater, K.G. Park, C.P. Kuo, T.D Osentowski, M.J. Peanasky, J.G. Yu, R.M. Fletcher, D.A. Steigerwald, M.G. Craford, and V.M. Robbins, *Appl. Phys. Lett.* **64**, 2839 (1994).

[14] C.P. Kuo, R.M. Fletcher, T.D. Osentowski, M.C. Lardizabal, M.G. Craford, and V.M. Robbins, *Appl. Phys. Lett.* **57**, 2937 (1990).

[15] J.A. Edmond, H.-S. Kong, and C.H. Carter, Jr., *Physica B* **185** 453 (1993).

[16] Y. Fan, J. Han, L. He, J. Saraie, R.L. Gunshor, M. Hagerott, H. Jeon, A.V. Nurmikko, G.C. Hua, and N. Otsuka, *Appl. Phys. Lett.* **61**, 3160 (1992).

[17] J.O. McCaldin, *J. Vac. Sci. Technol. A* **8**, 1188 (1990).

[18] S. Nakamura, T. Mukai, M. Senoh, *Appl. Phys. Lett.* **64**, 1687 (1994).

[19] H. Cheng, J.M. DePuydt, J.E. Potts, and T.L. Smith, *Appl. Phys. Lett.* **52**, 147 (1988).

[20] J.M. DePuydt, M.A. Haase, H. Cheng, and J.E. Potts, *Appl. Phys. Lett.* **55**, 1103 (1989).

[21] A. Taike, M. Migita, and H. Yamamoto, *Appl. Phys. Lett.* **56**, 1989 (1990).

[22] K. Ohkawa, T. Karasawa, and T. Mitsuyu, *J. Cryst. Growth* **111**, 797 (1991).

[23] R.M. Park, M.B. Troffer, C.M. Rouleau, J.M. DePuydt, and M.A. Haase, *Appl. Phys. Lett.* **57** 2127 (1990).

[24] J. Qiu, J.M. DePuydt, H. Cheng, and M.A. Haase, *Appl. Phys. Lett.* **59**, 2992 (1991).

[25] M.A. Haase, J. Qiu, J.M. DePuydt, and H. Cheng, *Appl. Phys. Lett.* **59**, 1272 (1991).

[26] H. Okuyama, K. Nakano, T. Miyajima, and K. Akimoto, *Jpn. J. Appl. Phys.* **30** L1620 (1991).

[27] H. Okuyama, T. Miyajima, Y. Morinaga, F. Hiei, M. Ozawa, and K. Akimoto, *Electronics Letters* **28** 1798 (1992).

[28] J.M. Gaines, R.R. Drenten, K.W. Haberern, T. Marshall, P. Mensz, and J. Petruzzello, *Appl. Phys. Lett.* **62** 2462 (1993).

[29] Y. Moringa, H. Okuyama, and K. Akimoto, *Jpn. J. Appl. Phys.* **32**, 678 (1993).

[30] Y. Lansari, J. Ren, B. Sneed, K.A. Bowers, J.W. Cook, Jr., and J.F. Schetzina, *Appl. Phys. Lett.* **61**, 2554 (1992).

[31] F. Hiei, M. Ikeda, M. Ozawa, T. Miyajima, A. Ishibashi, and K. Akimoto, *Electronics Letters* **29**, 878 (1993).

[32] P.M. Mensz, *Appl. Phys. Lett.* **64**, 2148 (1994).

[33] R.G. Dandrea and C.B. Duke *Appl. Phys. Lett.* **64**, 2145 (1994).

[34] H. Jeon, J. Ding, A.V. Nurmikko, W. Xie, M. Kobayashi, and R.L. Gunshor, *Appl. Phys. Lett.* **60**, 892 (1992).

[35] W. Xie, D.C. Grillo, R.L. Gunshor, M. Kobayashi, H. Jeon, J. Ding, A.V. Nurmikko, G.C. Hua, and N. Otsuka, *Appl. Phys. Lett.* **60**, 1999 (1992).

[36] M. Hagerott, J. Ding, H. Jeon, A.V. Nurmikko, Y. Fan, L. He, J. Han, J. Saraie, R.L. Gunshor, C.G. Hua, and N. Otsuka, *Appl. Phys.* **62**, 2108 (1993).

[37] J. Ren, D.B. Eason, Y. Lansari, Z. Yu, K.A. Bowers, C. Boney, B. Sneed, J.W. Cook, Jr., J.F. Schetzina, M.W. Koch, and G.W. Wicks, *J. Vac. Sci. Technol. B* **11**, 955 (1993).

[38] D.B. Eason, Z. Yu, C. Boney, J. Ren, L.E. Churchill, J.W. Cook, Jr., J.F. Schetzina, and N.A. El-Masry, to be published in *J. Cryst. Growth* (1994).

[39] Presented by J.F. Schetzina at the 1994 Device Research Conference in Boulder, CO.

[40] A. Salokatve, H. Jeon, J. Ding, M. Hovinen, A.V. Nurmikko, D.C. Grillo, L. He, J. Han, Y. Fan, M. Ringle, and R.L. Gunshor, Abstract from the 1994 Conference on Lasers and Electro-Optics (CLEO) in Anahiem, CA, pg. 202.

[41] Sony results in plenary talk by D. Olego at the 1994 Device Research Conference in Boulder, CO.

[42] S. Guha, J.M. DePuydt, M.A. Haase, J. Qiu, and H. Cheng, *Appl. Phys. Lett.* **63**, 3107 (1993).

[43] L.H Kuo, L. Salamanca-Riba, J.M. DePuydt, H. Cheng, and J. Qiu, *Appl. Phys. Lett.* **63**, 3197 (1993).

[44] J. Ren, D.B. Eason, Z. Yu, B. Sneed, J.W. Cook, Jr., J.F. Schetzina, N.A. El-Masry, X.H. Yang, J.J. Song, G. Cantwell, and W.C. Harsh, *J. Vac. Sci. Technol. B* **12**, 1262 (1994).

[45] S. Strite and H. Morkoç, *J. Vac. Sci. Technol. B* **10**, 1237 (1992).

[46] S. Strite, M.E. Lin, and H. Morkoç, *Thin Solid Films* **231**, 197 (1993).

[47] T. Matsuoka, *J. Cryst. Growth* **124**, 433 (1992).

[48] H. Amano, M. Kito, K. Hiramatsu, and I. Akasaki, *Jpn. J. Appl. Phys.* **28**, L2112 (1989).

[49] H. Amano, N. Sawaki, I. Akasaki, and Y. Toyada, *Appl. Phys. Lett.* **48**, 353 (1986).

[50] S. Nakamura, *Jpn. J. Appl. Phys.* **30**, L1705 (1991).

[51] S. Nakamura, T. Mukai, and M. Senoh, *Jpn. J. Appl. Phys.* **30**, L1998 (1991).

[52] N. Yoshimoto, T. Matsuoka, T. Sasaki, and A. Katsui, *Appl. Phys. Lett.* **59** 2251 (1991).

[53] S. Nakamura, T. Mukai, and M. Senoh, *Jpn. J. Appl. Phys.* **31**, L16 (1993).

[54] S. Nakamura, M. Senoh, and T. Mukai, *Jpn. J. Appl. Phys.* **32**, L8 (1993).

[55] S. Nakamura, M. Senoh, and T. Mukai, *Appl. Phys. Lett.* **62**, 2390 (1993).

[56] I. Akasaki, H. Amano, N. Koide, M. Kotaki, and K. Manabe, *Physica B* **185**, 428 (1993).

[57] S. Nakamura, T. Mukai, M. Senoh, and N. Iwasa, *Jpn. J. Appl. Phys.* **31**, L139 (1992).

[58] S. Nakamura, N. Iwasa, M. Senoh, and T. Mukai, *Jpn. J. Appl. Phys.* **31**, 1258 (1992).

[59] H. Morkoç and B. Sverdlov, *Evaluation of Nichia Blue and Blue-Green InGaN LEDs*, unpublished.

[60] T. Detchprohm, K. Hiramatsu, H. Amano, and I. Akasaki, *Appl. Phys. Lett.* **61**, 2688 (1992).

[61] E.R. Brown, J.R. Söderström, C.D. Parker, L.J. Mahoney, K.M. Molvar, and T.C. McGill, *Appl. Phys. Lett.* **58**, 2291 (1991).

[62] M. Sweeny and J. Xu, *Appl. Phys. Lett.* **54**, 546 (1989).

[63] J.R. Söderström, D.H. Chow, and T.C. McGill, *Appl. Phys. Lett.* **55**, 1094 (1989).

[64] L.F. Luo, R. Beresford, and W.I. Wang, *Appl. Phys. Lett.* **55**, 2023 (1989).

[65] D.A. Collins, E.T. Yu, Y. Rajakarunanayake, J.R. Söderström, D.Z.-Y. Ting, D.H. Chow, and T.C. McGill, *Appl. Phys. Lett.* **57**, 683 (1990).

[66] D.L. Smith and C. Mailhiot, *J. Appl. Phys.* **62**, 2545 (1987).

[67] R.H. Miles, D.H. Chow, J.N. Schulman, and T.C. McGill, *Appl. Phys. Lett.* **57**, 801 (1990).

[68] H.K. Choi, and S.J. Eglash, *Appl. Phys. Lett.* **61**, 1154 (1992).

[69] D.A. Collins, D.H. Chow, and T.C. McGill, *Appl. Phys. Lett.* **58**, 1673 (1991).

[70] H. Kroemer, *J. Vac. Sci. Technol. B* **1**, 126 (1983).

[71] S.L. Delage, M.A. DiForte-Poisson, H. Blanck, C. Bryliinski, E. Chartier, and P. Collot, *Electronics Letters* **27**, 254 (1991).

[72] B.I. Miller, J.H. McFee, R.J. Martin, and P.K. Tien, *Appl. Phys. Lett.* **31**, 44 (1978).

[73] W.T. Tsang, F.S. Choa, M.C. Wu, Y.K. Chen, A.M. Sergent, and P.F. Sciortino, Jr., *Appl. Phys. Lett.* **58**, 2610 (1991).

[74] J.P. Landesman, J.C. Garcia, J. Massies, G. Jezequel, P. Maurel, J.P. Hirtz, and P. Alnot, *J. Vac. Sci. Technol. B* **10**, 1761 (1992).

[75] D.H. Chow, R.H. Miles, and A.T. Hunter, *J. Vac. Sci. Technol. B* **10**, 888 (1992).

[76] G. Tuttle, H. Kroemer, and J.H. English, *J. Appl. Phys.* **67**, 3032 (1990).

[77] J.R. Waldrop, G.J. Sullivan, R.W. Grant, E.A. Kraut, and W.A. Harrison, *J. Vac. Sci. Technol. B* **10**, 1773 (1992).

[78] T.C. McGill and D.A. Collins, *Semicond. Sci. Technol.* **8**, S1 (1993).

[79] D.K. Arch, G. Wicks, T. Tonaue, and J.L Staudenmann, *J. Appl. Phys.* **58**, 3933 (1985).

[80] E.R. Youngdale, J.R. Meyer, C.A. Hoffman, F.J. Bartoli, C.H. Grein, P.M. Young, H. Ehrenreich, R.H. Miles, and D.H. Chow, *Appl. Phys. Lett.* **64**, 3160 (1994).

[81] B.F. Levine, K.K. Choi, C.G. Bethea, J. Walker, and R.J. Malik, *Appl. Phys. Lett.* **50**, 1092 (1987).

[82] B.F. Levine, C.G. Bethea, G. Hasnain, V.O. Shen, E. Pelve, R.R. Abbott, and S.J. Hsieh, *Appl. Phys. Lett.* **56**, 851 (1990).

[83] M.A. Kinch and A. Yariv, *Appl. Phys. Lett.* **55**, 2093 (1989).

[84] R.H. Miles, D.H. Chow, J. N. Schulman, D.A. Collins, M.W. Wang, R.W. Grant, and T.C. McGill, submitted to *J. Elect. Materials* .

Part I

Graded Electron Injector, II-VI Wide Bandgap Light Emitters

Chapter 2

Light Emitter Simulation and Design

2.1 Introduction and Outline

A fundamental problem in fabricating wide gap binary II-VI light emitting diodes (LEDs) has been the inability to obtain both n- and p-type doping in these materials by conventional doping techniques. Recently, this limitation has been partially overcome by nitrogen plasma doping to produce p-ZnSe with hole concentrations up to 10^{18} cm^{-3} [1]. Although such doping has led to the demonstration of the first blue-green laser diodes [2], hole concentrations are still not high enough to afford ohmic contacts to p-ZnSe. Researchers have developed sophisticated contacting schemes such as pseudo-graded ZnSeTe layers [3], ZnTe/ZnSe superlattices [4], and Hg-based contacts [5] in order to obtain a low resistance contact to p-ZnSe. Thus, the realization of highly doped p-ZnSe is still a major obstacle to the further development of ZnSe based LEDs and laser diodes. An alternative solution to the dopability problem is to use a heterojunction formed between a naturally n-type and a naturally p-type material.

In this chapter, we examine the simulation and design of II-VI heterostruc-

ture LEDs based on n-CdSe and p-ZnTe. We choose these two semiconductors because of their favorable dopability and close lattice match. The drift-diffusion model, modified to account for heterojunctions, is used in our simulations. To determine LED design feasibility, bulk and interfacial recombination are included in the model. Details of the model are given in Section 2.2. Some of the more important parameters accounted for in the design process are band offsets, lattice mismatch, dopability, and interfacial effects. Where unknown, band offsets used in the simulations are estimated using the common anion rule [6]. We emphasize here that the simulation results are not dependent on the validity of this rule, as demonstrated in one simulation in which an undesirable deviation from the common anion rule is used. Details of the design methodology are discussed in Sections 2.2 and 2.4. Simulation results are presented in Section 2.4. A simple CdSe/ZnTe heterojunction is first presented, followed by a CdSe/$Mg_xCd_{1-x}Se$/ZnTe heterostructure design utilizing a graded injector to facilitate electron injection [7]. Next, a design incorporating a $Mg_xZn_{1-x}Te$ electron confining layer is presented. Finally, a device design that allows tunability of the wavelength of light emission from green to blue is proposed and analyzed. Recent developments in the graded injector device design and a proposal for a lattice matched quaternary-based LED structure are presented in Section 2.5. Section 2.6 concludes the chapter.

2.2 Design Methodology

In the design of heterostructure devices, it is often useful to first examine a diagram which simultaneously exhibits lattice parameters, band offsets, and dopability for the materials of interest. The McCaldin diagram [8] of Figure 2.1 shows the common wide bandgap binary II-VI compounds, along with other common semiconductors for comparison purposes. The band offsets are those predicted by Harrison's linear combination of atomic orbitals (LCAO) method [9].

Examining Figure 2.1, we note first that none of the wide bandgap II-VI com-

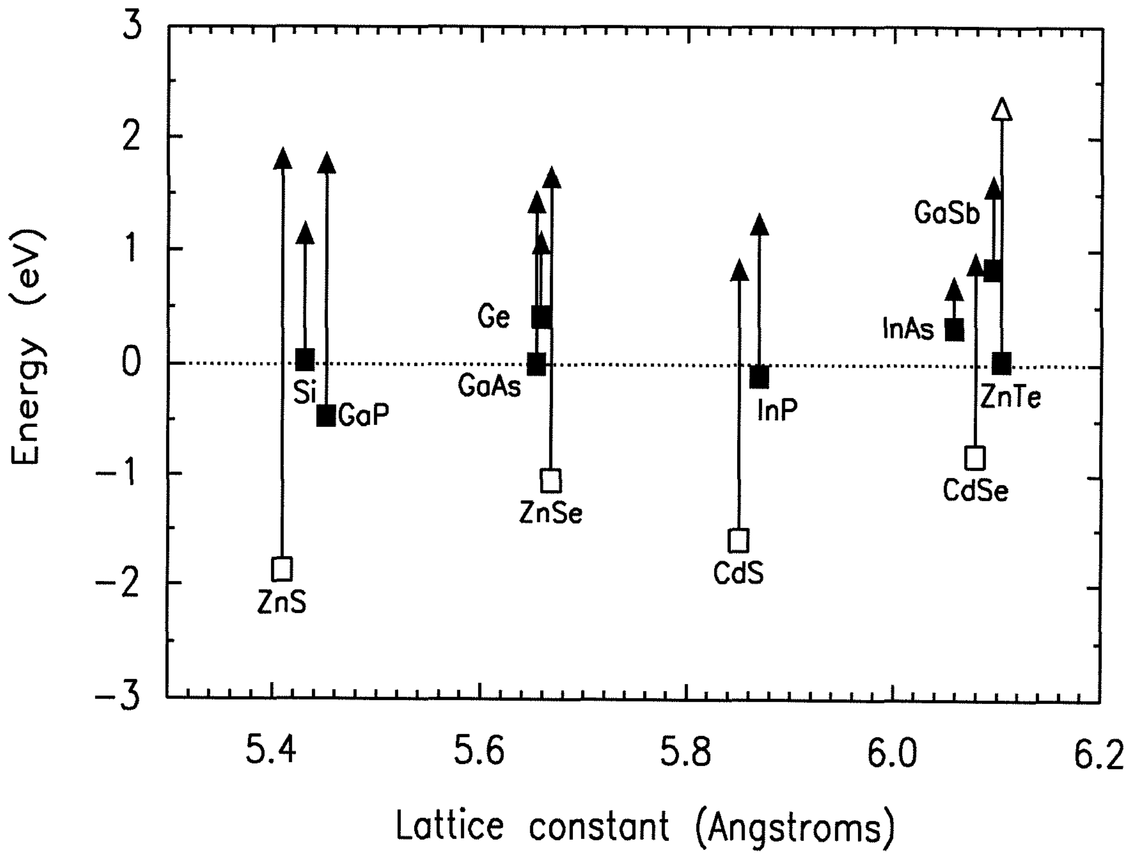

Figure 2.1: McCaldin diagram for common semiconductors. Each material is represented by a vertical line with a square at the bottom, corresponding to the valence band edge, and a triangle at the top, corresponding to the conduction band edge. The horizontal position of each line is determined by the lattice parameter. The length of each line scales with the bandgap of the material that it represents. The vertical position of each line is determined by the respective valence band offset calculated using Harrison's LCAO method. Open triangles and squares represent semiconductors that cannot be doped n or p type respectively using conventional doping techniques. The zero of energy is chosen to be the valence band edge of GaAs.

pounds can be conventionally doped both n- and p-type, and only one, ZnTe, can be conventionally doped p-type. Thus, it is logical that a wide bandgap LED design should incorporate ZnTe. Also, since interface states caused by dislocations can have severely detrimental effects on the electrical and optical properties of a device, it is highly desirable to have a device design that uses only nearly lattice matched II-VI compounds. From Figure 2.1, we see that CdSe can be doped n-type and has only a 0.4% lattice mismatch to ZnTe. Thus, an n-CdSe/p-ZnTe heterojunction shows some promising characteristics for a wide bandgap LED. No other combination of II-VI compounds allows for both a small lattice mismatch and formation of a conventionally doped p-n heterojunction. However, the experimental valence band offset between CdSe and ZnTe is $0.64 \pm .07$ eV [10], with the ZnTe valence band edge higher than the CdSe valence band edge. Since the CdSe bandgap is 1.74 eV, this gives a conduction band offset of roughly 1.15 eV, resulting in a type II heterojunction which favors carrier injection into the smaller bandgap CdSe layer [11]. The simulations in Section 2.4.1 confirm that a simple n-CdSe/p-ZnTe heterojunction device suffers from interface recombination and hole injection.

To improve on the simple CdSe/ZnTe device, we need first to examine the properties of some magnesium based II-VI compounds. The McCaldin diagram in Figure 2.2 shows the familiar binary II-VI compounds, as well as MgS, MgSe, and MgTe. $Mg_xCd_{1-x}Se$ and $Mg_xZn_{1-x}Te$ ternaries are represented by the shaded regions in this diagram. Again, the LCAO method is used to determine the valence band offset in this diagram. In Chapter 3, XPS measurements of Mg-calcogenide band offsets show that the valence band maxima of MgSe and MgTe lie below the respective valence band maxima of $Cd_{0.54}Zn_{0.46}Se$ and $Cd_{0.88}Zn_{0.12}Te$; however, the simulations in Section 2.4 were performed prior to these measurements and so used band alignments based on the common anion rule. This assumption does not affect the conclusion drawn from the simulation results; which is that the graded injector concept is feasible, but it does influence the details of the LED structure, as will

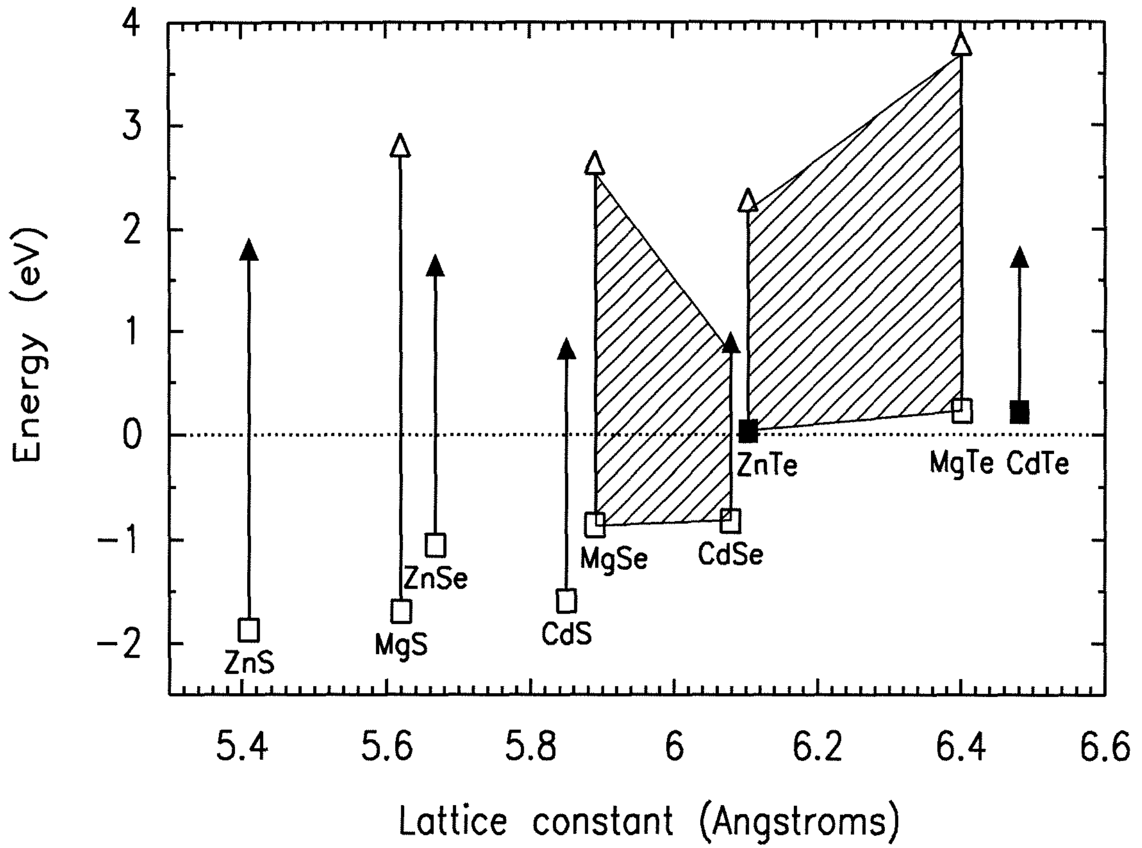

Figure 2.2: McCaldin diagram for some commonly used II-VI materials with the addition of MgS, MgSe and MgTe. $Mg_xCd_{1-x}Se$ and $Mg_xZn_{1-x}Te$ ternaries are represented by the two shaded regions.

be discussed in Section 2.5.

The room temperature bandgap of MgTe is 3.57 eV [12]. The bandgap of MgSe is more uncertain, with reported values ranging from 3.6 eV at 77K [13] to 5.63 eV at 90K [14]. The first value gives a room temperature bandgap of roughly 3.5 eV. In Chapter 4, the bandgap of MgSe is measured to be 4.54 eV from studies of $Mg_xCd_{1-x}Se$ ternaries. The simulations in Sections 2.4.1 to 2.4.4 used the least favorable of the published values (3.5 eV) for the bandgap of MgSe. Again, this does not affect the basic operation of the LED structures simulated, but is important for the proper fabrication of actual devices.

With the knowledge of the bandgaps and band alignments for MgSe and MgTe, we now observe that the MgSe to CdSe valence band offset is such that a $Mg_xCd_{1-x}Se$ ternary of the proper composition can have a zero conduction band offset to ZnTe while maintaining a valence band offset similar to that in a CdSe/ZnTe heterojunction. From Figure 2.3, we see that by grading from CdSe to $Mg_xCd_{1-x}Se$ we should be able to form a region that will facilitate electron injection into the ZnTe layer, while the valence band offset between $Mg_xCd_{1-x}Se$ and ZnTe will continue to block hole injection. This will hold as long as the valence band edge of $Mg_xCd_{1-x}Se$ is not more than a few tenths of an eV above the valence band edge of CdSe, as confirmed by the measurements presented in Chapter 3. Thus, the operation of this device is not very sensitive to the validity of the LCAO method or the common anion rule. This graded injector concept for wide bandgap light emission was first proposed in Ref. [7]. Details of the operation of this device and simulation results will be given in Section 2.4.2.

If we now study the $Mg_xZn_{1-x}Te$ ternary in Figure 2.2, we see that it has a large conduction band offset and a small valence band offset to ZnTe. This allows us to use $Mg_xZn_{1-x}Te$ layers to confine electrons without significantly affecting hole transport. Also, by forcing the bulk recombination to occur in a $Mg_xZn_{1-x}Te$ layer, we can potentially extend the wavelength of light emitted from our device into the blue. Sections 2.4.3 and 2.4.4 examine in more detail the use of $Mg_xZn_{1-x}Te$ layers

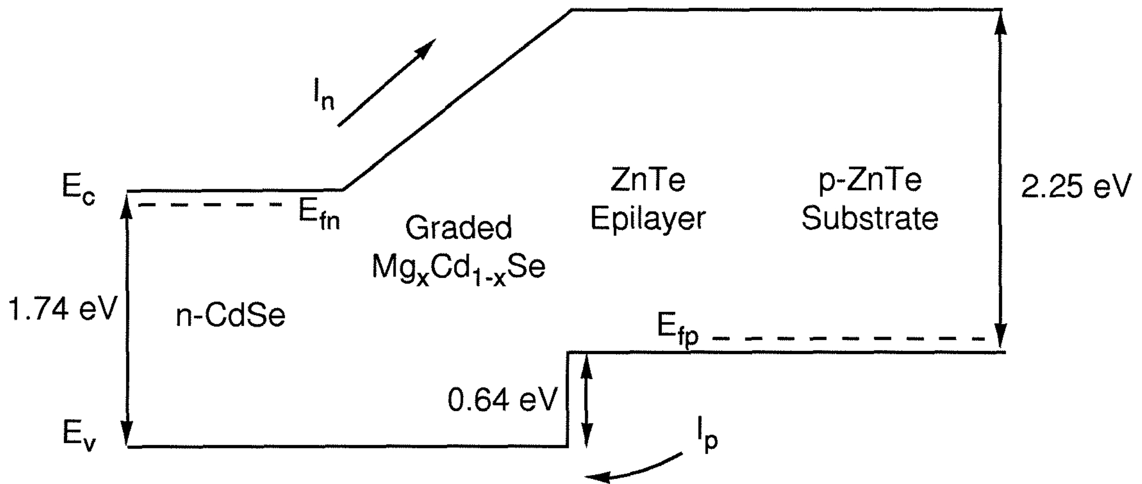

Figure 2.3: Schematic diagram showing the conduction and valence band edges for the graded injector device at flatband. The graded $Mg_xCd_{1-x}Se$ region facilitates electron injection into the higher bandgap material. The valence band offset between the $Mg_xCd_{1-x}Se$ and the ZnTe epilayer remains abrupt, blocking hole injection into the narrower bandgap CdSe material. Notice that the device operation is fairly independent of the $Mg_xCd_{1-x}Se$ to CdSe valence band offset as long as it does not deviate from the common anion rule by more that a few tenths of an eV.

in wide bandgap LEDs.

One major disadvantage of using these Mg-based ternary layers in the LED designs is the large lattice mismatch that is introduced into the structure. One possible approach which allows bandgap engineering without introducing significant strain is to use quaternary layers. Figure 2.4 shows some of the possible quaternaries available with lattice parameters near 6.1 Å as well as the $Zn_{1-x}Mg_xS_ySe_{1-y}$ quaternary used in ZnSe-based LDs. Studies of devices incorporating $Zn_{1-x}Mg_xSe_yTe_{1-y}$ and $Cd_{1-x}Mg_xSe_yTe_{1-y}$ quaternaries and issues relating to the growth of Se/Te compounds will be presented in Section 2.5.

2.3 Model

Using the drift-diffusion transport equations, we can solve for the conduction and valence band edges, as well as the charge and current densities as a function of position. For a homostructure, the basic equations to be solved in the drift-diffusion model are Poisson's equation, the electron and hole current equations, and the electron and hole continuity equations. In one dimension, assuming steady state conditions and spatially constant temperatures, these are:

$$\frac{dE}{dx} = \frac{e}{\epsilon}(p - n + N_d^+ - N_a^-) \tag{2.1}$$

$$j_p = e\mu_p pE - eD_p\frac{dp}{dx} \tag{2.2}$$

$$j_n = e\mu_n nE + eD_n\frac{dn}{dx} \tag{2.3}$$

$$\frac{dj_p}{dx} = -eU - eB(pn - n_i^2) \tag{2.4}$$

$$\frac{dj_n}{dx} = eU + eB(pn - n_i^2) \tag{2.5}$$

where E is the electric field, e is the electron charge, n_i is the intrinsic carrier concentration, n and p are the electron and hole concentrations, and ϵ is the dielectric constant. D, μ, and j refer to the diffusion constant, mobility and current

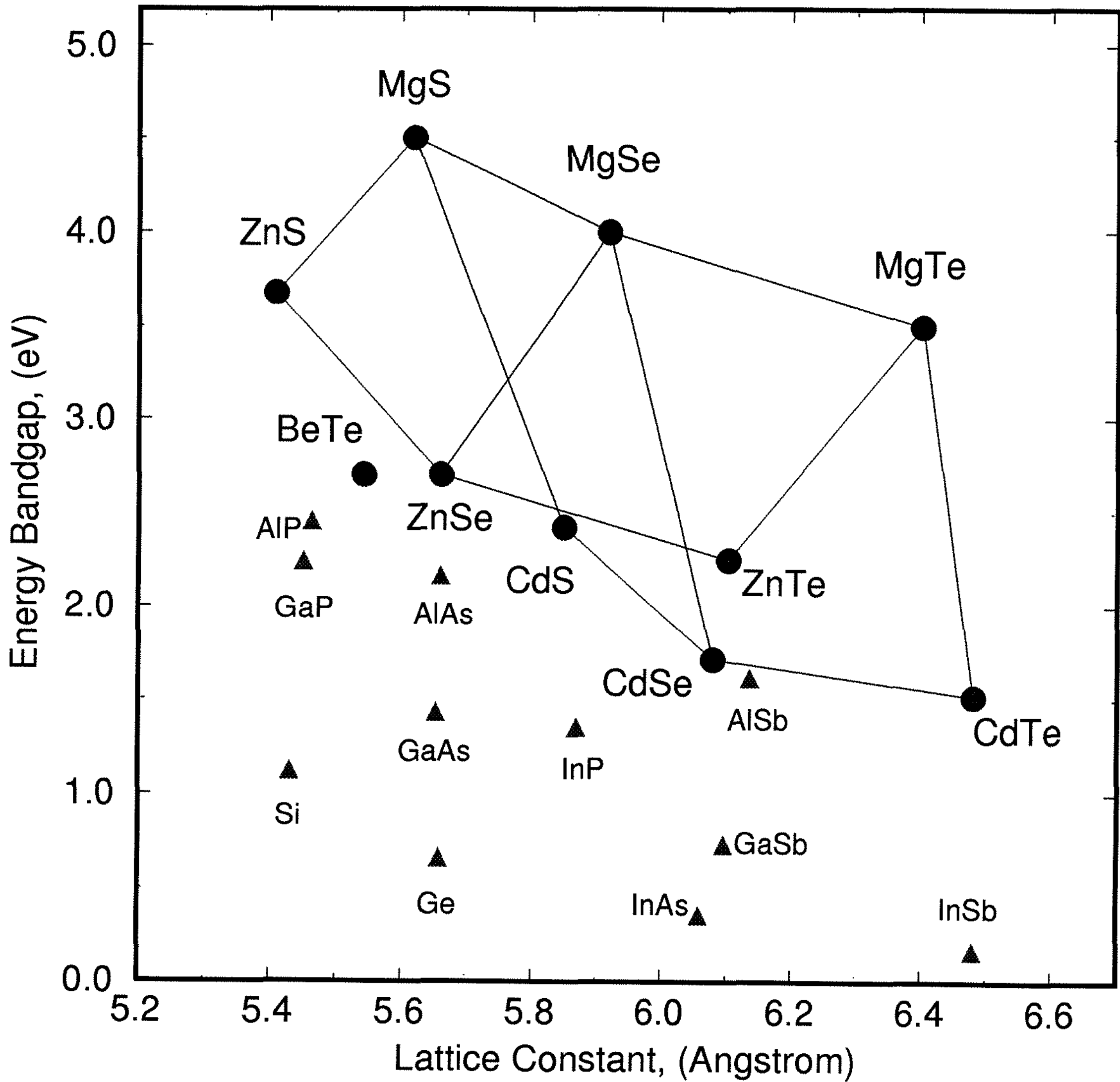

Figure 2.4: Diagram showing the bandgap and lattice parameter of II-VI (circles) and other (triangles) semiconductor compounds. Lines are drawn to schematically show some of the possible quaternary II-VI compounds.

density respectively, where the subscripts p and n refer to holes and electrons respectively. B is the probability for radiative recombination and U is the indirect recombination rate, described in detail below. N_d^+ and N_a^- are the concentrations of ionized donors and acceptors given by

$$N_d^+ = \frac{N_d}{1 + 2\exp\left((E_{fn} - E_d)/k_b T\right)} \tag{2.6}$$

$$N_a^- = \frac{N_a}{1 + 4\exp\left((E_a - E_{fp})/k_b T\right)} \tag{2.7}$$

where E_{fn} and E_{fp} are the electron and hole quasi-Fermi levels, respectively. E_a and E_d are the acceptor and donor ionization energies respectively. The electron and hole quasi-Fermi levels are determined from the carrier concentrations using standard Fermi-Dirac statistics.

The van Roosbroeck-Shockley method of equating equilibrium band-to-band recombination and absorption rates [15] is used to estimate B. The optical absorption coefficient required for this calculation is determined as detailed in Ref. [16]. The final expression for the radiative recombination rate is

$$B = \left(\frac{2\pi}{k_b T c^2 (m_e + m_h)}\right)^{3/2} \frac{\hbar e^2 n_r}{12\pi\epsilon_0}\left(\frac{1}{m} + \frac{1}{m_e} + \frac{1}{m_h}\right) E_g^2, \tag{2.8}$$

where n_r is the index of refraction, E_g is the bandgap of the semiconductor, ϵ_0 is the permittivity of free space and c is the speed of light in vacuum.

The indirect recombination rate, U, for a single trapping level is given by standard Shockley-Read-Hall statistics [17]:

$$U = \frac{np - n_i^2}{(p + p_1)\tau_n + (n + n_1)\tau_p}. \tag{2.9}$$

where τ_n and τ_p are the electron and hole lifetimes, and n_1 and p_1 are given by

$$n_1 = N_c exp((E_t - E_c)/k_b T) \tag{2.10}$$

$$p_1 = N_v exp((E_v - E_t)/k_b T). \tag{2.11}$$

N_c and N_v are the effective densities of states for electrons and holes respectively, and E_t is the energy of the trap level.

To model heterostructures, equations (2.1) - (2.5) must be modified slightly [18] [19] as follows:

$$\frac{dE}{dx} = \frac{e}{\epsilon}(N_d^+ - N_a^- - n + p) - \frac{E}{\epsilon}\frac{d\epsilon}{dx} \tag{2.12}$$

$$j_p = e\mu_p pE - \mu_p p\frac{d(\chi + E_g)}{dx} - eD_p\frac{dp}{dx} + \frac{eD_p p}{N_v}\frac{dN_v}{dx} \tag{2.13}$$

$$j_n = e\mu_n nE - \mu_n n\frac{d\chi}{dx} + eD_n\frac{dn}{dx} - \frac{eD_n n}{N_c}\frac{dN_c}{dx} \tag{2.14}$$

$$\frac{dj_p}{dx} = -eU_b - eU_i - eB(pn - n_i^2) \tag{2.15}$$

$$\frac{dj_n}{dx} = eU_b + eU_i + eB(pn - n_i^2) \tag{2.16}$$

where χ and E_g are the electron affinity and bandgap of the semiconductor. U_b and U_i refer to the bulk and interfacial recombination rates.

The physical interpretation of the additional heterostructure terms in Equations (2.12) - (2.16) are given below. More detailed derivations and discussions of the above heterostructure drift-diffusion equations can be found in Refs. [18] and [20]. The last term in Equation (2.12) simply imposes continuity of displacement at the interface between two different materials. The second term on the right-hand side of Equations (2.13) and (2.14) is a drift component due to a so-called quasi-electric field for holes or electrons [20] [21] . The hole quasi-electric field,

$$\frac{1}{e}\frac{d(\chi + E_g)}{dx}, \tag{2.17}$$

is an additional field influencing holes in graded regions and at interfaces, where the valence-band has an additional slope due to valence-band offsets between the materials in question. Similarly, electrons feel a quasi-electric field,

$$\frac{1}{e}\frac{d\chi}{dx}, \tag{2.18}$$

due to conduction-band offsets. Known or estimated band offsets are used to determine the positional variation of the electron affinity. The last term of Equation

(2.13) is a diffusion-like term resulting from a position-dependent effective density of states (DOS). This term causes holes to diffuse from regions of low DOS to regions of high DOS. A similar term appears in Equation (2.13) for electrons. The bulk recombination, U_b, is given by Equation (2.9). Finally, an additional interfacial recombination term has been added to Equations (2.15) and (2.16), since interfacial recombination can have a significant effect on heterostructure device operation. The interfacial recombination due to trap levels produced by dangling bonds was implemented using a modified Shockley-Read-Hall model [19, 22], as given below.

$$U_i = \frac{(np - n_i^2)}{t(p + p_1)/S_n + t(n + n_1)/S_p}. \tag{2.19}$$

where

$$S_n = v_{th}\sigma_n N_{st} \tag{2.20}$$

$$S_p = v_{th}\sigma_p N_{st} \tag{2.21}$$

$$N_{st} = \frac{4(a_2^2 - a_1^2)}{a_1^2 a_2^2}. \tag{2.22}$$

In Equation (2.19) S_n and S_p are the surface recombination velocities for electrons and holes respectively and t is the thickness of the interface between the two semiconductors. In Equations (2.20) - (2.22) v_{th} is the thermal velocity, N_{st} is the trap density per unit area, σ_n and σ_p are the capture cross sections for holes and electrons respectively and a_1 and a_2 are the lattice parameters of the two semiconductors comprising the interface. Note that Equation (2.19) assumes a single trap level at mid gap, and Equation (2.22) assumes that the growth is in the [100] direction, and that all of the lattice mismatch between the two semiconductors comprising an interface is taken up by dislocations and not by strain. In regions where part of the lattice mismatch is taken up by strain, Equation (2.22) gives the upper limit for N_{st}.

In regions where the composition, x, varies, the dielectric constant and effective

mass are given by [23]

$$\frac{\epsilon - 1}{\epsilon + 2} = \mathrm{x}\left(\frac{\epsilon_1 - 1}{\epsilon_1 + 2}\right) + (1 - \mathrm{x})\left(\frac{\epsilon_2 - 1}{\epsilon_2 + 2}\right) \tag{2.23}$$

$$\frac{1}{m^*} = \frac{\mathrm{x}}{m_1^*} + \frac{1 - \mathrm{x}}{m_2^*} \tag{2.24}$$

where x is the mole fraction of material 1. The bandgap in graded regions can be modeled by [24]

$$E_g = A + B\mathrm{x} + C\mathrm{x}^2, \tag{2.25}$$

where A is the bandgap for material 1 and B and C are experimentally determined parameters. The devices that we are modeling have graded regions where Equation (2.25) is applicable; however, values for B and C are not known for the materials in certain regions. In these regions, we have assumed a linear dependence of E_g on material composition. Also, we have neglected the effects of strain on band structure in lattice mismatched graded regions.

In heterostructures, regions with high electric fields and carrier concentrations are common, so the assumption of a constant mobility and the use of the non-degenerate form of Einstein's equation is no longer valid. The mobility as a function of both the field strength and the doping concentration is given by [25, 26]

$$\mu_{n,p}^* = \mu_{n0,p0} + \mu_{n1,p1}\left[1 + \left(\frac{N_d + N_a}{N_{n,p}}\right)^{\alpha_{n,p}}\right]^{-1} \tag{2.26}$$

$$\mu_n = \left[\mu_n^* + \frac{V_{sat}}{E}\left(\frac{E}{E_0}\right)^4\right]\left[1 + \left(\frac{E}{E_0}\right)^4\right]^{-1} \tag{2.27}$$

$$\mu_p = \mu_p^*\left[1 + \frac{\mu_p^* E}{v_m}\right]^{-1}. \tag{2.28}$$

where E is the electric field, N_d and N_a refer to donor and acceptor concentrations respectively and subscripts n and p refer to electrons and holes respectively. $N_{n,p}$, $\alpha_{n,p}$, E_0, V_{sat} and v_m are experimentally determined parameters. These parameters are not generally known for the materials used in our devices, so as an initial approximation, we have used $N_{n,p}$, $\alpha_{n,p}$ and E_0 as determined for GaAs. $\mu_{n0,p0}$

and $\mu_{n1,p1}$ are determined by using the same ratio of $\mu_{n0,p0}$ to $\mu_{n1,p1}$ as for GaAs, while constraining μ^* equal to experimental values of mobility in our materials for zero field and low doping concentrations. The high field saturation velocities, V_{sat} and v_m, are set to one-half the peak velocities estimated from E_0 and μ^*. While not ideal, the method outlined above will give, to first order, trends in the change in mobility with respect to variations in field strength and doping concentration. It is necessary to include field dependent mobilities in the model, because in regions with high fields the ratio of diffusivity to mobility becomes large. If the decrease in mobility with increasing field is not accounted for, unrealistically large diffusion constants will result.

As mentioned above, in regions of high carrier concentrations, the ratio of diffusivity to mobility can deviate significantly from k_bT/e. If the original derivation of the drift-diffusion equations from Boltzmann's equation is done without assuming Boltzmann statistics, then the following general form of Einstein's relation is obtained [20]:

$$\frac{D}{\mu} = \frac{2k_bTF_{1/2}(\eta)}{eF_{-1/2}(\eta)}, \tag{2.29}$$

where F_j is the Fermi-Dirac integral of order j, and η is $(E_{fn} - E_c)/k_bT$ for electrons, and $(E_v - E_{fp})/k_bT$ for holes. Analytic expressions approximating $F_{1/2}$ and $F_{-1/2}$ [27] were used to evaluate Equation (2.29).

The numerical solution of Equations (2.12) - (2.16) was carried out using the relaxation method [28]. Successful implementation relies on reasonable choices of scaling factors and initial guesses [29]; the latter were determined as in Ref. [30]. Variable mesh spacing was incorporated, with larger mesh densities used in regions of rapid potential variation. Finally, abrupt junctions were graded over a distance of a few angstroms to avoid numerical instabilities that are introduced by singularities at an abrupt interface. The simulation results do not depend on the grading distances of the interfaces as long as they are not unreasonably large. For example, shortening the grading distance of an interface causes only the individual

derivative terms in Equation (2.13) to increase in magnitude, with no net effect on the overall current density.

2.4 Simulation Results

2.4.1 CdSe/ZnTe

As discussed in Section 2.2, an n-CdSe/p-ZnTe heterojunction has favorable lattice match and dopability characteristics for a wide bandgap LED; however, the band alignments in this heterojunction favor interfacial recombination over thermionic injection. In this section we examine results from numerical simulations of an n-CdSe/p-ZnTe heterojunction in order to determine the feasibility of such a device. All of the simulations presented below were done at room temperature. We assumed a donor concentration of 1×10^{19} for n-CdSe and an acceptor concentration of 1×10^{17} cm^{-3} for p-ZnTe. Ionized donor and acceptor concentrations are given by equations (2.6) and (2.7). For the interfacial traps we assumed a density of 1 $\times$ 10^{11} cm^{-2} and cross sections of 1×10^{-14} cm^2.

Figure 2.5 shows the conduction and valence band edges for a CdSe/ZnTe heterojunction at forward biases of 0.0 and 1.25 V. Figure 2.6 shows the electron and hole concentrations at these same biases. At zero bias, we note that both the CdSe and the ZnTe are depleted at the interface. As we apply a forward bias, the depletion width decreases, and at a large enough bias, electrons and holes begin to accumulate at the interface. Figure 2.7 shows the electron current densities at 0.75 and 1.25 V forward biases. Referring to Equations (2.15) and (2.16) we note that the slope of a current density plot at a given point gives a direct measure of the rate of recombination at that point. At a bias of 0.75 V, we see that all of the recombination occurs at the CdSe/ZnTe interface. At a higher bias of 1.25 V, all of the bulk recombination occurs in the CdSe region, indicating that holes are being injected into the CdSe layer rather than electrons into the wider bandgap

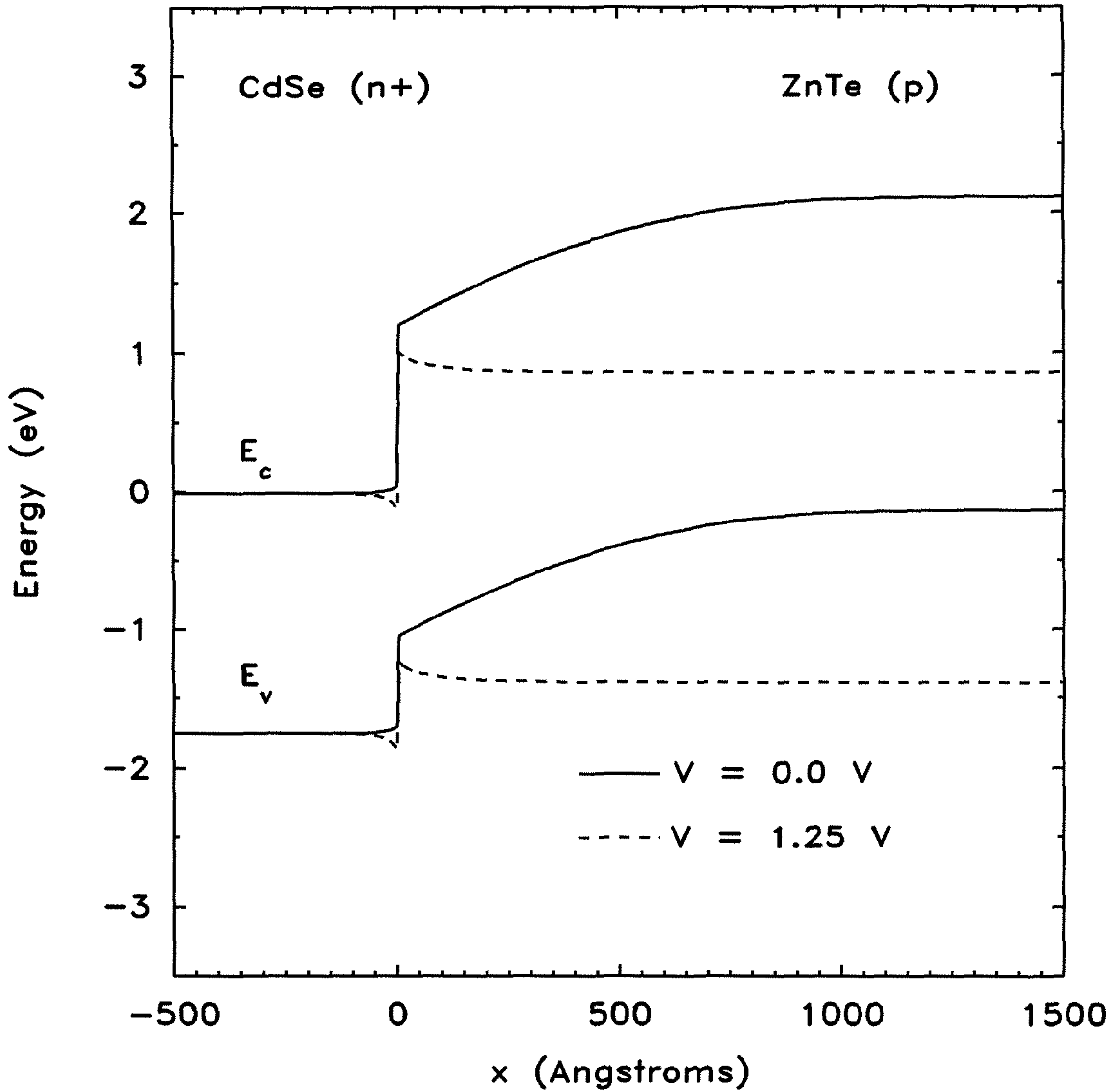

Figure 2.5: Conduction and valence band edges for an n-CdSe/p-ZnTe heterostructure at 0.0 V and 1.25 V forward bias. Zero on the horizontal axis corresponds to the CdSe/ZnTe interface.

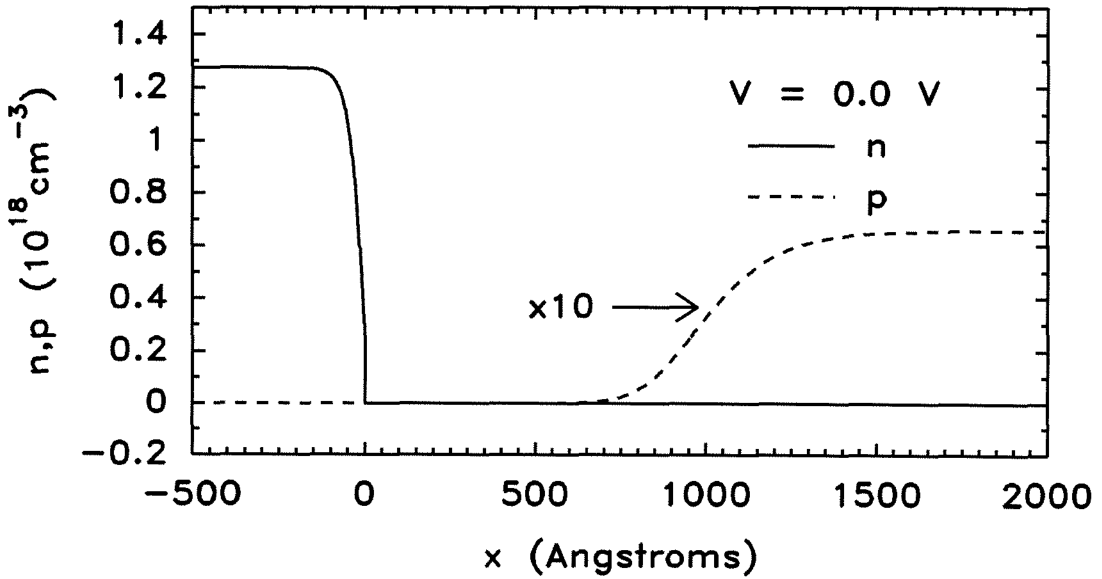

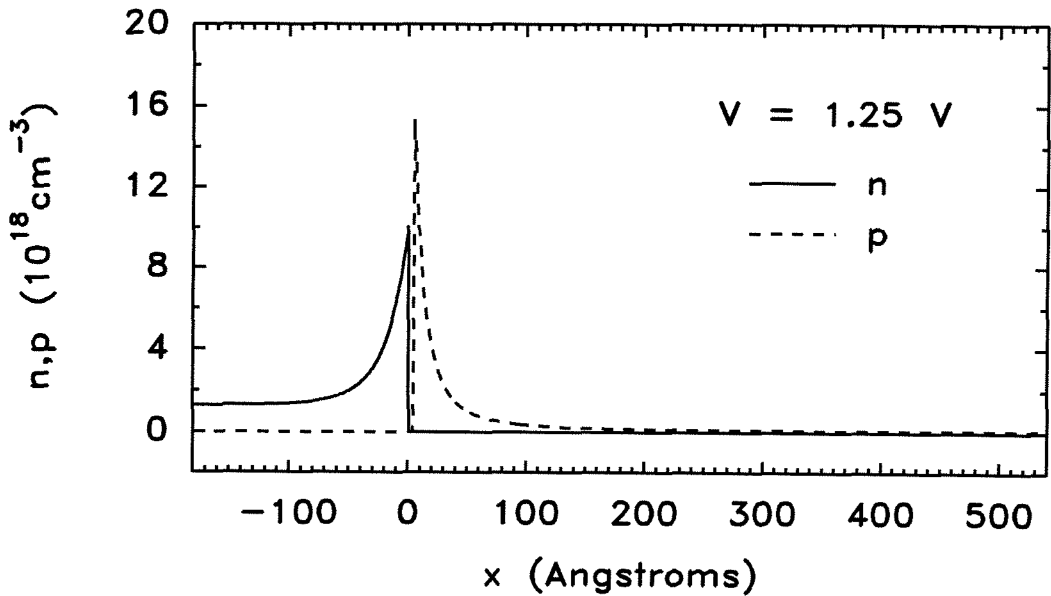

Figure 2.6: (a) Electron and hole charge densities for an n-CdSe/p-ZnTe heterostructure at 0.0 V forward bias. (b) At 1.25 V forward bias, high carrier concentrations occur at the heterojunction interface.

(a)

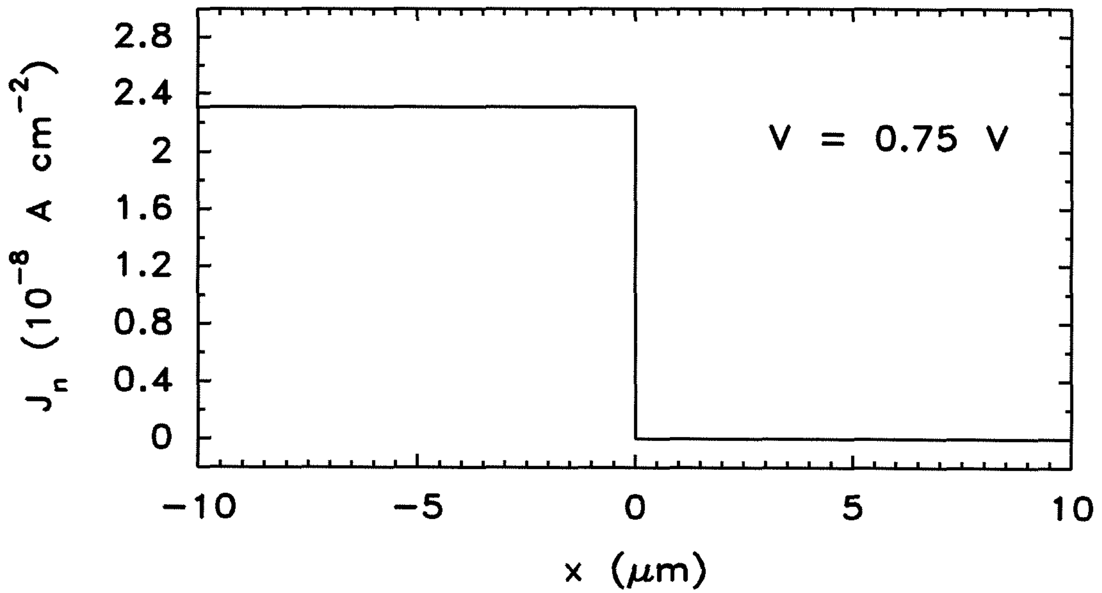

(b)

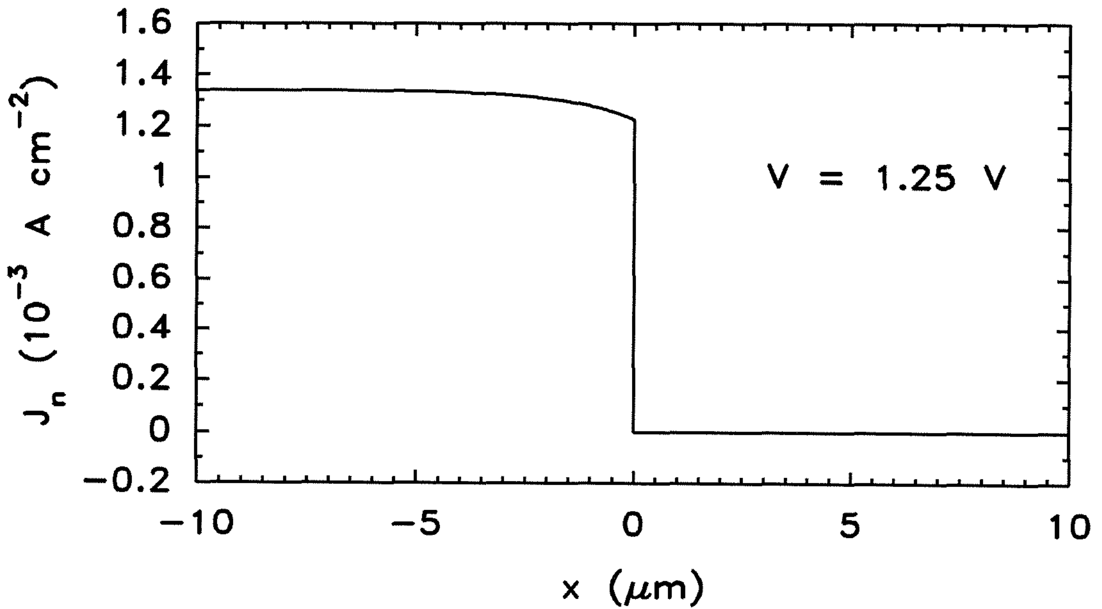

Figure 2.7: Electron current densities for an n-CdSe/p-ZnTe heterostructure at (a) 0.75 V applied bias and (b) 1.25 V applied bias. Since the recombination rate is proportional to the slope of the current density, this figure shows that interfacial recombination dominates the device operation at lower applied biases, and that holes are injected into the CdSe at higher applied biases.

ZnTe region. Thus, numerical simulations of an n-CdSe/p-ZnTe heterojunction explicitly demonstrate that this design will not produce efficient light emission in the wide bandgap ZnTe material. Instead, recombination in the CdSe and at the CdSe/ZnTe interface will dominate.

2.4.2 Graded Injector

The next device that we present offers an improvement on the CdSe/ZnTe design. By including a graded $Mg_xCd_{1-x}Se$ region between the CdSe and ZnTe layers, we hope to facilitate electron injection while continuing to block hole injection into the CdSe layer. The material parameters for the CdSe layer are the same as in the previous device. Two types of ZnTe are used in this simulation: an undoped ZnTe epilayer, and a lightly ($1 \times 10^{17} cm^{-3}$) doped p-ZnTe substrate with an oxygen center 0.4 eV below the conduction band edge [31, 32]. The oxygen center is needed to accurately model the substrates used in actual devices. Due to the poor quality of the ZnTe substrates, recent devices have been grown on GaSb substrates. Also, growth of p-type ZnTe layers has recently been achieved. These and other recent developments to the graded electron injector structure are discussed in more detail in Section 2.5.

The $Mg_xCd_{1-x}Se$ layer is graded from zero Mg concentration to a concentration such that there is no conduction band offset to ZnTe (see Figure 2.3). Since Harrison's LCAO method predicts a small valence band offset between CdSe and MgSe and since small changes in the CdSe/MgSe valence band offset do not significantly affect the operation of this device, we use the common anion rule in our calculations for this device. For a MgSe bandgap of 3.5 eV, this gives a value of 0.66 for x at the $Mg_xCd_{1-x}Se$/ZnTe interface. The doping of the graded $Mg_xCd_{1-x}Se$ region is n-type at the CdSe interface and undoped at the ZnTe interface. These doping parameters account for the likelihood that $Mg_xCd_{1-x}Se$ will not be dopable n-type for high Mg concentrations. The thickness of the graded region was chosen

to be 200 Å. A thinner graded region decreases the accumulation of electrons near the CdSe/$Mg_xCd_{1-x}Se$ interface, making electron injection more difficult, while increasing the thickness might prevent the graded $Mg_xCd_{1-x}Se$ from being coherently strained to the ZnTe.

Figure 2.8 shows the conduction and valence band edges for this device at 0.0 and 2.0 V forward bias. Figure 2.9 gives the hole and electron charge densities at the same biases. At zero bias the ZnTe layer is depleted at its interface with the graded $Mg_xCd_{1-x}Se$ region, while electron accumulation occurs at the interface between the CdSe and the graded $Mg_xCd_{1-x}Se$ region. As a forward bias is applied to the device, the depletion width in the ZnTe layer decreases and eventually holes accumulate at the $Mg_xCd_{1-x}Se$/ZnTe interface. An important point to note here is that in the CdSe/ZnTe device, electron and hole accumulation at the heterojunction interface led to high rates of non-radiative recombination. In the graded device, however, electron and hole accumulations are spatially separated, leading to a considerable reduction in the amount of non-radiative recombination occurring at the interfaces. As we continue to increase the forward bias, Figure 2.10 shows that electron injection occurs prior to any significant hole injection. Recall that the slope in the current density is a measure of the recombination rate, so the right-hand side of Figure 2.10 shows that injected electrons are recombining in the ZnTe material. Since the total current is constant throughout the device, the slope in j_p is simply the negative of the slope of j_n. Notice that interfacial recombination dominates the operation of the device only at lower voltages, and that bulk recombination begins to dominate at higher voltages.

The graded $Mg_xCd_{1-x}Se$ layer facilitates electron injection as follows. At zero bias, the barrier to electron injection is essentially the same in the graded device as it is in the CdSe/ZnTe device. As we forward bias the CdSe/ZnTe device, the barrier to electron injection remains essentially constant, determined by the fixed conduction band offset between the two materials. In the graded device, however, as we apply a forward bias, more and more electrons accumulate within

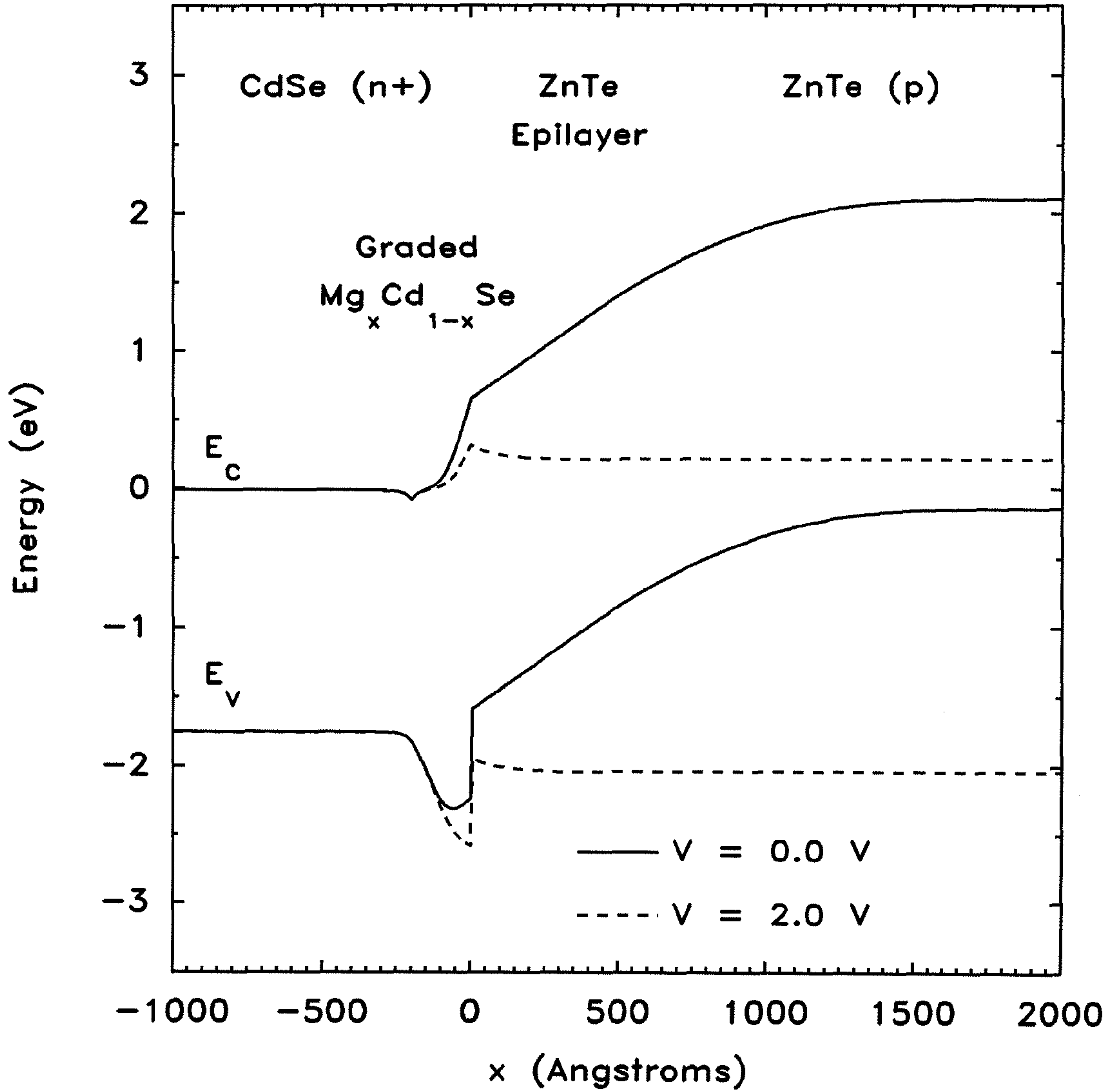

Figure 2.8: Conduction and valence band edges for the graded injector device at 0.0 and 2.0 V forward bias. In this figure and in all succeeding figures, zero on the horizontal axis corresponds to the right-hand side of the graded $Mg_xCd_{1-x}Se$ layer.

(a)

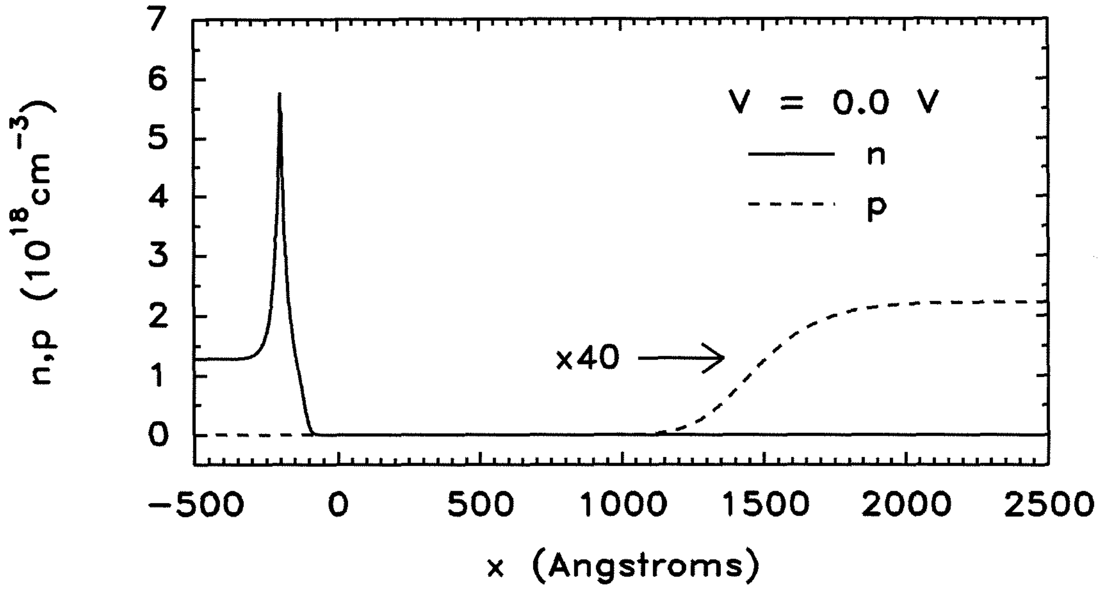

(b)

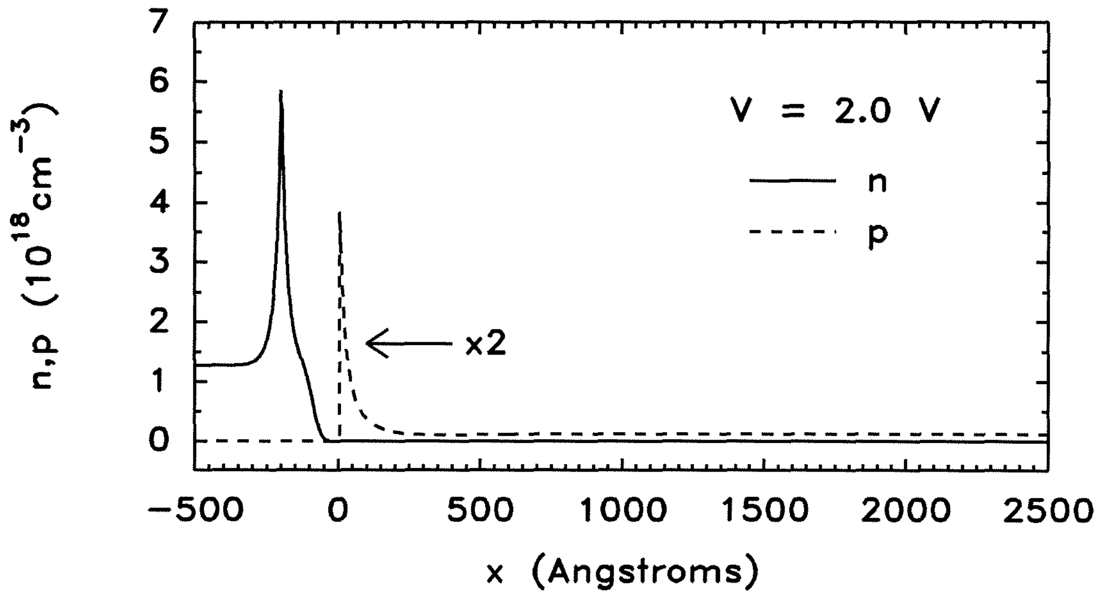

Figure 2.9: Electron and hole charge densities for the graded injector device at (a) 0.0 V forward bias and (b) 2.0 V forward bias. Notice the spatial separation of accumulated charge.

(a)

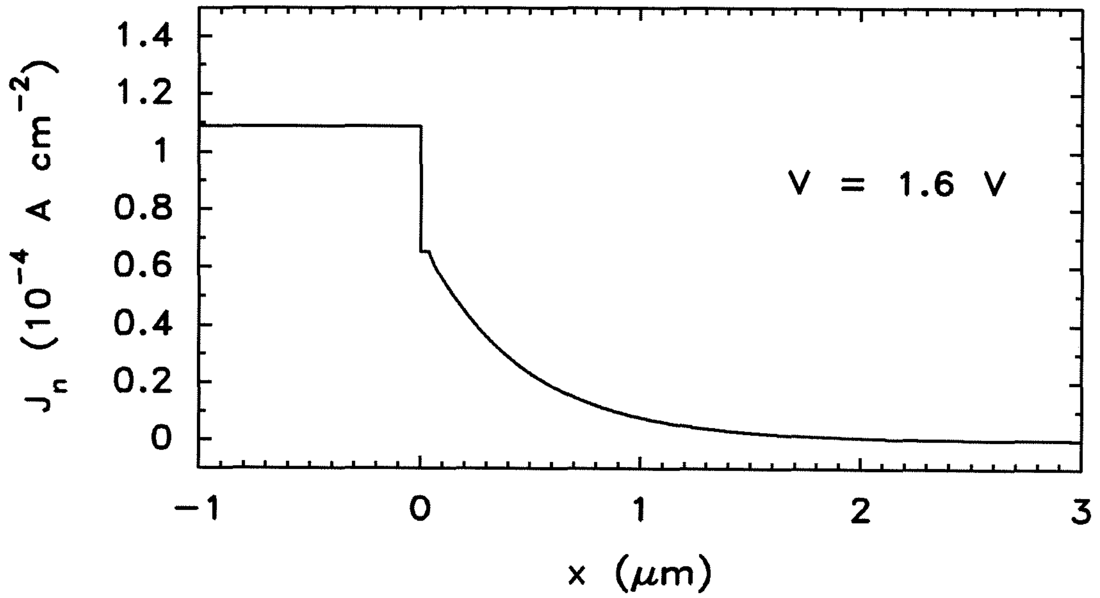

(b)

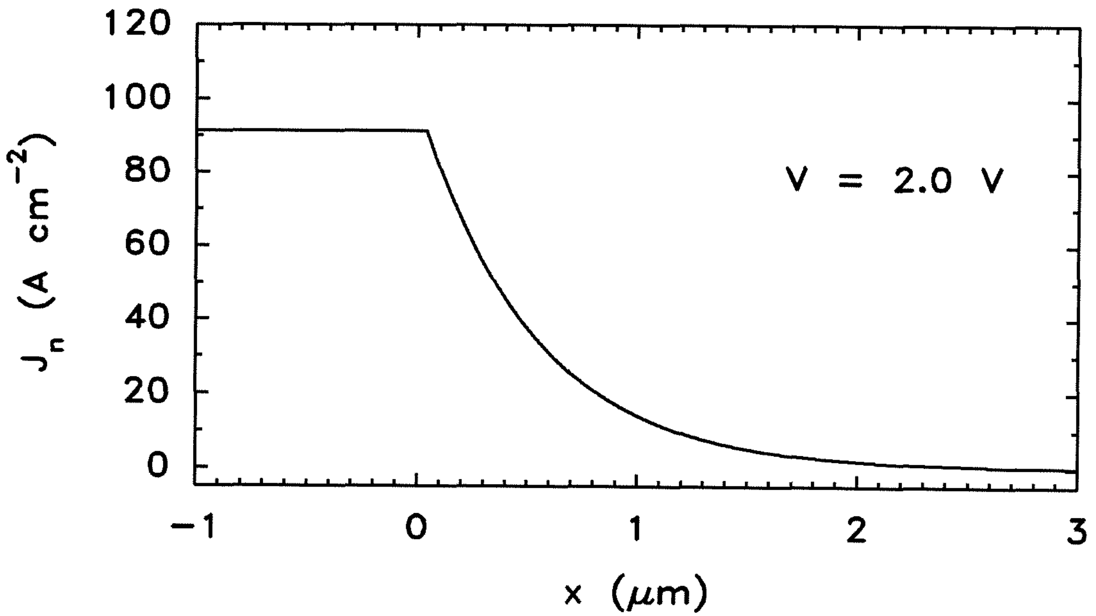

Figure 2.10: Electron current density for the graded injector device at (a) 1.6 V forward bias and (b) 2.0 V forward bias. The second flat portion in (a) corresponds to the ZnTe epilayer.

the graded $Mg_xCd_{1-x}Se$ layer. This accumulation of electrons causes the bands to bend downwards, as seen in Figure 2.8, thereby reducing the barrier to electron injection.

Figure 2.10 shows the electron and hole current densities at 1.6 and 2.0 V forward bias. Very few of the injected electrons actually recombine in the ZnTe epilayer, since the diffusion length in the ZnTe epilayer is much greater than the epilayer thickness used in our devices. Most of the electrons recombine in the ZnTe substrate, which results in red light emission because of the oxygen center. Thus, for the purposes of high efficiency green light emission, and for laser applications, we need to be able to confine injected electrons to the ZnTe epilayer. In more recent devices grown on GaSb substrates, the p-ZnTe is grown thicker, but is still less than the diffusion length so the confinement of injected electrons is important for these devices as well. The next design proposes a method to achieve this.

2.4.3 Graded Injector with Confining Layer

To confine injected electrons to the ZnTe epilayer, we refer again to Figure 2.2. This figure shows that a $Mg_xZn_{1-x}Te$ ternary will have a larger bandgap than ZnTe, with most of the difference going into the conduction-band. We propose to insert a $Mg_yZn_{1-y}Te$ confining layer between the ZnTe epilayer and the ZnTe substrate. Again, there have been no reports in the literature of experimental measurements of the valence band offset between MgTe and ZnTe (see Chapter 4); however, the LCAO method predicts a small valence band offset, which is desirable for our device operation. In our calculations, we assume a less favorable case with two-thirds of the band offset going into the conduction-band and one-third in the valence-band. We do this to demonstrate that the performance of our devices is not highly dependent on the validity of the common anion rule.

Using the MgTe bandgap of 3.57 eV and choosing a conduction-band barrier height of 0.5 eV gives a value $y = 0.57$ at the $Mg_yZn_{1-y}Te/ZnTe$ epilayer interface.

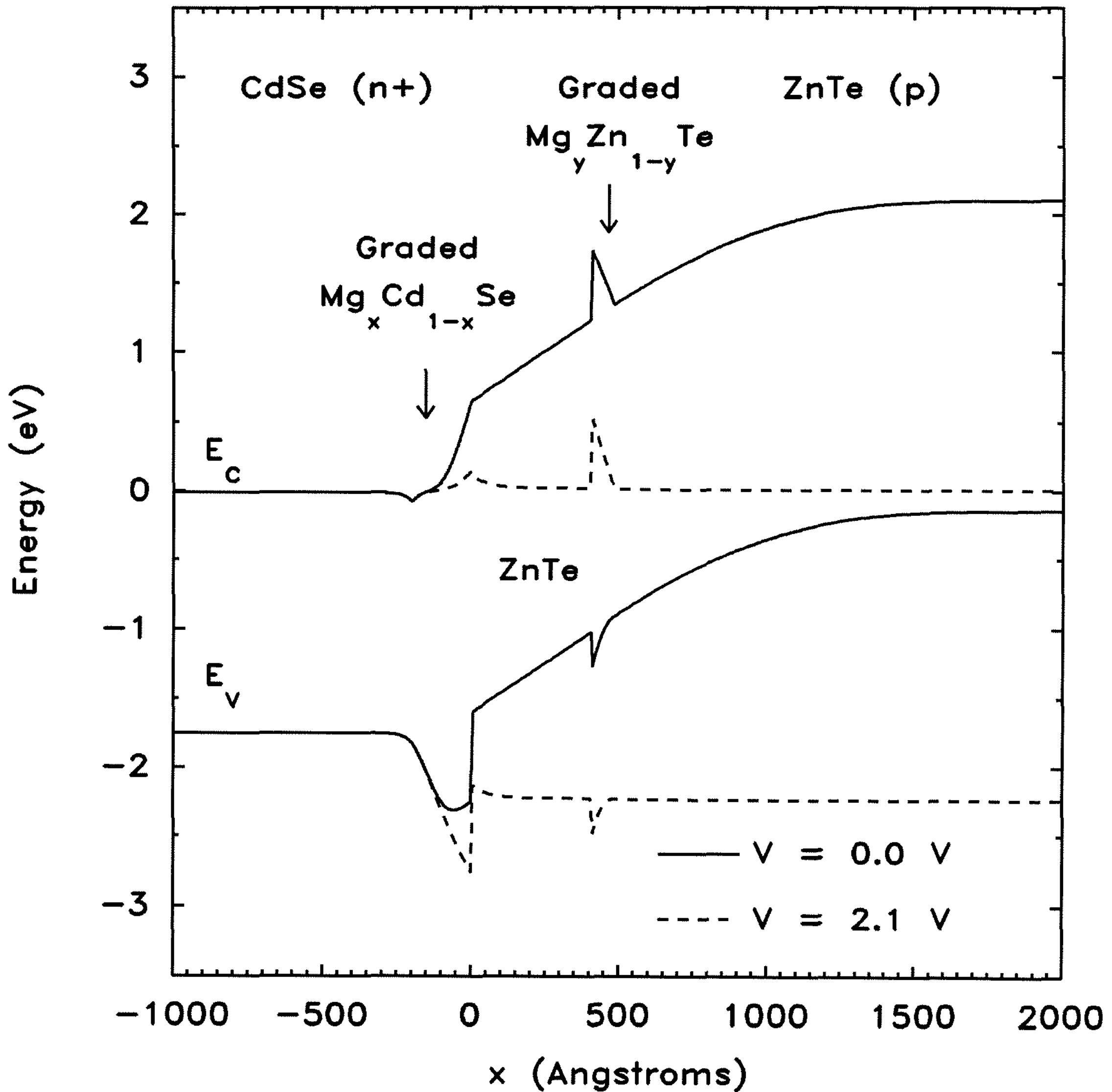

Figure 2.11: Conduction and valence band edges for the graded injector device with an electron confining layer at 0.0 and 2.1 V forward biases. Note the undesirable deviation from the common anion rule used for the $Mg_yZn_{1-y}Te$ to ZnTe band offset.

(a)

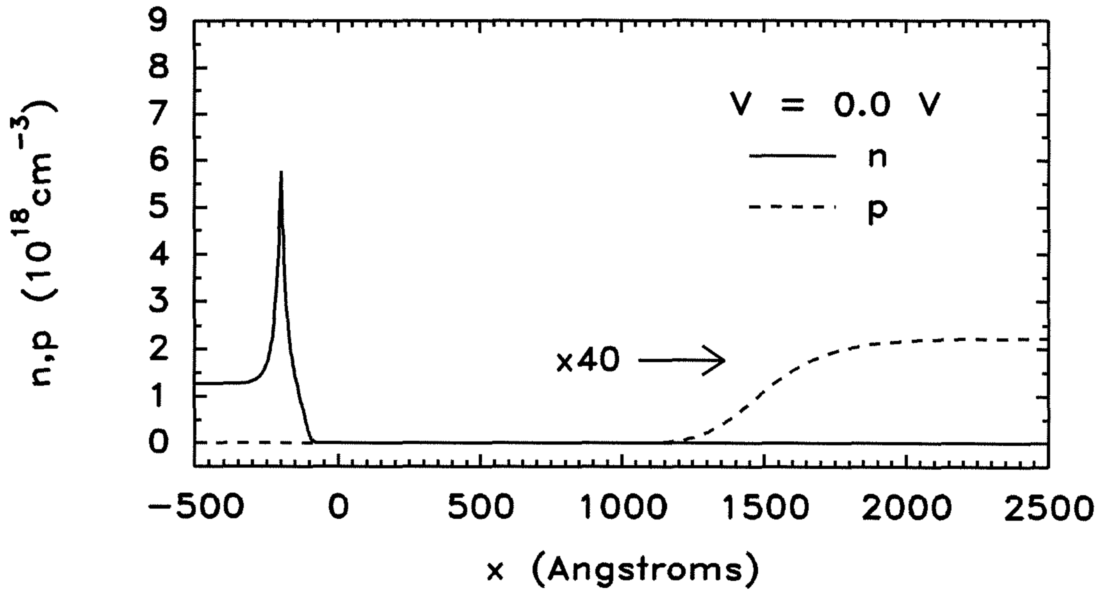

(b)

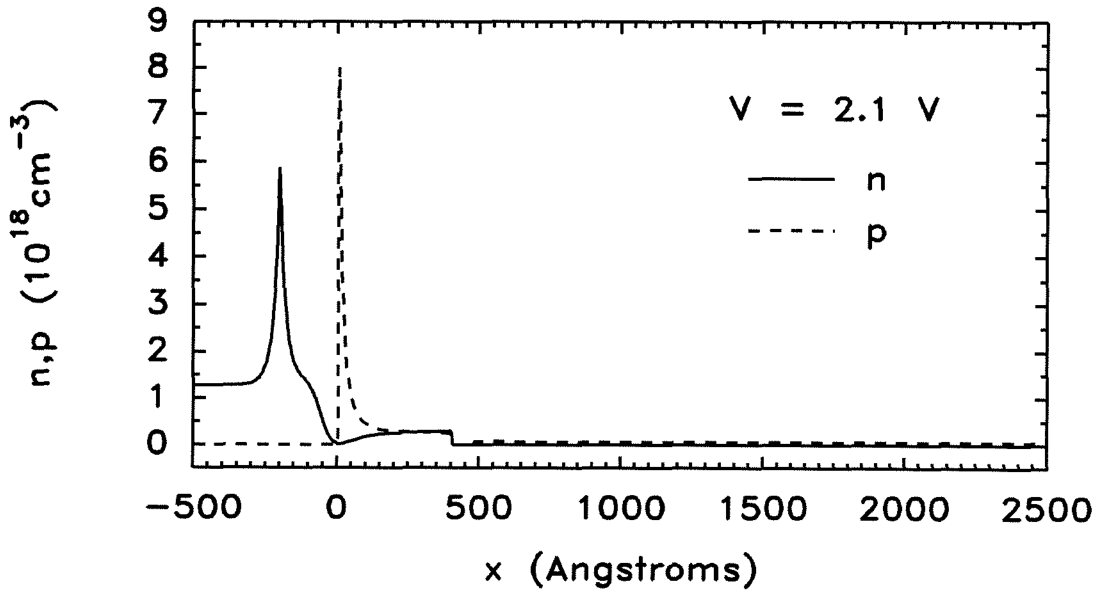

Figure 2.12: Electron and hole charge densities for the graded injector device with a confining layer at (a) 0.0 V forward bias and (b) 2.1 V forward bias.

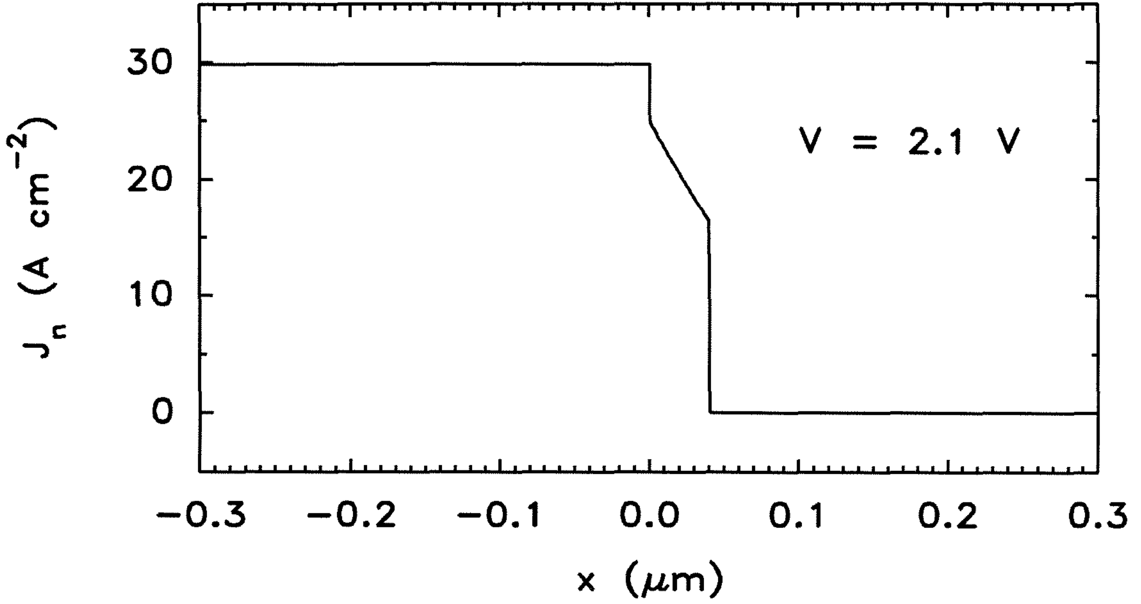

Figure 2.13: Electron current densities for the graded injector device with a confining layer at a forward bias of 2.1 V. The two regions showing a very large slope in the current density plot correspond to the $Mg_xCd_{1-x}Se/ZnTe$ and $ZnTe/Mg_yZn_{1-y}Te$ interfaces respectively.

The $Mg_yZn_{1-y}Te$ confining layer is graded to avoid blocking holes from entering the ZnTe epilayer. If a more favorable valence band offset is used, then the $Mg_yZn_{1-y}Te$ confining layer need not be graded and the Mg concentration will be less for the same barrier height, resulting in less strain. The width of the graded $Mg_xZn_{1-x}Te$ region only needs to be thick enough to prevent significant electron tunneling through to the ZnTe substrate. We use 75 Å in our calculations, but this can be increased significantly, if required, without introducing too much strain.

Figure 2.11 shows the conduction and valence band edges for this device at forward biases of 0.0 and 2.0 V. Figure 2.12 gives the hole and electron charge densities at these same biases. Until the onset of electron injection, this device behaves in much the same way as the previous one. After the onset of electron injection, however, we see that the confining layer prevents electrons from entering

the ZnTe substrate. In Figure 2.13, the electron current densities for this device at a forward bias of 2.0 V show that with the addition of the electron confining layer, the bulk recombination in the device is confined to the ZnTe epilayer. Also notice that interfacial recombination comprises a significant portion of the total recombination in the device. In general, interfacial recombination plays a larger role at small biases and becomes less significant as the bias is increased; however, quantitative calculations of radiative recombination rates and quantum efficiencies will depend largely on the specific properties of the interfaces in each device.

2.4.4 Tunable Bandgap LED

We next consider a device design that will allow the wavelength of emitted light to be tuned continuously from the green to the blue wavelength regimes. This design was first proposed in Ref. [7]. The basic idea behind the device is to have the radiative recombination occur in a $Mg_yZn_{1-y}Te$ layer, where y can be adjusted to obtain the desired band-to-band recombination energy. Figure 2.14 shows a schematic of the proposed device at flatband. Note that we have used the common anion rule in simulating this device, so there is no valence band offset between ZnTe and MgZnTe ternaries. This allows us to forego the grading of the $Mg_zZn_{1-z}Te$ confining layer that was needed in the previous device. We do this for convenience and clarity of presentation only; the device concept does not depend on the validity of the common anion rule. Figure 2.15 shows the conduction and valence band edges of the device at 0.0 and 2.25 V forward bias. Figure 2.16 shows the hole and electron charge densities at these same biases. From these figures we again see that the graded $Mg_xCd_{1-x}Se$ layer enhances electron injection into the wider bandgap material, while spatially separating regions of interfacial charge accumulation. Figure 2.17 shows the electron current densities for this device at a forward bias of 2.25 V. In this figure we see that all of the bulk recombination occurs in the $Mg_yZn_{1-y}Te$ epilayer. Thus, the wavelength of light emitted from

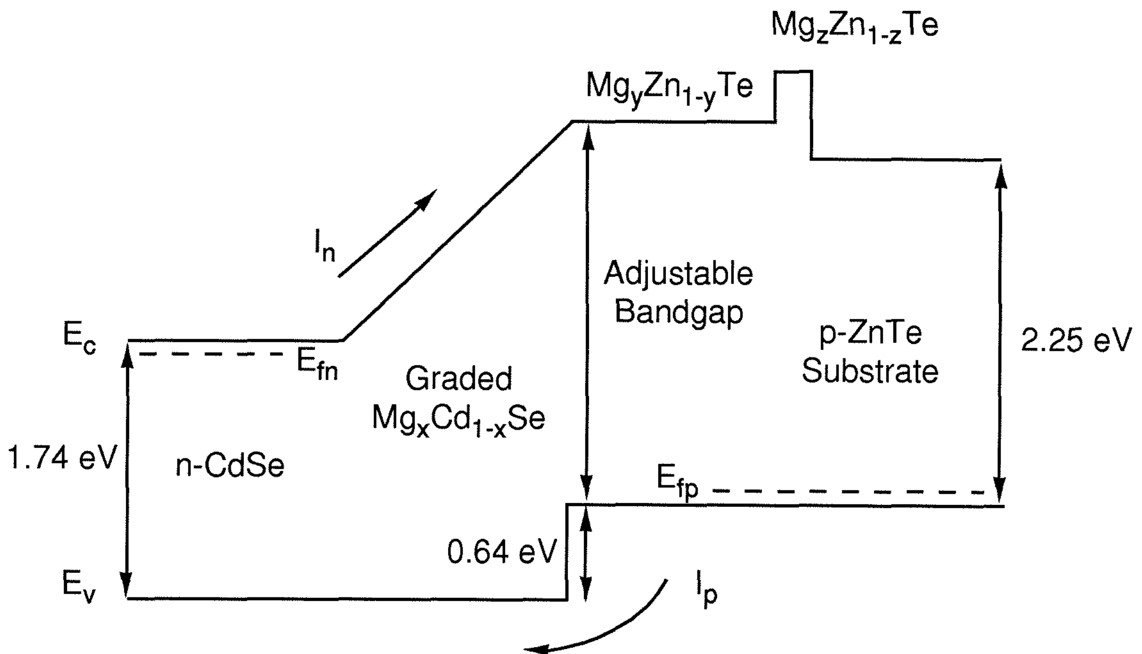

Figure 2.14: Schematic diagram showing the conduction and valence band edges for the tunable bandgap LED at flatband. Electrons are injected into the wide bandgap $Mg_yZn_{1-y}Te$ but are blocked from entering the ZnTe by the $Mg_zZn_{1-z}Te$ layer.

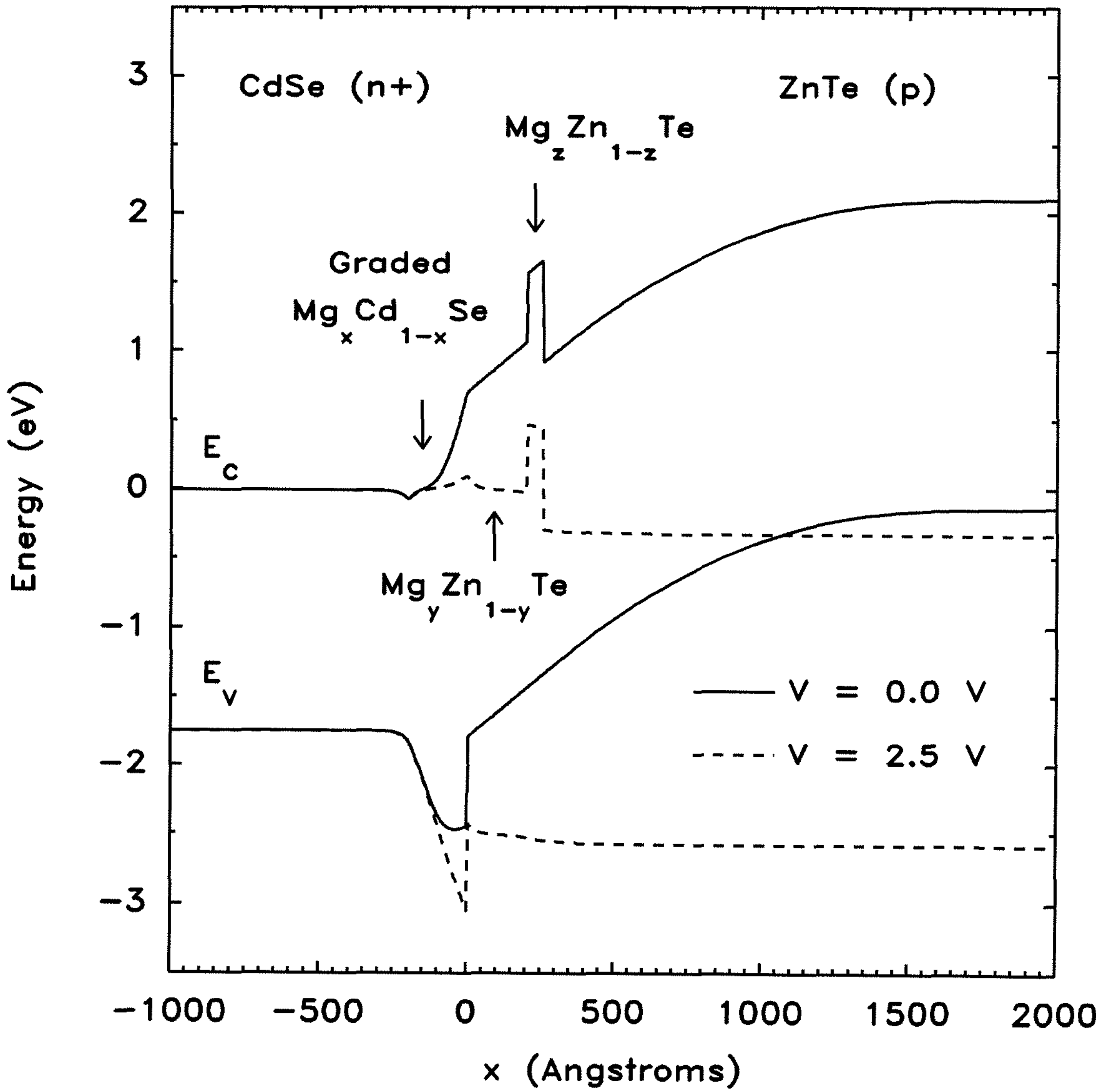

Figure 2.15: Conduction and valence band edges for the tunable bandgap LED at 0.0 and 2.5 V forward bias.

(a)

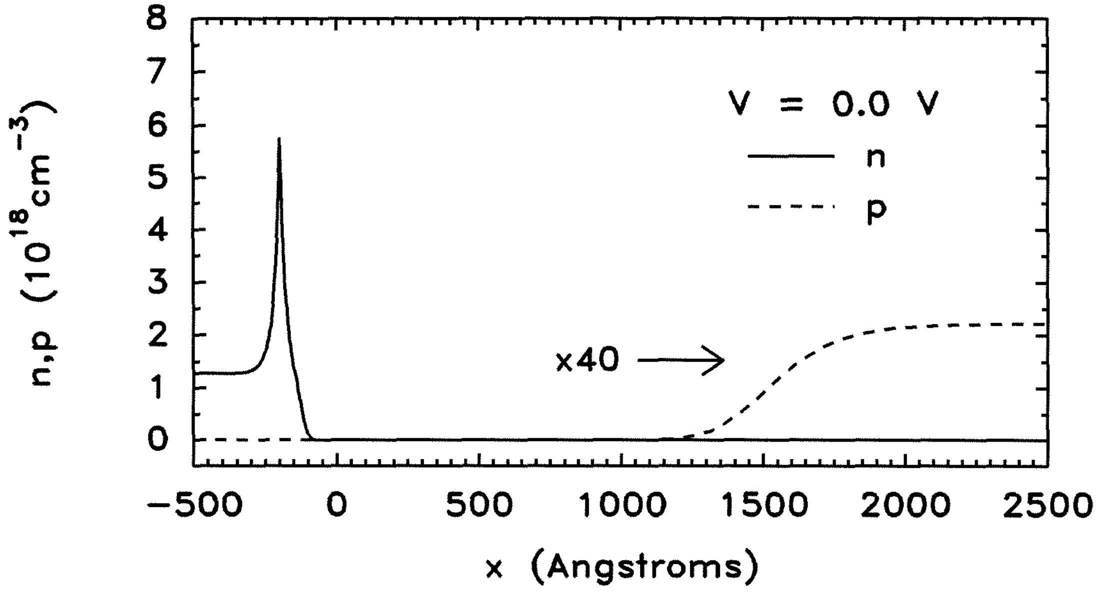

(b)

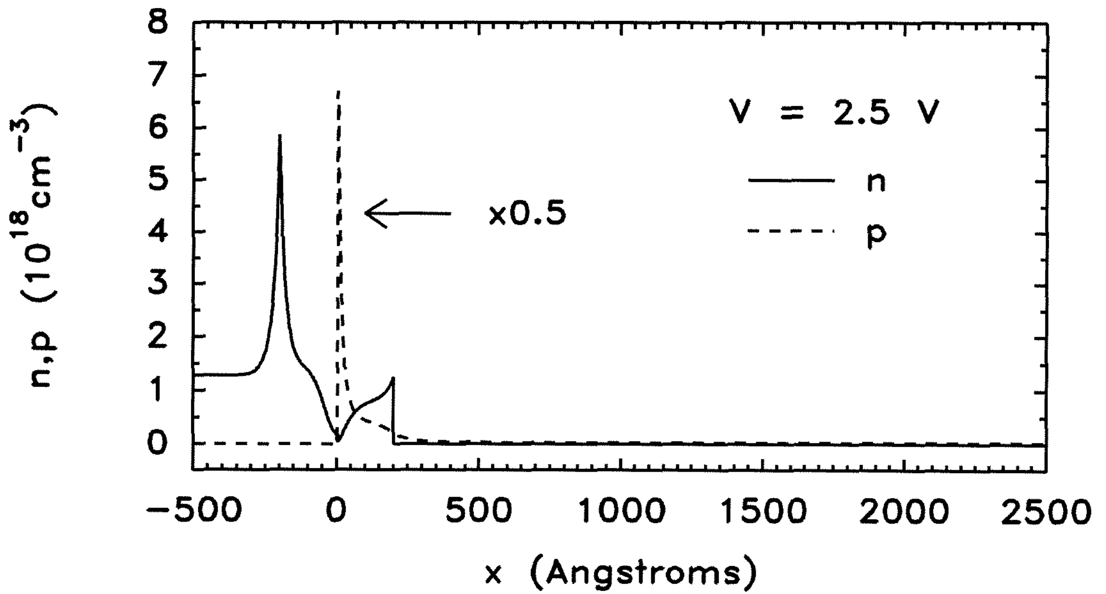

Figure 2.16: Electron and hole charge densities for the tunable bandgap LED at (a) 0.0 V forward bias and (b) 2.5 V forward bias. Notice the accumulation of both holes and electrons in the $Mg_yZn_{1-y}Te$ layer at 2.5 V bias.

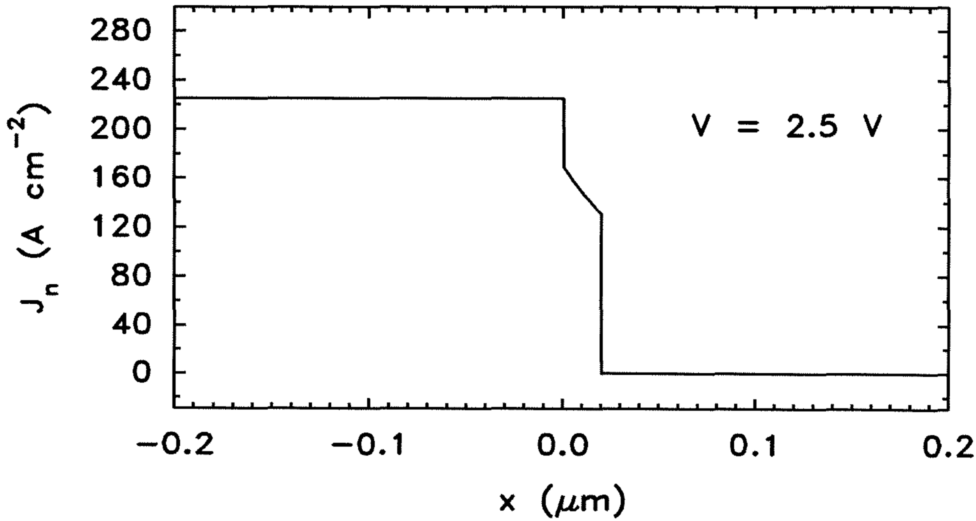

Figure 2.17: Electron current density for the tunable bandgap LED at 2.5 V forward bias. The slope in the electron current density plot in the $Mg_yZn_{1-y}Te$ layer indicates successful electron injection and confinement with this layer. The wavelength of light emitted from this layer can be tuned into the blue.

this device can be varied from green to well into the blue wavelength regime, depending on the the Mg concentration used in the $Mg_yZn_{1-y}Te$ epilayer. The tunable bandgap LED operates in much the same manner as the previous device, with the exception that the wavelength of light emission is tunable from green to blue.

2.5 Recent Developments

2.5.1 Current LED Structure

As was mentioned, the four devices simulated in Section 2.4 did not incorporate some recent developments to the graded electron injector design. These modifications do not affect the validity of the simulations, but are important factors in the fabrication of actual devices. For completeness, these recent developments and their influence on the device structure are discussed below.

Early LED structures using the graded injector scheme were grown on lightly doped ZnTe substrates purchased from Eagle-Picher. These substrates were initially very useful, because p-type doping of MBE grown ZnTe had not yet been developed, so only thin ZnTe epilayers could be used in the LEDs before series resistance became too large. In effect, the ZnTe substrates were used for the active regions wherein the radiative recombination took place. At roughly the same time that the very efficient N-doping of ZnTe was developed, it was also discovered that the ZnTe substrates being used had serious problems with surface and structural quality, as well as reproducibility problems. These two developments led to the use of GaSb substrates instead of ZnTe substrates, and thick p-type ZnTe epilayers for the active regions. This made the processing somewhat more complicated since both contacts to the LED had to be made from the top of the sample, but it did not affect the basic operation of the device.

The other recent developments were measurement of the MgSe bandgap and the MgSe and MgTe band alignments. The primary impact of these measurements was to change the desired composition of the $Mg_xCd_{1-x}Se$ graded region at the Se/Te interface. A larger MgSe bandgap means that less Mg is required to grade the conduction band edge to match that of ZnTe, while a lowering of the valence band edge with the addition of Mg necessitates more Mg at the Se/Te interface. Accounting for both the bandgap and the band offset measurements, the desired

$Mg_xCd_{1-x}Se$ composition at the Se/Te interface is roughly 70% Mg and 30% Cd.

2.5.2 Possible Quaternary LED Designs

One of the primary disadvantages of the graded injector concept is the strain induced in the graded region. Preliminary TEM studies (see Chapter 4) have shown that this region can have a very high density of defects. Another problem lies in the CdSe layer which, if too thick, will absorb a substantial fraction of the light emitted from the ZnTe active region. To solve these problems, it is necessary to use either ternary or quaternary layers which have a range of bandgaps and lattice parameters. The added advantage in using quaternary semiconductors is that the bandgap and lattice parameter can be independently varied. This section proposes one possible LED design based on the use of quaternary II-VI semiconductor compounds.

To gain insight into the design of wide bandgap LEDs using quaternary layers we first study the $Zn_{1-x}Mg_xS_ySe_{1-y}$ quaternary already used in ZnSe-based LDs and LEDs. This quaternary is indicated schematically in Figure 2.4 by the lines connecting ZnSe, MgSe, MgS, and ZnS. We see that the bandgap of $Zn_{1-x}Mg_xS_ySe_{1-y}$ can be varied while still maintaining complete lattice match to either ZnSe or GaAs. The difficulty currently being encountered is that Mg and S both pull down the valence band edge when added to ZnSe. This makes $Zn_{1-x}Mg_xS_ySe_{1-y}$ quaternaries layers even less p-type dopable than the already difficult to dope ZnSe. Since the $Zn_{1-x}Mg_xS_ySe_{1-y}$ is being used for the thick cladding layers, series resistance in these layers may eventually be the limiting factor for attaining shorter wavelength LEDs and LDs. Also, some of the reliability problems in these devices may be related to the difficulties in p-type doping either in the form of contacting problems or in the active layers.

One way to avoid this problem is to use two different quaternary layers, one of which is easily dopable p-type and the other n-type, while maintaining the design

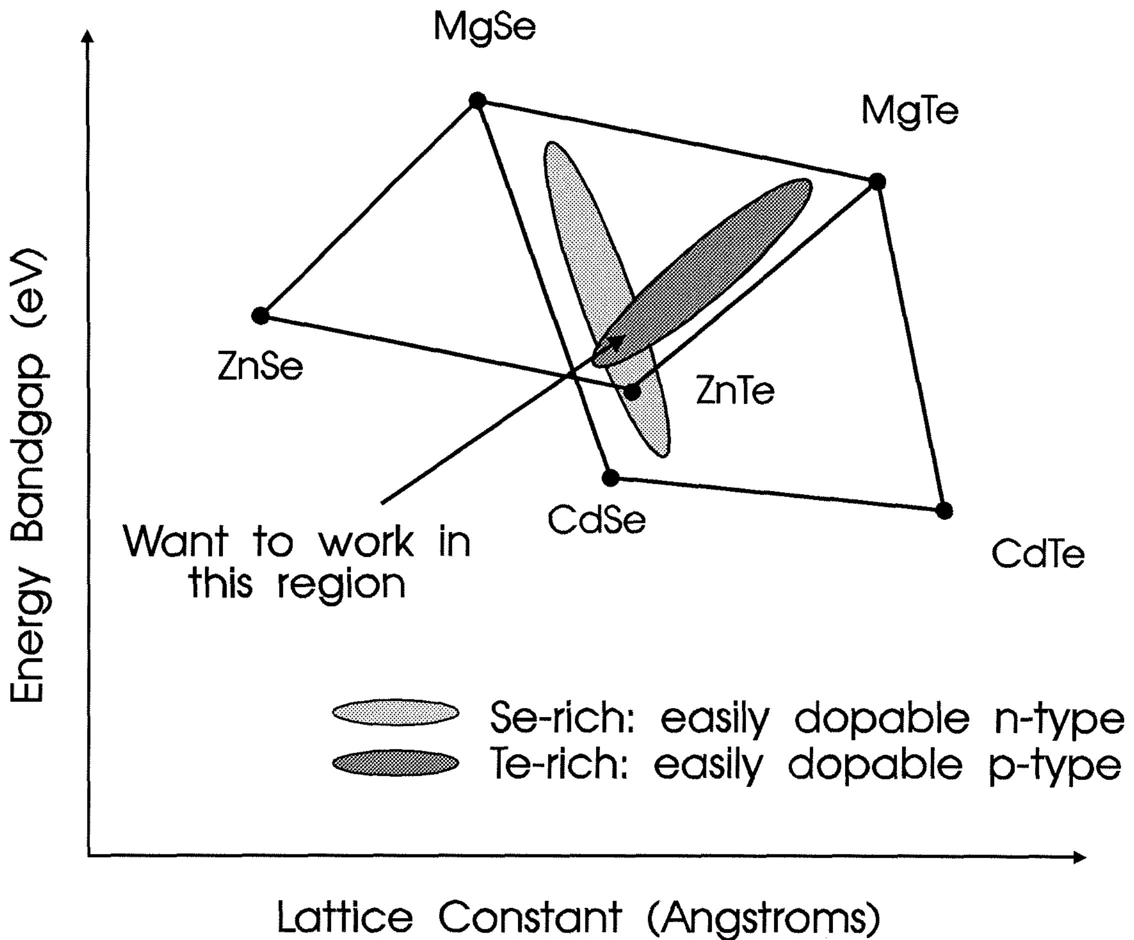

Figure 2.18: Schematic diagram of the $Zn_{1-x}Mg_xSe_yTe_{1-y}$ and $Cd_{1-x}Mg_xSe_yTe_{1-y}$ quaternaries. Shaded areas denote the Te-rich and Se-rich composition which should allow easy p-type and n-type dopability respectively. Where the two shaded regions overlap, both n- and p-type dopability can be achieved without sacrificing lattice matching.

constraints of close lattice match and substrate availability. An example of such a combination is shown in Figure 2.18. The two quaternaries, $Zn_{1-x}Mg_xSe_yTe_{1-y}$ and $Cd_{1-x}Mg_xSe_yTe_{1-y}$, indicated by the solid lines, have regions of overlapping lattice parameter which can also be lattice matched to GaSb, InAs or ZnTe substrates. The advantage in using two quaternary layers can be noted by observing that Se-based semiconductors such as ZnSe and CdSe tend to be easily dopable n-type, while Te-based semiconductors such as ZnTe and CdTe tend to be easily dopable p-type (see also Figures 2.1 and 2.2). Thus, Te-rich $Zn_{1-x}Mg_xSe_yTe_{1-y}$ should be p-type dopable, while Se-rich $Cd_{1-x}Mg_xSe_yTe_{1-y}$ should be n-type dopable.

With the addition of Mg and small amounts of Te to CdSe, and small amounts of Se and Mg to ZnTe, we should be able to obtain two semiconductors with the following properties: 1) perfect lattice match to each other and to a suitable substrate, 2) both p- and n-type dopability, 3) flexibility in bandgap engineering at a single lattice parameter, and 4) both layers can have bandgaps larger that the wavelength of emitted light. A schematic diagram of an LED structure incorporating such layers is shown in Figure 2.19. As shown in this figure, another critical element to the successful implementation of an LED based on two quaternary layers is the graded injector layer which facilitates carrier injection into the desired semiconductor layer.

To implement the design described above, a number of very important experimental concerns must be addressed. The most critical of these is the existence of miscibility gaps for certain ternary and quaternary compounds. In particular, $ZnTe_{1-y}Se_y$ is known to have miscibility gaps under certain growth conditions; however, researchers at Bellcore have been successful in growing $ZnTe_{1-y}Se_y$ over the entire range of composition using MBE [33]. Despite this encouraging result, it still remains to be determined whether or not the $Zn_{1-x}Mg_xSe_yTe_{1-y}$ and $Cd_{1-x}Mg_xSe_yTe_{1-y}$ quaternaries can actually be grown with the desired composition. Another important, but not critical, factor is band bowing. Band bowing in the quaternaries of interest will require higher Mg and Se or Te concentrations,

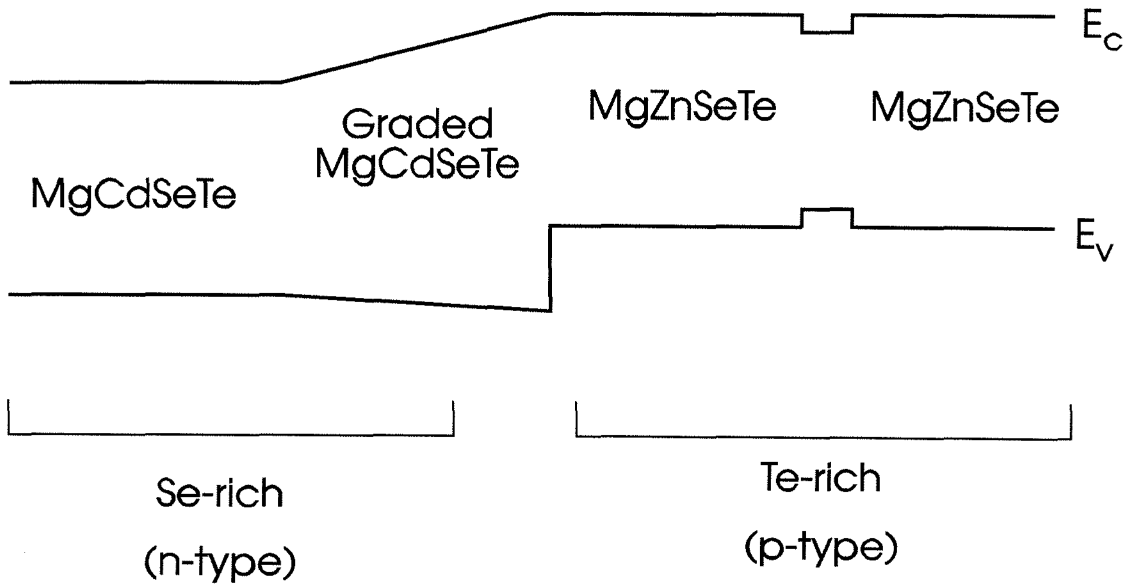

Figure 2.19: Schematic diagram of fully lattice matched graded injector structure. The use of quaternaries allows flexibility in bandgap engineering while still allowing lattice matched conditions. The use of two quaternaries also facilitates both n- and p-type dopability.

and if great enough, could prevent the development of shorter wavelength blue and violet LEDs and LDs.

2.6 Summary

We present the numerical simulation and design of novel wide bandgap II-VI LEDs. The drift-diffusion model, modified to account for heterojunctions, is used in the simulations. All of the designs we present incorporate both n-CdSe and p-ZnTe. ZnTe is chosen because it is the only wide bandgap II-VI compound that can be doped p-type using conventional techniques. CdSe, with its small lattice mismatch to ZnTe and its n-type dopability, is then the best compound to use for the formation of a II-VI p-n heterojunction with ZnTe. A simple n-CdSe/p-ZnTe

heterostructure is first analyzed. Simulation results for this design show high interface recombination rates and hole injection into the smaller bandgap CdSe layer. The CdSe/$Mg_xCd_{1-x}Se$/ZnTe device proposed by Phillips et al. improves on the CdSe/ZnTe heterojunction design by incorporating a graded $Mg_xCd_{1-x}Se$ electron injector. The addition of this layer significantly reduces interface recombination and facilitates electron injection into the wide bandgap ZnTe layer. A further improvement on this design utilizes a $Mg_xZn_{1-x}Te$ confining layer which restricts bulk recombination to the ZnTe epilayer. A tunable bandgap LED is demonstrated, in which the bulk recombination occurs in a $Mg_xZn_{1-x}Te$ epilayer. The Mg concentration then determines the wavelength of the light emitted from the device, which can be varied from green to well into the blue wavelength regime. Simulations of a device incorporating recent materials characterization results are presented and, finally, a design that potentially allows fully lattice-matched structures with flexible bandgap engineering is proposed.

Bibliography

[1] J. Qiu, J.M. DePuydt, H. Cheng, and M.A. Haase, *Appl. Phys. Lett.* **59**, 2992 (1991).

[2] M.A. Haase, J. Qiu, J.M. DePuydt, and H. Cheng, *Appl. Phys. Lett.* **59**, 1272 (1991).

[3] Y. Fan, J. Han, L. He, J. Saraie, R.L. Gunshor, M. Hagerott, H. Jeon, A.V. Nurmikko, G.C. Hua, and N. Otsuka, *Appl. Phys. Lett.* **61**, 3160 (1992).

[4] F. Hiei, M. Ikeda, M. Ozawa, T. Miyajima, A. Ishibashi, and K. Akimoto, *Electronics Letters* **29**, 878 (1993).

[5] Y. Lansari, J. Ren, B. Sneed, K.A. Bowers, J.W. Cook, Jr., and J.F. Schetzina, *Appl. Phys. Lett.* **61**, 2554 (1992).

[6] J.O. McCaldin, T.C. McGill, and C.A. Mead, *Phys. Rev. Lett.* **36**, 56 (1976).

[7] M.C. Phillips, M.W. Wang, J.F. Swenberg, J.O. McCaldin, and T.C. McGill, *Appl. Phys. Lett.* **61**, 1962 (1992).

[8] J.O. McCaldin, *J. Vac. Sci. Technol. A* **8**, 1188 (1990).

[9] W.A. Harrison, *J. Vac. Sci. Technol.* **14**, 1016 (1977).

[10] E.T. Yu, M.C. Phillips, J.O. McCaldin, and T.C. McGill, *J. Vac. Sci. Technol. B* **9**, 2233 (1991).

[11] J.O. McCaldin, *Growth and Optical Properties of Wide-Gap II-VI Low-Dimensional Semiconductors*, edited by T.C. McGill, C.M. Sotomayor Torres, and W.B. Gebhardt (Plenum, New York, 1989), pp. 39-51.

[12] J. Marine, T. Ternisien D'ouville, B. Schaub, A. Laugier, D. Barbier, J.C. Guillaume, J.F. Rommeluere, and J. Chevallier, Journal of Electronic Materials, **7**, 17 (1978).

[13] H. Okuyama, K. Nakano, T. Miyajima, and K. Akimoto, Jpn. J. Appl. Phys. Part 2-Letters **30**, L1620 (1991).

[14] H. Mittendorf, Z. Physik **183**, 113 (1965).

[15] W. van Roosbroeck and W. Shockley, *Phys. Rev.* **94**, 1558 (1954).

[16] R.N. Hall, Proc. Institution of Electrical Engineering **106B**, Suppl. No. 17, 923 (1960).

[17] W. Shockley and W.T. Read, *Phys. Rev.* **87**, 835 (1952).

[18] A.H. Marshak, *IEEE Trans. Electron Devices* **36**, 1764 (1989).

[19] J.E. Sutherland and J.R. Hauser, *IEEE Trans. Electron Devices* **24**, 363 (1977).

[20] A.H. Marshak and K.M. van Vliet, *Solid-State Electron.* **21**, 419 (1978).

[21] M.S. Lundstrom, *Fundamentals of Carrier Transport* (Addison-Wesley, Reading, 1990).

[22] P.E. Dodd, T.B. Stellwag, M.R. Melloch and M.S. Lundstrom, *IEEE Trans. Electron Devices* **38**, 1253 (1991).

[23] J.W. Harrison and J.R. Hauser, *J. Appl. Phys.* **47**, 292 (1976).

[24] A.G. Thompson and J.C. Woolley, Canadian J. of Phys. **45**, 255 (1967).

[25] M. Kurata and J. Yoshida, *IEEE Trans. Electron Devices* **31**, 467 (1984).

[26] H.C. Chan and T.J. Shieh, *IEEE Trans. Electron Devices* **38**, 2427 (1991).

[27] X. Aymerich-Humet, F. Serra-Mestres, and J. Millan, *Solid-State Electron.* **24**, 981 (1981).

[28] W.H. Press, B.P. Flannery, S.A. Teukolsky, and W.T. Vetterling, *Numerical Recipes* (Cambridge, New York, 1986).

[29] G.B. Tait, *Solid-State Electron.* **32**, 369 (1989).

[30] L.J. Turgeon and D.H. Navon, *IEEE Trans. Electron Devices* **25**, 837 (1978).

[31] J.L. Merz and R.T. Lynch, *II-VI Semiconducting Compounds 1967 International Conference*, 731 (1967).

[32] J.J. Hopfield, D.G. Thomas, and R.T. Lynch, *Phys. Rev. Lett.* **17**, 312 (1966).

[33] R.S. Turco-Sandroff, R.E. Nahory, M.J.S.P. Brazil, R.J. Martin, and H.L. Gilchrist, *Appl. Phys. Lett.* **58**, 1611 (1991).

Chapter 3

XPS Measurements of Band Offsets for Mg-based Semiconductor Compounds

3.1 Introduction and Outline

The importance of Mg-based semiconductor compounds for II-VI wide bandgap light emitters has recently been demonstrated. In particular, the blue-green laser diodes (LDs) initially demonstrated by Haase *et al.* [1] are now fabricated with $Zn_{1-x}Mg_xS_ySe_{1-y}$ cladding layers [2], resulting in the demonstration of the first blue LD [3] and the pulsed operation of pseudomorphic blue-green LDs up to temperatures as high as 394 K [4]. The latest results report blue (489.9 nm) and green (523.5 nm) LDs incorporating multiquantum well ZnSe/ZnTe contacts showing thresholds of < 4 V and 400 A/cm^2, and room temperature CW operation for greater than 9 minutes [5].

In addition, compositionally graded $Mg_xCd_{1-x}Se$ used as an electron injector in the LED design proposed by Phillips *et al.* [6] results in devices with nearly ideal current-voltage characteristics and promising device lifetimes [7]. There is also

interest in $Mg_xCd_{1-x}Te$ for light emitter applications, and growth of $Mg_xCd_{1-x}Te$ by molecular-beam epitaxy (MBE) has recently been achieved [8]. Finally, simulations show that $Mg_yZn_{1-y}Te$ layers can be used to shorten the wavelength of light emission in the graded electron injector devices [9].

As of yet there has been very little characterization of Mg-based semiconductors. In particular their valence band offset, or band alignment, to other semiconductor compounds has not been studied, except for a recent calculation reported by Nakayama [10]. To optimize the performance of these devices, an accurate measurement of the band offset between Mg-based semiconductors and other materials will be required. The importance of the valence band offset to LED and LD design is considerable: the appropriate Mg concentrations needed in both the graded $Mg_xCd_{1-x}Se$ region and the $Zn_{1-x}Mg_xS_ySe_{1-y}$ cladding layers are dependent on the respective valence band offsets, especially as the wavelength of light emission is extended into the blue. Currently, the LD designs incorporating $Zn_{1-x}Mg_xS_ySe_{1-y}$ layers assume a type I band lineup between $Zn_{1-x}Mg_xS_ySe_{1-y}$ and $ZnS_{1-z}Se_z$, based on the common anion rule and experimental data in Ref. [2] and on a semi-empirical tight binding method in Ref. [11]. The devices using $Mg_xCd_{1-x}Se$ for a graded injector were also designed using the common anion rule.

The original common anion rule [12] was observed not to apply to the one cation, Al, then studied from the third row of the periodic table, so we should not expect it to necessarily apply to Mg, another third row cation. Similarly, Wei and Zunger [13] predict that the common anion rule applies only when the d orbitals of the cations on both sides of a heterojunction, e.g., $MgSe/Cd_{0.54}Zn_{0.46}Se$, interact with their respective valence bands in a comparable manner. Since the $3d$ orbitals in Mg are unoccupied, as in the case of Al, we might expect a deviation from the common anion rule similar to that observed in the AlAs/GaAs system.

In this chapter, we report the measurement of ΔE_v in the lattice matched $MgSe/Cd_{0.54}Zn_{0.46}Se$ (5.89 Å, zincblende [2]) and $MgTe/Cd_{0.88}Zn_{0.12}Te$ (6.435 Å, zincblende [8]) heterojunctions by X-ray photoelectron spectroscopy (XPS).

$Cd_{0.54}Zn_{0.46}Se$ and $Cd_{0.88}Zn_{0.12}Te$ were chosen to avoid difficulties associated with measuring band offsets in lattice mismatched systems, and to test the validity of the common anion rule for Mg based compounds. Using our measured value for the $MgSe/Cd_{0.54}Zn_{0.46}Se$ valence band offset, we can estimate the $Zn_{1-x}Mg_xS_ySe_{1-y}/ZnS_{1-z}Se_z$ and $Mg_xCd_{1-x}Se/CdSe$ valence band offsets by linear interpolation.

Section 3.2 of this chapter describes the sample growth, and the XPS experimental setup. Section 3.3 outlines the XPS data analysis. The band offset results are presented in Section 3.4, and the chapter is concluded with Section 3.5.

3.2 Experiment

3.2.1 Sample Growth

The structures studied here were grown in two Perkin-Elmer 430P molecular-beam epitaxy (MBE) systems, one devoted to III-V and the other to II-VI semiconductor growth. GaSb buffer layers were grown on GaSb (100) substrates to provide a smooth growth surface. After the GaSb growth, the samples were transferred via an ultrahigh vacuum (UHV) transfer tube to the II-VI growth chamber. Thick ($>$ 3000 Å), relaxed $Cd_{0.54}Zn_{0.46}Se$ ($Cd_{0.88}Zn_{0.12}Te$) layers, followed by the band offset structures, were grown at a substrate temperature of 270 °C (300 °C) and a growth rate of approximately 53 Å/min. The $Cd_{0.54}Zn_{0.46}Se$ and $Cd_{0.88}Zn_{0.12}Te$ composition were calibrated using XPS and X-ray diffraction, to keep the lattice mismatch to a minimum. The measured $Cd_{0.54}Zn_{0.46}Se$ and $Cd_{0.88}Zn_{0.12}Te$ lattice parameters were 5.93 Å and 6.43 Å allowing us to neglect their small lattice mismatches (0.68% and 0.06%) to MgSe and MgTe respectively. All layers were grown in the cubic zincblende structure as indicated by reflection high energy electron diffraction patterns.

3.2.2 XPS Measurements

Following the II-VI growth, the samples were transferred via a UHV transfer tube to a Perkin-Elmer Model 5500 analysis system equipped with a monochromatic Al Kα X-ray source ($h\nu$ = 1486.6 eV) and a spherical capacitor electron-energy analyzer with multichannel detection capability. The base pressure in the XPS chamber was typically in the low 10^{-10} Torr range. Care was taken to ensure that the escape orientation of the photoelectrons remained constant from sample to sample to minimize any electron diffraction effects due to the single crystalline nature of the samples. The election binding energy scale was routinely calibrated using binding energy peaks from a sputter cleaned calibration sample consisting of Au, Cu and Al. Details of the determination of the instrumental resolution function from acquired Au spectra are given in Section 3.3. XPS energy separations measured on the same sample under identical conditions were typically reproducible to better than $\pm$ 0.02 eV, and all samples yielded energy separations that were reproducible to within experimental error.

For the $Cd_{0.54}Zn_{0.46}Se$/MgSe band offset measurement, the core level to valence band edge energy separations were measured on two bulk $Cd_{0.54}Zn_{0.46}Se$ and two bulk MgSe samples. The core level binding energy separations were measured on two thin ($\sim$ 20 Å) $Cd_{0.54}Zn_{0.46}Se$ on MgSe samples, and one thin MgSe on $Cd_{0.54}Zn_{0.46}Se$ sample. Thin overlayer thicknesses are necessary to acquire a reasonable photoelectron signal from both sides of the heterojunction, since photoelectron escape depths are $\sim$ 10-20 Å. For the $Cd_{0.88}Zn_{0.12}Te$/MgTe band offset measurement, the core level to valence band edge energy separations were measured on one each of bulk $Cd_{0.88}Zn_{0.12}Te$ and bulk MgSe samples. The core level binding energy separations were measured on one $Cd_{0.88}Zn_{0.12}Te$ on MgTe sample. Commutativity of the valence band offset was not verified for the $Cd_{0.88}Zn_{0.12}Te$/MgTe band offset measurement. Figures 3.1 and 3.2 show representative scans required for the $Cd_{0.54}Zn_{0.46}Se$/MgSe and $Cd_{0.88}Zn_{0.12}Te$/MgTe band offset measurements

respectively.

3.3 XPS Data Analysis

To determine the MgSe/$Cd_{0.54}Zn_{0.46}Se$ and $Cd_{0.88}Zn_{0.12}Te$/MgTe valence band offsets using XPS, the following relation was used:

$$\Delta E_v = (E_{Zn\ 3p\ 3/2} - E_v^{CdZnX}) - (E_{Mg\ 2s} - E_v^{MgX}) - (E_{Zn\ 3p\ 3/2} - E_{Mg\ 2s}), \quad (3.1)$$

where the X in CdZnX and MgX refers to either Te or Se. The core level to valence band maximum, E_v, binding energy separations were measured on bulk CdZnX and bulk MgX samples, and the core level binding energy separations were measured on thin (~ 20 Å) CdZnX on MgX samples and thin MgX (~ 20 Å) on CdZnX samples as shown in Figures 3.1 and 3.2. For MgSe and MgTe, the use of either the Mg $2s$ or the Mg $2p$ core level peaks in the analysis did not affect the results. For $Cd_{0.54}Zn_{0.46}Se$ and $Cd_{0.88}Zn_{0.12}Te$, the only resolvable core level peak was Zn $3p$, since Se and Te are common to both sides of the junction and both the Cd $4d$ and Zn $3d$ peaks overlap with states from the valence band.

To determine the core level peak positions, we first performed an integrated background subtraction and then fit the peaks to Voigt functions, allowing the binding energy, HWHM, Lorentzian fraction and intensity to vary. In the case of the MgX/CdZnX heterojunction samples, the Zn $3p$ 3/2 and Mg $2s$ core levels overlap, so it was necessary to constrain the peak shapes to those obtained from bulk MgX and CdZnX samples, so as to reduce the number of fit parameters from eight to four. A representative fit for the Zn $3p$ 3/2 and Mg $2s$ core levels for a sample consisting of 20 Å MgSe on $Cd_{0.54}Zn_{0.46}Se$ is shown in Figure 3.3. In the fitting procedure, only the intensity and binding energy are allowed to vary for each of the two core levels (Zn $3p$ 3/2 and Mg $2s$).

The determination of the precise energy of the valence band edge for the bulk semiconductors is complicated by the fact that instrumental broadening smears out

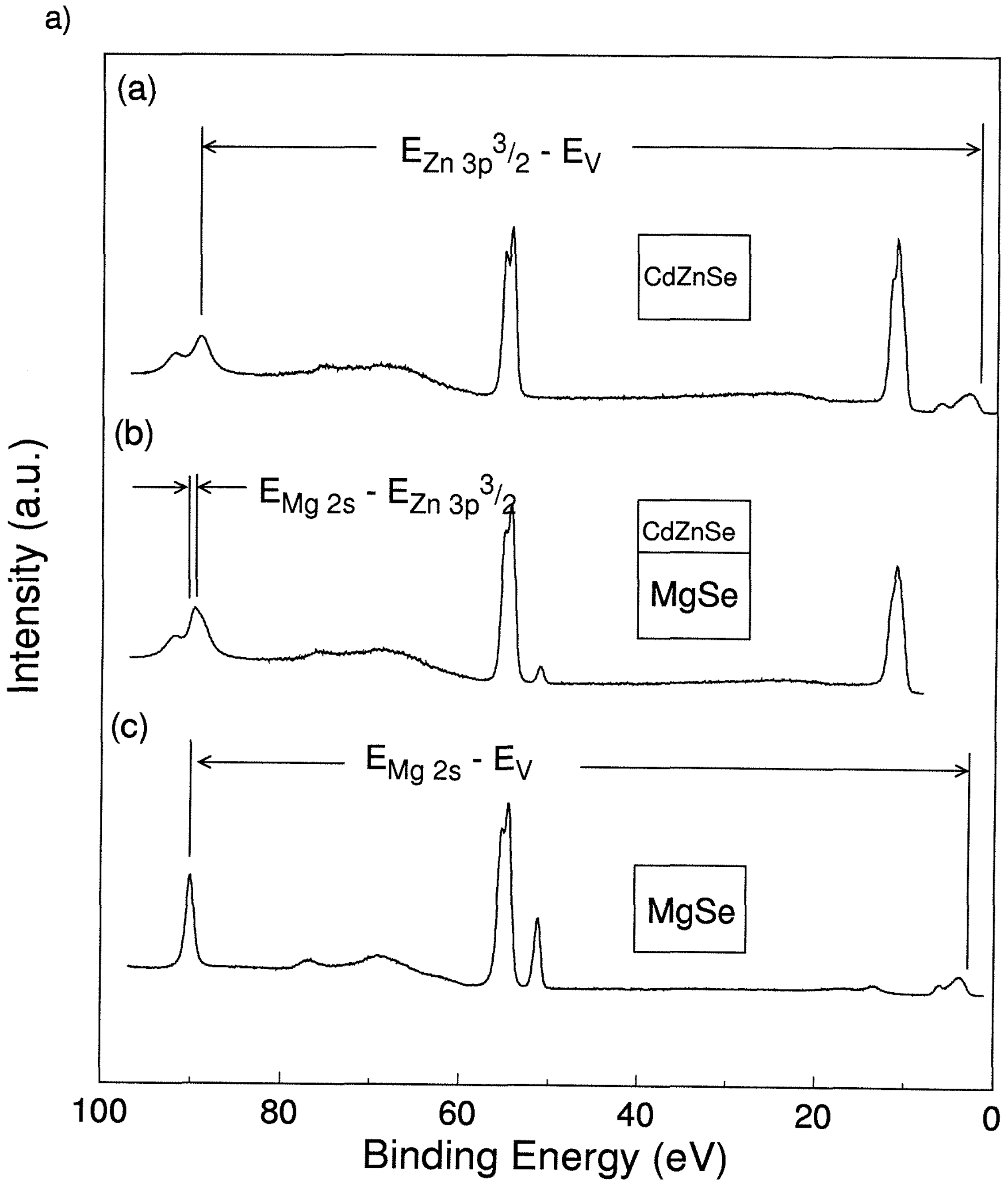

Figure 3.1: XPS spectra for (a) bulk $Cd_{0.54}Zn_{0.46}Se$, (b) thin (~ 20 Å) $Cd_{0.54}Zn_{0.46}Se$ on MgSe, and (c) bulk MgSe. Energy separations used in the band offset measurement are labeled.

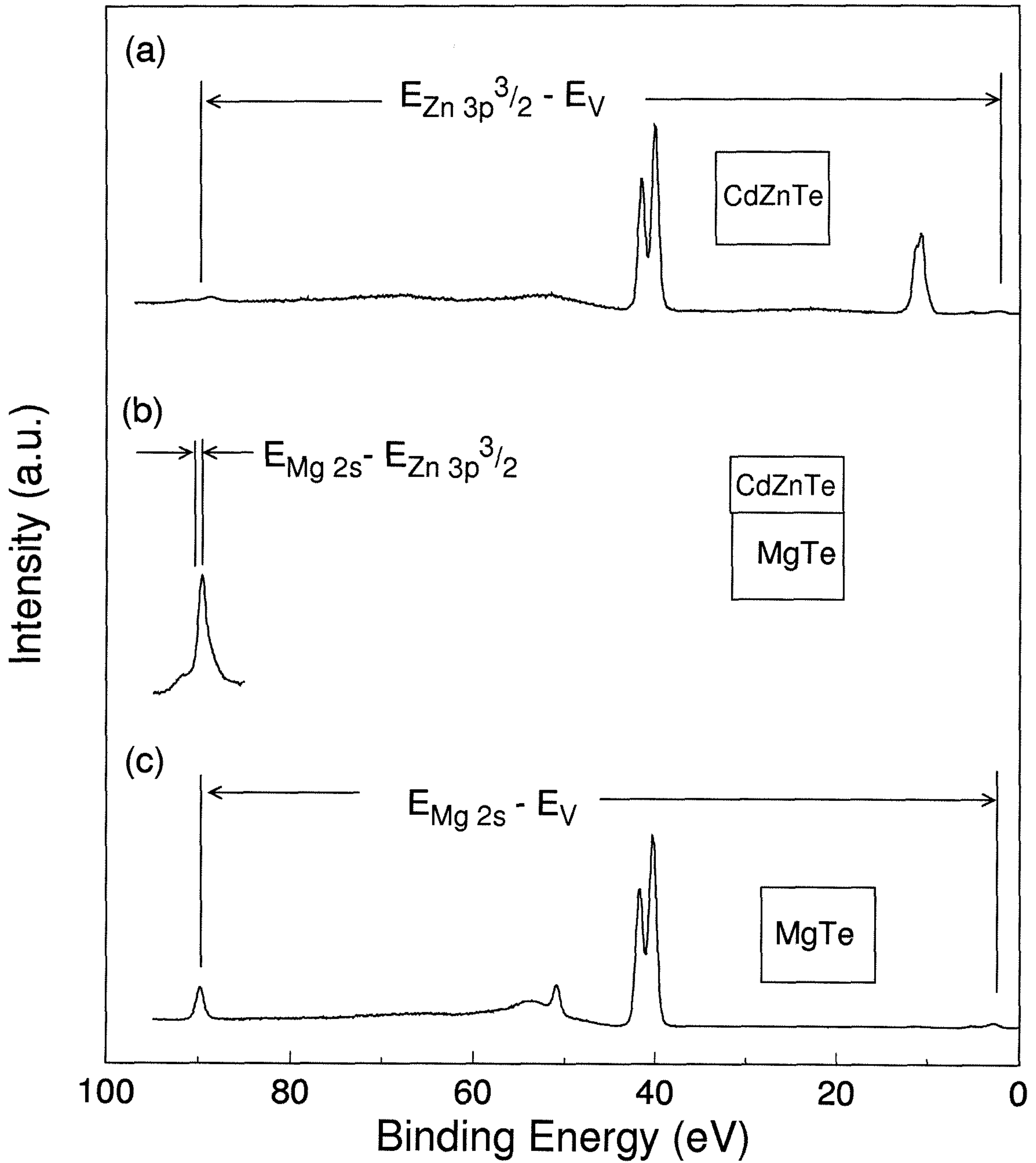

Figure 3.2: XPS spectra for (a) bulk $Cd_{0.88}Zn_{0.12}Te$, (b) thin (~ 20 Å) $Cd_{0.88}Zn_{0.12}Te$ on MgTe, and (c) bulk MgTe. Energy separations used in the band offset measurement are labeled.

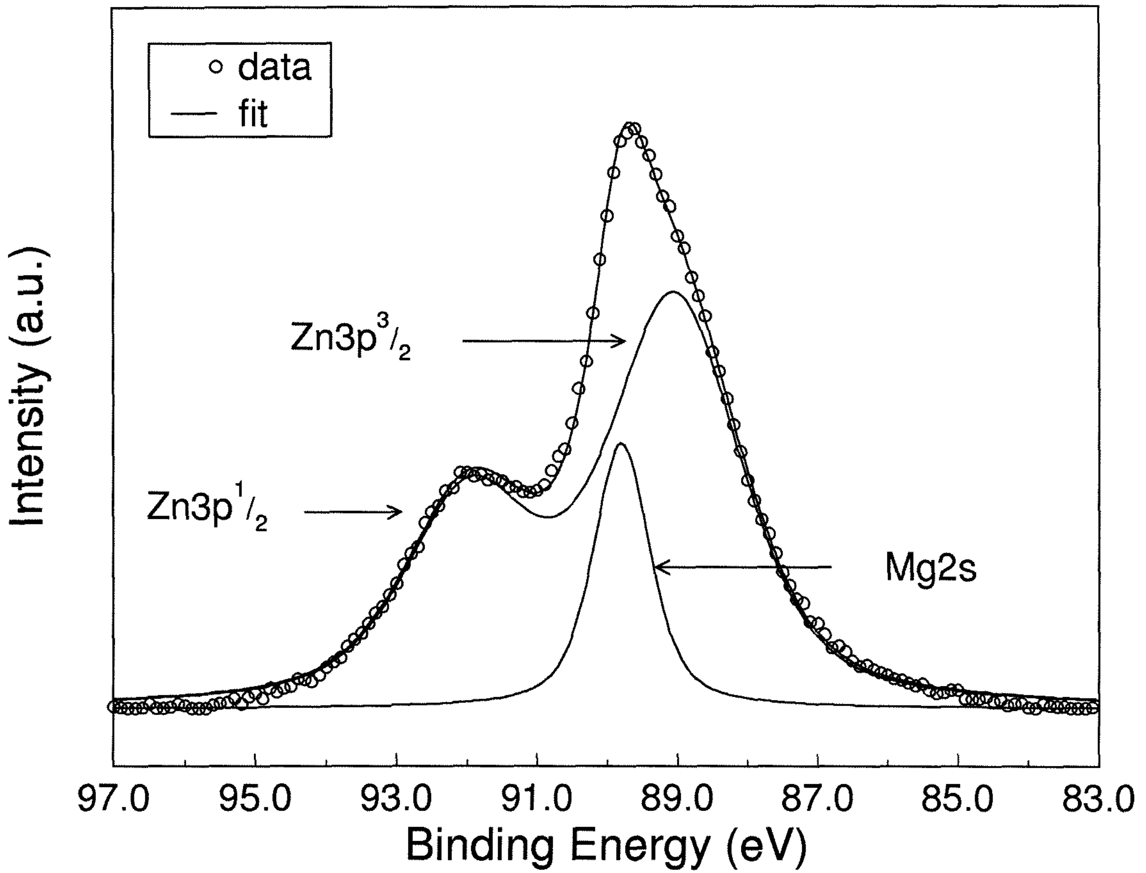

Figure 3.3: Least squares fit of Zn $3p$ 3/2 and Mg $2s$ core level peaks for a structure consisting of 20 Å MgSe grown on $Cd_{0.54}Zn_{0.46}Se$. Four parameters (the intensity and binding energy of each peak) were used in the fit. Background subtraction was performed prior to the fit.

the XPS spectra, so that simple linear extrapolation is not sufficient to accurately position the valence band edge. To overcome this difficulty, we use, following the procedure developed by Kraut *et al.* [14]. Basically, this involves calculating the band structure for each material and then integrating over the Brillouin zone to determine the theoretical valence band density of states (VBDOS). This VBDOS is then convolved with the instrumental resolution function as determined from experimentally acquired Au spectra. Finally, the instrumentally broadened theoretical VBDOS is fit to the experimental VBDOS to obtain the position of the valence band edge.

For the heterojunctions studied in this chapter, the calculation of the band structure was made more difficult by the fact that relatively little is know about the ternary $Cd_{0.54}Zn_{0.46}Se$ and $Cd_{0.88}Zn_{0.12}Te$ compounds, and even less is known about MgSe and MgTe. Thus, the empirical pseudopotential method cannot be used to directly calculate the band structure for these compounds. The methods used to determine the band structure for $Cd_{0.54}Zn_{0.46}Se$, $Cd_{0.88}Zn_{0.12}Te$, MgSe and MgTe are given below.

For $Cd_{0.54}Zn_{0.46}Se$ ($Cd_{0.88}Zn_{0.12}Te$) the band structure was calculated for a number of different semiconductors, but the best fit for the VBDOS was obtained using the band structure of ZnSe (ZnTe) calculated by the pseudopotential method [15], while allowing one additional energy scaling parameter to account for differences in the band structure of ZnSe (ZnTe) versus $Cd_{0.54}Zn_{0.46}Se$ ($Cd_{0.88}Zn_{0.12}Te$). Spin-orbit interactions [16, 17] and an electron effective mass parameter to incorporate the nonlocality of the pseudopotential [18] were included in the calculations. The critical point energies needed for the pseudopotential calculations, and parameters needed to determine the spin-orbit interactions, were obtained from Ref. [17] and [19, 20] respectively.

For MgSe and MgTe the empirical pseudopotential method could not be used since there have been almost no studies of these binary compounds because of their reactivity, so very little is known of their band structure. Instead of the

pseudopotential method, we calculated the MgSe band structure using the semi-empirical linear combination of atomic orbitals method [21], including spin orbit interactions [22], and allowing for the additional energy scaling parameter mentioned above. This resulted in theoretical VBDOSs in reasonably good agreement with the experimentally measured VBDOS.

The final step in determining the position of the valence band maximum is to determine the instrumental resolution function and fit the VBDOS, broadened with this function, to the experimentally measured VBDOS. Using measured XPS Au $4f$ core level peaks (HWHM=0.37eV), the instrumental resolution function can be determined, since the intrinsic linewidth of the Au $4f$ core level peak is well known. For this experiment, the instrumental resolution function of the system was determined to be a Voigt function with a Lorentzian fraction of 0.06, and a HWHM of 0.28eV.

Figure 3.4 shows the fitted VBDOS for MgTe, $Cd_{0.88}Zn_{0.12}Te$, MgSe and $Cd_{0.54}Zn_{0.46}Se$. The use of an energy scaling parameter requires verification of the validity of the calculated band structures. To do this we followed the procedure in Ref. [14] and varied the valence band edge fit region as shown in Figures 3.5 and 3.6. In these figures, the core level to valence band edge energy separation is plotted as a function of the upper limit of the interval over which the VBDOS is fitted. The reasoning here is that a theoretical VBDOS that accurately models the experimental VBDOS will result in the same fitted valence band edge position regardless of the fitting interval. The small variation of the fitted valence band edge position as a function of fit region indicates that the theoretical VBDOS used is in reasonable agreement with the experimental VBDOS.

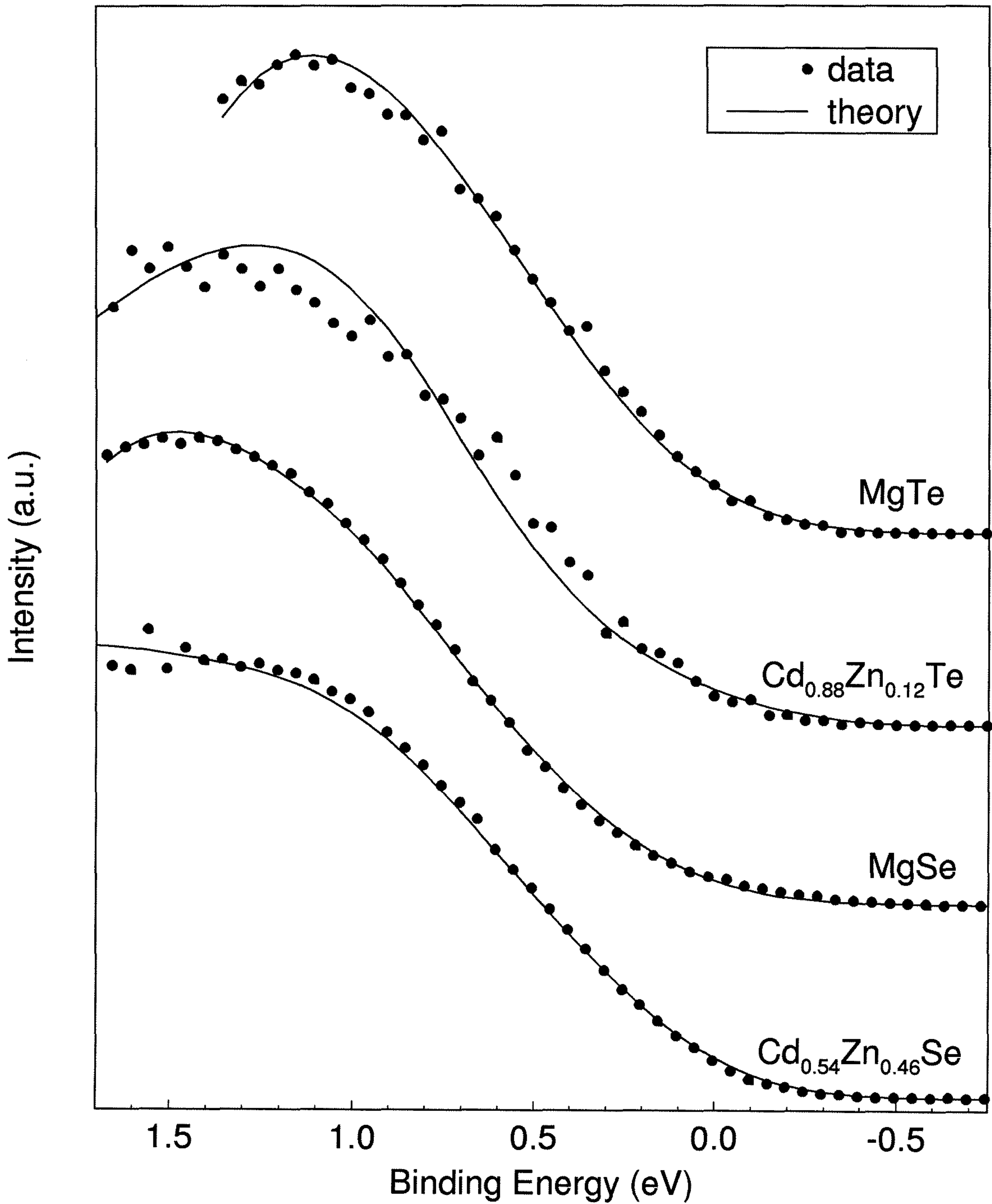

Figure 3.4: Fit of experimental VBDOS (circles), and instrumentally broadened theoretical VBDOS (solid lines) for (from top to bottom) MgTe, $Cd_{0.54}Zn_{0.46}Se$, MgSe, and $Cd_{0.88}Zn_{0.12}Te$.

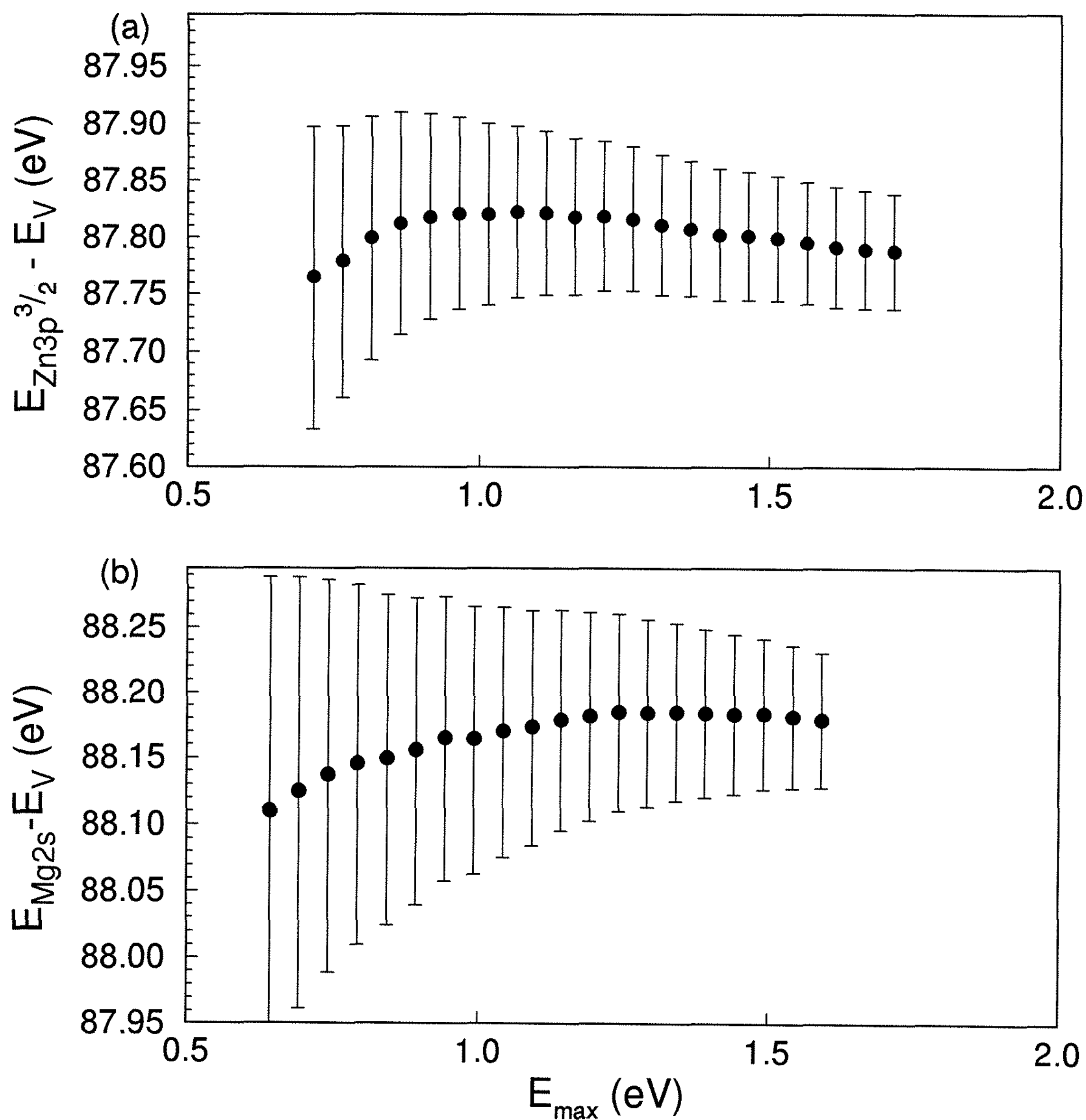

Figure 3.5: Core level to VBM separation as function of the maximum binding energy of the fitting interval for (a) $Cd_{0.88}Zn_{0.12}Te$and (b) MgTe. Low variance in the energy separations indicates accurate modeling of the experimental VBDOS.

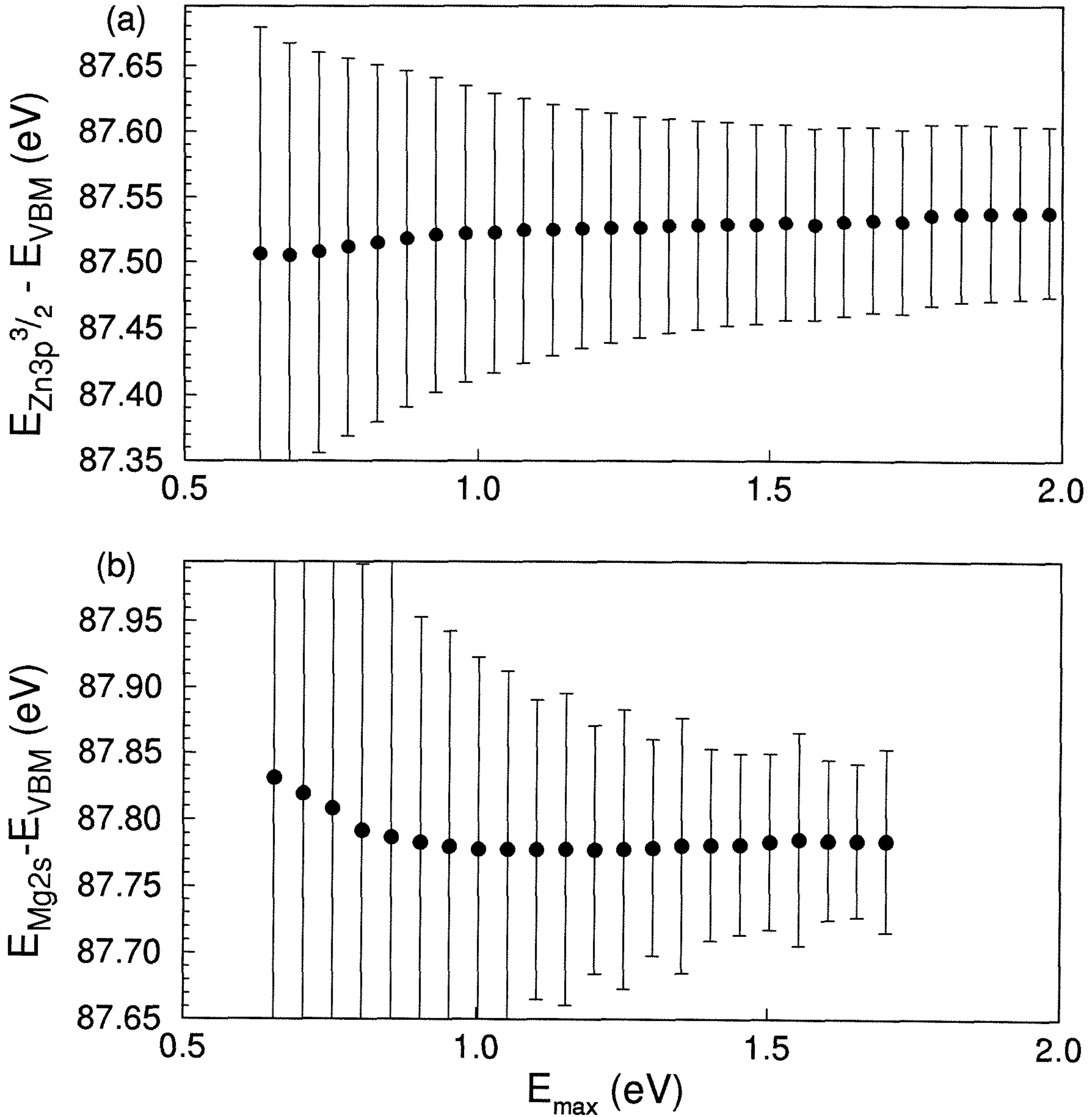

Figure 3.6: Core level to VBM separation as function of the maximum binding energy of the fitting interval for (a) $Cd_{0.54}Zn_{0.46}Se$and (b) MgSe. Low variance in the energy separations indicates accurate modeling of the experimental VBDOS.

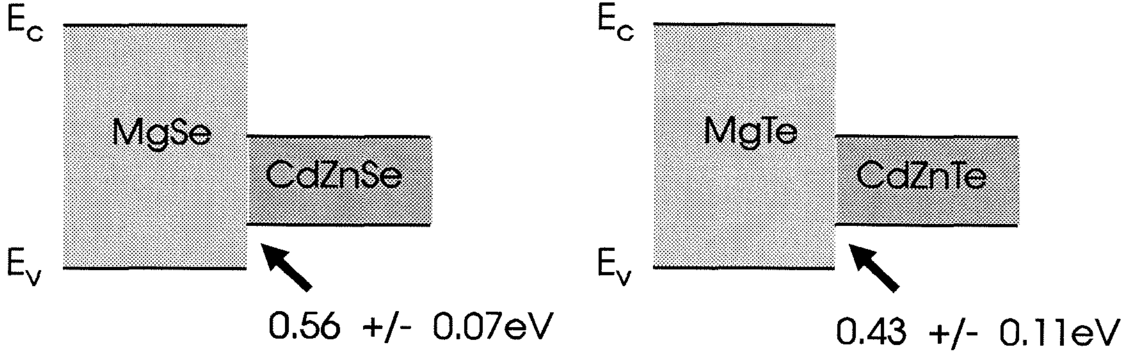

Figure 3.7: MgSe/$Cd_{0.54}Zn_{0.46}Se$ and MgTe/$Cd_{0.88}Zn_{0.12}Te$ valence band offsets measured using XPS. Bandgaps and offsets are not drawn to scale.

3.4 Results and Discussion

3.4.1 MgSe/$Cd_{0.54}Zn_{0.46}Se$ Valence Band Offset

The average results from the XPS measurements of the MgSe/$Cd_{0.54}Zn_{0.46}Se$ valence band offset are $(E_{Zn\ 3p\ 3/2} - E_{v(CdZnSe)}) = 87.52 \pm 0.04$ eV, $(E_{Mg\ 2s} - E_{v(MgSe)}) = 87.76 \pm 0.04$ eV, and $(E_{Zn\ 3p\ 3/2} - E_{Mg\ 2s}) = 0.80 \pm 0.04$ eV. From eq. (1) we obtain an average MgSe/$Cd_{0.54}Zn_{0.46}Se$ valence band offset of 0.56 ± 0.07 eV with the valence band edge of MgSe below that of $Cd_{0.54}Zn_{0.46}Se$ as shown schematically in Figure 3.7. This result has the same sign for the valence band offset as predicted by recent calculations [10]. This also deviates from the common anion rule in the same direction and with the same order of magnitude as the AlAs/GaAs system. Since both Mg and Al are third row elements in the periodic table and have unoccupied *d* orbitals, this supports the importance of including the repelling effects of cation *d* orbitals on the valence band edge in band offset predictions for common anion systems.

To apply the results of this band offset measurement to the design of current II-VI light emitters requires that we estimate the $Zn_{1-x}Mg_xS_ySe_{1-y}/ZnS_{1-z}Se_z$ and $Mg_xCd_{1-x}Se$/CdSe band offsets based on our new results. Using the

ZnSe/ZnS band offset obtained from Ref. [23], assuming a linear dependence of the band offset on composition, and neglecting strain effects, we estimate the $Zn_{0.79}Mg_{0.21}S_{0.3}Se_{0.7}/ZnS_{0.06}Se_{0.94}$ valence band offset to be roughly 0.29 eV versus 0.19 eV obtained using the common anion rule. The corresponding conduction band offsets are 0.04 eV and 0.14 eV respectively. These quantities are approximate; however, the qualitative trend indicates that the Mg and S concentrations in the $Zn_{1-x}Mg_xS_ySe_{1-y}$ layers may need to be increased in the LD design for adequate electron confinement, especially if the wavelength of light emission is extended further into the blue. Another important impact of this measurement is that we now know that both Mg and S pull down the valence band edge when added to ZnSe. Since p-type dopability tends to decrease for semiconductors with lower valence band edges, this would suggest that p-type doping of $Zn_{1-x}Mg_xS_ySe_{1-y}$ will be increasingly difficult as more Mg and S are added to increase the bandgap. This effect has already been observed in the form of compensation in nitrogen doped $Zn_{1-x}Mg_xS_ySe_{1-y}$ [24, 25], although the mechanism responsible for the compensation was attributed to impurities in the first of these studies. Our results also indicate that the Mg concentration in the $Mg_xCd_{1-x}Se$ layer for the graded electron injector device should be increased for efficient carrier injection; however, the exact composition will depend on the MgSe bandgap. Using the results presented in Chapter 4, the desired $Mg_xCd_{1-x}Se$ composition at the Se/Te interface is roughly 70% Mg and 30% Cd.

3.4.2 $MgTe/Cd_{0.88}Zn_{0.12}Te$ Valence Band Offset

The average results from the XPS measurements of the $MgTe/Cd_{0.88}Zn_{0.12}Te$ valence band offset are $(E_{Zn\ 3p\ 3/2} - E_{v(CdZnTe)}) = 87.80 \pm 0.04$ eV, $(E_{Mg\ 2s} - E_{v(MgTe)}) = 88.16 \pm 0.05$ eV, and $(E_{Zn\ 3p\ 3/2} - E_{Mg\ 2s}) = 0.79 \pm 0.09$ eV. From eq. (1) we obtain an average $MgTe/Cd_{0.88}Zn_{0.12}Te$ valence band offset of 0.43 ± 0.11 eV with the valence band edge of MgTe below that of $Cd_{0.88}Zn_{0.12}Te$ as shown

schematically in Figure 3.7. Again, this value deviates from the common anion rule in the same direction as in the AlAs/GaAs system, which supports the hypothesis of Wei and Zunger [13].

Since the addition of Mg to ZnTe pulls down the valence band edge, this result is consistent with experimental observations of enhanced compensation in phosphorus doped $Mg_yZn_{1-y}Te$ [26]. The impact of this on the graded electron injector devices is minimal as long as the deviation from the common anion rule is accounted for in the design. As was shown in Chapter 2, a small valence band offset between $Mg_yZn_{1-y}Te$ and ZnTe will not affect device performance as long as the confining $Mg_yZn_{1-y}Te$ layers are graded to allow holes to flow over the $Mg_yZn_{1-y}Te$ barriers.

3.5 Summary

We have used XPS to measure the valence band offset of the lattice matched $MgSe/Cd_{0.54}Zn_{0.46}Se$ and $MgTe/Cd_{0.88}Zn_{0.12}Te$ heterojunctions. The measured valence band offsets were 0.56 ± 0.07 eV and 0.43 ± 0.11 eV respectively, with the valence band edge of MgSe below that of $Cd_{0.54}Zn_{0.46}Se$, and the valence band edge of MgTe below that of $Cd_{0.88}Zn_{0.12}Te$. Both of these values deviate significantly from the common anion rule and support the importance of cation d orbitals in valence band offset predictions for common anion heterojunctions. Also, the measured $MgSe/Cd_{0.54}Zn_{0.46}Se$ valence band offset agrees favorably with trends predicted in recent calculations [10].

Our measured valence band offset indicates that the Mg and S concentrations in $Zn_{1-x}Mg_xS_ySe_{1-y}$ cladding layers may need to be higher than previously thought for adequate electron carrier confinement, particularly as the emission wavelength is shortened. The p-type dopability of these layers is also expected to decrease due to the pulling down of the valence band edge with the addition of Mg and S. This may be a limiting factor on the wavelength of light emission for the LD

structures incorporating $Zn_{1-x}Mg_xS_ySe_{1-y}$ layers due to high series resistance. For graded electron injector devices, the Mg concentration in the $Mg_xCd_{1-x}Se$ grading layers may need to be increased for efficient electron injection into the Te-based layers, depending on the bandgap of MgSe assumed. Using the value from Chapter 4, $\sim 70\%$ Mg is required at the Se/Te interface in these structures. Finally, $Mg_yZn_{1-y}Te$ confining layers will need to be graded to facilitate hole transport over the $Mg_yZn_{1-y}Te$ layers; however, this should not significantly affect device performance.

Bibliography

[1] M.A. Haase, J. Qiu, J.M. DePuydt, and H. Cheng, *Appl. Phys. Lett.* **59**, 1272 (1991).

[2] H. Okuyama, K. Nakano, T. Miyajima, and K. Akimoto, Japan J. Appl. Phys. 30, L1620 (1991).

[3] H. Okuyama, T. Miyajima, Y. Morinaga, F. Hiei, M. Ozawa, and K. Akimoto, Electron. Letters 28, 1798 (1992).

[4] J.M. Gaines, R.R. Drenten, K.W. Haberern, T. Marshall, P. Mensz, and J. Petruzzello, *Appl. Phys. Lett.* **62**, 2462 (1993).

[5] Sony results in plenary talk by D. Olego at the 1994 Device Research Conference in Boulder, CO.

[6] M.C. Phillips, M.W. Wang, J.F. Swenberg, J.O. McCaldin, and T.C. McGill, *Appl. Phys. Lett.* **61**, 1962 (1992).

[7] J.F. Swenberg, M.C. Phillips, M.W. Wang, J.O. McCaldin, and T.C. McGill, *J. Cryst. Growth* **138**, 692 (1994).

[8] A. Waag, H. Heinke, S. Scholl, C.R. Becker, and G. Landwehr, *J. Cryst. Growth* **131**, 607 (1993).

[9] M.W. Wang, M.C. Phillips, J.F. Swenberg, E.T. Yu, J.O. McCaldin, and T.C. McGill, *J. Appl. Phys.* **73**, 4660 (1993).

[10] T. Nakayama, *Jpn. J. Appl. Phys.* **33**, L211 (1994).

[11] Y. Morinaga, H. Okuyama, and K. Akimoto, Japan J. Appl. Phys. 32, 678 (1993).

[12] J.O. McCaldin, T.C. McGill, and C.A. Mead, *Phys. Rev. Lett.* **36**, 56 (1976).

[13] S. Wei and A. Zunger, *Phys. Rev. Lett.* **59**, 144 (1987).

[14] E.A. Kraut, R.W. Grant, J.R. Waldrop, and S.P. Kowalczyk, *Phys. Rev. B* **28**, 1965 (1983).

[15] M.L. Cohen and T.K. Bergstresser, *Phys. Rev.* **141**, 789 (1966).

[16] L.R. Saravia and D. Brust, *Phys. Rev.* **176**, 915 (1968).

[17] J.R. Chelikowsky and M.L. Cohen, *Phys. Rev. B* **14**, 556 (1976).

[18] J. Chelikowsky, D.J. Chadi, and M.L. Cohen, *Phys. Rev. B* **8**, 2786 (1973).

[19] F. Herman and S. Skillman, *Atomic Structure Calculations* (Prentice-Hall, Englewood Cliffs, NJ, 1963).

[20] F. Herman, C.D. Kuglin, K.F. Cuff, and R.L. Kortum, *Phys. Rev. Lett.* **11**, 541 (1963).

[21] W.A. Harrison, *J. Vac. Sci. Technol.* **14**, 1016 (1977).

[22] M.D. Jaffe and J. Singh, *Solid State Commun.* **62**, 399 (1987).

[23] K. Shahzad, D.J. Olego, and C.G. Van de Walle, *Phys. Rev. B* **38**, 1417 (1988).

[24] P.M. Mensz, S. Herko, K.W. Haberern, J. Gaines, and C. Ponzoni, *Appl. Phys. Lett.* **63**, 2800 (1993).

[25] H. Okuyama, Y. Kishita, T. Miyajima, A. Ishibashi, and K. Akimoto, *Appl. Phys. Lett.* **64**, 904 (1994).

[26] K. Somogyi, J. Chevallier, J.F. Rommeluere, J. Marine, and B. Schaub, *IEEE Trans. Electron Devices* **26**, 1198 (1979).

Chapter 4

Status of the Graded Electron Injector Project

4.1 Introduction and Outline

In this chapter, brief descriptions of materials characterization results and recent graded electron injector device performance characteristics are presented. These results are presented because of their importance to understanding both the current status of the graded electron injector project as well as some of the important issues that still need to be addressed.

XRD is used to study the long range structural quality of the devices, while TEM probes the structural quality on a more local scale. SIMS, a chemical analysis technique, is utilized to investigate chemical impurities in the epilayers. Current-voltage and electroluminescence (EL) characteristics of the graded electron injector LED structures are presented. The external quantum efficiency of recent devices and possible approaches to improving light extraction and internal quantum efficiencies are given. Finally, the reliability of the LED structures is discussed. It should be emphasized here that the TEM, SIMS and EL studies were all performed by other researchers [1].

4.2 Material Characterization

4.2.1 XRD

XRD is a standard tool for characterizing the long range structural quality of semiconductor layers. The XRD data shown in Figure 4.1 was acquired with a Philips' Materials Research Diffractometer equipped with a four-crystal Ge-monochrometer in the (220) reflection setting. In this setting, the Cu $K\alpha_1$ ($\lambda = 1.54056\,\text{Å}$) X-ray line has a divergence of ~ 12 arc seconds.

Figure 4.1(a) shows a typical XRD $\Omega/2\theta$ scan for the graded electron injector structure consisting of a GaSb substrate, a ~ 1 μm ZnTe buffer layer, a 300-600 Å graded $Mg_xCd_{1-x}Se$ layer and a $\sim$ 300 Å CdSe layer at the sample surface. The XRD FWHM for the GaSb and the ZnTe layers are 25 and 39 arc seconds respectively. The CdSe layer has an expectedly very broad peak (~ 6 arc minutes) due to the thinness of the layer, and the peak corresponding to the thin graded $Mg_xCd_{1-x}Se$ layer is too broad and weak to be discernible above the noise. The $\Omega/2\theta$ plot shown in Figure 4.1(a) is essentially what one would expect for a graded injector device with good structural characteristics.

In contrast, Figure 4.1(b) shows a XRD $\Omega/2\theta$ scan of a very similar structure grown under nominally the same growth conditions. It can be seen that the FWHM of all of the layers are increased significantly, with a corresponding loss of signal intensity. In fact, the CdSe peak is no longer discernible. The structural quality of this device is very poor as characterized by XRD.

Interestingly, the device with the poor structural quality as measured by XRD had the highest external quantum efficiency measured to date, while the structural with the excellent structural quality had relatively poor external quantum efficiency. In fact, initial analysis of the XRD data compiled on the graded injector devices shows no correlation between structural quality LED performance. These XRD results imply that other factors unrelated to the long range structural quality

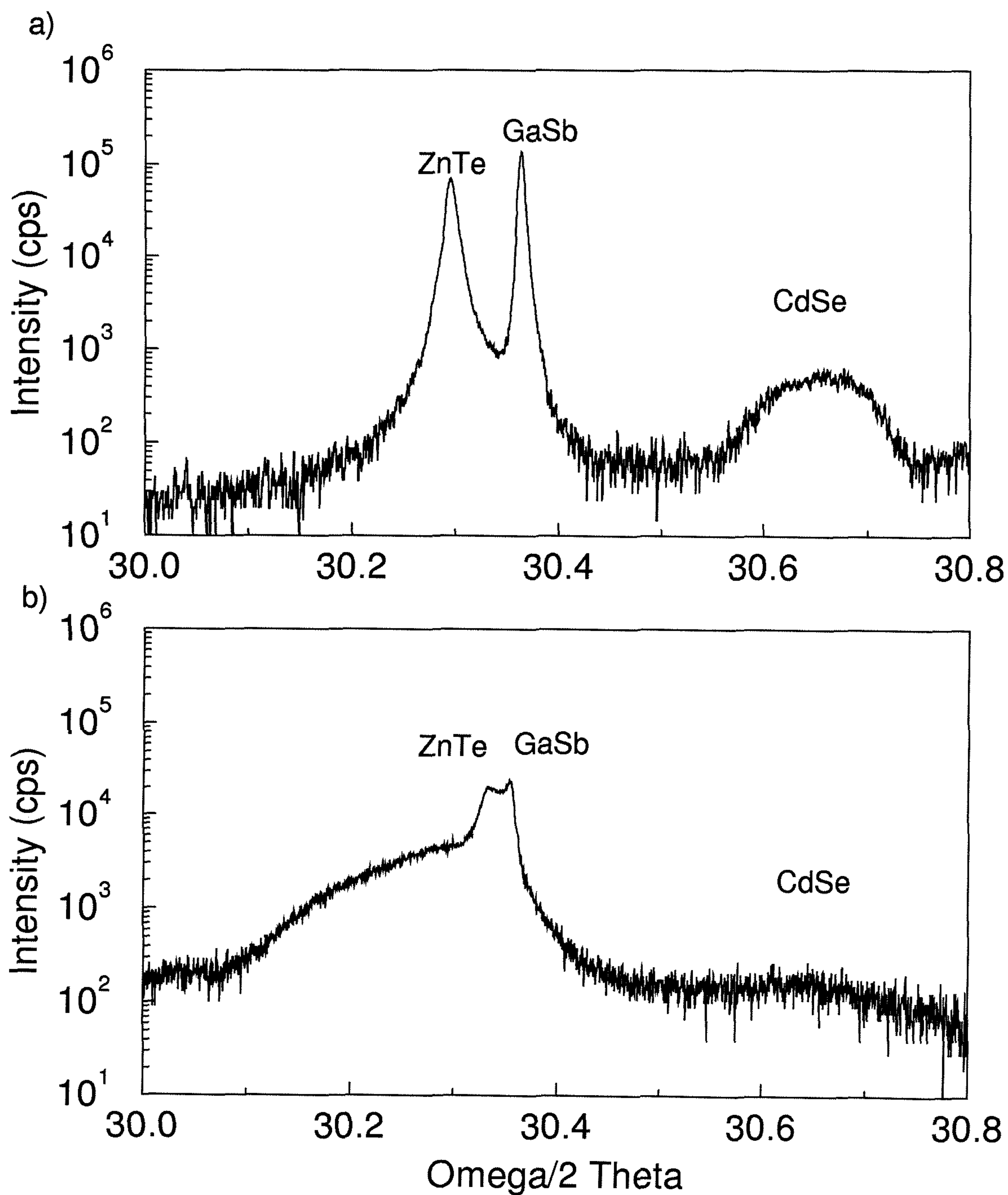

Figure 4.1: XRD data for graded electron injector device. Representative data for a structure with (a) desirable XRD characteristics and (b) poor XRD characteristics. No correlation between XRD linewidths and LED performance was observed.

of the films are presently limiting the performance of the LEDs.

Graded injector LEDs with good long range structural quality as measured by XRD have been reproduced, although not consistently. More importantly, LEDs that simultaneously exhibit both excellent XRD characteristics and device properties have not been achieved.

4.2.2 TEM

TEM is used to study the structural quality of the graded electron injector structures on a more local scale. The TEM image shown in Figure 4.2 was acquired with a Philips' EM430 microscope using 300 keV electrons. Ion milling of the samples was performed at low incident angles using 3-4 keV Ar ions. The low ion energy was used in order to minimize damage to the fragile II-VI materials.

Figure 4.2 shows a representative TEM image of the top ~1500 Å of a graded electron injector LED structure. The growth is in the [001] direction and the [110] direction is perpendicular to plane of the page. The ZnTe/$Mg_xCd_{1-x}Se$ interface is readily apparent, while the exact location of the CdSe/$Mg_xCd_{1-x}Se$ interface is not clear, since the Mg concentration is graded down to less than 10% at that interface.

The two main features relevant in Figure 4.2 are the high density of defects and the total thickness of the Se layers. Two defects are indicated by the arrows labeled A and B. The defects originate from the ZnTe/$Mg_xCd_{1-x}Se$ interface and often extend all the way through to the sample surface (arrow B). The intersection of the defects with the (110) milled surface forms an angle of roughly 55 degrees, indicating that the defects are likely to be stacking faults in the [111] direction originating from point defects at the ZnTe/$Mg_xCd_{1-x}Se$ interface. Although it is difficult to properly determine defect densities from cross-sectional TEM images, a *very* rough estimate using 4 defects in a 1500 Å by ~500 Å (thickness of milled region) gives a defect density of greater than 5×10^{10} cm^{-2}. This is well above the

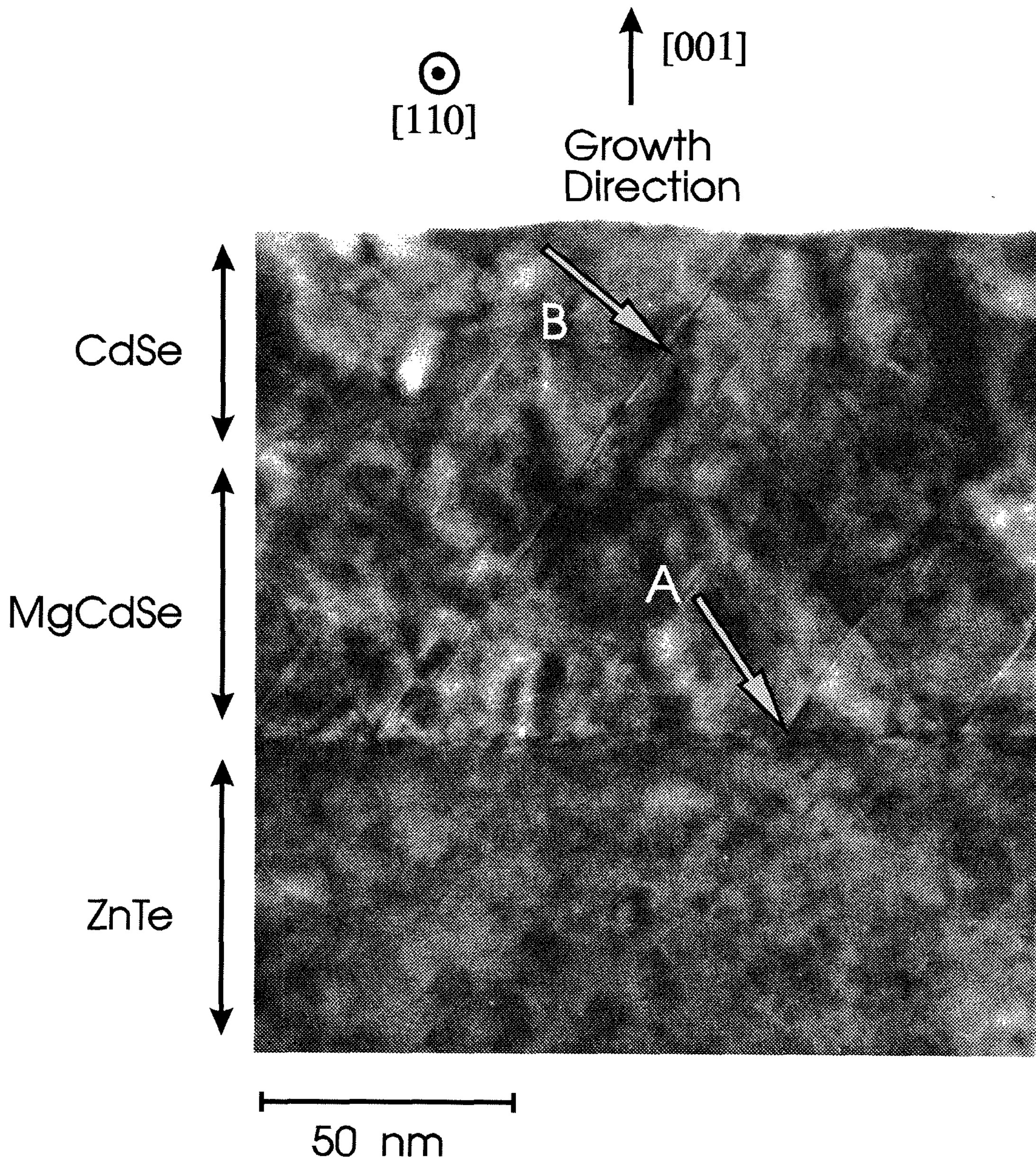

Figure 4.2: TEM image of a graded electron injector device. Growth direction is indicated by an arrow in the [001] direction. The [110] direction is perpendicular to plane of the page. Two of the defects are indicated by arrows A and B.

desired defect density of $< 10^4 - 10^5$ cm^{-2}.

In addition to the high defect density, the total thickness of the CdSe and $Mg_xCd_{1-x}Se$ layers is significantly larger than expected (1000 Å instead of 600 Å): this is most likely due to a faster $Mg_xCd_{1-x}Se$ growth rate compared to the well-calibrated growth rates for CdSe and ZnTe. The additional 300-400 Å of thickness contributes significantly to the defect density, since $Mg_xCd_{1-x}Se$ has a lattice mismatch to ZnTe of 0.4% to 3.5% depending on the Mg concentration. Ideally, the thickness of the graded region should remain below $\sim$300 Å to keep the structure below the critical thickness. Thus, reducing the thickness of the lattice-mismatched $Mg_xCd_{1-x}Se$ region could significantly reduce the defect density in the LED structures. Currently, the grading in the $Mg_xCd_{1-x}Se$ region is implemented by shutting off power to the Mg cell shortly before growth of the Se layers, so the thickness of the graded region is determined by the cooling time of the Mg source cell. To reduce the thickness of the graded region requires implementation of a valved Mg source, a shuttering scheme for the Mg source, or a small Mg cell with fast thermal time constant.

4.2.3 SIMS

Secondary ion mass spectrometry (SIMS) is often used for studying impurities because of its excellent chemical sensitivity (parts per million to parts per billion) and reasonably good depth resolution (> few nm). The underlying principle of SIMS is to chemically profile a sample by performing mass spectrometry on ions that have been sputtered from the sample surface. More details on the SIMS technique are given in Chapter 6.

The SIMS data shown in Figure 4.3 was taken by researchers at Charles Evans and Associates using 14.5 keV Cs^+ ion bombardment for the C, O and Sb profiles, and 8.0 keV O_2^+ ion bombardment for the As profile. It should be noted that Al, Ga, In and N were also profiled with roughly the same results, but were not shown

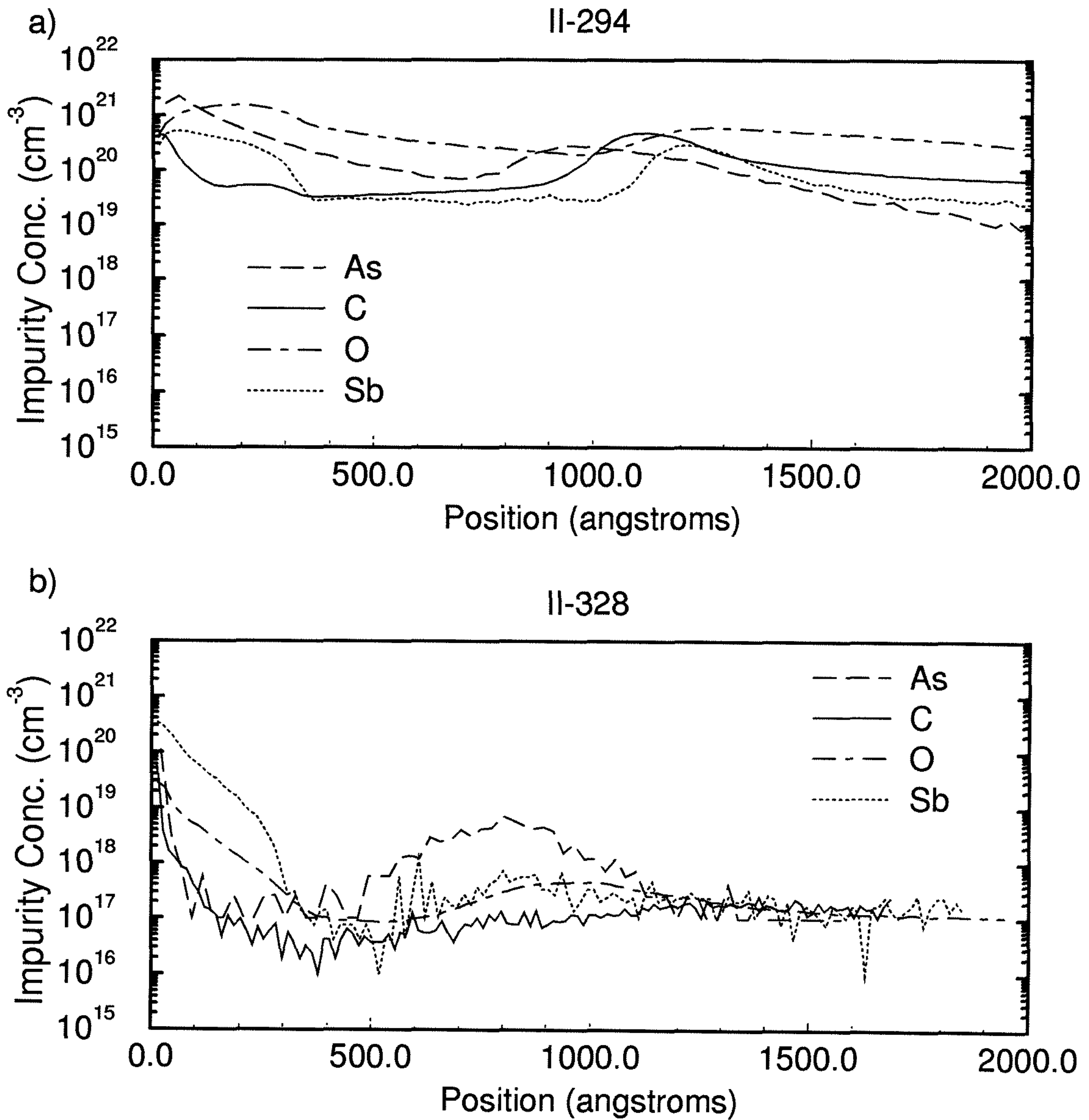

Figure 4.3: Representative SIMS impurity profiles for an LED structure with (a) high impurity concentrations, and (b) low impurity concentrations. No correlation between impurity concentration and LED performance was observed.

for clarity purposes. The sputtering was performed over a 350 μm $\times$ 350 μm area, while the detected secondary ions were extracted from a 85 μm diameter area in the center of the sputtered crater.

The first thing to notice in Figure 4.3 is that the impurity concentration is significantly reduced in the sample shown in Figure 4.3(b) compared to sample shown in Figure 4.3(a). Both samples are graded injector structures as described in Section 4.2.1. The sample surface corresponds to a position of 0 Å on the horizontal axis. Similar to what occurred for the XRD data, no correlation between impurity concentration and electroluminescence characteristics was observed. In fact, despite the high impurity concentration in the sample shown in Figure 4.3(a), it had much better electroluminescence properties than the sample shown in Figure 4.3(b), which luminesced primarily in the red. Thus, at present it is believed that some mechanism other than impurity concentration is the limiting factor in determining the electroluminescence properties of the LEDs.

A final observation regarding Figure 4.3 is that the impurity profiles for both plots peak near the graded region ($\sim$ 1000 Å). This could be due either to a matrix effect in the graded region or to the gettering properties of Mg. So far, no correlation has been observed between the impurity concentration within the graded region and LED performance; however, this could be because other factors are still limiting device performance.

4.3 Device Performance

4.3.1 Current-Voltage Characteristics

Figure 4.4 shows the current-voltage characteristics for a typical graded electron injector LED using both linear and logarithmic scales for the current density. The current-voltage characteristics for the devices are excellent, with almost no reverse bias leakage current and a low forward bias turn-on voltage, indicative of good

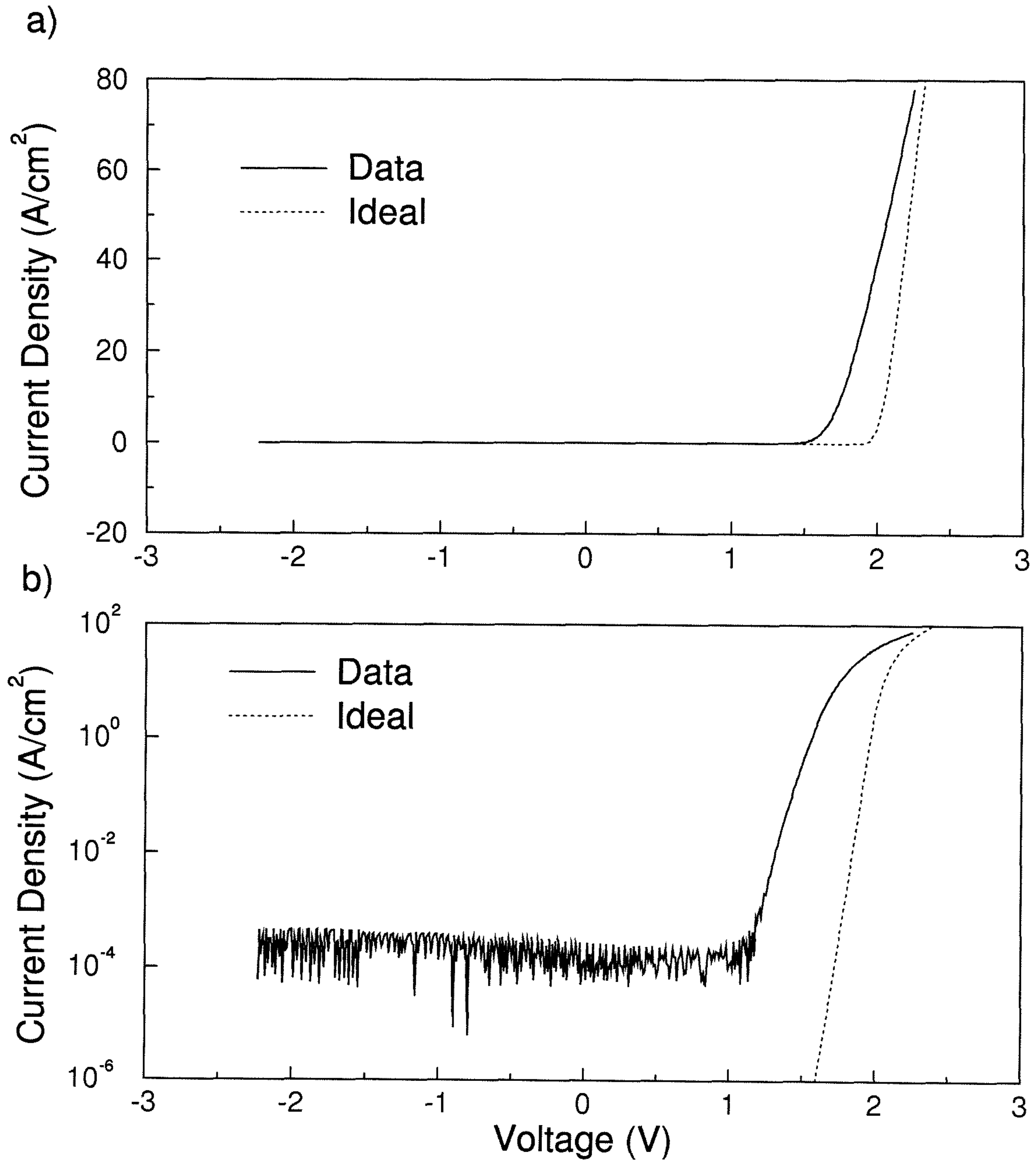

Figure 4.4: Experimental (solid) and calculated (dashed) current-voltage characteristics for a graded injector device, plotted on (a) linear and (b) logarithmic scales. Deviation of the data from the ideal, calculated values is due to leakiness in the LED structure.

ohmic contacts and a reasonably low series resistance. This is expected, given that the underlying principle of the graded electron injector concept is to avoid doping and contacting problems by using a heterojunction design.

The current-voltage characteristics shown in Figure 4.4 are comparable to the best obtained in the ZnSe-based material system [2], and the only deviation from an ideal current-voltage curve is that the current onset occurs at a slightly lower voltage than in an ideal structure, as indicated by the dotted lines. This is most likely due to leakage current caused by non-optimal grading of the $Mg_xCd_{1-x}Se$ layer and could probably be remedied by better control of the graded region, as will be discussed in more detail elsewhere [3].

4.3.2 Electroluminescence

Figure 4.5 shows a representative electroluminescence (EL) spectra from a graded electron injector structure biased at 2.8 V. The dominant peak at ~ 2.23 eV and the absence of a peak at ~ 1.74 eV indicate that electrons have been successfully injected into the ZnTe layer while holes have been blocked from entering the CdSe layer. This is further evidence for the successful implementation of the graded electron injector scheme. The feature at ~ 1.95 eV is present to some extent in all of the graded injector devices fabricated thus far. The intensity of this peak relative to the ZnTe peak varies from sample to sample even when grown under nominally identical conditions. Depending on the relative intensities of the 1.95 eV and 2.23 eV peaks, the EL can appear yellow or even red, when the intensity of the 1.95 eV peak is large enough. It should be noted that the low-energy peak is also observed in photoluminescence (PL) studies. The source of this low energy EL/PL peak is currently not known and is still under investigation.

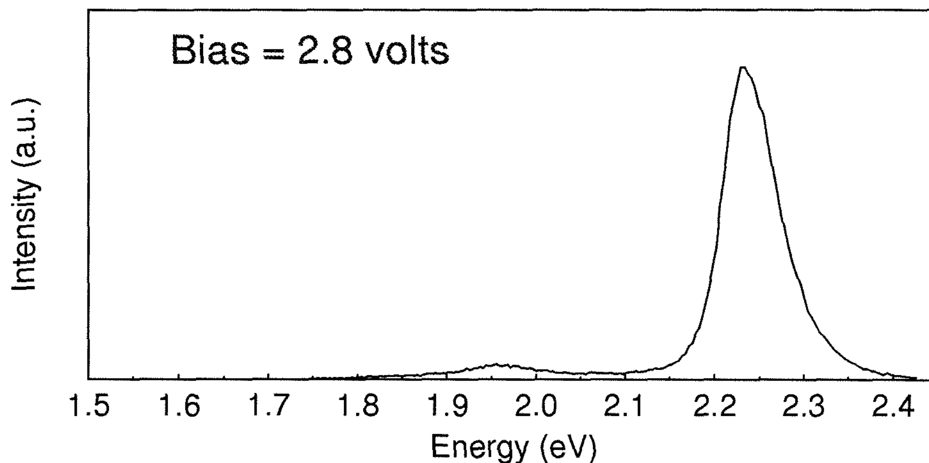

Figure 4.5: Electroluminescence data from a graded electron injector LED structure.

4.3.3 External Quantum Efficiency

The external quantum efficiency of the graded electron injector LEDs is still not very high, with the best efficiency to date being 0.007%. There are a number of reasons for this rather low value, the first of which is related to extraction of the light radiated from the ZnTe active region. It has been shown that the external quantum efficiency of an LED can be drastically affected by the efficiency of the light extraction [4, 5]. Figure 4.6 shows a schematic view of the graded injector device and some possible contacting schemes to the CdSe. Since the CdSe cannot be grown very thick, due to strain and absorption considerations, a contacting scheme must be devised which spreads current over the entire surface of the mesa while still allowing radiated light to escape.

The first contacting scheme used was a thick Zn cap. During the etch step of the processing, the Zn cap etched at a much faster rate than the II-VI materials, resulting in a narrow region around the edge of the device where light could escape. This procedure was not ideal, as only a small fraction of the radiated light was extracted from the device. Another approach used a thick Au/Ge pad to contact

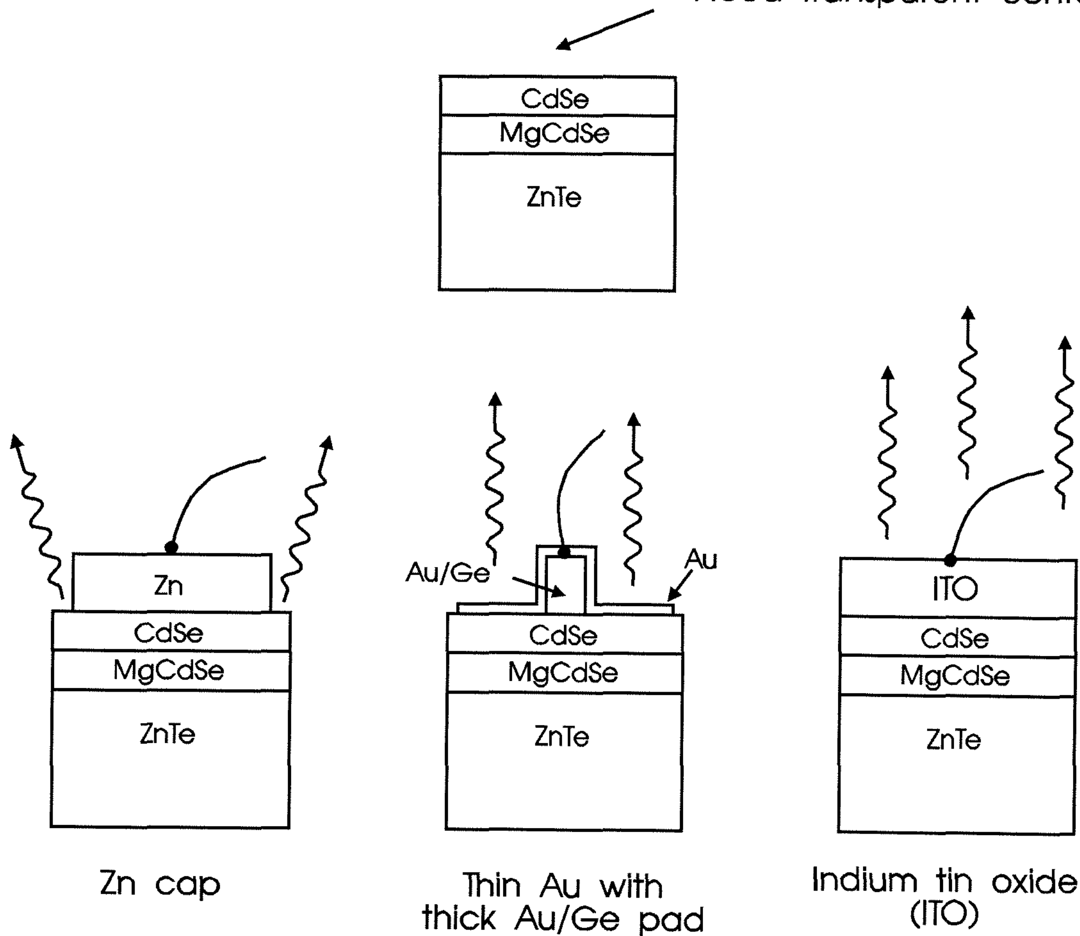

Figure 4.6: Schematic diagrams of the graded electron injector device (top) and some possible contacting schemes (bottom). The Zn cap (left) allows light extraction from only a thin region at the edge of the mesa. The thin Au and thick Au/Ge contacting scheme (center) improves on the Zn cap, and the ITO contacting scheme (right) should result in even better light extraction.

the CdSe layer and a thin Au layer (a few 100 Å) to uniformly spread the current over the surface of the mesa. This approach is better than the Zn cap in that less of the mesa surface is light-absorbing; however, it is still not ideal since the Au/Ge is completely opaque and the thin Au layer is partially absorbing and not very robust. This is the method used in present devices. A better approach being investigated would be to use indium tin oxide (ITO), which is both transparent and conductive. This scheme would significantly improve external quantum efficiencies by allowing light to escape over the entire top surface of the mesa without significant absorption.

Another light extraction issue is the substrate. The GaSb substrates used in present devices completely absorb any light emitted in the downward direction. If ZnTe substrates of sufficient quality were available, the external quantum efficiency would be further improved since light emitted into the substrate would not be absorbed.

Another component of the external quantum efficiency is the actual efficiency of radiative recombination at the desired wavelength. Mechanisms such as non-radiative recombination via leakage current through the graded region could considerably lower the overall external quantum efficiency. Thus, it is important to optimize the $Mg_xCd_{1-x}Se$ graded region so as to reduce leakage current to a minimum. The thickness of the ZnTe active region also plays an important role in the radiative recombination efficiency. If this layer is thinner than the electron diffusion length, a significant fraction of the carriers will reach the GaSb buffer layer before recombining, lowering the external quantum efficiency. One way to alleviate this problem is to use QWs or confining layers (see Chapter 2) to trap the carriers and increase the radiative recombination efficiency. This is currently being investigated.

Thus, the external quantum efficiency of the graded electron injector LEDs is currently not very high. However, a number of approaches are available to increase both the extraction and the radiative recombination efficiencies, thereby increasing

the overall external quantum efficiency.

4.3.4 Device Degradation Studies

The most important issue in determining the feasibility of LEDs and LDs based on II-VI semiconductors is that of device reliability. II-VI semiconductors materials are well known for their softness, especially when compared to the very rugged nitrides. Preliminary studies of LEDs based on the graded electron injector design have shown evidence for long device lifetimes, but in general the device lifetimes have been poor.

Figure 4.7 shows plots of normalized photodiode current versus time for two separate devices. Figure 4.7(a) shows the lifetime characteristics for an early device grown on a ZnTe substrate with undoped ZnTe epilayers. The current-voltage characteristics and efficiencies for this device were very poor; however, the device reliability was relatively good, with less than 50% degradation after $\sim$1500 hours. After subsequent implementation of p-type doping of ZnTe, higher purity Mg and better quality substrates (GaSb), the device lifetimes are as shown in Figure 4.7(b). Despite much improved external quantum efficiencies and current-voltage characteristics, the device lifetimes are much poorer than in earlier devices. Notice the change in scale for the time-axes in the two plots.

The cause for the reduction in device lifetimes is still uncertain. One possibility is that it is related to the N-doping of the ZnTe. Another possibility is that growing on GaSb instead of ZnTe substrates results in a higher defect density which will reduce device lifetimes. These and other explanations are still under investigation.

4.4 Summary

In conclusion, successful implementation of the graded electron injector scheme has been demonstrated. The current-voltage characteristics show diode-like behavior

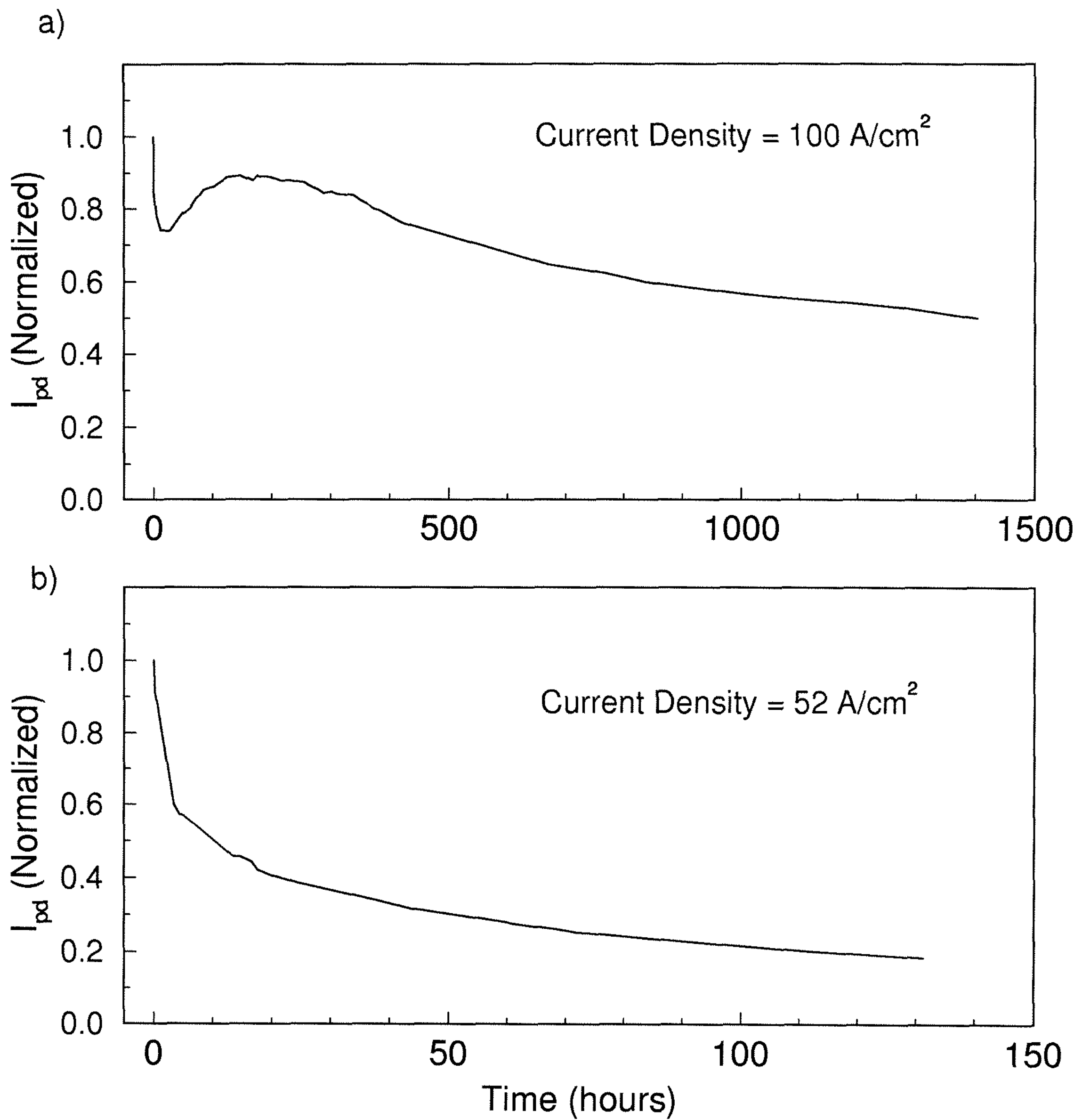

Figure 4.7: Device lifetime measurements for two devices: (a) an early device grown on a ZnTe substrate without p-type doping of ZnTe and (b) a more recent device grown on a GaSb substrate with N-doping of the p-ZnTe. Note the difference in scale for the time axes.

with low turn-on voltages and low series resistances. Also, green luminescence from radiative recombination within the ZnTe layer shows that the graded $Mg_xCd_{1-x}Se$ layer is functioning properly.

However, a number of issues still need to be addressed in order to achieve high-performance LEDs based on the graded electron injector design. These include structural quality, spectral purity, external quantum efficiency and device lifetimes. Poor structural quality of the devices was observed in the form of high defect densities in the TEM data and large FWHMs in some of the XRD data. SIMS analysis shows high impurity concentrations in some of the devices. Although no correlation was observed between LED performance and defect densities, XRD FWHM and impurity concentrations, reduction of these quantities should eventually improve overall device performance.

Spectral purity problems were indicated by the presence of a variable intensity, low energy luminescence peak observed in the EL spectra. This peak must be eliminated in order to consistently achieve high-performance LEDs. The external quantum efficiency is still not optimal, and a number of improvements on the present LED design should allow for much higher efficiencies. The issue of device lifetimes is another issue critical to the long term feasibility of the graded electron injector device. Present device lifetimes are poor, and it remains to be determined whether this is a consequence of the N-doping of ZnTe, due to lack of control of the graded region, or a problem intrinsic to the relatively soft II-VI semiconductors.

In conclusion, the graded electron injector LED design shows promising results, but a number of important issues must be addressed before the long term feasibility of this approach can be demonstrated.

Bibliography

[1] TEM studies performed by Carol Garland, SIMS studies performed by researchers at Charles Evans and Associates and EL studies performed by Johanes Swenberg.

[2] D.B. Eason, Z. Yu, C. Boney, J. Ren, L.E. Churchill, J.W. Cook, Jr., J.F. Schetzina, and N.A. El-Masry, to be published in *J. Cryst. Growth* (1994).

[3] J.F. Swenberg, Ph.D. thesis dissertation (1994).

[4] K.H. Huang, J.G. Yu, C.P. Kuo, R.M. Fletcher, T.D. Osentowski, L.J. Stinson, M.G. Craford, and A.S.H. Liao, *Appl. Phys. Lett.* **61**, 1045 (1992).

[5] F.A. Kish, F.M. Steranka, D.C. DeFevere, D.A. Vanderwater, K.G. Park, C.P. Kuo, T.D, Osentowski, M.J. Peanasky, J.G. Yu, R.M. Fletcher, D.A. Steigerwald, M.G. Craford, and V.M. Robbins, *Appl. Phys. Lett.* **64**, 2839 (1994).

Part II

XPS Studies of the Mixed Anion InAs/GaSb Heterointerface

Chapter 5

Surface Exchange Reaction Studies

5.1 Introduction and Outline

The mixed anion arsenide/antimonide system has a number of technologically interesting applications, including InAs/AlSb oscillators operating at frequencies greater than 700 GHz [1], novel InAs/AlSb/GaSb based [2, 3, 4] and InAs/GaSb based [5] tunnel structures and InAs/$Ga_{1-x}In_xSb$ infrared (IR) superlattice (SL) detectors [6, 7]. One of the main problems in growing such devices is controlling the structural and chemical properties of the interface. However, this is very difficult because of the different bond strengths, surface free energies and bond lengths at the interfaces in these systems. As well, III-V structures are typically grown with group V overpressures, since their vapor pressures are much larger than those of the group III elements. For growth of mixed anion structures, this overflux of the group V element becomes a problem and can lead to cross-incorporation of the anion species and variation in interface composition [8]. In IR SL structures cross-incorporation of the anion species can result in shorter carrier lifetimes and poor quality material, while interfacial composition affects the type

and level of background doping as well as the SL bandgap, due to changes in the strain configurations at the interface [9]. Furthermore, the interface composition in the InAs/AlSb system affects the carrier mobility, carrier concentration and the InAs/AlSb valence band offset [10, 11]. Thus, it is important to be able to grow arsenide/antimonide structures with no anion cross-incorporation and with abrupt, composition controllable interfaces. To do this, the detailed mechanisms of the interface formation must be understood.

In this chapter, we use X-ray photoelectron spectroscopy (XPS) and reflection high energy electron diffraction (RHEED) to study interface formation during molecular beam epitaxy (MBE) growth of GaSb/InAs structures. The GaSb/InAs system is more amenable to XPS study than $In_xGa_{1-x}Sb$/InAs due to the presence of unique elements on both sides of the heterojunction. Furthermore, since the problems in controlling arsenide/antimonide interfaces are associated with their mixed anion nature, the results of our study should be extendible to any of the arsenide/antimonide structures described above.

The XPS experiments study the core level peak intensities and binding energy separations as a function of cracker power and soak time. The soaks, or interrupts as they are sometimes called, consist of exposing an InAs or GaSb surface to an Sb or As flux, respectively, and are intended to mimic the soaks used in GaSb/InAs heterostructure growths. The XPS core level peak intensities and binding energy separations are used to determine the extent of the exchange reactions. Results from both As soaks of GaSb surfaces and Sb soaks of InAs surfaces are presented.

RHEED specular streak intensity analysis was also used to monitor the exchange reactions during growth. The advantage of RHEED as a method to characterize these reactions is that it is a real-time, *in situ* measurement. However, it provides only near surface structural information, hence it is necessary to correlate the RHEED data with a chemical analysis technique such as XPS in order to accurately characterize exchange reactions.

In Section 5.2, we describe the MBE growth and the details of the XPS and

RHEED experiments. Section 5.3 contains brief descriptions of the data analysis procedures used. Section 5.4 presents the results from the XPS and RHEED studies. In Section 5.5 we discuss the results and their significance to interface abruptness studies, and Section 5.5 concludes the chapter.

5.2 Experiment

5.2.1 Sample Growth

All of the structures studied here were grown in a Perkin-Elmer Model 430 MBE system equipped with cracked Sb and As sources. Two cracker powers, 80% and 40%, were used to emulate growth systems with and without cracked sources respectively. We refer to the source fluxes by their primary component; Sb_4 and As_4 (uncracked) at 40% cracker power, and Sb_2 and As_2 (cracked) at 80% cracker power. The structures were grown on a number of different (100) substrates (GaAs, n-GaSb, p-GaSb), with no variation in results. Samples were grown on thick stress relaxed GaSb buffer layers at a substrate temperature of $\sim 380\,^{\circ}$C. Multiple samples grown on the same substrate were separated by buffer layers thick enough to prevent detection of underlying layers with XPS. More details of the growth may be found in Ref. [12].

5.2.2 XPS and RHEED Measurements

The XPS measurements were obtained using a Perkin-Elmer Model 5100 analysis system with a monochromatic Al Kα source (hv = 1486.6 eV). All of the samples studied were transferred from the growth chamber to the XPS chamber via an ultrahigh vacuum transfer tube. The base pressure in the XPS chamber was typically ~ 1 to 5×10^{-10} Torr. Care was taken to ensure that the escape orientation of the photoelectrons remained constant from sample to sample to minimize any electron diffraction effects due to the single crystalline nature of the samples. More

details of the XPS experimental setup are given in Section 1.3.4.

The RHEED studies presented here were performed by another researcher. Some details of the RHEED experimental setup are given in Section 1.3.4. More details of the RHEED experiment can be found in Ref. [13]. Briefly, the RHEED pattern on the phosphor screen is acquired using a CCD camera and digitized into a 640 $\times$ 480 array of single-byte data. From this, the streak separation and specular streak intensity can be extracted. In this study, only the specular streak intensity was used to characterize the exchange reactions.

5.3 Data Analysis

Figure 5.1 shows two sample XPS spectra. Figure 5.1 (a) shows a spectrum from an InAs epilayer after exposure to a 15 second Sb_2 soak, and Figure 5.1 (b) shows a spectrum from a GaSb epilayer after exposure to a 240 second As_2 soak. The data analysis for the Sb soaks of InAs surfaces consisted of isolating the Sb $4d$, In $4d$ and As $3d$ core level peaks, performing an integrated background subtraction on each peak, fitting these peaks to Voigt functions and finally determining the corresponding integrated intensities and core level binding energies. From the peak intensities, we were able to estimate the Sb coverage on InAs. A similar procedure was used for analysis of the As soaks of GaSb surfaces, except that the As $3d$, Ga $3d$ and Sb $4d$ peaks were used. To estimate the group V coverage, we used a simple attenuation model based on published effective photoelectron mean free paths (MFPs) [14, 15, 16]. Due to the uncertainty in these MFPs, this procedure cannot be used to determine precise compositions; however, comparisons between samples and qualitative estimates of surface coverage are valid.

Some care must be taken in the data analysis described above. As seen in Figure 5.1(a), some of the XPS features overlap. For example, the In $4d$ plasmon loss tail interferes with the Sb $4d$ peak. To isolate the Sb $4d$ peak, we first fit the In $4d$ peak while constraining the peak shape to that obtained from a bulk InAs

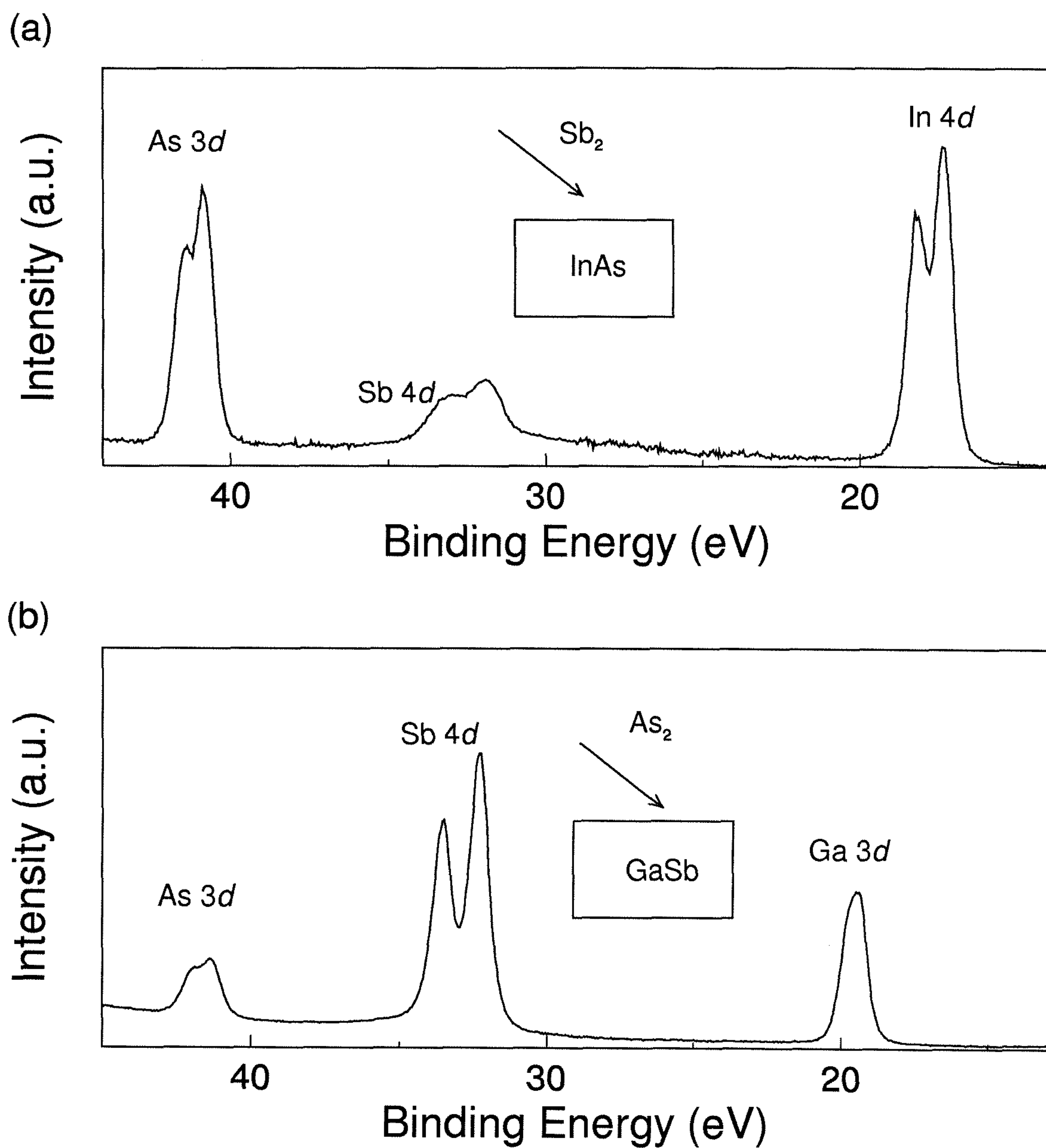

Figure 5.1: XPS binding energy spectra of (a) 15 sec. Sb_2 soak of an InAs surface and (b) 240 sec. As_2 soak of a GaSb surface.

standard. Then, using the same InAs standard, we perform spectrum stripping to remove the In 4*d* loss tail from the Sb 4*d* signal. Figure 5.2 shows a representative Sb 4*d* peak after background subtraction (dots), and the resulting fitted Voigt functions (solid). The dotted lines denoting the individual Sb 4*d* components are discussed below. The Sb 4*d* loss tail was stripped from the As 3*d* peak following the same procedure, using GaSb as the standard from which to obtain the shape of the plasmon loss tail. An analogous procedure was used to isolate the Ga 3*d*, Sb 4*d* and As 3*d* peaks for the spectra obtained from As soaks of GaSb surfaces.

In addition to interferences from overlapping features, chemically shifted components must also be properly accounted for in the analysis. Chemically shifted XPS peaks are important because they are an indication of multiple bonding configurations, and because they can skew measured peak intensities if not properly analyzed. Figure 5.2 shows the Sb 4*d* signal from a sample consisting of a 15 second Sb_2 soak of an InAs surface. The two spin split doublets comprising the Sb 4*d* peak were obtained by stripping off the In 4*d* loss tail, subtracting the integrated background function and fitting the resulting spectra to two Sb 4*d* peaks with their peak shapes constrained to that of Sb 4*d* from a GaSb standard. Only a vertical scale and a binding energy (BE) parameter were allowed to vary for each of these doublets for a total of four parameters. Using this technique, core level binding energy separations and peak intensities on identical samples were typically reproducible to better than $\pm$ 0.03 eV and $\pm 5\%$.

The RHEED data analysis was performed by another researcher, and a detailed explanation can be found in Ref. [13]. Briefly, the RHEED specular streak intensity was monitored in real time as a function of soak time and cracker power. Figure 1.11 in Chapter 1 shows a schematic diagram of the experimental setup used to extract the RHEED specular streak intensity. Upon initiation of an Sb soak, the specular streak intensity decreases and then recovers with a characteristic time dependent on the Sb source cracker power. By studying the time-dependency of the RHEED intensity and comparing it with the XPS results, we hope to infer a

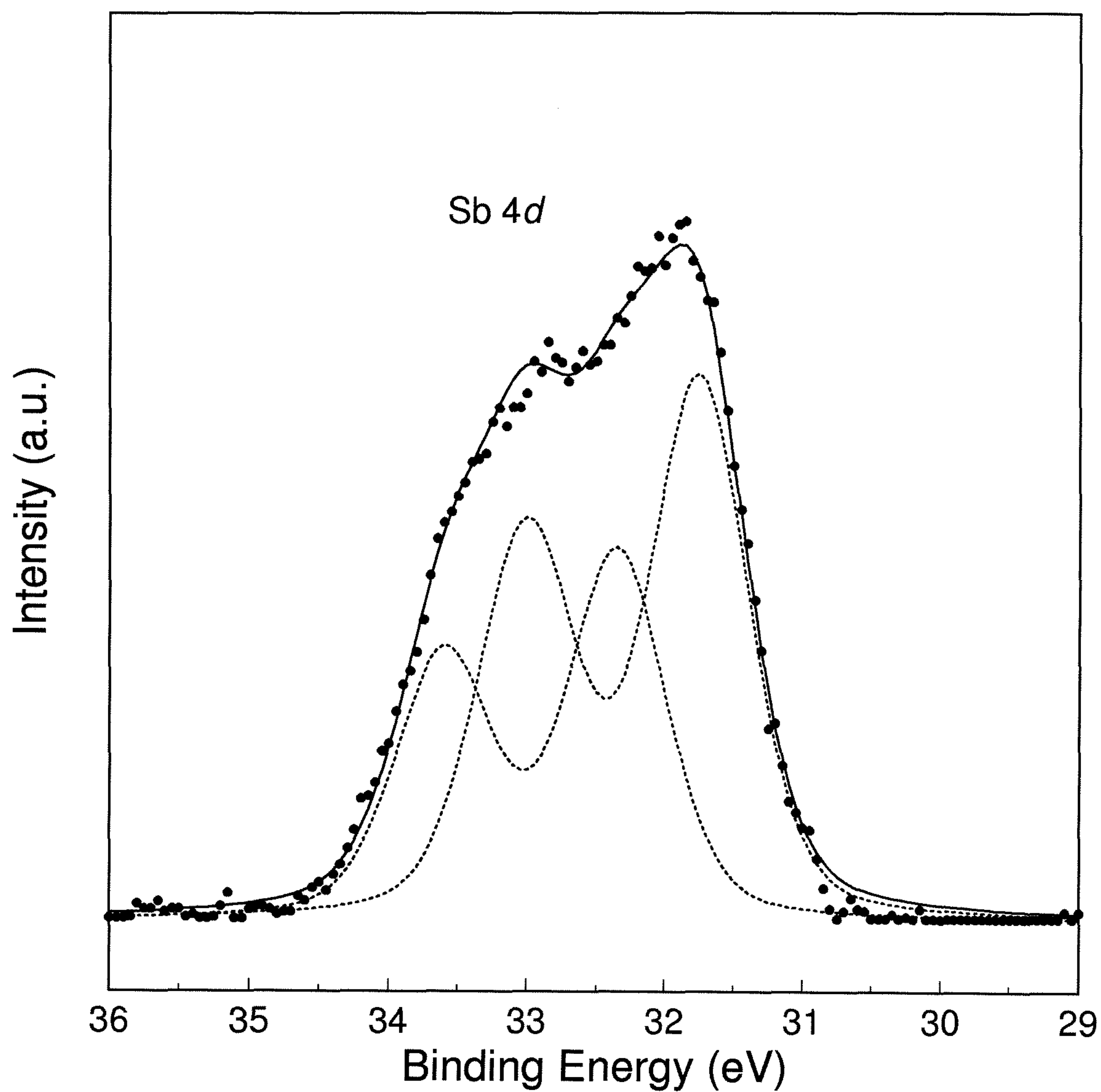

Figure 5.2: Sb 4*d* peak from 15 sec. Sb_2 soak of an InAs surface. Data is fitted with two chemically shifted peaks with lineshapes constrained to that of Sb 4*d* from bulk GaSb.

correlation between the RHEED data and the chemical exchange reaction at the surface of the samples.

5.4 Results

5.4.1 Sb Soaks of InAs Surfaces

The experiments on Sb soaks of InAs surfaces were done in two parts. In the first experiment, the Sb cracker power and soak time were chosen to duplicate the conditions during growth of actual devices. For the 5 second Sb soaks of InAs surfaces, the As $3d$ to In $4d$ peak intensity ratio relative to that of bulk InAs decreased by 18% and 1% for Sb_2 and Sb_4 soak species respectively. We also observed a much larger Sb component for the Sb_2 soak as shown in Figure 5.3. Using the simple attenuation model mentioned above, this corresponds to a majority of the terminating As layer being exchanged during the Sb_2 soak, and very minimal exchange during the Sb_4 soak. Due to the uncertainty in published MFPs, we can only estimate relative changes in coverage, and cannot quote exact values.

In the second Sb soak experiment, Sb coverage on InAs as a function of both cracker power and soak time was studied. Since the 5 second Sb_2 soak at growth conditions resulted in roughly complete exchange of the As terminated surface, the bulk evaporator temperature was lowered to reduce the total Sb flux impinging on the sample surface by roughly 80%. This increases the exchange time, allowing better temporal resolution of the exchange process. Figure 5.4 shows the ratio of the Sb $4d$ to In $4d$ peak intensities as a function of soak time for (a) 40% cracker power, and (b) 80% cracker power. As expected, the Sb coverage increases with time of soak and, at low soak times, is significantly greater for cracked soaks than for uncracked soaks. The dotted and dashed lines in Figure 5.4 and the chemically shifted Sb $4d$ component shown in Figure 5.2 are discussed below.

It should be noted that some concern has been raised over why the exchange

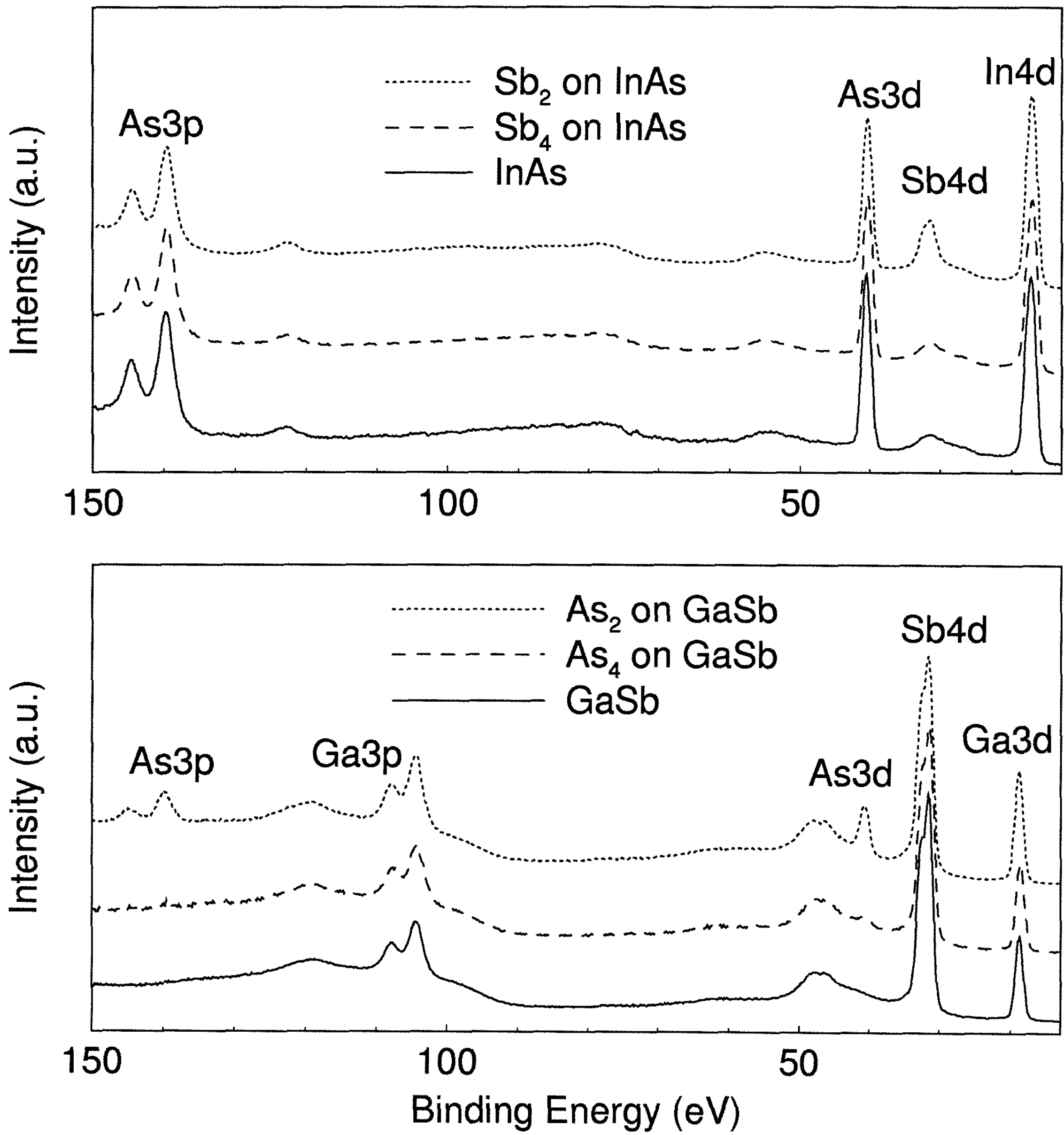

Figure 5.3: XPS spectra for Sb soaks of InAs surfaces (top) and As soaks of GaSb surfaces (bottom). Spectra from bulk samples (solid), uncracked sources (dashed) and cracked sources (dotted) are shown.

(a)

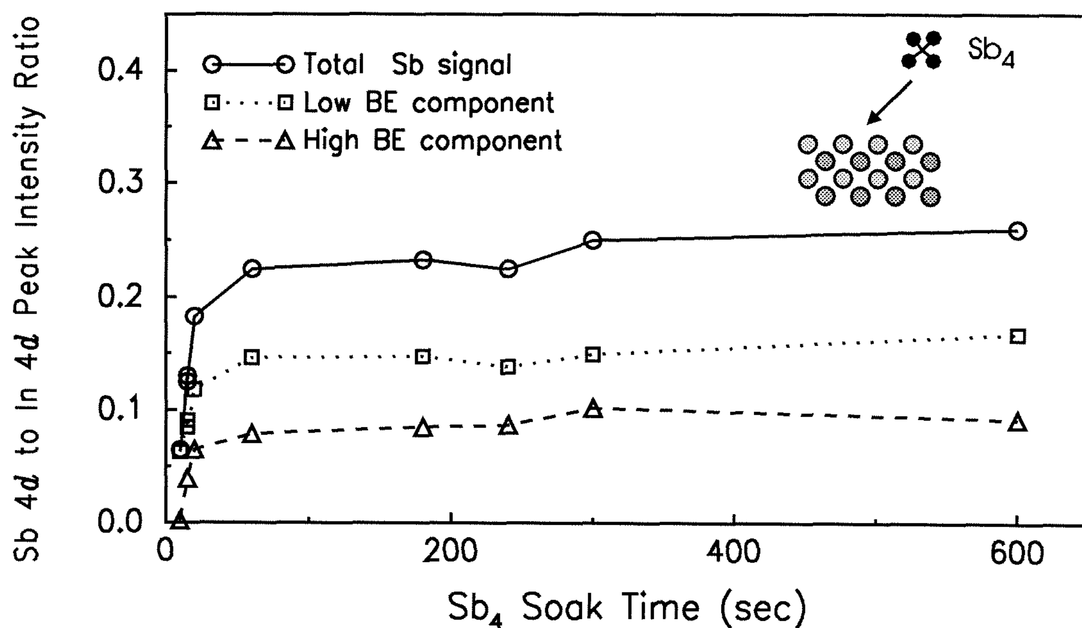

(b)

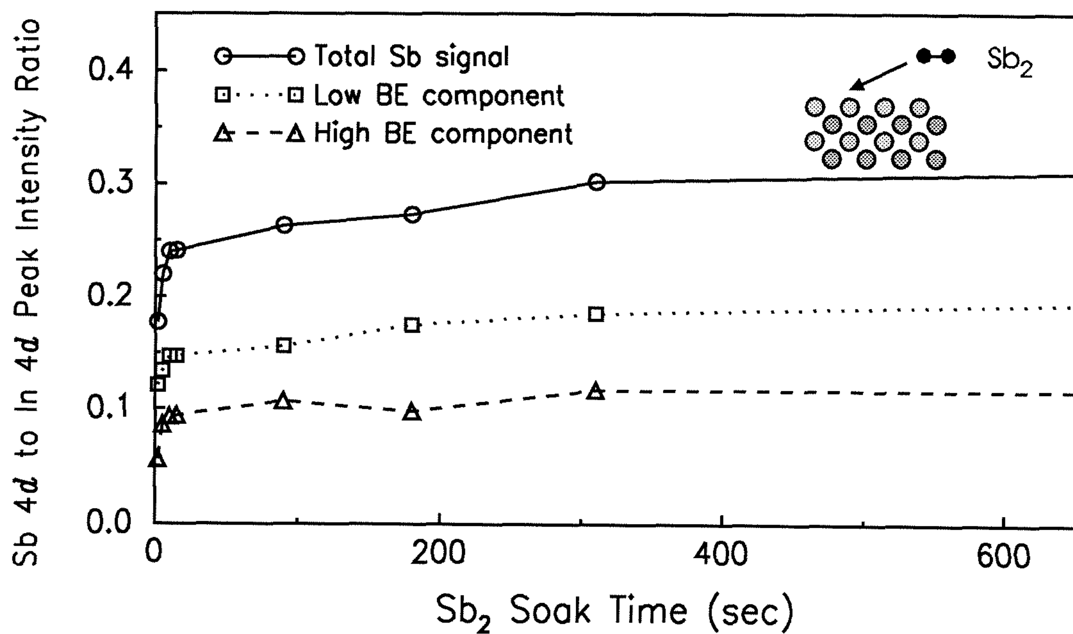

Figure 5.4: Sb 4*d* to In 4*d* peak intensity ratio as a function of soak time for (a) cracked, and (b) uncracked Sb sources. Components of the total peak are also shown (dotted and dashed lines). Lines are drawn to guide the eye. In plot (b) lines extend to additional data points at 1800 s.

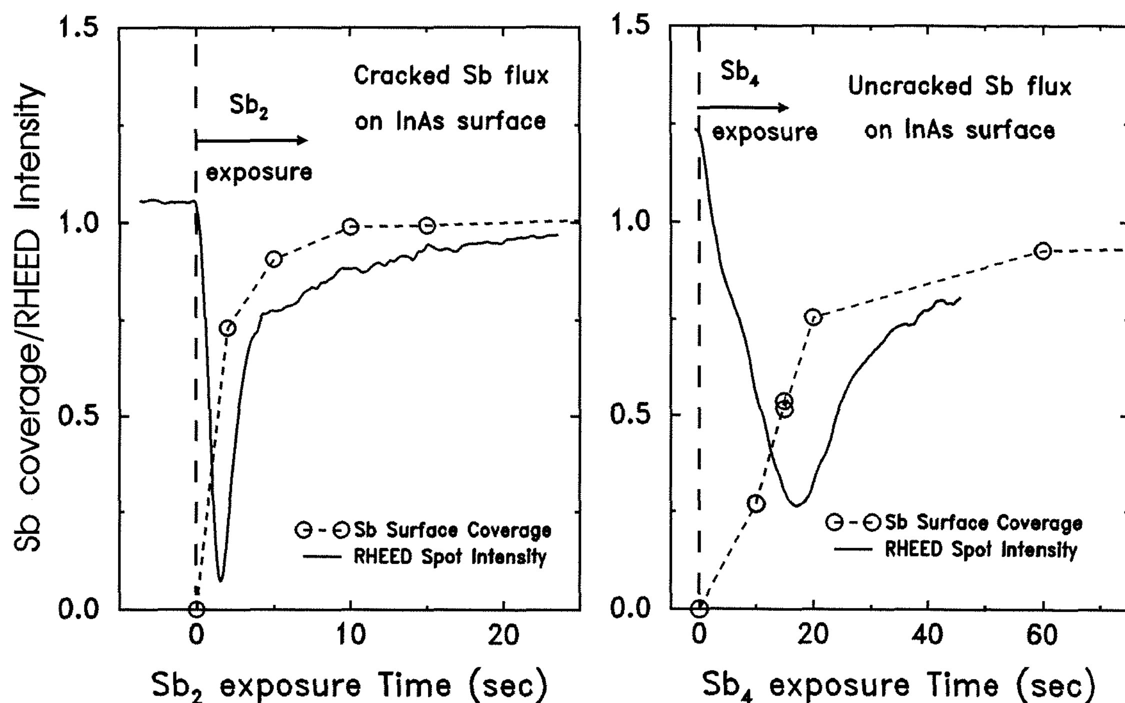

Figure 5.5: RHEED (solid) and XPS measured Sb coverage (dashed with open circles) versus exposure, or soak, time for Sb_2 (left) and Sb_4 (right). Commencement of exposure is indicated by vertical dashed line.

reaction should proceed at all, given that the InAs bond strength is greater than that of InSb. The explanation is that even though the displacement of As with Sb to form InSb from InAs is unlikely, due to the differing bond strengths, the constant flux of Sb coupled with the absence of a source of As allows the exchange reaction to proceed.

Figure 5.5 shows a comparison of RHEED and XPS data for Sb soaks of InAs surfaces. The vertical axis in each plot shows both the normalized RHEED specular streak intensity (solid lines) and the normalized Sb coverage as determined by XPS (dashed lines with open circles). The horizontal axis shows the exposure, or equivalently, soak time for a cracked (left plot) or an uncracked (right plot) Sb flux incident on the InAs surface. The vertical dashed line in each plot represents

the start of the exposure. In these plots we see the characteristic drop off and subsequent recovery in the RHEED specular streak intensity, but more importantly we see that the recover time of the RHEED profile is similar to the rise time of the XPS Sb coverage profile. The significance of this is discussed in Section 5.5.

5.4.2 As Soaks of GaSb Surfaces

The studies of As soaks of GaSb surfaces consisted of two parts. In the first experiment, the soak time was held constant at 5 seconds, while the cracker power was varied. The bottom plot of Figure 5.3 shows the results of this experiment. Examining the As $3d$ peak, we immediately observe a qualitative increase in the extent of the exchange reaction when using As_2 as compared to As_4. In addition, for the 5 second As_2 soak of a GaSb surface, the Sb $4d$ to Ga $3d$ peak intensity ratio decreased by 26% relative to bulk GaSb. The decrease in the same peak intensity ratio for an As_4 soak is 7%. This corresponds to roughly complete exchange of the terminating Sb layer for the As_2 soak and partial exchange for the As_4 soak. Again, exact values for the extent of the exchange reaction cannot be determined due to uncertainties in the photoelectron MFPs.

In the second soak experiment, As coverage on GaSb as a function of As_2 soak time was studied. Figure 5.6 shows the ratio of the As $3d$ to Ga $3d$ peak intensities as a function of soak time. Similar to the Sb soaks of InAs surfaces, the occurrence of an exchange reaction is readily observed. However, for the As_2 soak of a GaSb surface we observe no saturation in the As $3d$ for longer soak times. This indicates that the exchange reaction of As for Sb proceeds past the terminating Sb layer, down into the underlying GaSb. More justification for this conclusion is given in the next section.

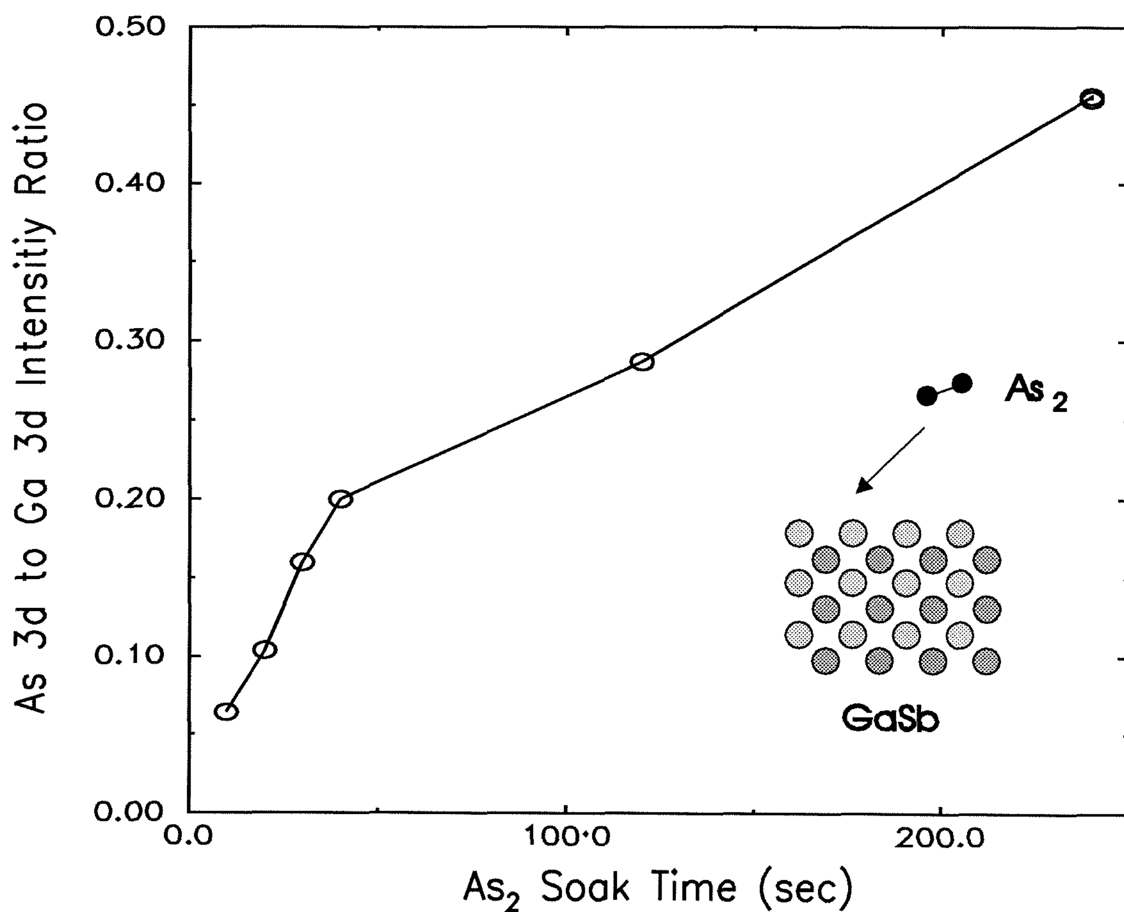

Figure 5.6: Ratio of As $3d$ to Ga $3d$ core level peak intensity ratios as a function of As_2 soak time on a GaSb surface. Notice that the As $3d$ peak intensity does not saturate for longer soak times as in the case for Sb soaks of InAs surface.

5.5 Discussion

5.5.1 Sb Soaks of InAs Surfaces

Since there is so much uncertainty in the published electron MFPs [14, 15, 16], we are not able to accurately calculate surface coverages for any given group V soak experiment. However, we can estimate these surface coverages by studying the time dependent soak experiments. To do this for the Sb soaks of InAs surfaces, we need to determine the source of the chemically shifted Sb 4*d* component shown in Figure 5.2. A detailed analysis of this peak shows a variation in the magnitude of the chemical shift of more than 0.1 eV. This is a large variation considering that the chemical shift is only ~ 0.5 eV; however, as can be seen in Figure 5.7, analysis of the higher BE Sb $3d_{5/2}$ core level reveals a nearly identical variation in the separation between its constituent peaks. This demonstrates that the variation in peak separation is a real effect and not an artifact of the XPS data acquisition. A representative, fitted Sb $3d_{5/2}$ peak is shown in the inset in Figure 5.7, and a representative, fitted Sb $4d_{5/2}$ peak is show in Figure 5.2. In both cases, the peak shapes were constrained to those obtained from bulk GaSb.

One possible explanation for the second Sb component might be a surface reconstruction related shift; however, the lack of a shifted component at very low soak times argues against this theory. Another possible explanation for the two Sb components is the formation of metallic Sb islands. If true, then based on the direction of the observed chemical shift, the higher BE Sb peak should be due to the islands [17]. To check this, we measured the BE of metallic Sb 4*d*, from a thin metallic Sb layer grown on InAs. The measured Sb 4*d* BE was less than the BE of the shifted Sb 4*d* peak, which is consistent with the shifted peak being due to metallic Sb islands, since islanding can shift peaks to higher binding energy. Island formation also provides an explanation of the variation in the position of the chemically shifted peak, since changes in average island size can cause a change

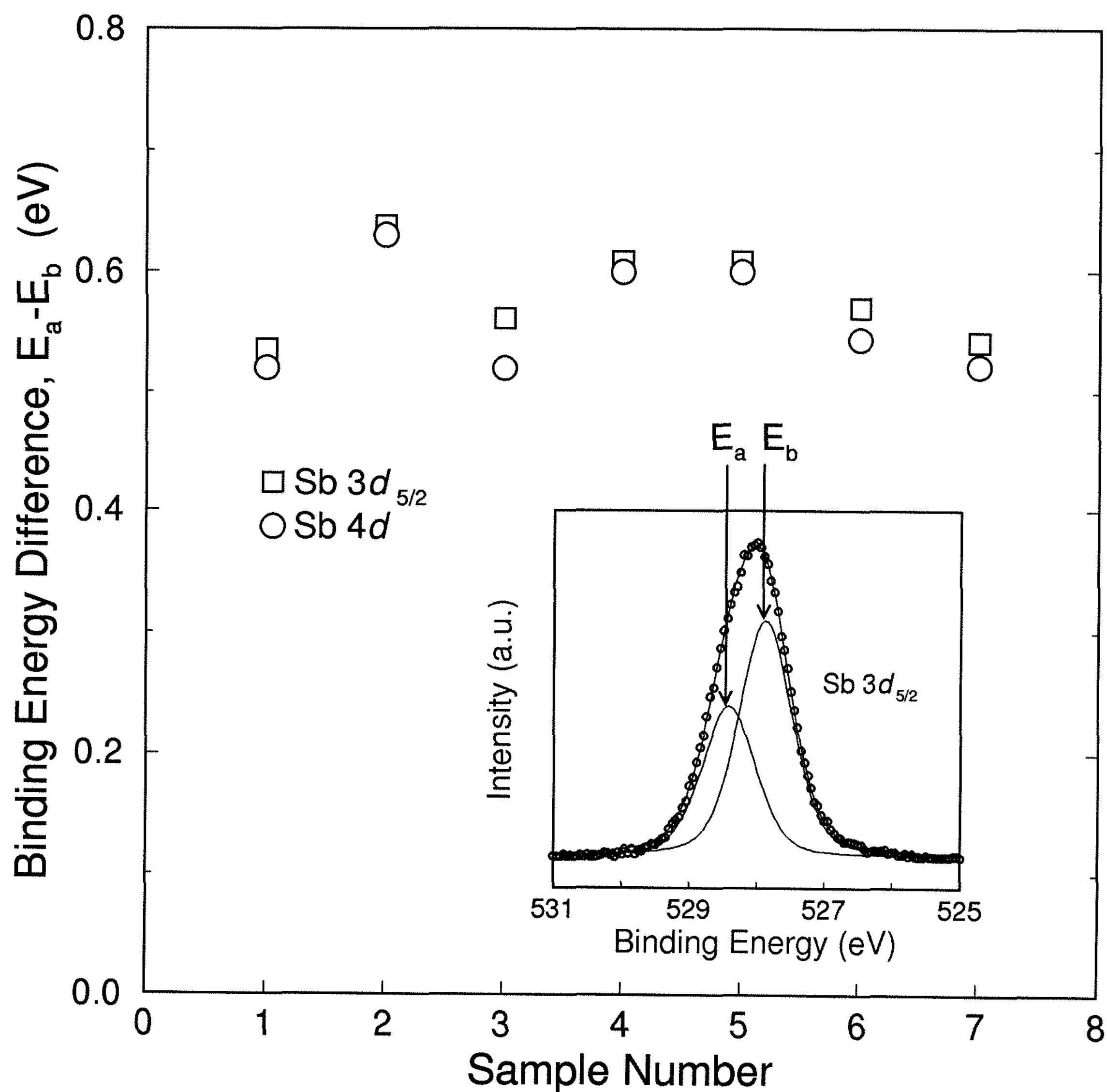

Figure 5.7: Energy separation between the two component peaks for the Sb $3d$ and Sb $4d$ core levels. The same fluctuation in separation is observed for both peaks. Inset shows components comprising Sb $3d$ peak. Sb $4d$ peak is shown in Figure 5.2.

in the magnitude of the chemical shift.

In addition, the energy separation between the lower BE Sb 4*d* peak and the In 4*d* peak is stable, making it reasonable to believe that this peak is due to an exchanged layer of Sb bonded to In which should be stable from sample to sample, while the higher BE peak, due to islanding, is more apt to vary from sample to sample. Also, referring to Figure 5.4, we see that since the low BE Sb peak in both the cracked and uncracked soaks stabilize at roughly the same value, it is quite possible that the steady state value corresponds to exactly one monolayer of Sb atoms exchanging with the As terminated InAs surface. If this is the case, then the coverage obtained with the Sb_2 device-like soaks is slightly less than one monolayer, as indicated by the arrow in Figure 5.4 (b). It should be noted that even if the islanding explanation proposed above is incorrect, the fact that the soaks currently used in heterojunction growth occur in a region where the coverage is dependent on the time of soak indicates that further optimization of growth parameters may be possible.

The conclusion that the Sb exchange with As is self-terminating at one monolayer is significant in that it predicts that a GaSb-on-InAs interface should be able to be grown with abrupt InSb interfaces. This can be done by terminating an InAs layer with As, soaking the sample with Sb until the exchange has proceeded to completion, leaving InSb bonds, and finally, proceeding with GaSb growth. The excess metallic Sb produced by the soak will be consumed during the GaSb growth and will not interfere with the interface abruptness. Chapter 6 examines in more detail the issue of interface abruptness for GaSb/InAs interfaces.

Another important result of the Sb on InAs soak studies is the correlation between the RHEED and XPS results shown in Figure 5.5. The agreement between the recovery time in the RHEED data and the rise time in the XPS data is significant, especially considering that the two analysis techniques measure very different quantities: the RHEED profile is a measure of the structural properties of the sample surface during the Sb soak of a single InAs surface, while the XPS profile is a

direct chemical measurement of the exchange reaction for a number of InAs samples, each exposed to an Sb soak of differing durations. The similarity between the RHEED and XPS profiles, coupled with the observation that the minima in the RHEED profiles correspond to roughly 50% exchange as determined from XPS, indicate that the drop in the RHEED streak intensity may be due to differences in the Sb and As form factors for electron scattering. This would explain the recovery in the RHEED streak intensity as the exchange proceeds towards full exchange of the terminating As layer with Sb. Another possible explanation is that partial exchange of the As layer with Sb causes surface roughening which will also reduce the specular streak intensity.

Regardless of the exact mechanism for the behavior of the RHEED specular streak intensity, the close correlation between the RHEED and XPS recovery and rise times indicates that RHEED can be used to monitor surface exchange reactions. This is very important, since RHEED is a real-time analysis technique which can be used during the growth of actual devices.

5.5.2 As Soaks of GaSb Surfaces

It was shown in Section 5.4.2 that for As soaks of GaSb surfaces, the As signal as measured by XPS is not self terminating (see Figure 5.6). Without further investigation, it cannot be concluded whether the continued increase in the As signal is due to accumulation of As at the sample surface, or continued exchange of As for Sb down into the underlying GaSb.

Figure 5.8 shows Sb $4d$ to Ga $3d$ and Ga $3p$ to Ga $3d$ peak intensity ratios plotted as a function of As_2 soak time. The peak intensity ratios are normalized to peak intensity ratios for bulk GaSb. We see a significant drop in the Sb $4d$ to Ga $3d$ peak intensity ratio for longer soak times, which strongly indicates that the exchange of As for Sb is proceeding past the top monolayer. However, since the binding energy of the Sb $4d$ core level is larger than that for Ga $3d$, part of the

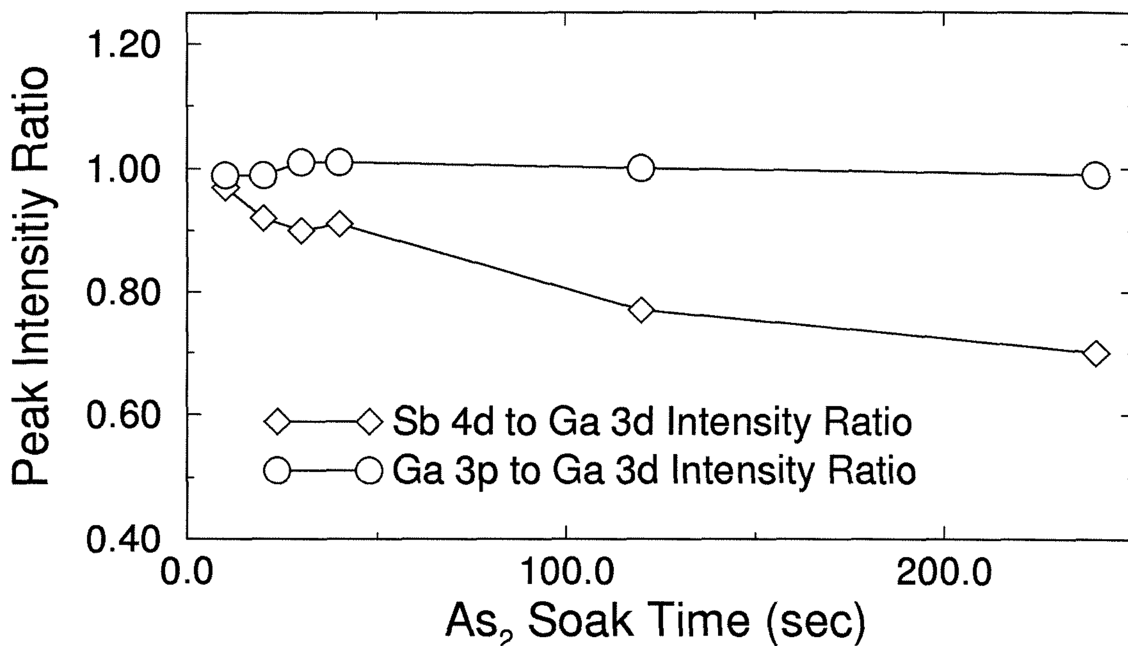

Figure 5.8: Sb $4d$ to Ga $3d$ and Ga $3p$ to Ga $3d$ peak intensity ratios for As_2 soaks of GaSb surfaces. Peak intensity ratios are normalized to those obtained from bulk GaSb.

decrease in the Sb to Ga peak intensity ratio could be attributed to the stronger attenuation of the Sb $4d$ peak if there existed an overlayer of As on the sample surface. Recall that a larger binding energy corresponds to a smaller photoelectron kinetic energy, which translates into a shorter MFP.

If this were true then we should observe an even stronger decrease in the Ga $3p$ to Ga $3d$ peak intensity ratio, because the binding energy of the Ga $3p$ peak is larger than that of the Sb $4d$ peak. Since the Ga $3p$ to Ga $3d$ peak intensity ratio is independent of the As_2 soak time, we can safely conclude that both the continued increase in the As $3d$ peak intensity and the continued decrease in the Sb $4d$ to Ga $3d$ peak intensity ratio for longer soak times is due to exchange of As for Sb past the terminating monolayer of Sb, and into the underlying GaSb.

The exchange of Sb with As was somewhat expected, given that the GaAs bond

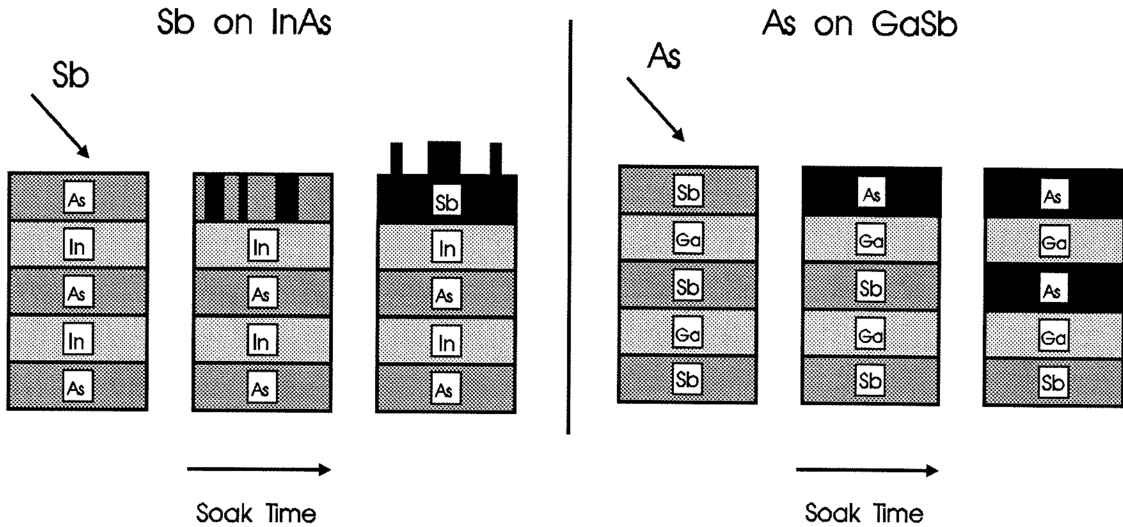

Figure 5.9: Schematic diagrams of the surface exchange reactions for Sb soaks of InAs surfaces (left), and As soaks of GaSb surfaces (right). Note the self-terminating nature of the exchange shown on the left as compared to the exchange shown on the right.

strength is greater than that of GaSb. However, the exchange into the underlying GaSb was unexpected and is very significant to studies of interface abruptness. What the XPS results show is that an InAs-on-GaSb interface grown using an As soak at the interface will result in an extended GaAs-like interface unless the As soak time is very precisely monitored. Even with precise monitoring it may be that the interface will not be abrupt, with As exchanging deep into the GaSb in some regions, and less than complete exchange in other regions. The issue of interface abruptness for InAs/GaSb heterojunctions is discussed in more detail in Chapter 6.

5.6 Summary

In conclusion, we have used XPS and RHEED to study *in situ*, the dynamics of the formation of the mixed anion InAs/GaSb interface as a function of cracker power and soak time. For the studies of exchange as a function of cracker power, it was found that anion exchange occurs more readily when using cracked versus uncracked sources during the soak. This was true for both Sb soaks of InAs surfaces, and As soaks of GaSb surfaces.

Varying the soak time for Sb soaks of InAs surfaces showed a saturation of the Sb coverage for longer soak times. Based on detailed analysis of the XPS core level peaks, we see evidence for island formation and conclude that the steady state coverage may correspond to monolayer exchange of the As terminated surface with Sb and the formation of metallic Sb islands. This is shown schematically in Figure 5.9. Since soaks used in actual device growths presently lie in a region where variations in soak time may vary the extent of the group V exchange, further optimization of interface characteristics may be obtained by modifying these soak times. The saturation of the exchange reaction after one monolayer for Sb soaks of InAs surfaces suggests that the growth of GaSb-on-InAs interfaces can be made abrupt with InSb interfaces.

Parallel studies, during the surface exchange reaction, of the RHEED specular streak intensities correlate well with the XPS data. The recovery times for the RHEED intensities profiles were similar to the soak times for saturation of the XPS Sb signals. It was concluded that the partial exchange of the terminating monolayer of As causes the RHEED intensity to decrease through differing form factors for As and Sb, or through surface roughening, and that full exchange restores the specular streak intensity. This is significant in that the RHEED pattern can be used to monitor the surface exchange reaction in real-time, during the growth of device structures, which cannot be accomplished using XPS alone.

For As_2 soaks of GaSb surfaces it was found that the measured XPS As $3d$ to Ga $3d$ peak intensity ratios did not saturate for longer soak times. This was in contrast to the results obtained for the Sb soaks of InAs surfaces. By studying the

Sb $4d$ to Ga $3d$ and Ga $3p$ to Ga $3d$ peak intensity ratios, it was determined that As was exchanging with not only the terminating Sb layer at the surface of the GaSb, but was also exchanging with Sb in the underlying GaSb. This is shown schematically in Figure 5.9. This result is very significant, because it shows that an InAs-on-GaSb heterojunction grown using an As interrupt will result in an extended GaAs-like interface, and that very precise shuttering would be required to obtain an abrupt GaAs interface for the InAs-on-GaSb growth order.

Bibliography

[1] E.R. Brown, J.R. Söderström, C.D. Parker, L.J. Mahoney, K.M. Molvar, and T.C. McGill, *Appl. Phys. Lett.* **58**, 2291 (1991).

[2] M. Sweeny and J. Xu, *Appl. Phys. Lett.* **54**, 546 (1989).

[3] J.R. Söderström, D.H. Chow, and T.C. McGill, *Appl. Phys. Lett.* **55**, 1094 (1989).

[4] L.F. Luo, R. Beresford, and W.I. Wang, *Appl. Phys. Lett.* **55**, 2023 (1989).

[5] D.A. Collins, E.T. Yu, Y. Rajakarunanayake, J.R. Söderström, D.Z.-Y. Ting, D.H. Chow, and T.C. McGill, *Appl. Phys. Lett.* **57**, 683 (1990).

[6] D.L. Smith and C. Mailhiot, *J. Appl. Phys.* **62**, 2545 (1987).

[7] R.H. Miles, D.H. Chow, J.N. Schulman, and T.C. McGill, *Appl. Phys. Lett.* **57**, 801 (1990).

[8] T.D. Golding, H.D. Shih, J.T. Zborowski, W.C. Fan, C.C. Horton, P.C. Chow, A. Vigliante, B.C. Covington, A. Chi, J.M. Anthony, and H.F. Schaake, *J. Vac. Sci. Technol. B* **10**, 880 (1992).

[9] D.H. Chow, R.H. Miles, and A.T. Hunter, *J. Vac. Sci. Technol. B* **10**, 888 (1992).

[10] G. Tuttle, H. Kroemer, and J.H. English, *J. Appl. Phys.* **67**, 3032 (1990).

[11] J.R. Waldrop, G.J. Sullivan, R.W. Grant, E.A. Kraut, and W.A. Harrison, *J. Vac. Sci. Technol. B* **10**, 1773 (1992).

[12] D.H. Chow, R.H. Miles, C.W. Nieh, and T.C. McGill, *J. Cryst. Growth* **111**, 683 (1991).

[13] D.A. Collins, M.W. Wang, R.W. Grant, and T.C. McGill, *J. Appl. Phys.* **75**, 259 (1994).

[14] M.P. Seah and W.A. Dench, *Surf. Interface Anal.* **1**, 2 (1979).

[15] C.M. Kwei and L.W. Chen, *Surf. Interface Anal.* **11**, 60 (1988).

[16] S. Tanuma, C.J. Powell, and D.R. Penn, *Surf. Interface Anal.* **17**, 927 (1991).

[17] M.K. Wagner, J.C. Hansen, R. deSouza-Machado, S. Liang, J.G. Tobin, M.G. Mason, S. Brandt, Y.T. Tan, A.-B. Yang, and F.C. Brown, *Phys. Rev. B* **43**, 6405 (1991).

Chapter 6

InAs/GaSb Heterojunction Studies

6.1 Introduction and Outline

This chapter presents two studies of the InAs/GaSb heterointerface. The first set of experiments examine the InAs/GaSb band alignment using XPS. The valence band offset is measured as a function of both the nominal interface composition and the growth order. In the second part of the chapter, we present a detailed study of the abruptness of the InAs/GaSb interface, again as a function of both nominal interface composition and growth order. A number of characterization techniques (XPS, RHEED, cross-sectional STM and SIMS) were used in this study. It should be noted that the RHEED, cross-sectional STM and SIMS studies were performed by other researchers, but are included here for completeness [1].

Section 6.2 presents the XPS measurements of the InAs/GaSb valence band offset. The interface abruptness studies are presented in Section 6.3, and the results from both studies are summarized in Section 6.4.

6.2 InAs/GaSb Band Alignment Studies

6.2.1 Motivation

The InAs/GaSb valence band offset is an important parameter for a number of device applications, and is relevant to fundamental studies of band alignments in mixed anion/cation material systems. The device applications in the InAs/GaSb/AlSb material system include: InAs/AlSb oscillators operating at frequencies greater than 700GHz [2], novel InAs/AlSb/GaSb based [3, 4, 5] and InAs/GaSb [6] tunnel structures, and InAs/$Ga_{1-x}In_xSb$ infrared (IR) superlattice (SL) detectors [7, 8]. For many of these applications, the band alignment plays a critical role in the device performance; however, determination of band alignments in mixed anion/cation systems is complicated by the fact that two different types of interfaces can be formed. In the case of an InAs/GaSb heterojunction, both InSb-like and GaAs-like interfaces can be formed. It is very important to determine what effect changing the interface composition has on band alignments in the InAs/GaSb material system as well as in other mixed anion/cation systems.

The InAs/GaSb valence band offset has been experimentally measured by a variety of techniques [9, 10, 11, 12]; however, none of these studies addressed the issue of interface composition. A number of theoretical studies have predicted that the InAs/GaSb valence band offset should depend on the interface composition [13, 14, 15]. These theories predict that the InAs/GaSb valence band offset should be larger for an InSb-like interface compared to a GaAs-like interface; however, the magnitude of this effect ranges considerably, from 31 to 150 meV, depending on which theory is used. Additionally, Gualtieri *et al.* [12] observed a 50 meV larger valence band offset for InAs grown on GaSb compared to GaSb grown on InAs; however, this was deemed to be within the experimental uncertainty.

The effect of interface composition and growth order on the valence band offset has also been studied in other material systems. For example, the InP/GaInAs

valence band offset shows a 180 meV asymmetry with growth order due to a change in the interface composition, whereas the GaInP/GaAs valence band offset shows no such asymmetry [16]. The InP/GaInAs result is in contradiction with Hybertsen's calculations [17], which predict no dependency of the valence band offset on interface composition or growth order. The InAs/AlSb interface has also been studied for both InSb-like and AlAs-like interface compositions [18, 19]. In those studies, a slight increase in the valence band offset was observed for the AlAs-like interface compared to the InSb-like interface, but no change in the valence band offset was noted for changes in the growth order.

Thus, there is significant motivation for studying the InAs/GaSb band alignment, both for device applications and as a fundamental study of band alignments to be applied to other material systems. We report measurements on the InAs/GaSb valence band offset as a function of both interface composition and growth order using X-ray photoelectron spectroscopy (XPS).

6.2.2 Experiment

All of the structures used in this study were grown in a Perkin-Elmer 430 molecular beam epitaxy (MBE) system. A number of different (100) substrates (GaAs, n-GaSb, p-GaSb) were used with no variation in results. Samples were grown on thick stress relaxed GaSb buffer layers at a substrate temperature of $\sim 380\,^{\circ}$C. Multiple samples grown on the same substrate were separated by buffer layers thick enough to prevent detection of underlying layers with XPS. Heterojunction samples were grown with thin ($\sim 20\,$Å) overlayers, such that an XPS signal is detected from both sides of the interface. X-ray diffraction of superlattice structures was used to verify that the growth schemes used produced the correct nominal interface compositions. Growth details may be found in Ref. [20].

The XPS measurements were obtained using a Perkin-Elmer Model 5500 analysis system with a monochromatic Al $K\alpha$ source ($h\nu$ = 1486.6 eV). All of the

samples studied were transferred from the growth chamber to the XPS chamber via an ultrahigh vacuum transfer tube. The base pressure in the XPS chamber was typically $\sim 3 \times 10^{-10}$ Torr. Care was taken to ensure that the escape orientation of the photoelectrons remained constant from sample to sample to minimize any electron diffraction effects due to the single crystalline nature of the samples.

The standard approach to determine valence band offsets using XPS is to measure core level to valence band maximum separations in bulk samples and core level to core level separations in heterojunction structures. For example, referring to Fig. 6.1, $E_{CL}^{InAs} - E_v^{InAs}$, $E_{CL}^{GaSb} - E_v^{GaSb}$, and $E_{CL}^{GaSb} - E_{CL}^{InAs}$ would be measured in bulk InAs, bulk GaSb, and InAs/GaSb heterojunction samples respectively, where the E_{CL} and E_v denote core level and valence band maximum binding energies for the indicated material. The valence band offset is determined using

$$\Delta E_v \equiv E_v^{InAs} - E_v^{GaSb} = (E_{CL}^{GaSb} - E_v^{GaSb}) - (E_{CL}^{InAs} - E_v^{InAs}) - (E_{CL}^{GaSb} - E_{CL}^{InAs}). \quad (6.1)$$

Since we are only interested in *changes* in the valence band offset, and since core level to valence band maximum separations are constant, variations in the valence band offset are given by

$$\delta(\Delta E_v) = \delta(E_{CL}^{InAs} - E_{CL}^{GaSb}). \quad (6.2)$$

Thus, to determine changes in the valence band offset as a function of interface composition, we need only to measure changes in core level separations in heterojunctions with varying interface compositions. For the InAs/GaSb interface, four different core level separations may be used to monitor changes in the valence band offset: Ga $3d$ - As $3d$, Ga $3d$ - In $4d$, Sb $4d$ - As $3d$, and Sb $4d$ - In $4d$.

To determine core level energy separations, we use the following procedure, given in more detail in Ref. [21]. For each core level we remove any interfering loss tails, implement an integrated background subtraction, and finally perform a least square fit to Voigt functions. Since the In $4d$ and Ga $3d$ peaks overlap, we constrain their shapes to be those obtained from InAs and GaSb bulk standards,

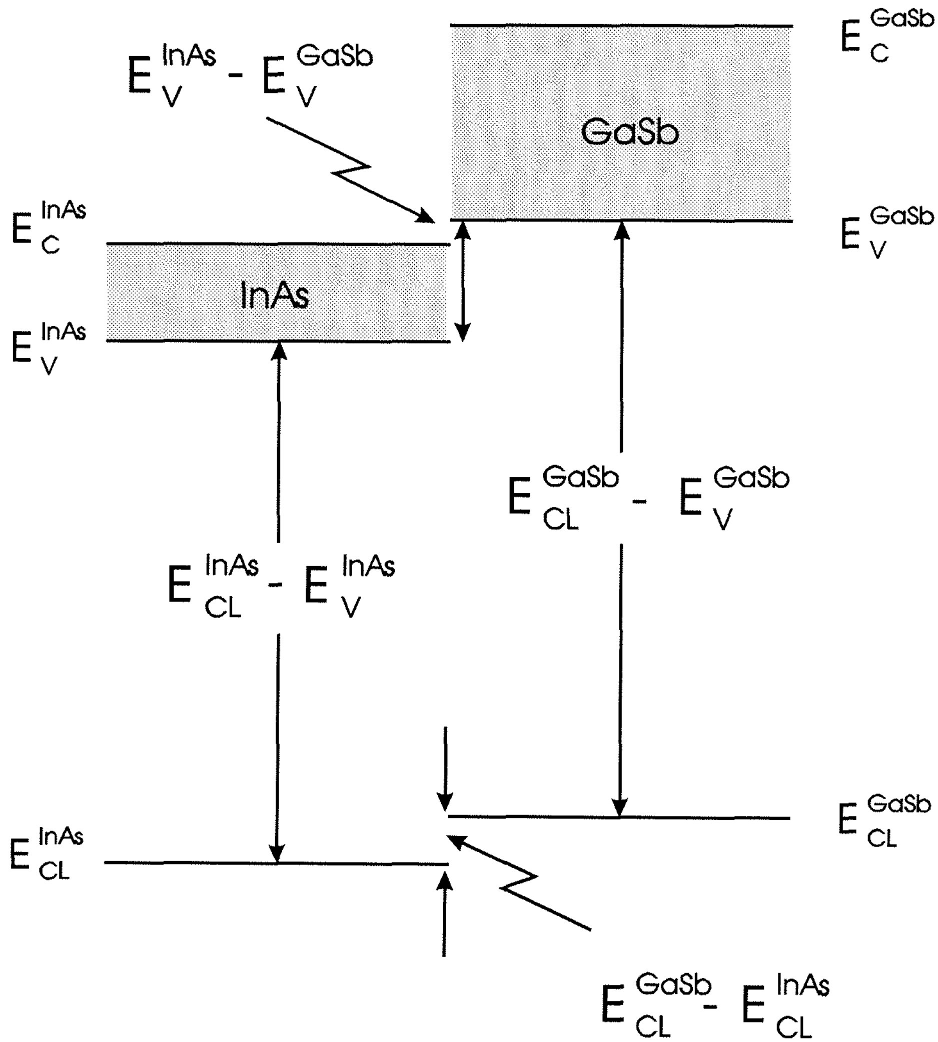

Figure 6.1: Schematic diagram showing XPS binding energy separations used in valence band offset measurements.

in order to reduce the number of fitting parameters. The Ga $3d$ and In $4d$ loss tails which interfere with the Sb $4d$ core level were stripped using InAs and GaAs bulk standards respectively. Figure 6.2 (a) shows a representative unprocessed XPS spectrum for a GaSb-on-InAs heterojunction. Figure 6.2 (b) shows the resulting normalized fit of the As $3d$, Sb $4d$, Ga $3d$ and In $4d$ core level peaks. Core level separations for a given sample are typically reproducible to better than 0.02 eV.

6.2.3 Results and Discussion

The resulting average core level energy separations for both InAs-on-GaSb and GaSb-on-InAs growth orders, and for both InSb-like and GaAs-like interface compositions are shown in Table 6.1. Multiple XPS spectra and structures were analyzed for each of the growth orders and interface compositions as indicated by x:y where x and y represent the number of samples and the total number of XPS spectra acquired, respectively. From Equation 2, changes in the peak separations reflect changes in the valence band offset, $\delta(\Delta E_V)$. For the GaSb-on-InAs growth order, the average change in the valence band offset with change in interface composition is 0.003 eV. For the InAs-on-GaSb growth order, this value is 0.014 eV. Both of these values are less than our experimental uncertainty ($\sim$0.02eV). Thus, we observe no dependence of ΔE_V on the interface composition for both growth orders to within our experimental uncertainty.

Since the core level energy separations for a given growth order are independent of interface composition, we can average these values for each growth order to determine if the valence band offset changes in going from one growth order to another. This is shown in Table 6.2. The first row in this table shows the average of the core level separations for the GaSb-on-InAs growth direction for both interface compositions. The second row in Table 6.2 shows the corresponding average core level separations for the InAs-on-GaSb growth direction. The change in the valence band offset in going from the GaSb-on-InAs to the InAs-on-GaSb growth direction

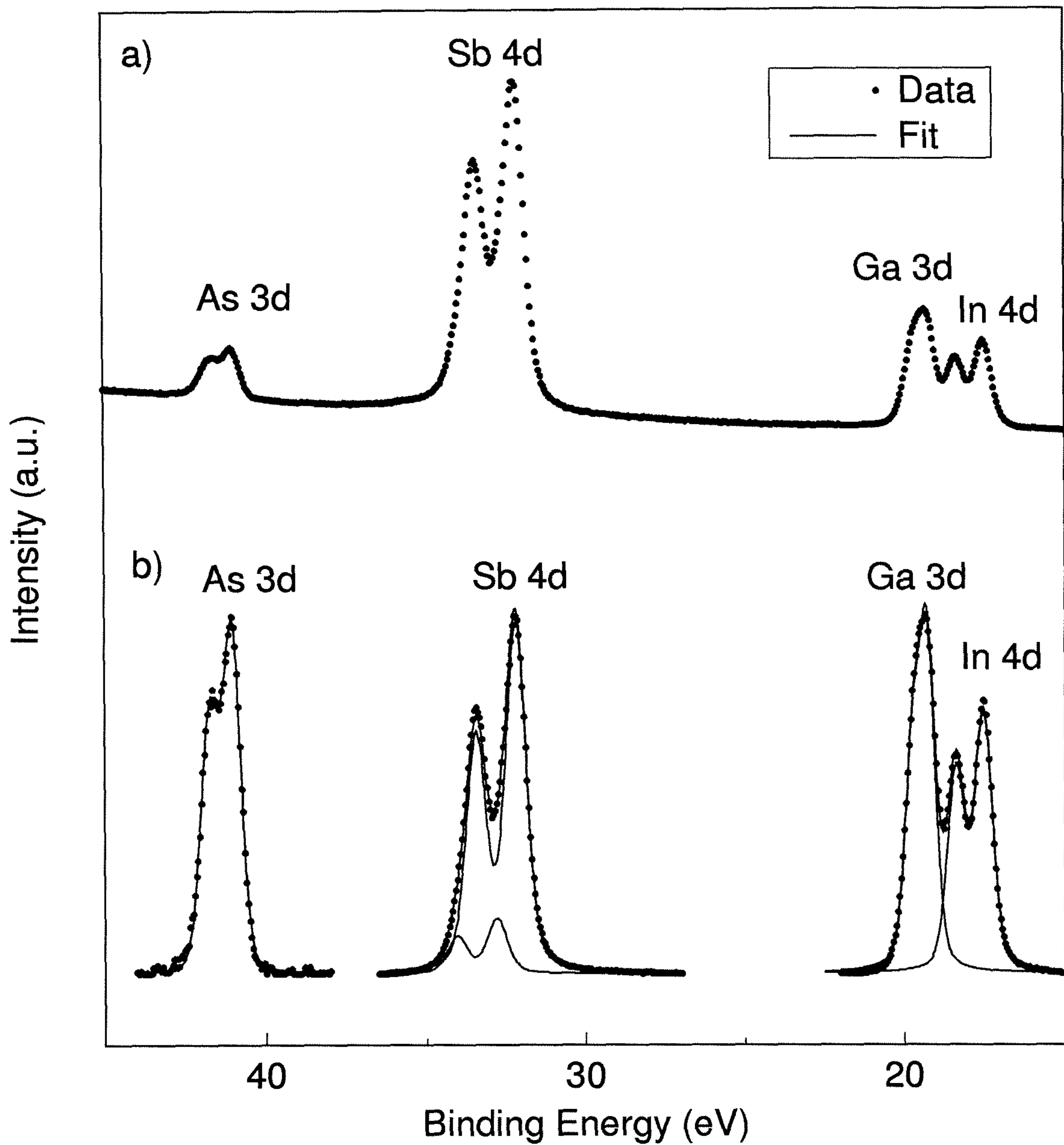

Figure 6.2: Figure (a) shows an example of an unprocessed XPS scan of a GaSb-on-InAs heterojunction. Figure (b) shows the fitted As 3d, Sb 4d, Ga 3d, and In 4$d$core level peaks after removal of interfering peaks, background subtraction, normalization, and least squares fitting to Voigt functions.

Sample	Core Level Separations (eV)			
	$E_{In\ 4d}$- $E_{Sb\ 4d}$	$E_{In\ 4d}$- $E_{Ga\ 3d}$	$E_{As\ 3d}$- $E_{Sb\ 4d}$	$E_{As\ 3d}$- $E_{Ga\ 3d}$
GaSb-on-InAs				
GaAs-like	-14.698	-1.753	8.822	21.766
2:3	(0.003)	(0.010)	(0.003)	(0.006)
InSb-like	-14.685	-1.728	8.802	21.759
2:4	(0.003)	(0.004)	(0.013)	(0.009)
δ (ΔE_V)	0.013	0.025	-0.019	-0.008
InAs-on-GaSb				
GaAs-like	-14.572	-1.680	8.917	21.810
3:6	(0.007)	(0.019)	(0.016)	(0.016)
InSb-like	-14.570	-1.646	8.912	21.836
5:6	(0.011)	(0.037)	(0.015)	(0.026)
δ (ΔE_V)	0.002	0.034	-0.005	0.026

Table 6.1: The measured core level separations for InSb-like and GaAs-like interface compositions. The notation 2:4 represents two growths with a total of four scans acquired. Values in parenthesis are the standard deviations for the respective core level splittings. All spin-orbit split peak positions are measured with respect to the J = 5/2 component.

Sample	Core Level Separations (eV)			
	$E_{In\ 4d}$-$E_{Sb\ 4d}$	$E_{In\ 4d}$-$E_{Ga\ 3d}$	$E_{As\ 3d}$-$E_{Sb\ 4d}$	$E_{As\ 3d}$-$E_{Ga\ 3d}$
GaSb-on-InAs				
	-14.691	-1.741	8.812	21.763
InAs-on-GaSb				
	-14.571	-1.663	8.915	21.823
δ (ΔE_V)	0.120	0.078	0.103	0.060
extended GaSb-on-InAs				
	-14.635	-1.695	8.869	21.809
δ (ΔE_V)	0.056	0.046	0.057	0.046

Table 6.2: The measured core level separations for both InAs-on-GaSb and GaSb-on-InAs growth orders. Also included are the core level separations for an intentionally extended GaSb-on-InAs interface. All spin-orbit split peak positions are measured with respect to the J = 5/2 component.

is shown in the third row of this table. The average change is 0.090 eV with a standard deviation among the four values of 0.027 eV, where the InAs-on-GaSb interface has the larger valence band offset. This value is significantly larger than the experimental uncertainty in the core level energy separations.

The exact reason why the valence band offset depends on the growth order is still under investigation; however, it is most likely related to the asymmetry in the InAs/GaSb interface. STM studies and recent growth studies provide a possible

explanation for the difference in valence band offsets in terms of the interface structure [22, 23]. The GaSb-on-InAs interface is found to be more abrupt than the InAs-on-GaSb interface, with the latter exhibiting signs of Sb incorporation in the InAs overlayer and an As/Sb exchange reaction in the underlying GaSb. More details of the interface abruptness studies and the exchange reaction studies are given in Section 6.3 and Chapter 5 respectively.

To verify this dependence of the valence band offset on interface structure, an intentionally extended GaSb-on-InAs heterojunction was studied. The structure was grown by opening the Sb shutter during the last three monolayers of the InAs growth, producing an extended InSb-like interface. The measured core level separations for this structure are shown in Table 6.2. From the core level binding energy separations for this structure, we obtain a valence band offset that is 51 meV greater than that for the nominally abrupt GaSb-on-InAs growth direction. This value lies between that of the nominally abrupt GaSb-on-InAs and the extended InAs-on-GaSb structures.

This is consistent with the hypothesis that the extended nature of the InAs-on-GaSb interface is responsible for the difference in the InAs/GaSb valence band offset for the two growth orders. Also, a detailed analysis of core level peak shapes shows no evidence for chemical shifts or broadening. This result strongly indicates that the change in valence band offset is not due to either band-bending effects from surface fermi level pinning of the InAs surface or surface-induced chemical shifts. Attempts to test these conclusions by altering the composition of the InAs-on-GaSb interface produced no significant change in the InAs/GaSb valence band offset, probably due to the inherent difficulty in growing abrupt InAs-on-GaSb interfaces [23].

We still have not explained how an extended InAs/GaSb interface would produce a change in the valence band offset for this system. One possible explanation is that an anti-structure defect [24], related to Sb cross-incorporation or As exchange, may produce a dipole moment, resulting in the observed change in the

valence band offset. Initial estimates of the magnitude of this effect are consistent with the observed change in the valence band offset and realistic concentrations ($\sim$ 10 % of a monolayer) of anti-structure defects. The sign of the measured change in the valence band offset is consistent with an anti-structure in the InAs-on-GaSb samples, with group III atoms on group V sites followed by group V atoms on group III sites as viewed from the sample surface down. Further investigations are currently underway to determine the validity of this explanation.

To summarize, we have used XPS to measure the variation in the InAs/GaSb valence band offset as a function of both interface composition (InSb-like and GaAs-like) and growth order (InAs-on-GaSb and GaSb-on-InAs). The InAs/GaSb valence band offset was observed to be independent of interface composition irrespective of growth order; however, between the two different growth orders, a 90 meV difference in the InAs/GaSb valence band offset is observed, with the InAs-on-GaSb interface showing the larger valence band offset. The difference in valence band offset is attributed to the extended nature of the InAs-on-GaSb interface.

6.3 Abruptness of the InAs/GaSb Heterointerface

6.3.1 Motivation

The technological and scientific importance of arsenide/antimonide heterointerfaces has already been well motivated in Chapter 1 and in Sections 6.2.1 and 5.1. Specific studies of the interface abruptness in the InAs/GaSb material system are motivated primarily by InAs/$In_xGa_{1-x}Sb$ IR SL detector applications, and as a fundamental study of mixed anion interface formation. Despite the advantages of the InAs/$In_xGa_{1-x}Sb$ IR SL design, detectors competitive with $Hg_xCd_{1-x}Te$ technologies have yet to be fabricated [25]. This poor performance has been attributed to the shorter extrinsic lifetime in InAs/$In_xGa_{1-x}Sb$ IR SL devices, due to the

presence of Shockley-Read-Hall (SRH) centers [26]. One possible mechanism for this is that the generation of SRH centers is related to interdiffusion of the group V sublattice at the mixed-anion As/Sb interface, which could result in antisite defects, leading to SRH centers.

Since the length scales for interdiffusion are potentially quite short, it was necessary to draw on a number of different characterization techniques in order to properly assess the existence of interdiffusion at the InAs/GaSb interface. The techniques used were XPS, RHEED, cross-sectional STM and SIMS, each of which provided a unique piece of information about the InAs/GaSb interface: XPS provided *in situ*, near surface chemical analysis; RHEED provided real-time, *in situ*, near surface structural characterization; cross-sectional STM provided very high resolution imaging, electronic structure information, and interface roughness analysis for a SL structure; and SIMS provided chemical analysis with excellent sensitivity.

6.3.2 Experiment

Details of the growth and transfer of the samples used in this experiment are given in Sections 5.2.1 and 6.2.2. In addition, brief descriptions of the XPS experimental setup have already been presented in Chapters 1, 3, 5 and earlier in this chapter. In the remainder of this chapter, XPS is used primarily to study core level peak intensity ratios as opposed to the core level energy separations. A number of InAs-on-GaSb and GaSb-on-InAs samples were studied, each grown with both InSb-like and GaAs-like interfaces. For each of these samples, the ratio of the As $3d$ to In $4d$ peak intensities were measured and normalized to the same ratio obtained from an As terminated (2×4 reconstruction) InAs standard. Similarly, the Ga $3d$ to Sb $4d$ peak intensity ratios were normalized to an Sb terminated (1×3 reconstruction) GaSb standard. From the variation in these peak intensity ratios, we are able to infer relative interface abruptness and to study anion cross-incorporation. The

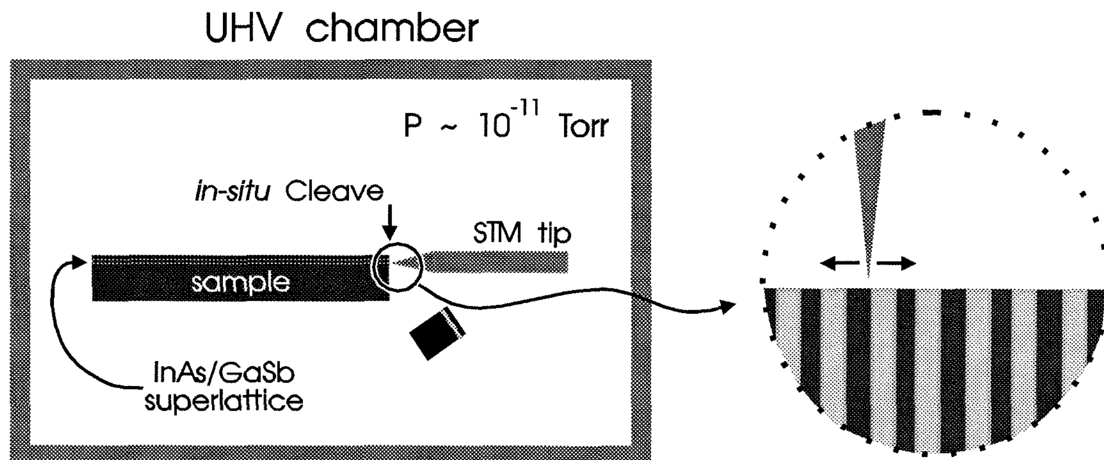

Figure 6.3: Schematic Diagram of Cross-sectional STM setup used to study InAs/GaSb SLs.

spectrum stripping and peak fitting procedures for the XPS samples are the same as those presented in Section 6.2.2.

Brief descriptions of the RHEED experimental setup have already been presented in Chapters 1 and 5. In this chapter RHEED is used to study interface asymmetry through analysis of the RHEED reconstruction patterns and specular streak intensity oscillations. Figure 1.11 shows a schematic diagram of the experimental setup used to extract the RHEED data.

Figure 6.3 shows a schematic diagram of the cross-sectional STM setup used in our studies. Briefly, the cross-sectional STM procedure consisted of cleaving a sample *in situ* at a pressure of $\sim 4 \times 10^{-11}$ Torr. STM imaging and spectroscopy can then be performed on the cleaved surface without exposure to atmospheric contaminants. Some of the advantages of this characterization technique are high resolution imaging, contamination free surface, and the ability to perform cross-sectional imaging which is not possible with standard STM.

The STM images shown in this chapter were acquired with a constant current of 0.1 nA. Carefully prepared and characterized single crystal tungsten probe tips

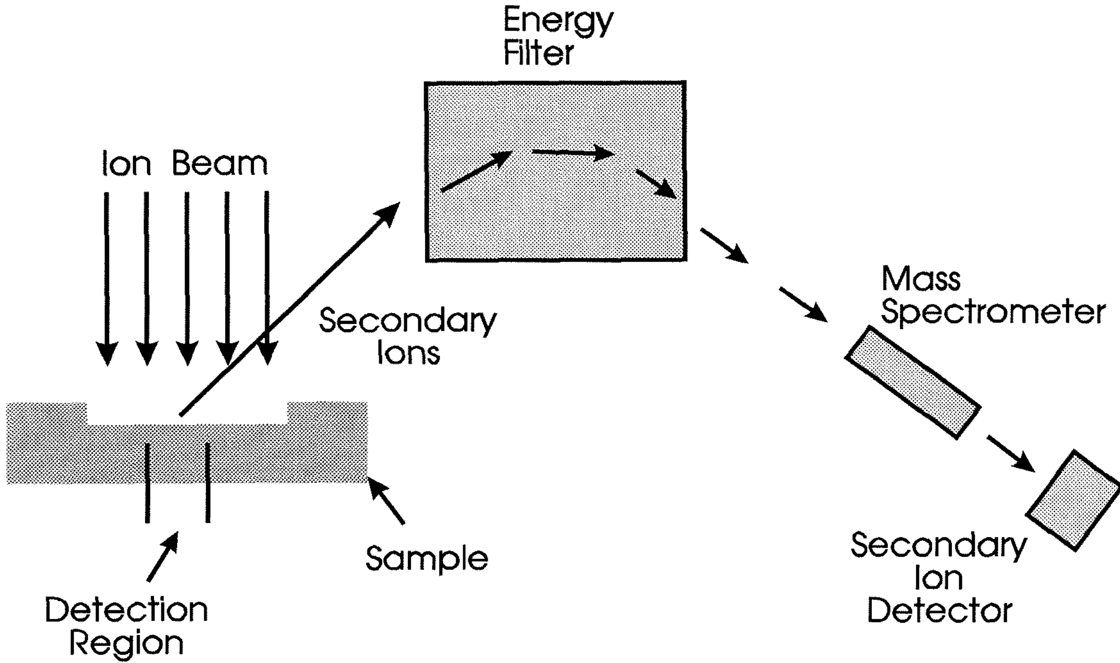

Figure 6.4: Schematic Diagram of the SIMS setup used to profile InAs-on-GaSb interfaces.

were used in the STM data acquisition. A detailed description of the STM experimental technique can be found in Ref. [22]. It should be emphasized that the STM studies were performed by another researcher, but are included in this chapter for completeness and clarity [1].

Figure 6.4 shows a schematic diagram of a standard SIMS experimental setup. Briefly, SIMS analysis consists of sputtering a sample over a region of a few 100 μm on a side. Secondary ions are then detected over a much smaller region ($<$ 100 μm diameter) in the center of the sputtered crater. Before reaching the detector, the secondary ions pass through first an energy filter and then a mass spectrometer.

Some of the advantages of SIMS are excellent sensitivity down to parts per million or even parts per billion, profiling capability and good chemical specificity. Disadvantages include the destructive nature of the measurement and relatively poor depth resolution (a few nm at best). The SIMS analysis presented in

this chapter were performed by researchers at Charles Evans and Associates on a CAMECA IMS-4f machine using 3.0 keV O_2^+ bombardment. Cs ion bombardment was also attempted, but resulted in poorer depth resolution.

6.3.3 Observation of Interfacial Asymmetry

In this section, we report on observations of interfacial asymmetry in InAs/GaSb heterointerfaces using XPS, RHEED, and cross-sectional STM. The asymmetry was observed in the form of an increased broadening, or roughness, of the InAs/GaSb interface for the InAs-on-GaSb growth direction compared to the GaSb-on-InAs growth direction.

XPS Results

Tables 6.3 (a) and (b) show summaries of XPS results which demonstrate this asymmetry. In these tables we tabulate the Sb 4d to Ga 3d and As 3d to In 4d peak intensity ratios after normalization to bulk GaSb and InAs standards. The peak intensity ratios are tabulated for both (a) GaSb-on-InAs and (b) InAs-on-GaSb growth directions, and for both InSb-like and GaAs-like interface compositions. Each tabulated entry specifies the range of peak intensity ratios compiled from a number of samples and XPS spectra.

The purpose of this method of tabulation is to infer information about relative interface abruptness by simultaneously displaying the results from a number of different samples. Due to uncertainties in photoelectron MFPs [27, 28, 29], it is impossible to unambiguously evaluate interface abruptness on a single sample using a simple attenuation model for the XPS signal. Essentially, the difficulty is that a single XPS spectrum can be accurately modeled with a number of different interface configurations depending on the photoelectron MFPs used in the fitting. By displaying variations in peak intensity ratios over a number of samples, as shown in Tables 6.3 (a) and (b), it is possible to infer relative interface abruptness.

(a)

Minimum and Maximum Peak Intensity Ratios (Normalized)

	Sb4d/Ga3d	As3d/ In4d
InSb-like	1.26-1.31	0.63-0.74
GaAs-like	1.20-1.25	0.74-0.86
Range	1.20-1.31	0.63-0.86

(b)

Minimum and Maximum Peak Intensity Ratios (Normalized)

	Sb4d/Ga3d	As3d/ In4d
InSb-like	1.06-1.24	0.81-0.96
GaAs-like	0.55-0.80	1.28-1.37
Range	0.55-1.24	0.81-1.37

Table 6.3: XPS peak intensity ratios, for both growth orders and both interface compositions. Each entry shows the range (minimum-maximum) of values for a given interface composition and growth order. The total range for each growth order is also given.

Specifically, if we examine the bottom row in each table, we see that the range of values for a given peak intensity ratio (e.g., Sb $4d$ to Ga $3d$) is much larger for the InAs-on-GaSb growth direction compared to the GaSb-on-InAs growth direction. In fact, for the InAs-on-GaSb growth direction, the range in the values is much greater than the experimental uncertainty for a given peak intensity ratio, and is inconsistent with the range of values expected for a simple change in the interface composition [23]. That is, even allowing for variation in the photoelectron MFPs, the data in Table 6.3 (b) cannot be modeled as an abrupt interface due to the large range in the values for a given peak intensity ratio. This is true even though any *one* of the XPS spectra used to compile the data in this table could be modeled with an abrupt interface.

For the GaSb-on-InAs growth direction, the range in values is consistent with an abrupt interface, but could also be modeled with a non-abrupt interface, so it is not possible to conclude with certainty whether or not this interface is abrupt. However, since the range in the peak intensity ratios is much smaller than for the InAs-on-GaSb growth direction, it can be concluded that the GaSb-on-InAs growth direction is the more abrupt of the two growth directions.

Individual peak intensity ratios shown in Table 6.2 are studied in more detail in Section 6.3.4, in order to extract the mechanisms underlying the asymmetry in the abruptness of the InAs/GaSb interface.

RHEED Results

Another characterization technique that was used to observe the asymmetry in the InAs/GaSb interface was RHEED. Both the RHEED reconstruction patterns and the RHEED intensity oscillations showed abnormal behavior for the InAs-on-GaSb growth direction. Figure 6.5(a) shows a schematic diagram of the progression of the RHEED reconstruction pattern during the growth of an InAs-on-GaSb heterojunction. During the GaSb growth the RHEED pattern showed a 1×3 reconstruction pattern which switched to a 1×5 reconstruction pattern

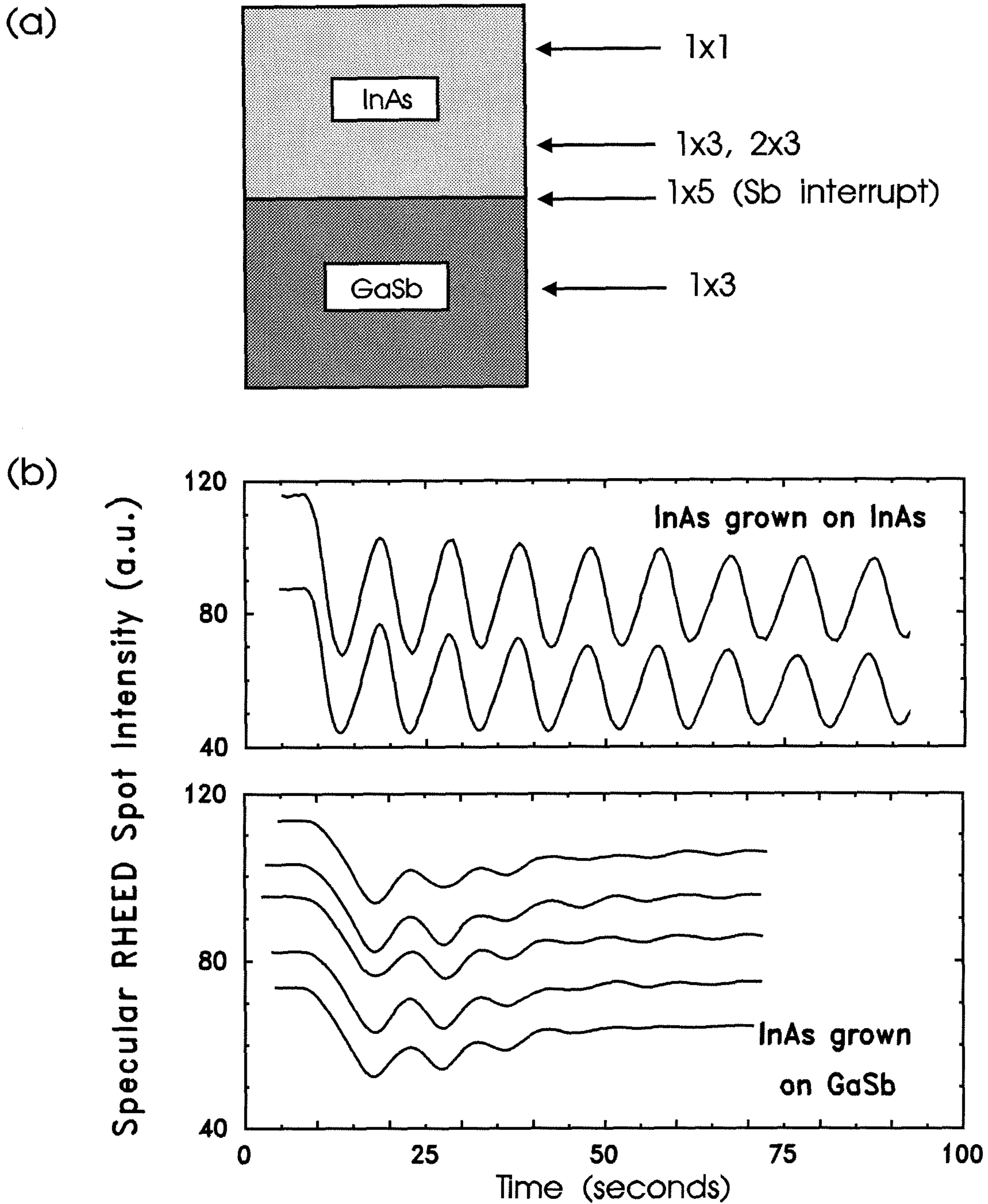

Figure 6.5: RHEED studies of interface asymmetry. Unusual 1×3, 2×3 reconstruction is observed in the InAs reconstruction patterns shown schematically in (a). RHEED intensity oscillation profiles also show unusual behavior for the InAs-on-GaSb growth direction.

during the Sb interrupt at the interface. This is typical behavior for a Sb terminated GaSb layer. At the onset of the InAs growth, however, unusual behavior is observed in the reconstruction pattern. Instead of the usual 1×1 reconstruction pattern observed for InAs at the growth temperatures and fluxes used, we observed a 1×3 or faint 2×3 reconstruction for the first few monolayers of InAs growth. This type of unusual behavior in the RHEED reconstruction pattern was not observed for the GaSb-on-InAs growth direction.

One possible cause for the 1×3, 2×3 reconstruction pattern is Sb incorporation into InAs from the underlying GaSb. This explanation is consistent with RHEED studies of $InAs_xSb_{1-x}$ layers which also show a 1×3 reconstruction pattern, and also offers an mechanism for the transition from the 1×3 to the 1×1 reconstruction in the form of decreasing Sb concentration in the InAs layer after the first few monolayers of growth. Another explanation for the 1×3, 2×3 reconstruction pattern is that GaAs forms at the interface causing the subsequent InAs layer to have a 3-D growth mode. This is consistent with the reconstruction patterns observed for the growth of InAs-on-GaAs. The transition from the 1×3 to the 1×1 reconstruction is then explained by the coalescing of the InAs islands. Because of the qualitative and structural nature of the information obtained from RHEED reconstruction patterns, it is not possible to determine with certainty which of the two explanations offered above is valid. In Section 6.3.4, more quantitative chemical characterization of the interface formation is presented.

Figure 6.5(b) shows the RHEED specular spot (or streak) intensity oscillations for (top) InAs grown on InAs and (bottom) InAs grown on GaSb. Multiple profiles are plotted for both cases to demonstrate the reproducibility of the measurement. In both plots, the top InAs growth is initiated at roughly $t = 10$ seconds, after a growth interrupt. For the InAs grown on InAs we observe the standard RHEED intensity oscillations indicative of smooth 2-D growth. For the InAs grown on GaSb, however, we observe very unusual behavior during the first few monolayers of growth. This type of behavior is not observed during the growth of GaSb-on-

InAs interfaces. Another study which also reported this type of behavior in the RHEED intensity profile proposed Sb incorporation into the InAs as a possible cause, but no quantitative justification was given [30]. Although the RHEED data presented above cannot, by itself, be used to determine the exact mechanisms of the InAs/GaSb interface formation, it does provide clear evidence for the asymmetry between the InAs-on-GaSb and the GaSb-on-InAs growth directions.

Cross-sectional STM Results

Figure 6.6 shows two representative cross-sectional STM images of InAs/GaSb SLs: one grown with (a) InSb-like interfaces and the other with (b) GaAs-like interfaces. Both images were acquired using a sample voltage of -1.3 V with the InAs layers shown in dark and the GaSb layers in bright. The growth directions and scales are indicated on the images.

The main feature to be observed from these images is the asymmetry in interface roughness for the two growth directions. For both interface types, the InAs-on-GaSb growth direction is observed to have an increased interface roughness when compared to the GaSb-on-InAs growth direction, although this is difficult to discern visually for the sample grown with InSb-like interfaces. Detailed analyses of the interface roughness by taking the Fourier transform of the horizontal derivative of the images shown in Figure 6.6 can be found in Refs. [22, 31].

The interfacial asymmetry can also be observed in cross-sectional STM spectroscopy studies. In these studies, STM spectra were acquired every 1.06 Å along the growth direction over a distance greater than one SL period. Subsequent analysis of the spatially resolved spectroscopy results showed that for the InAs-on-GaSb growth direction, the interface spectra are smeared out over a range of ~ 6 Å. These results have been reproduced over a number of data sets using different samples and probe tips. Thus, the cross-sectional STM imaging and spectroscopy results both show direct evidence of the asymmetry in the InAs/GaSb interface. However, since STM doesn't have direct chemical sensitivity, it was not possible

(a) InSb-like Interfaces

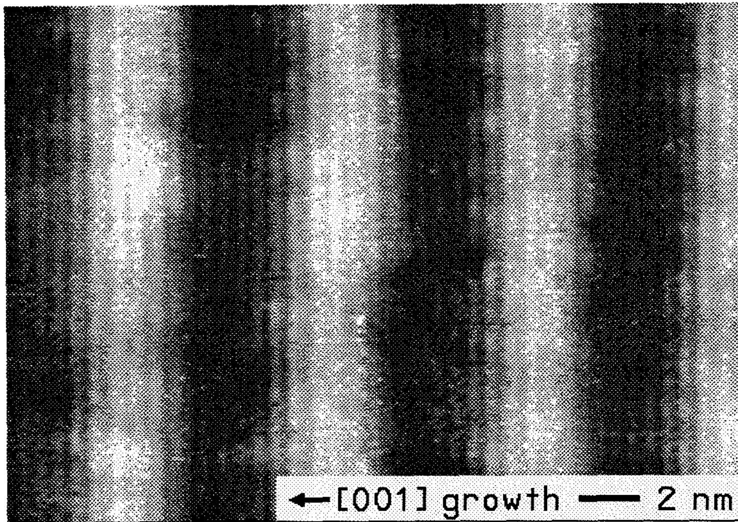

(b) GaAs-like Interfaces

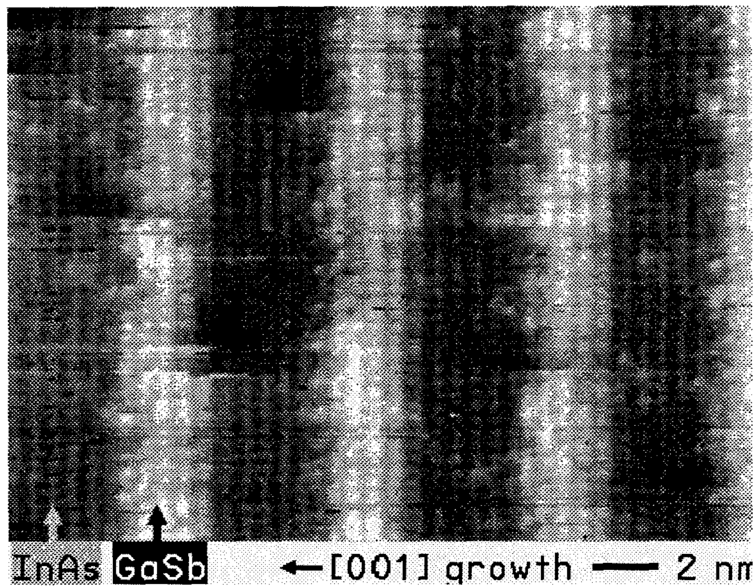

Figure 6.6: Cross-sectional STM images of the InAs/GaSb SLs grown with (a) InSb-like interfaces and (b) GaAs-like interfaces.

to determine the exact mechanism for the asymmetry.

6.3.4 Underlying Causes of Interfacial Asymmetry

In order to determine the underlying causes for the observed asymmetry in the InAs/GaSb interface, chemically sensitive characterization techniques were required. Two techniques were used in this study: XPS and SIMS. As mentioned previously, XPS has the advantages of being a near surface, *in situ* characterization technique, while SIMS offers high chemical sensitivity and depth profiling capabilities.

Two possible mechanisms for non-abruptness of the InAs-on-GaSb interface were proposed but not proved in the previous section: GaAs growth during the interface formation and Sb cross-incorporation into the InAs from the underlying GaSb. The first of the possibilities has already been demonstrated. The exchange reaction studies in Chapter 5 showed conclusively that an Sb to As exchange can occur during the formation of an InAs-on-GaSb interface, resulting in an extended GaAs-like interface. Also, referring to the GaAs-like interface entries in Table 6.3 (b) we see that the Sb $4d$ to Ga $3d$ and As $3d$ to In $4d$ peak intensity ratios are much smaller and larger than the respective values for GaSb and InAs standards. While by itself this data is not conclusive, comparing it with the data for the other interface types and growth directions leads to the conclusion that at least some of the GaAs-like interfaces for the InAs-on-GaSb growth direction are extended into the underlying GaSb.

Confirmation of cross-incorporation of Sb from underlying GaSb layers into InAs overlayers was much more difficult. While incorporation of Sb from background Sb in the chamber has been observed, cross-incorporation of Sb from underlying layers has never been confirmed. *In situ* XPS and ion sputtering results are shown in Figure 6.7. The top profile in this figure shows an XPS spectrum for an InAs-on-GaSb heterojunction grown with a nominal InSb-like interface and a $\sim$

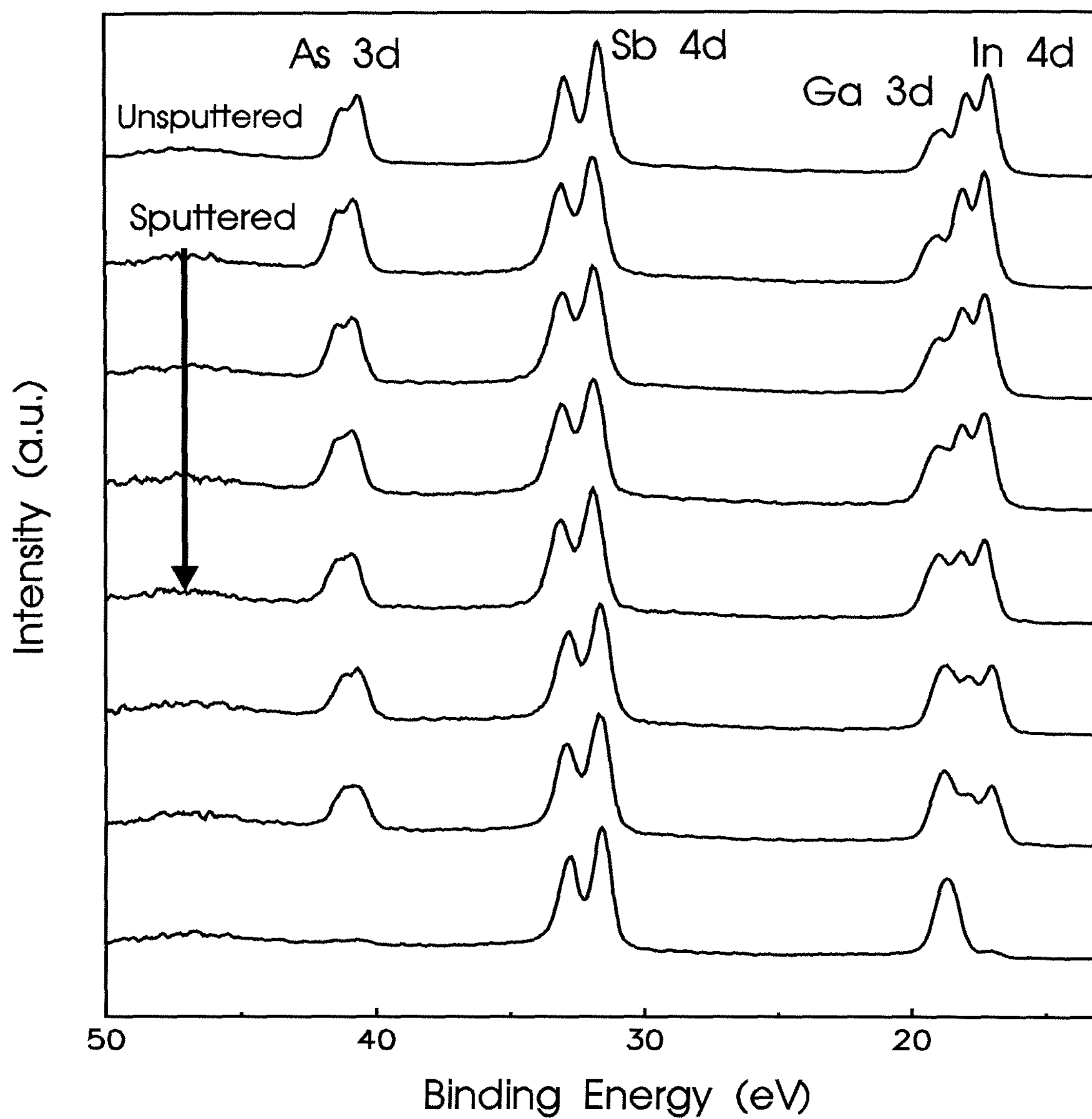

Figure 6.7: XPS/ion sputtering studies. Top profile shows XPS spectra for an unsputtered InAs-on-GaSb heterojunction. Profiles below were acquired after successive ion sputtering sequences.

20 Å InAs overlayer. After acquisition of the top spectrum, the sample was lightly sputtered using 2.5 keV Ar^+ ions at an incident angle of 61 degrees to the surface normal, and another XPS spectrum was acquired. This procedure was repeated until a clear decrease in the In and As core level peak intensities was observed. The duration of each sputter, except for the final one, was 12 seconds. The bottom profile was acquired after almost all of the InAs overlayer had been removed. The system did not have a Faraday cup installed so the ion beam current is unknown.

The effect of the ion sputtering is clearly seen in the decrease in the As $3d$ and In $4d$ peak intensities. Detailed analysis of the peak intensity ratios show two important features. First, the Sb $4d$ to Ga $3d$ peak intensity ratio decreases after the first sputter. This is very significant in that, based on the photoelectron MFPs for the two peaks, this ratio should increase as the InAs layer is thinned. The most likely explanation for the observed decrease in the Sb to Ga peak intensity ratio, given the well known surfactant properties of Sb, is that Sb is riding up on the InAs growth surface.

To verify that Sb can ride up on the InAs growth surface, a second sample consisting of 0.25 μm of InAs grown on AlSb was studied. The results of this study are shown in Figure 6.8. This figure shows the XPS core level peaks for Sb $3d$ just after growth. To ensure that the Sb signal was not due to incorporation from background Sb within the growth chamber, the sample was ion sputtered to a depth of a few tens of angstroms. The absence of an XPS Sb signal after the sputtering indicates that the Sb signal was originating from the surface of the sample and was due to Sb riding up on the InAs growth front.

The other important feature in Figure 6.7 is that the Sb $4d$ to Ga $3d$ peak intensity ratio continues to decrease even after the first few sputter/XPS sequences. This suggests the possible existence of Sb incorporation within the InAs near the interface. Unfortunately, it is not possible to determine with certainty whether or not this is true from the XPS/sputter results. This is due to the fact that sputter induced drive-in of Sb, that was originally residing on the surface of the sample

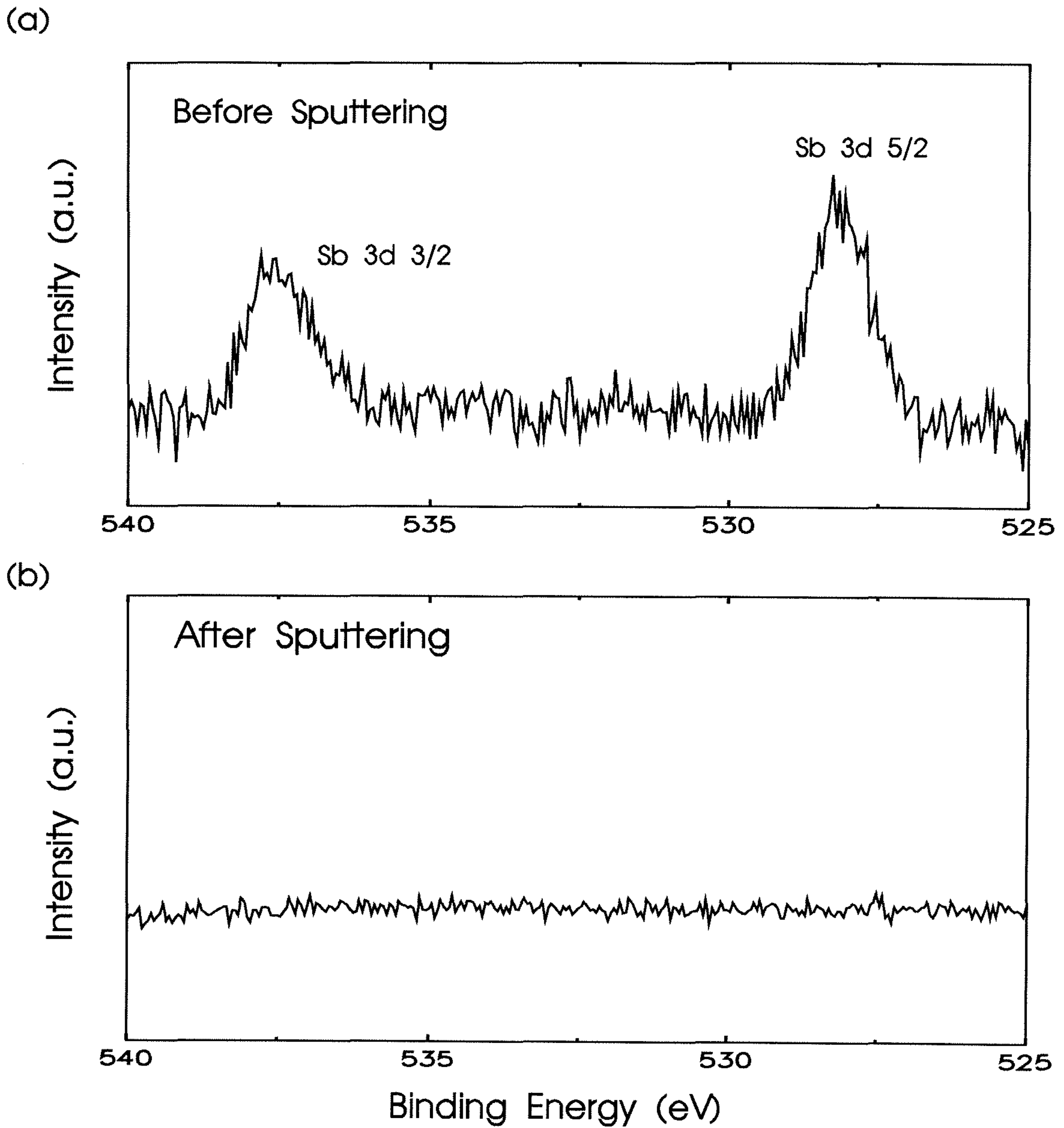

Figure 6.8: XPS studies of Sb riding on the InAs growth front. (a) shows 0.25 μm InAs layer grown on AlSb. (b) shows same sample after Ar ion sputtering to a depth of a few nm.

prior to the first sputter sequence, could result in an anomalous Sb signal from within the unsputtered InAs. This would have the same effect on the sputtering results as Sb cross-incorporation.

Since one of the main purposes of this study was to determine the mechanisms for non-abruptness of the InAs-on-GaSb interface, it was very important to determine with certainty whether or not Sb incorporates within the InAs layer. The difficulty in determining this using XPS is that any Sb signal within the InAs layer must be distinguished from the very strong Sb signal originating from the GaSb layer and the signal originating from the Sb at the surface of the InAs. The latter signal is also relatively strong, since it originates from the surface of the sample and is therefore not attenuated. Angle resolved XPS studies and analysis of higher binding energy peaks was performed; however, it was not possible to determine whether or not Sb was cross-incorporating into the InAs.

The characterization technique that eventually succeeded in determining with certainty that Sb was incorporating into the InAs was SIMS. The first attempt at this was basically to SIMS depth profile a sample consisting of a series of InAs-on-GaSb heterointerfaces. The hope was that, by overlaying the Sb and Ga profiles from the SIMS data, any cross-incorporated Sb would show itself in the form of a broader onset for the Sb signal compared to the Ga signal. That is, if cross-incorporation was occurring, then as the depth profiling proceeded through the InAs to the GaSb, the Sb signal would increase before the Ga signal. Unfortunately, the depth resolution of the SIMS was not fine enough to conclude either the existence or non-existence of cross-incorporation. It was estimated that an ideal abrupt GaSb interface would have an onset slope of 25 Å/decade due to sputter roughening and drive-in effects. Since the concentration of any Sb incorporation would be small and would decrease rapidly away from the InAs/GaSb interface, it would not be distinguishable from the inherent broadening of the signal.

The results from a second SIMS profile experiment are shown in Figure 6.9. In this experiment, the SIMS sample consisted of only two InAs on GaSb interfaces:

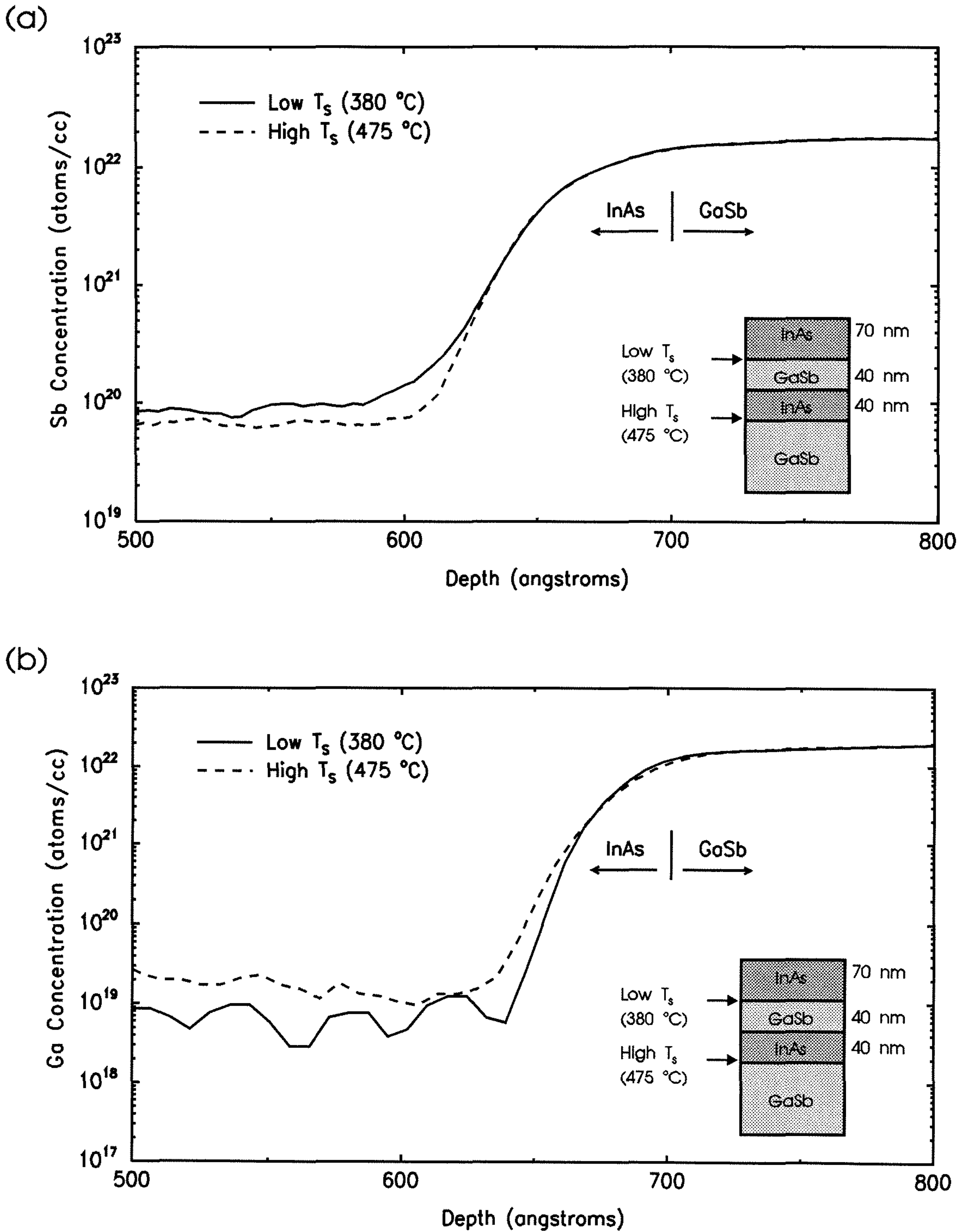

Figure 6.9: SIMS analysis of InAs-on-GaSb interface abruptness. (a) shows Sb concentration profiles for both a high and a low temperature grown InAs-on-GaSb interface. (b) shows corresponding Ga concentration profiles. The results shows cross-incorporation of Sb into InAs from the underlying GaSb.

one grown at the usual growth temperature (~380 °C), and one grown at a higher growth temperature (~475 °C), where cross-incorporation is expected to be less of an effect. At the higher growth temperatures, background As incorporates more readily into the GaSb, which is an undesirable effect for devices, but this does not affect the SIMS analysis. The hope was that by a comparison of the Sb profiles for the two growth temperatures, existence or non-existence of cross-incorporated Sb could be confirmed. The order in which the two interfaces were grown was critical in this experiment. Since the bottom interface suffers additional broadening due to sputtering effects, it was necessary to have the low temperature grown interface closer to the sample surface, so that any broadening in that interface compared to the high temperature grown interface could not be attributed to artifacts of the ion sputtering.

In Figure 6.9(a) we see that the low temperature grown interface does have a broader onset profile in the region of ~580-640 Å, despite being closer to the sample surface. Notice that we are interested in the shape of the onset profile, not in the absolute concentrations at the left-hand side of each plot. This effect in the Sb profiles was duplicated in two separate SIMS data acquisitions. To verify that this effect was indeed due to Sb cross-incorporation and not a result of anomalously high sputter induced roughness in the low temperature grown interface, the Ga profiles were also analyzed. In Figure 6.9(b) we see that the high temperature interface has a broader onset profile than the low temperature grown interface. This is consistent with increased sputter induced roughness as the SIMS profiling proceeds, and verifies that the effect seen in Figure 6.9(a) is due to cross-incorporation of Sb into the InAs from the underlying GaSb.

6.4 Summary

In conclusion, we have measured the variation in the InAs/GaSb valence band offset as a function of both interface composition (InSb-like and GaAs-like) and growth

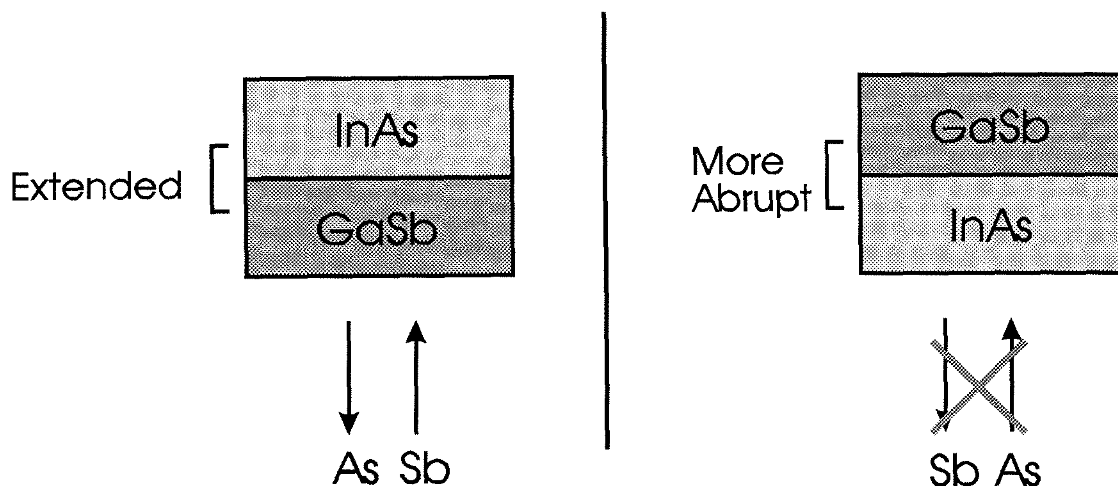

Figure 6.10: Schematic diagram of the interface asymmetry observed in the InAs/GaSb material system.

order (InAs-on-GaSb and GaSb-on-InAs). The InAs/GaSb valence band offset was observed to be independent of interface composition for both growth orders; however, upon comparison between the two growth orders, a 90 meV difference in the InAs/GaSb valence band offset was observed, with the InAs-on-GaSb interface showing the larger valence band offset. The difference in valence band offset is attributed to the extended nature of the InAs-on-GaSb interface. To test this, a GaSb-on-InAs sample was grow with an intentionally extended InSb-like interface. This resulted in a valence band offset between that obtained for the nominally abrupt GaSb-on-InAs samples and the extended InAs-on-GaSb samples. This confirmed our hypothesis that the change in the valence band offset was due to the non-abrupt nature of the InAs-on-GaSb interface.

Initial studies of interface abruptness for the InAs/GaSb heterointerface revealed an asymmetry in the abruptness for the two growth orders: InAs-on-GaSb and GaSb-on-InAs. XPS, RHEED and cross-sectional STM results showed that the InAs-on-GaSb interface was more extended than the GaSb-on-InAs interface. This is shown schematically in Figure 6.10. XPS analysis of core level peak in-

tensity ratios in heterojunction samples and studies of surface exchange reactions showed that one mode of broadening was As exchanging into the GaSb, forming an extended GaAs-like interface. The driving force for this is the large GaAs bond strength compared to that of GaSb. XPS analysis was also used to show that Sb can ride up on the InAs growth front, but cross-incorporation of Sb into the InAs from the underlying GaSb could not be confirmed with certainty. SIMS analysis was used to clearly determine that Sb cross-incorporation was occurring. The relative abruptness of the GaSb-on-InAs interface can be explained first by the fact that As is much less of a surfactant than Sb, so As cross-incorporation into GaSb from the underlying InAs is less likely, and secondly by the fact that the InSb bond strength is much less than that of InAs. Thus, as was shown in the surface exchange reactions in Chapter 5, Sb does not exchange for As into the underlying InAs.

These basic forces causing the InAs-on-GaSb interface to be extended can potentially cause problems in devices implementing As/Sb interfaces. However, in some of these devices, abruptness of the interfaces may not be crucial. In those devices where interfaces comprise a large fraction of the device and are critical to device performance (e.g., $InAs/In_xGa_{1-x}Sb$ IR SLs), it will be very important to determine first of all what effect the broadening of the InAs-on-GaSb interface has on device performance. Secondly, if the extended interface is detrimental to device performance, it must be determined whether or not the extended InAs-on-GaSb interface is fundamental or if different growth conditions and procedures can be used to grow an abrupt InAs-on-GaSb interface.

Bibliography

[1] RHEED studies performed by Dr. D.A. Collins, STM studies performed by Dr. R.M. Feenstra at IBM Watson, and SIMS studies performed by researchers at Charles Evans and Associates.

[2] E.R. Brown, J.R. Söderström, C.D. Parker, L.J. Mahoney, K.M. Molvar, and T.C. McGill, *Appl. Phys. Lett.* **58**, 2291 (1991).

[3] M. Sweeny and J. Xu, *Appl. Phys. Lett.* **54**, 546 (1989).

[4] J.R. Söderström, D.H. Chow, and T.C. McGill, *Appl. Phys. Lett.* **55**, 1094 (1989).

[5] L.F. Luo, R. Beresford, and W.I. Wang, *Appl. Phys. Lett.* **55**, 2023 (1989).

[6] D.A. Collins, E.T. Yu, Y. Rajakarunanayake, J.R. Söderström, D.Z.-Y. Ting, D.H. Chow, and T.C. McGill, *Appl. Phys. Lett.* **57**, 683 (1990).

[7] D.L. Smith and C. Mailhiot, *J. Appl. Phys.* **62**, 2545 (1987).

[8] R.H. Miles, D.H. Chow, J.N. Schulman, and T.C. McGill, *Appl. Phys. Lett.* **57**, 801 (1990).

[9] H. Sakaki, L.L. Chang, R. Ludeke, C.-A. Chang, G.A. Sai-Halasz, and L. Esaki, *Appl. Phys. Lett.* **31**, 211 (1977).

[10] G.A. Sai-Halasz, L.L. Chang, J.-M. Welter, C.-A. Chang, and L. Esaki, *Solid State Commun.* **27**, 935 (1978).

[11] L.M. Claessen, J.C. Maan, M. Altarilli, and P. Wyder, *Phys. Rev. Lett.* **57**, 2556 (1986).

[12] G.J. Gualtieri, G.P. Schwartz, R.G. Nuzzo, R.J. Malik, and J.F. Walker, *J. Appl. Phys.* **61**, 5337 (1987).

[13] Y. Foulon and C. Priester *Phys. Rev. B* **45**, 6259 (1992).

[14] R.G. Dandrea, C.B. Duke, and A. Zunger, *J. Vac. Sci. Technol. B* **10**, 1744 (1992).

[15] L.A. Hemstreet, C.Y. Fong, and J.S. Nelson, *J. Vac. Sci. Technol. B* **11**, 1693 (1993).

[16] J.P. Landesman, J.C. Garcia, J. Massies, G. Jezequel, P. Maurel, J.P. Hirtz, and P. Alnot, *J. Vac. Sci. Technol. B* **10**, 1761 (1992).

[17] M.S. Hybertsen, Materials Science and Engineering **B14**, 254 (1992).

[18] G.J. Gualtieri, G.P. Schwartz, R.G. Nuzzo, and W.A. Sunder, *Appl. Phys. Lett.* **49**, 1037 (1986).

[19] J.R. Waldrop, G.J. Sullivan, R.W. Grant, E.A. Kraut, and W.A. Harrison, *J. Vac. Sci. Technol. B* **10**, 1773 (1992).

[20] D.H. Chow, R.H. Miles, C.W. Nieh, and T.C. McGill, *J. Cryst. Growth* **111**, 683 (1991).

[21] M.W. Wang, D.A. Collins, T.C. McGill, and R.W. Grant, *J. Vac. Sci. Technol. B* **11**, 1418 (1993).

[22] R.M. Feenstra, D.A. Collins, D.Z.-Y. Ting, M.W. Wang, and T.C. McGill, *Phys. Rev. Lett.* **72**, 2749 (1994).

[23] D.A. Collins, M.W. Wang, R.W. Grant, R.M. Feenstra, and T.C. McGill, submitted to *Appl. Phys. Lett.* (1994).

[24] W.A. Harrison, E.A. Kraut, J.R. Waldrop, and R.W. Grant, *Phys. Rev. B* **18**, 4402 (1978).

[25] R.H. Miles, D.H. Chow, J. N. Schulman, D.A. Collins, M.W. Wang, R.W. Grant, and T.C. McGill, submitted to *J. Elect. Materials.*

[26] E.R. Youngdale, J.R. Meyer, C.A. Hoffman, F.J. Bartoli, C.H. Grein, P.M. Young, H. Ehrenreich, R.H. Miles, and D.H. Chow, *Appl. Phys. Lett.* **64**, 3160 (1994).

[27] M.P. Seah and W.A. Dench, *Surf. Interface Anal.* **1**, 2 (1979).

[28] C.M. Kwei and L.W. Chen, *Surf. Interface Anal.* **11**, 60 (1988).

[29] S. Tanuma, C.J. Powell, and D.R. Penn, *Surf. Interface Anal.* **17**, 927 (1991).

[30] W.C. Fan, J.T. Zborowski, T.D. Golding, and H.D. Shih, *J. Appl. Phys.* **71**, 2249 (1992).

[31] R.M. Feenstra, D.A. Collins, D.Z.-Y. Ting, M.W. Wang, and T.C. McGill, to be published in *J. Vac. Sci. Technol. B* (1994).